FLORIDA INTERNATIONAL UNIVERSITY

Miami, Florida

DISCOVERY OF FIRST-IN-CLASS SMALL MOLECULE AGONISTS OF THE RXFP2 RECEPTOR AS THERAPEUTIC CANDIDATES FOR OSTEOPOROSIS

A dissertation submitted in partial fulfillment of

the requirements for the degree of

DOCTOR OF PHILOSOPHY

in

BIOMEDICAL SCIENCES

by

Maria Esteban Lopez

2022

To: Interim Dean Juan Cendan
College of Medicine

This dissertation, written by Maria Esteban Lopez, and entitled Discovery of First-in-Class Small Molecule Agonists of the RXFP2 Receptor as Therapeutic Candidates for Osteoporosis, having been approved in respect to style and intellectual content, is referred to you for judgment.

We have read this dissertation and recommend that it be approved.

_____
Irina Agoulnik

_____
Barry Rosen

_____
Yuan Liu

_____
Juan Marugan

_____
Alexander Agoulnik, Major Professor

Date of Defense: June 21, 2022

The dissertation of Maria Esteban Lopez is approved.

_____
Interim Dean Juan Cendan
College of Medicine

_____
Andrés G. Gil
Vice President for Research and Economic Development
and Dean of the University Graduate School

Florida International University, 2022

DEDICATION

To my parents, who always supported and encouraged me to pursue my dreams.

ACKNOWLEDGMENTS

A PhD dissertation is the end result of years of hard work and commitment that you could never have accomplished alone. There are so many people that helped me during this process and shape me to become the scientist I am today. I would like to thank my mentor, Dr. Alexander Agoulnik, who has been the pillar for my success. You have always been there to point me in the right direction, but also provided me with the flexibility and independence to work and achieve my goals. I will never be able to thank you enough for all the support, guidance, and opportunities you have provided me with during these years. Thank you for making me feel valued every day and cultivate my passion for science. I am so lucky I had the opportunity to share my days in the lab with Courtney Myhr. I appreciate your patience and dedication to teach me experimental design and troubleshooting. My PhD experience would not have been the same without you. I am also grateful I had the opportunity to work with Dr. Elena Kaftanovskaya, who always had time to help me and share her knowledge. I would like to thank my committee members, Dr. Irina Agoulnik, Dr. Barry Rosen, Dr. Yuan Liu and Dr. Juan Marugan, for always providing valuable guidance and advice to improve my research and grow as a scientist. Thanks to FIU Graduate School for awarding me with the DEA and DYF fellowships.

I believe that the beauty of my dissertation resides in the interdisciplinary nature of the project, that ultimately gave me the opportunity to collaborate with many great scientists. I am extremely grateful to all our collaborators at NCATS/NIH whom I had the honor to work side by side and ensure the success of this project. Dr. Juan

Marugan, Dr. Ken Wilson, Dr. Mark Henderson, Dr. Noel Southall, Dr. Xin Hu and Dr. Abhijeet Kapoor, I am incredibly lucky that I had the opportunity to work with all of you and I will be forever grateful for all that you have taught me. I also cannot thank enough our collaborator at UAMS, Dr. Roy Morello, who taught me so much about bone physiology and also trained me in his lab for one summer to learn several bone analysis techniques.

I would also like to thank my family and friends who always believed in me, most of the time even more than I do myself. I owe everything I am today to my dearest parents, Manuel Esteban Lopez and Resurreccion Lopez Sevillano, who always put my education and happiness first. I would not have been able to come this far without your endless love and support. Finally, I am eternally grateful to my boyfriend, Hong Weng Pang. You have been my rock during these years, always there to cheer me up in my lows and also celebrate every little accomplishment. You gave me the confidence and strength to never give up. There are not enough words to express how fortune I am to have you in my life.

ABSTRACT OF THE DISSERTATION

DISCOVERY OF FIRST-IN-CLASS SMALL MOLECULE AGONISTS OF THE RXFP2 RECEPTOR AS THERAPEUTIC CANDIDATES FOR OSTEOPOROSIS

by

Maria Esteban Lopez

Florida International University, 2022

Miami, Florida

Professor Alexander Agoulnik, Major Professor

Osteoporosis is a chronic bone disease characterized by decreased bone mass and increased risk of developing fractures, predominantly observed in the elderly. The pathophysiological cause of the disease is a decrease in the activity of the bone-forming cells (osteoblasts) that alters bone remodeling in favor of bone resorption, leading to a decrease in bone mass. Recent studies identified the relaxin family peptide receptor 2 (RXFP2), the G protein-coupled receptor (GPCR) for insulin-like 3 peptide (INSL3), as an attractive target expressed in osteoblast cells to increase bone formation. The goal of this dissertation is to discover and characterize small molecule agonists of RXFP2 that are stable and can be delivered orally to promote bone growth. Several low molecular weight compounds were identified as agonists of the RXFP2 receptor using a cAMP high-throughput screen of the NCATS small molecule library. An extensive structure-activity relationship campaign resulted in highly potent and efficient full RXFP2 agonists. The selectivity and specificity of these compounds for human and mouse RXFP2 was shown in counter-screens against the related relaxin receptor RXFP1 and

other GPCRs. Using a series of RXFP2/RXFP1 chimeric receptors, *in silico* modeling and RXFP2 point mutants, we established that the compounds are allosteric agonists of the RXFP2 receptor and identified the GPCR transmembrane domains as the specific region for compound interaction. We also showed that the candidate compounds promoted mineralization in primary human osteoblasts and had low cytotoxicity in various cell types. The compound with the highest activity *in vitro* was selected for pharmacokinetics profiling in mice, showing oral bioavailability and bone exposure. Moreover, an efficacy study in wild-type female mice treated orally with the lead compound showed a significant increase of the vertebral trabecular number and thickness compared to vehicle treated controls. Overall, our study has successfully identified and characterized the first-in-class small molecule series of RXFP2 agonists, which may lead to the development of a new class of orally bioavailable drugs for the treatment of diseases associated with bone loss.

TABLE OF CONTENTS

LIST OF TABLES

TABLE PAGE

LIST OF FIGURES

FIGURES PAGE

ABBREVIATIONS AND ACRONYMS

GPCR	G protein-coupled receptor
RXFP2	Relaxin family peptide receptor 2
INSL3	Insulin-like 3 peptide
EC	Extracellular domain
LDLa	Low-density lipoprotein domain
TM	Transmembrane domain
LRR	Leucine rich repeat domain
ECL	Extracellular loop
SAR	Structure-activity relationship
HTS	High throughput screening
HTRF	Homogeneous time resolved fluorescence
RUNX2	RUNX family transcription factor 2
COL1A1	Collagen type I alpha 1 chain
ALP	Alkaline phosphatase
DMP1	Dentin matrix acidic phosphoprotein 1
M-CSF	Macrophage colony-stimulating factor
RANK	Nuclear factor kappa-B
RANKL	Nuclear factor kappa-B ligand
TRAP	Tartrate-resistant acid phosphatase
TGF-β	Transforming growth factor-beta
BMP	Bone morphogenic protein

OPG	Osteoprotegerin
PTH	Parathyroid hormone
PTHR1	Parathyroid hormone 1 receptor
β_2AR	Beta2-adrenergic receptor
LHCGR	Luteinizing hormone–choriogonadotropin receptor
LH	Luteinizing hormone
FSH	Follicle stimulating hormone
hCG	Human chorionic gonadotropin
AMH	Anti-Müllerian hormone
CAV1	Caveolin 1
GVBD	Germinal vesicle breakdown
HCO	Human calvarial osteoblasts
HAVSMC	Human aortic vascular smooth muscle cells
ADORA1	Adenosine A1 receptor
NECA	5′-(N-Ethylcarboxamido)adenosine
PKA	Protein kinase A
GMQE	Global model quality estimate
XP	Extra precision
MD	Molecular dynamics
RMSD	Root mean squared deviation
WT	Wild type
IV	Intravenous
IP	Intraperitoneal

PO	Oral
HRP	Horseradish peroxidase
BV/TV	Bone volume per tissue volume
Tb.Th	Trabecular thickness
Tb.N	Trabecular number
Tb.Sp	Trabecular separation
Conn.D	Connectivity density
Mat.D	Material density

CHAPTER 1: GENERAL INTRODUCTION

Parts of this chapter appear in the Journal of Endocrinology. October 2020. “Diverse functions of insulin-like 3 peptide”. doi:10.1530/JOE-20-0168

1.1 Osteoporosis epidemiology

Osteoporosis is a chronic bone-debilitating disease that affects approximately 10 million people in the US (1). It is also estimated that over 54 million adults are at risk of developing osteoporosis in the coming years. Osteoporosis leads to an increased risk of fractures in those over the age of 50 and is twice more common in women than men (1, 2). Furthermore, peri/post-menopausal women who have experienced prior fractures are again two times more likely to experience future fractures (3). Although deficiency in sex steroid hormone levels is believed to trigger the onset of osteoporosis in the aging population, a list of other factors have also been reported in its contribution to the disease pathogenesis, such as calcium and vitamin D malabsorption (4), decreased physical activity (5), and side effects of particular medical treatments such as glucocorticoids (6). In addition to age-related osteoporosis, there are many common diseases that can cause secondary osteoporosis, including renal osteodystrophy (7), cystic fibrosis (8), type I diabetes (9), and celiac disease (10).

Cortical bone is the outer compact bone layer that surrounds the trabecular bone, which is found in the inner porous compartment of bone (Figure 1). One of the major difference between trabecular and cortical bone is the 20% versus 80% bone

mass composition respectively (11). A biphasic mechanism of pathological bone remodeling in osteoporosis describes an initial rapid bone loss impacting the trabecular bone while the latter phase is longer lasting and affects both the trabecular and cortical bone (12, 13). Therefore, depending on age, the incidence of where fractures occur varies. Between ages 50-74, women and men tend to have higher incidences of experiencing fractures in vertebral bones, composed largely with trabecular bone. While later in life, a shift occurs where higher incidences of cortical bone fractures were reported in femur and hip (14, 15). Hospitalization data collected over the span of 12 years showed 4.9 million patients were hospitalized due to osteoporotic fractures. Of which, more than half were hip fractures, followed by vertebral fractures being the second most common (16). Osteoporotic patients who had hip fractures caused by weakened bones can suffer chronically from its effects, as 75% of these fracture patients never fully regain function and mobility. Furthermore, in severe cases 25% of these patients have died within a year of their injury (17).

The current annual cost of osteoporosis treatment to the US health system is about $57 billion (18). With an increasingly aging global population, osteoporosis will become more widespread with costs expected to increase to $95 billion annually by 2040 (18). To alleviate the projected healthcare burden that is anticipated in the coming years, it is important to educate the aging or elderly population on the resources available to them for osteoporosis diagnosis and treatment. It is staggering that approximately 80% of patients who suffered from fractures were

not been tested or provided treatment for osteoporosis (17). However, with proper care, fractures that occur in osteoporosis patients may be prevented (19), hence bringing down healthcare costs.

1.2 Osteoporosis pathology and current treatments

Bone remodeling is a process in which osteoblasts (bone-forming cells) and osteoclasts (bone-resorbing cells) maintain homeostasis of the bone tissue (20). The balanced activity of bone-forming osteoblasts and bone-resorbing osteoclasts maintains a healthy skeleton. Reduced bone density in osteoporosis is the result of increased bone resorption and decreased bone formation that ensues with aging (21).

Osteoblast differentiation involves 3 distinct stages which include cell proliferation, extracellular matrix secretion and finally matrix mineralization (22). Expression of RUNX family transcription factor 2 (RUNX2) by mesenchymal stem cells is the key driver of osteoblast linage commitment and the early proliferative phase of osteoblasts differentiation. Subsequently, RUNX2 enhances the expression of Osterix in pre-osteoblast, which further promotes expression of important osteoblastogenic factors (23). After the proliferative phase, immature osteoblasts start secreting collagen type I alpha 1 chain (COL1A1) and alkaline phosphatase (ALP) which are critical for extracellular matrix formation. Mature osteoblasts secrete osteocalcin, osteonectin and osteopontin, which are anabolic components required for mineralization of the extracellular matrix allowing calcium

hydroxyapatite to be deposited and form bone (22, 24). After finalizing the mineralization process, mature osteoblasts can become bone-lining cells, differentiate into osteocytes or dye by apoptosis (Figure 2). The majority of bone cells are composed of osteocytes, functioning as mechanosensors in regulating the activity of osteoblast and osteoclasts. Osteocyte differentiation is controlled by dentin matrix acidic phosphoprotein 1 (DMP1) expression and mature osteocytes secrete sclerostin to modulate bone turnover (25).

Osteoclasts derive from hematopoietic stem cell lineage and osteoclastogenesis is also a stepwise process regulated by two key molecular factors. The macrophage colony-stimulating factor (M-CSF) promotes proliferation and survival of pre-osteoblasts while the receptor activator of nuclear factor kappa-B ligand (RANKL) plays a major role during osteoclasts maturation and activation. RANKL binds to the RANK receptor stimulating the expression of tartrate-resistant acid phosphatase (TRAP) and cathepsin K, which are secreted by highly activated osteoclasts. To resorb bone, osteoclasts attach to the calcified matrix, create an acidic microenvironment by secreting hydrochloric acid (HCl) and degrade the collagen matrix by secreting cathepsin K (26) (Figure 2). The natural interplay between osteoblast and osteoclast intercellular signaling is critical in bone remodeling and normal bone homeostasis. Transforming growth factor-beta (TGF-β)-related bone morphogenic proteins (BMPs) stimulate osteoprotegerin (OPG) production by osteoblasts, which blocks the RANKL-RANK interaction and inhibits osteoclastogenesis (27). The characterization of cross talk between bone cells and

molecular factors regulating bone dynamics has allow researchers to identify key components which are targetable by therapeutic intervention.

The currently available treatment options for osteoporosis work by either inhibiting osteoclast bone resorption or by promoting osteoblast bone formation, both of which result in increased bone (2) (Figure 3). Bisphosphonates and RANKL inhibitor denosumab are widely prescribed anti-resorptive drugs to treat osteoporosis. Bisphosphonates are molecular analog of inorganic phosphates that promote skeletal retention through its high affinity binding to the bone mineral hydroxyapatite and induce osteoclast apoptosis (28, 29). Denosumab is a monoclonal antibody that targets RANKL to reduce its binding to RANK in osteoclasts, thereby reducing bone resorption (30). However, rare but severe side effects including atypical bone fractures and osteonecrosis of the jaw have been documented with prolonged use of these medications (31-33). Parathyroid hormone (PTH) analogs are bone-anabolic drugs prescribed only to patients that are intolerant to anti-resorptive medications, since they are expensive and require daily subcutaneous injections (34, 35). Numerous positive bone building attributes have been ascribed to using PTH as a treatment such as promoting osteoblast-precursor differentiation and osteoblast survival (36, 37). The signal for PTH-induced activation of osteoblasts is transduced through classical G-protein mediated pathway and stimulation of adenylyl cyclase for production of cAMP as intracellular stimuli (38). PTH also docks on the receptor Frizzled and in concert with other co-receptors activate canonical WNT pathway signal transduction (39).

Through a series of downstream cascades, this pathway results in an accumulation of unphosphorylated β-catenin which leads to its translocation into the nucleus to modulate WNT target genes that increase bone formation (40, 41). The newest osteoporosis treatment is a monoclonal antibody, Romosozumab, targeted against sclerostin that has the dual effect of increasing bone formation and decreasing bone resorption (42, 43). Sclerostin effectively inhibits WNT and BMP signaling pathways to block osteoblast proliferation and activity (44, 45). At the same time, sclerostin also stimulates RANKL secretion by osteocytes to increase osteoclasts maturation (46). Hence, blocking sclerostin promotes osteoblast function and bone formation. However, Romosozumab is only available as a monthly subcutaneous injection at a high cost and has been associated with the risk of adverse cardiovascular events (47, 48).

This highlights the urgent need to identify new pharmacological targets and develop cost-effective drugs that are stable, safe, and orally bioavailable for the treatment of osteoporosis.

1.3 The relaxin peptide family: RXFP2 and INSL3

The relaxin family peptide receptor 2, RXFP2 (previously known as GREAT or LGR8) is a G protein-coupled receptor (GPCR) from the relaxin family peptide receptors, which also contains 3 other members: RXFP1, RXFP3, and RXFP4 (49). The RXFP2 cognate ligand is the insulin-like 3 peptide (INSL3), which has an essential role during the transabdominal descent of the testis in embryogenesis.

Relaxin is the cognate ligand for RXFP1 and is the most studied ligand-receptor pair of the family, being well-known for its vasodilatory and antifibrotic properties. The neuropeptide Relaxin-3, the cognate ligand for RXFP3, has a role in stress and feeding responses, while INSL5 is the cognate ligand for RXFP4 and is involved in gut contractility. RXFP1 and RXFP2 are structurally highly similar and share 60% amino acid sequence identity (49). INSL3 is produced as a prepro-hormone which, after removal of the signal peptide and cleavage of the C-peptide, gives rise to the mature active hormone consisting of A and B chains linked by 2 disulfide bonds and an additional disulfide bond within the A chain. INSL3 activation of the RXFP2 receptor causes an increase in cAMP production (50, 51). Relaxin peptides from some species, like porcine relaxin (52) and human H2 relaxin (53), are capable of activating this receptor as shown in cAMP assays *in vitro*, but only at concentrations far above physiological levels. Interestingly, mouse and rat relaxin do not activate RXFP2 (53, 54).

The effect of the INSL3/RXFP2 system on male reproductive tract development was first discovered two decades ago in gene-deficient male mice with cryptorchidism or undescended testes (55-57). In humans this genital malformation has an overall incidence of around 1-3% in newborn boys and is more common in those who are born prematurely (58). Spontaneous resolution of this abnormality by 1 year of age was reported in less than 10% to more than 50% of affected boys in different studies (59, 60). For others, the most common treatment is an orchiopexy, a surgical procedure where the undescended testes

are brought into the scrotum. If left untreated, cryptorchidism can lead to infertility and testicular cancer (58, 61). In females, INSL3 is involved in ovarian follicle maturation and could play a role in the pathology of Polycystic Ovary Syndrome (PCOS) (62). In addition, a recent line of investigation has elucidated the anabolic functions of the INSL3/RXFP2 system in osteoblasts, highlighting for the first time the role of this ligand-receptor pair outside reproductive physiology (63).

1.3.1 Mechanisms of INSL3 binding and activation of RXFP2

INSL3 treatment of HEK293T cells transfected with RXFP2 causes activation of the classical adenylyl cyclase pathway via activation of $G_{\alpha s}$, resulting in increased cAMP production. At its N-terminus, RXFP2 contains a large extracellular domain (EC) with a low-density lipoprotein domain (LDLa) joined with a linker to a ten leucine rich repeat domain (LRR), followed by a seven transmembrane helical domain (TM) (Figure 4). Within the GPCR receptor family, the LDLa module is only present in RXFP1 and RXFP2 (49). Mutagenesis studies have shown the importance of the module for receptor expression on the cell surface and cell signaling (64, 65). Mutation of amino acid residues C71 and D70, which are involved in Ca-stabilization of the LDLa molecule, have been shown to decrease cell surface expression of the RXFP2 receptor and abrogate cAMP production in response to INSL3 (64). Moreover, a RXFP2 splice variant expressed in human uterine tissue that lacks the LDLa module had intact ligand binding affinity but an impaired cAMP signaling when tested in HEK293-RXFP2 cells (65). Recent studies have shown that upon receptor binding to INSL3, the RXFP2 linker region

located between the LDLa and LRRs may help to direct the LDLa to interact with the TM and activate the receptor together with the INSL3 A-chain (66).

Several structure-activity relationship (SAR) studies based on homology models have characterized the RXFP2 structure and interactions with its ligand INSL3, however no high-resolution crystal structure of the receptor has been solved to date. A model was proposed where the B-chain of INSL3 binds to high-affinity binding sites in the LRRs of RXFP2, while the A chain of INSL3 binds to low-affinity binding sites in the TM (53) (Figure 4). Mutation analysis has shown that specific residues from the LRR domain are essential for receptor cell surface expression and binding of the receptor with the B-chain of INSL3 (67). A human uterine splice variant of RXFP2 lacking one LRR repeat was found incapable of binding INSL3 and H2 relaxin (68), emphasizing the crucial role of the LRR domains in ligand binding. A study using chimeric RXFP2 receptors also demonstrated that there is a high-affinity INSL3 binding site in the LRR domain (53). When the LRR of RXFP2 was replaced with the RXFP1 LRR, the affinity of the receptor was lower than the wild-type (WT) RXFP2 receptor (53). Studies using RXFP2 chimeric receptors also suggested that there is a low-affinity INSL3 binding site in the extracellular loops of the TM domain, since RXFP2 chimeras with the LRR and extracellular loops replaced with RXFP1 were unable to bind INSL3 or induce cAMP production (69). In INSL3, H36, R40, V43, R44, and T53 located within the B-chain form a receptor binding motif, with T53 appearing to be the most crucial (51, 70, 71). Shortened mimetics of the B-chain demonstrated micromolar range binding affinity to RXFP2

and antagonistic activity when used in combination with INSL3 (72, 73). More potent antagonists based on the B-chain sequence have been designed through systematic efforts to induce α-helicity in the isolated INSL3 B-chain by constraining the B-chain with a short region of A-chain or dimerizing the B-chain (71).

1.3.2 RXFP2 cellular signaling

Signal transduction has been primarily studied in HEK293T cells transfected with RXFP2. Stimulation of RXFP2 in these cells results in its coupling to $G_{\alpha s}$, which leads to cAMP production and further activates CRE-dependent gene transcription (74). On the other hand, coupling of $G_{\alpha oB}$ also occurs, which is involved in negative modulation of cAMP accumulation in HEK293T cells (75). Unlike in relaxin/RXFP1 signaling, there is no evidence of RXFP2 signaling in HEK293T cells through the $G_{\alpha i3}$ isoform, which inhibits cAMP production (76) (Figure 4).

Additional studies performed on cells that endogenously express RXFP2 have provided insight into cell-dependent responses to INSL3 treatment. Rat gubernacular and mouse Leydig cells showed increased production of cAMP upon stimulation with INSL3 (50, 77) while the opposite effect was reported in rat female and male primary germ cells (78). Stimulation with INSL3 resulted in an inhibition of intraoocyte cAMP levels and forskolin-induced cAMP in seminiferous tubular cells. Studies using myotubes derived from C2C12 cells have shown increased phosphorylation of AKT, mTOR, and S6 after INSL3 treatment, identifying a possible downstream cAMP pathway activated by INSL3/RXFP2 (79). In the

human osteoblast cell line MG-63, INSL3 stimulation also increased intracellular cAMP production (63). Further investigations of INSL3/RXFP2 signaling in primary human osteoblasts have shown increased MEK and ERK1/2 phosphorylation via the AC/cAMP/PKA pathway (80). Surprisingly, a classical regulatory mechanism of GPCR signaling, beta-arrestin-induced internalization and desensitization, does not appear to be a major factor in RXFP2 regulation. RXFP2 has a sustained cAMP response when stimulated with INSL3, which may be due to reduced recruitment of beta-arrestin to the cell surface and attenuated internalization of the receptor (81).

To date, only a few studies have been performed to analyze whole transcriptome changes in response to INSL3. To identify downstream pathways activated by INSL3/RXFP2 signaling, rat gubernacular bulb cells isolated from embryos on day 17 were treated with INSL3 and analyzed using Affymetrix microarrays (82). Male gubernacular bulb cells responded to INSL3 with changes in expression of genes involved in cAMP, BMP, WNT/β-catenin, pluripotency and several other signaling pathways, including genes playing a role in osteoblasts, osteoclasts, and chondrocyte participation in rheumatoid arthritis. As expected, Gene Ontology (GO) analysis revealed changes in genes involved in GPCR signaling, extracellular, and plasma membrane functions. In addition, several GO related to neurogenesis were altered by INSL3 (82).

More studies need to be conducted to fully understand the signaling mechanisms of INSL3/RXFP2 in various cells and their biological significance. This is also important for efficient targeting of this receptor in future therapeutic applications, providing for specificity of response while avoiding potential harmful off-target effects.

1.3.3 INSL3 in male reproductive physiology

In mammalian male reproductive organs, INSL3 is produced mainly in the testicular Leydig cells (83-86) and RXFP2 is expressed in testis in Leydig cells as well as in germ cells, especially at the post-meiotic stage (86-88). INSL3 is considered an indicator of normal Leydig cell function and overall reproductive health in men (89). Human male fetuses produce INSL3 during gestation, measured at approximately 0.12 ng/ml in amniotic fluid (90). This level of circulating INSL3 is maintained from birth until the age of 3 months, at which point it begins to decrease (91). The INSL3 level rises again through puberty and is sustained between 0.5-1 ng/ml in adult men (92). During puberty, luteinizing hormone (LH) drives Leydig cell maturation, which coincides with a spike in INSL3 production that positively correlates with an increase of sex hormones such as follicle stimulating hormone (FSH), LH, and testosterone (93). Low INSL3 serum levels are characterisitic of orchidectomized and infertile men, individuals with Klinefelter's syndrome, hypogonadotropic hypogonadism, and cryptorchidism (92, 94). Males with anorchism have no detectable levels of INSL3 (92). To further investigate the correlation between INSL3 and LH, subjects with unilateral

orchiectomy were treated with a single dose of human chorionic gonadotropin (hCG), resulting in elevated testosterone levels around 3 days after treatment but no impact on INSL3 levels (92). However, when hypogonadotropic hypogonadism subjects were treated with repeated doses of hCG over several months, INSL3 levels increased (92). In agreement with these findings, normal human male subjects who were gonadotropin deprived had decreased INSL3 levels. Such patients had spontaneous partial recovery of INSL3 to 38.9% of baseline as opposed to an almost complete recovery of testosterone at 80.2% (95). It was also shown that direct hCG stimulation of Leydig cells *in vitro* does not increase INSL3 expression (96). These findings suggest that long-term LH stimulation of Leydig cells is required for INSL3 expression but testosterone production is not co-regulated with INSL3 in mature Leydig cells.

Testicular descent during embryogenesis consists of a transabdominal phase followed by an inguinoscrotal phase. The INSL3/RXFP2 system has a determining role in the development of the gubernaculum ligament and testicular descent during the transabdominal phase (55-57, 88). The inguinoscrotal phase of testes descent is known to be androgen mediated, but studies have also shown the possible synergistic involvement of INSL3/RXFP2 during this phase (97). Genetic ablation of *Insl3* in mice has resulted in various degrees of intraabdominal cryptorchidism, the most common congenital birth defect in newborn boys. *Insl3*$^{-/-}$ adult mice showed decreased testes size, lesions in the seminiferous tubules, absence of spermatid and mature sperm, and gubernaculum underdevelopment

(55, 56). Interestingly, *Insl3*$^{-/-}$ males have normal copulatory behavior and normal seminal vesicles and prostate weights, which demonstrates that this form of cryptorchidism is androgen independent (55, 56). On the other hand, transgenic female mice overexpressing *Insl3* develop bilateral inguinal hernias due to the descent of the ovaries toward the processus vaginalis via outgrowth of the gubernaculum (98).

Rxfp2 involvement in cryptorchidism was discovered in mutant mice with a 550kb deletion containing the gene in chromosome 5 (57). Breeding of these mutant mice, known as *crsp*, resulted in bilateral intraabdominal cryptorchidism in male homozygotes. All *crsp/crsp* adult males had small testes size and epididymis, absence of spermatogenesis, vacuolization of Sertoli cells, lesions of the seminiferous tubules and were infertile (57). Recently, more sophisticated genetic tools were used to generate transgenic mouse lines to further prove the involvement of *Insl3* and *Rxfp2* in testicular descent. *Rxfp2* with knockin LacZ reporter allowed for detection of *Rxfp2* expression in gubernaculum, Leydig cells, and postmeiotic spermatogenic cells in testis (88). Cryptorchidism was also observed when *Rxfp2* was deleted specifically in gubernacular embryonic mesenchymal tissue using a Cre/loxP approach, but the abnormal phenotype was not found after deletion of *Rxfp2* in gubernacular striated or smooth muscle cells (88). This finding further demonstrates the importance of *Rxfp2* for testicular transabdominal descent via regulation of the outgrowth of the gubernaculum in mice.

INSL3/RXFP2 signaling induces WNT and BMP developmental pathways and drives morphogenetic changes in gubernaculum (82). It was shown that *Rxfp2-/-* male mice embryos experienced a dramatic decrease in expression of developmental signaling molecules β-catenin, NOTCH1, and WNT1 in the gubernaculum (99). The disruption of normal RXFP2 expression resulted in the failure of the testes to descend away from the caudal pole of the kidney at day E16.5, as well as an underdeveloped gubernaculum (99). To further understand the pathways leading to the failure of gubernacular development, *β-catenin* or *Notch1* was ablated in the gubernacular ligament. In these males, the gubernacular ligament had a lack of muscle layers, which was consistent with previous observations in *Rxfp2*-deficient mice (99).

Recently, a mammalian phylogenetic study in Afrotherians revealed that 4 testicond species from this lineage had loss of functional *RXFP2* and *INSL3,* which correlates with a lack of gubernaculum and testes descent, demonstrating the highly evolutionarily conserved function of this ligand-receptor pair (100).

Orchidopexy in *Insl3*$^{-/-}$ and *crsp/crsp* male mice recovered spermatogenesis at least partially, suggesting that the increased testicular temperature as a result of cryptorchidism may be a contributing factor for the defects observed in mouse male germ cell differentiation (56, 57). Additionally, conditional deletion of *Rxfp2* in germ cells of adult male mice did not affect spermatogenesis, fertility, or germ cell survival (88).

Although studies in mice showed that deletion of *Insl3* or *Rxfp2* does not appear to have a direct impact on spermatogenesis or germ cell survival, other studies have drawn links between INSL3 levels and improved survivability of germ cells. Studies in gonadotropin compromised male rats showed the ability of INSL3 to suppress germ cells apoptosis (78). In a human contraceptive study, subjects who were given a combination of testosterone and progesterone as contraceptive treatment for 24 weeks but did not display azoospermia had higher serum INSL3 levels compared to those who were azoospermic (101). This suggests that INSL3 may prevent apoptosis in male germ cells as non-azoospermic subjects also have higher sperm concentration, which positively correlated with INSL3 serum levels (101). Treatment of boar with neutralizing antibody against INSL3 also showed similar results, in that lower levels of available INSL3 reduced anti-apoptotic XIAP and BCL2 levels and sperm concentration (102). Taken together, these studies demonstrate that INSL3 may play a role in regulating apoptosis and turnover of male germ cells, especially when spermatogenesis is under stress conditions.

Clinical case studies in cryptorchid patients have identified dozens of mutations in *INSL3* and *RXFP2* genes (64, 103-106) (Figure 5). Functional analysis of these *INSL3* mutants in cells transfected with the RXFP2 receptor showed a decreased cAMP response for V18M, P49S, R73X and R102C mutants, suggesting potential clinical relevance (103, 104). A recent genetic analysis in patients with testicular torsion has also described mutations in the *INSL3* gene, including a T60A polymorphism in the C-peptide region (107), a common polymorphism that was previously identified with the same frequency in cryptorchid and control patients

(108). A missense mutation variant T222P in the LRR of RXFP2 impairs receptor expression on the cell surface and has been strongly associated with cryptorchidism (64, 105). However, a more recent screen of cryptorchid subjects in Spanish and Italian populations revealed that carrying this mutation may lead to increased risk of cryptorchidism only in the Italian population (109). Another missense mutation, G499E, was identified in the third TM domain of RXFP2 by conducting whole exome sequencing of 4 brothers who presented with bilateral cryptorchidism (106). A mutagenesis study further validated that G499E is a loss of function mutation. The G499E RXFP2 receptor showed no ligand binding or activation when stimulated with INSL3, and the mutant receptor expression on the cell surface was about 12% of the WT RXFP2 (106). Significantly, in all studies only heterozygous mutant carriers were found. Thus, while mutation analysis in cryptorchid patients suggests a possible contribution of *INSL3* and *RXFP2* in this abnormality in men, further studies are necessary to prove a direct cause-effect relationship.

1.3.4 INSL3 in female reproductive physiology

In females INSL3 is produced primarily in the follicular theca interna cells of the ovary, where RXFP2 expression is also found (78, 84, 110, 111). Lower levels of INSL3 and RXFP2 expression have also been detected in the corpus luteum and uterus (83, 84, 110-112). INSL3 in healthy women is first detectable during the late stages of puberty (113), and serum levels remain around 79 pg/ml, which is much lower than in men (114). INSL3 levels in women fluctuate in a phasic manner

throughout the menstrual cycle and become undetectable after menopause (115). The secretion of INSL3 is at its lowest levels during menses and spikes to significantly higher levels during the follicular phase of the menstrual cycle, concordant with the recruitment of growing antral follicles (114). The highest levels of INSL3 positively correlated with pre-ovulatory ovarian hormones such as Anti-Müllerian hormone (AMH) and Inhibin B (114). The LH spike during ovulation negatively correlates with INSL3 and pre-ovulatory hormones and this is a causal relationship that was also described in studies on bovine theca cells (114, 116). In primary bovine theca interna cells, LH at low doses stimulates production of INSL3, but higher LH levels comparable to those measured during ovulation had an inhibitory effect on INSL3 production (116). Through further testing, it was revealed that INSL3 production is stimulated by LH and estradiol, acting through the protein kinase A pathway (116). A feedback loop between INSL3 and steriodogenesis in theca cells was established when siRNA knockdown of RXFP2 sharply reduced *CYP17A1* expression and androstenedione secretion (117). Further, the inhibition of CYP17A1 reduced androgen secretion and *INSL3* and *RXFP2* expression. Additionally, treatment of theca cells with BMP6 dramatically down-regulated expression of *INSL3* along with *CYP17A1* and several other key steroidogenesis genes. Taken together, these studies showed that estrogen-induced INSL3 production is a key mediator during follicular phase steroidogenesis, and levels of LH that peak at ovulation negatively regulate INSL3.

Abnormal levels of INSL3 in woman have been shown to correlate with Polycystic Ovary Syndrome, PCOS (62, 118, 119). Patients with PCOS were categorized by their menstrual cycles into amenorrheic, eumenorrheic, or oligomenorrheic (62). Amenorrheic and oligomenorrheic groups had significantly higher levels of INSL3 and AMH compared to control women, which suggests a potential role in the follicle arrest and anovulation typically seen in this disease (62). Women with abnormal anatomical characteristics such as ectopic ovaries were also identified from a sample of PCOS women with positively correlated INSL3 and androgen levels. (118). A recent study suggested that the common polymorphism T60A of the *INSL3* gene could increase the risk of developing PCOS (119). Although this finding would need to be confirmed, it provides an argument towards a relationship between INSL3 and development of PCOS.

Rodent models have also proved useful in establishing the role of the INSL3/RXFP2 system in female reproduction (55, 78, 112) . Deletion of the *Insl3* gene resulted in abnormal estrous cycle and reduced fertility (55) further demonstrating the involvement of INSL3 in maintaining healthy reproductive functions. *Rxfp2* and *Caveolin 1* (*Cav1*) have been associated with epithelial and stromal cell growth and overall homeostasis in the mouse uterus, as the rate of uterine cyst development sharply increased when both *Cav1* and *Rxfp2* were deleted in females (112). INSL3 induces oocyte maturation in rats, shown by a dose-dependent increase in germinal vesicle breakdown (GVBD) after INSL3 treatment (78).

1.3.5 Role of INSL3 in bone and skeletal muscle physiology

INSL3/RXFP2 signaling has been shown to play a role in maintaining normal bone characteristics in both mouse and human (63, 80). Young men with cryptorchidism carrying the T222P mutation in the *RXFP2* gene have significantly reduced bone density, resulting in osteopenia and osteoporosis (63). Expression of RXFP2 has been shown in human osteoblasts and osteocytes, as well as in mouse osteoblasts (63, 120). Treatment of primary human osteoblasts with INSL3 showed a dose-dependent increase in proliferation (63). Moreover, femurs from *Rxfp2*$^{-/-}$ mice had significantly decreased bone mass and trabecular number compared to WT mice. A histomorphometric analysis of the lumbar spine of mutant mice also revealed reduced bone formation rate and mineralization surface compared to WT (63). Furthermore, INSL3 has been shown to regulate the expression of genes involved in differentiation and maturation of primary human osteoblasts, such as *ALP*, *COL1A1*, *COL6A1*, and *Osteonectin* (80). Treatment of primary human osteoblasts with INSL3 improved mineralization of the bone matrix (80). Decreased INSL3 levels in Klinefelter's syndrome patients are correlated with increased levels of serum sclerostin, which is involved in bone catabolism by inhibiting osteoblasts differentiation and stimulating osteoclasts activation (120). This relationship was further explored in cultured osteocytes, which had reduced expression of sclerostin when treated with INSL3. The negative correlation between INSL3 and sclerostin provides insights into the impact of INSL3 on bone health and its potential therapeutic value (120).

RXFP2 was also suggested to have an important role in maintaining proper function of muscular tissues (79). INSL3 treatment of myotubes differentiated from C2C12 skeletal muscle cells resulted in increased cell size compared to untreated control. Expression of myosin heavy chain can be induced by INSL3, which leads to increased protein synthesis in these cells (79). Denervated muscles in *Rxfp2* $^{-/-}$ mice developed greater muscle loss compared to WT mice. Additionally, the tibialis anterior muscle had significantly decreased beta-oxidative fibers, while the soleus muscle showed a significant decrease in fast and slow fibers in these mice. The soleus muscle absolute force, when normalized to the muscle mass of *Rxfp2*$^{-/-}$ mice, was also decreased compared to WT mice (79).

The emerging role of INSL3/RXFP2 in the musculoskeletal system reveals potential new targets for INSL3 and synthetic RXFP2 agonists in the treatment of diseases associated with bone and muscle loss.

1.3.6 INSL3 role in other organs

In adult rat forebrain, high *Rxfp2* gene expression has been found in the thalamus, frontal and motor cortices. Receptor autoradiography showed INSL3 radioligand binding of RXFP2 in the thalamus and striatum nucleus (121), suggesting a potential role of the INSL3/RXFP2 system in motor and sensory brain functions. Additionally, INSL3 and RXFP2 in the eye may play a role in wound healing (122). Protein expression has been found in the human and mouse ocular surface and tears. A scratch test assay performed on human conjunctival and corneal epithelial

cells showed increased migration and proliferation when treated with INSL3 (122). A mouse corneal ulcer model was used to test topical application of INSL3, which was determined to be effective in re-epithelialization and healing of corneal wounds (122). INSL3 radioligand binding was also detected in the glomeruli of the renal cortex of post-natal and adult rats (123). It has been proposed that INSL3 in the kidney inhibitions glomerular cell proliferation, which may be beneficial in targeting glomerular diseases that are associated with uncontrolled mesangial cell proliferation (123).

The role of INSL3/RXFP2 system has also been tested in cancer pathology (124, 125). INSL3 *in situ* hybridization and immunoreactivity was shown in benign prostate hyperplasia and neoplasia. Stimulation of human prostate carcinoma cell line PC-3 with INSL3 resulted in cAMP production and showed a positive correlation with increased cell migration (124). RXFP2 expression has also been detected in human thyroid carcinoma tissues (125). Expression of INSL3 in xenotransplants with the FTC133 human thyroid carcinoma cell line showed increased tumor growth in nude mice compared to FTC133 cells not transfected with INSL3 (125). Additionally, *in vitro* INSL3 treatment of these tumor cells led to increased motility, which is indicative of enhanced tumor metastatic capacity. Treatment of HUVECs with INSL3 also showed significant tube formation, similar to the VEGF control, which suggested promotion of angiogenesis (125). As future studies elucidate the role of the INSL3/RXFP2 in these systems, there may be

additional opportunities for therapeutic intervention with RXFP2 agonists or antagonists.

1.4 Thesis hypothesis and specific aims

The role and involvement of the INSL3/RXFP2 system in health and disease has greatly expanded beyond the initial finding of its role in testicular descent. The unique RXFP2 structural features, cell surface expression, and confined expression pattern make it a potentially desirable pharmacological target for various diseases including osteoporosis. To date, no clinical studies have been conducted targeting INSL3 or RXFP2, nor has a systemic analysis of recombinant INSL3 stability *in vivo* been reported. Studies of the effect of INSL3 injections on testicular functions in rats have shown that INSL3 can pass through the blood-testis barrier (126) and protect against GnRH antagonist-induced apoptosis in germ cells (78). Various approaches previously used to improve the stability of relaxin (127-129) can be applied to INSL3 to design biologicals with the full spectrum of INSL3/RXFP2 downstream signaling. Alternatively, small molecule agonists have proven to be an attractive alternative to therapies with peptide ligands due to improved stability and potential oral bioavailability. A high-throughput screening (HTS) of small molecules successfully identified the first RXFP1 agonist, compound ML290, which has antifibrotic effects recently demonstrated in a mouse model of liver fibrosis (130). Due to the structural similarities of RXFP1 and RXFP2, the same approach that was used for the selection and optimization of ML290 can be applied to identify a small molecule

agonist that specifically targets RXFP2. The development of such stable agonists will provide not only novel insights into RXFP2 signaling mechanisms, but potentially also become a useful osteoanabolic agents for the treatment of chronic bone diseases like osteoporosis.

Specific Aim 1: Identification, optimization, and characterization of specific RXFP2 small molecule agonists. The identification of RXFP2 agonists will be accomplished through a primary HTS of a small molecule compound library at NCATS/NIH using a Homogeneous Time Resolved Fluorescence (HTRF) cAMP assay, followed by an extensive SAR study to increase agonist activity and efficacy, as well as to optimize the pharmacological and physical properties of the identified compounds. The identified hits will be further confirmed using a series of secondary assays including an orthogonal luciferase cAMP assay, counter-screen assays, as well as cytotoxicity studies in various primary human cells. The bone formation activity of the final leads will be assessed by measuring osteoblast mineralization *in vitro,* followed by RNAseq gene expression profile analysis.

Specific Aim 2: Identification of agonist-receptor interactions for RXFP2 activation. An agonist-receptor binding model will be further establish using *in silico* molecular dynamics modeling combined with the analysis of RXFP2 agonist cAMP activity in a series of RXFP2/RXFP1 chimeric receptors and site-directed receptor mutagenesis studies.

Specific Aim 3: Determination of the biological activity of lead RXFP2 agonists *in vivo*. To demonstrate that the final lead compounds can activate the mouse RXFP2 receptor and are biologically active *in vivo*, gubernaculum development will be assessed in female embryos after injecting pregnant females with compounds. Pharmacokinetics studies of the compound with the highest osteoblast mineralization *in vitro* will determine oral bioavailability and bone exposure for *in vivo* studies. The bone formation activity of the final compound will be evaluated by micro-CT analysis in WT female mice in comparison to transgenic female mice overexpressing INSL3 as positive controls. Biomechanical analysis will also be used to measure bone strength after compound treatment.

We hypothesize that the experimental approaches described will lead to the identification and biological characterization of the first-in-class RXFP2 small molecule agonist as a potential therapeutic candidate for the treatment of osteoporosis.

1.5 Figures and tables

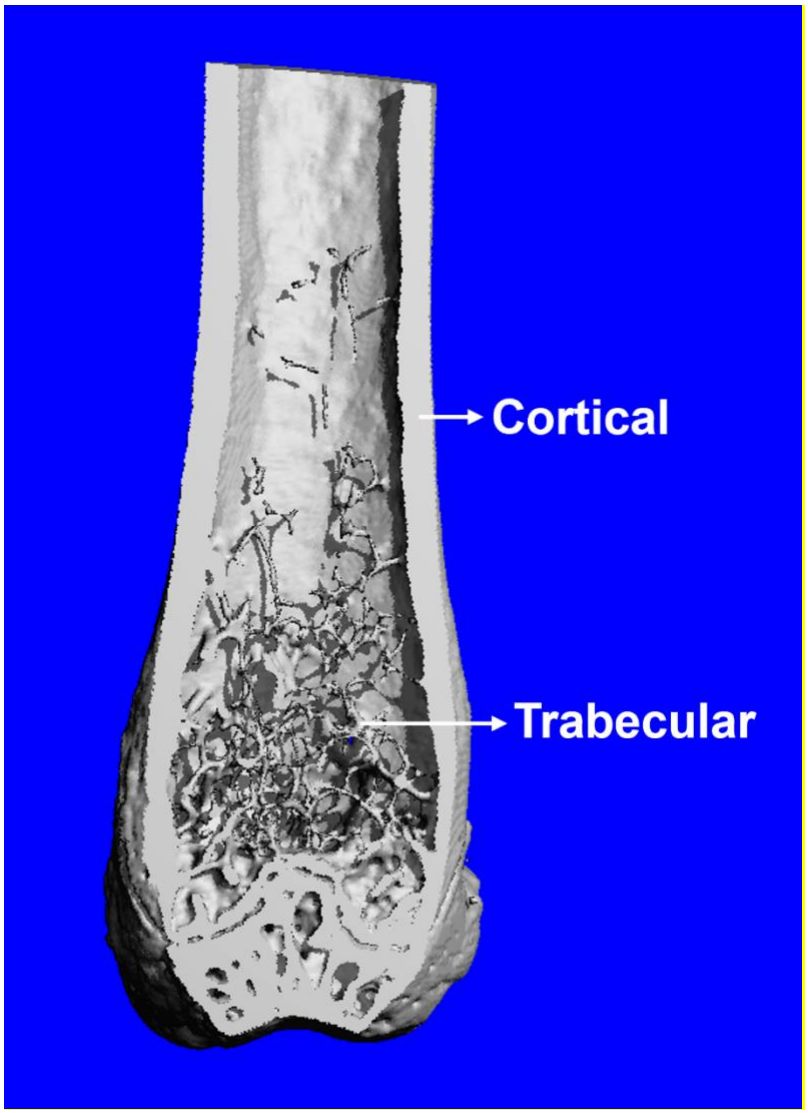

Figure 1. Micro-CT 3D reconstruction of a mouse distal femur. Median coronal view showing location of cortical and trabecular bone.

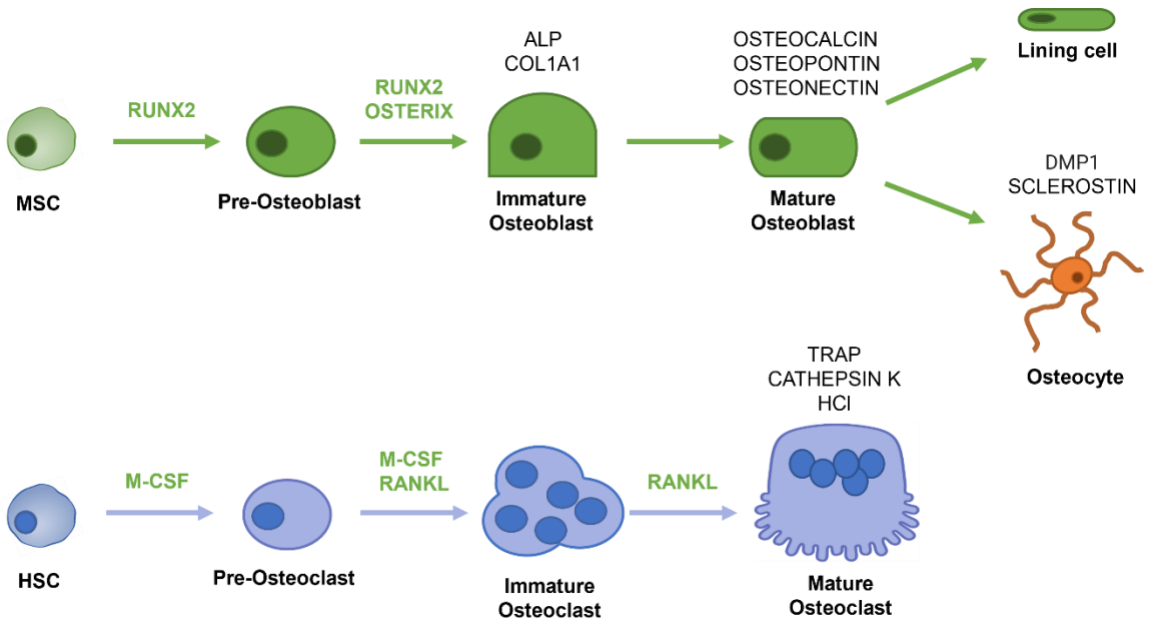

Figure 2. Schematic representation of osteoblast and osteoclast differentiation. Runx2 drives mesenchymal stem cells (MSC) commitment to the osteoblast linage, which is further supported by Osterix. Committed immature osteoblasts start secreting the extracellular bone matrix and when osteoblasts maturation is completed, they will mineralize the matrix and form mature bone. After the mineralization process is finalized, the mature osteoblasts can become bone lining cells or progressively differentiate into osteocytes of the bone matrix. Osteoclasts derive from hematopoietic stem cells (HSC). M-CSF and RANKL are secreted by osteoblasts and have a primordial role during early osteoclasts differentiation and activation of mature osteoclasts respectively.

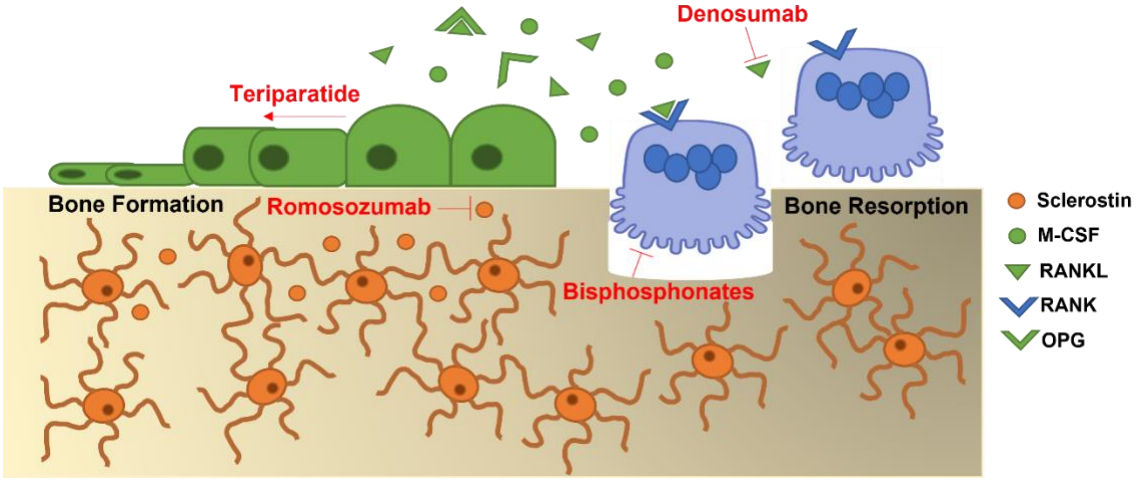

Figure 3. Bone remodeling and effects of osteoporosis treatments. During normal bone remodeling, osteoblasts (bone-forming cells, green), osteoclasts (bone-resorbing cells, blue), and osteocytes (mature bone cells, orange) work together to maintain heathy bones. Osteoblasts secrete RANKL that binds to the RANK receptor in osteoclasts and activates bone resorption. Osteoblasts also secrete OPG, which targets RANKL to prevent its binding to the RANK receptor and inhibits osteoclasts activity. Osteocytes secrete sclerostin that inhibits the Wnt/β-catenin signaling pathway in osteoblasts and decreases bone formation. Bisphosphonates are anti-resorptive drugs that induce osteoclasts apoptosis. Denosumab is also an anti-resorptive medication that inhibits RANKL and suppresses the activity of osteoclasts. Teriparatide is an anabolic drug that promotes osteoblasts differentiation, activation, and survival. Romosozumab works by inhibiting sclerostin and therefore, increases osteoblast activity while decreases osteoclast maturation.

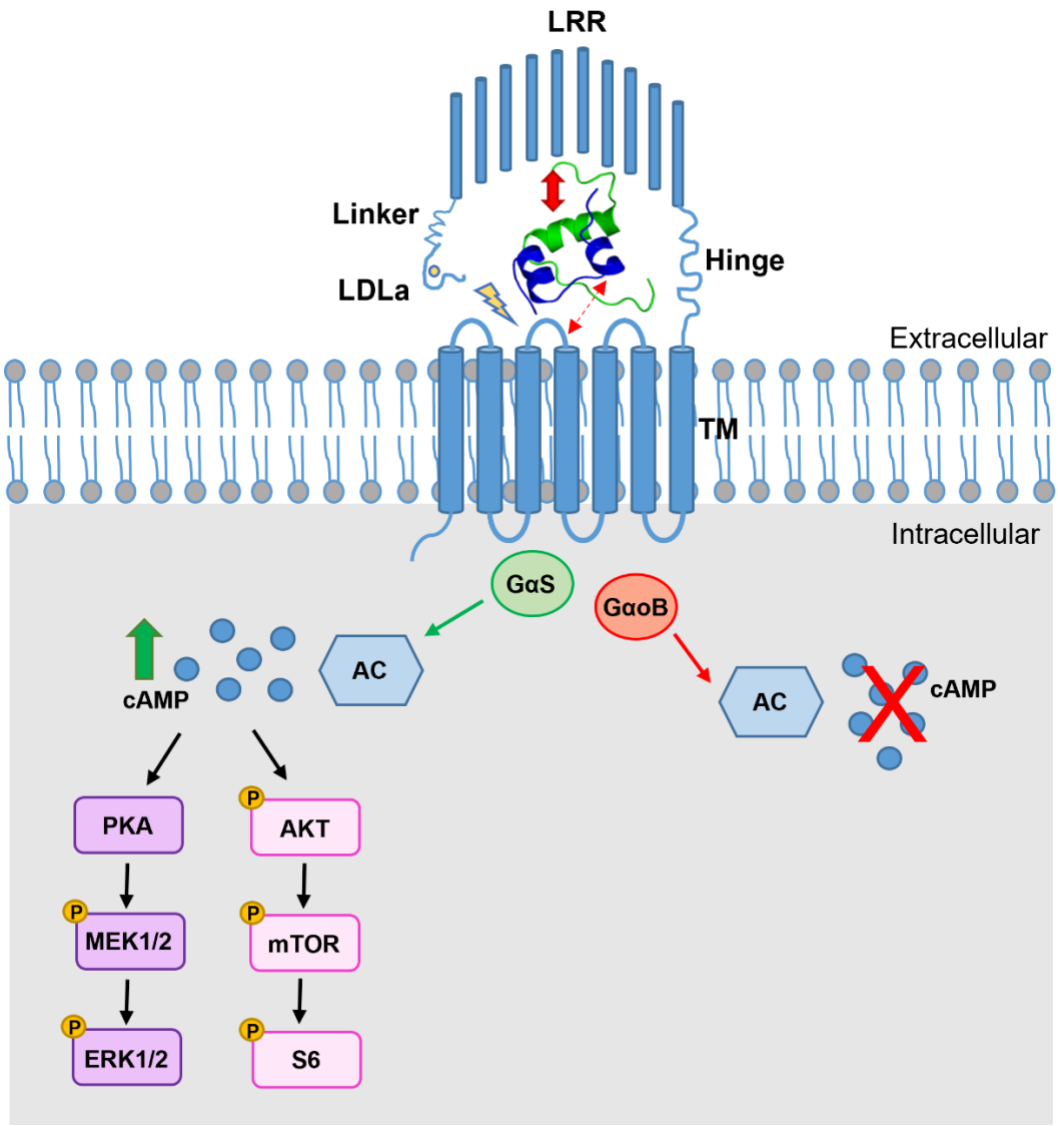

Figure 4. INSL3/RXFP2 binding-activation model and signaling mechanisms. The RXFP2 receptor consists of a low-density lipoprotein (LDLa), 10 leucine rich repeat domains (LRR) and 7 transmembrane helical domains (TM). The mature INSL3 hormone is formed by a B-chain and A-chain joined by disulfide bonds. The predicted INSL3/RXFP2 binding model shows a B-chain high affinity-binding site in the LRR (bold arrow), as well as an A-chain low affinity-binding site in the extracellular loops of the TM (dotted arrow). After binding, the Linker region helps direct the LDLa module towards the extracellular loops of the TM to activate the receptor, together with the N-terminal region of the INSL3 A-chain (lightning symbol). INSL3 activates the RXFP2 receptor causing coupling to the $G_{\alpha s}$ subunit, which activates adenylyl cyclase and increases cAMP levels. This signaling mechanism has been proven in mouse Leydig and C2C12 cells, rat gubernacular cells, MG63 cells and primary human osteoblasts. cAMP downstream signaling through phosphorylation of AKT, mTOR, and S6 has been found in C2C12 cells, as well as activation of the MAPK/ERK pathway in primary human osteoblasts. In rat female and male germ cells, INSL3 activation of RXFP2 has been shown to cause coupling to the $G_{\alpha oB}$ subunit, which inhibits adenylyl cyclase and decreases cAMP levels. *INSL3 structure from PDBe (entry 2H8B).*

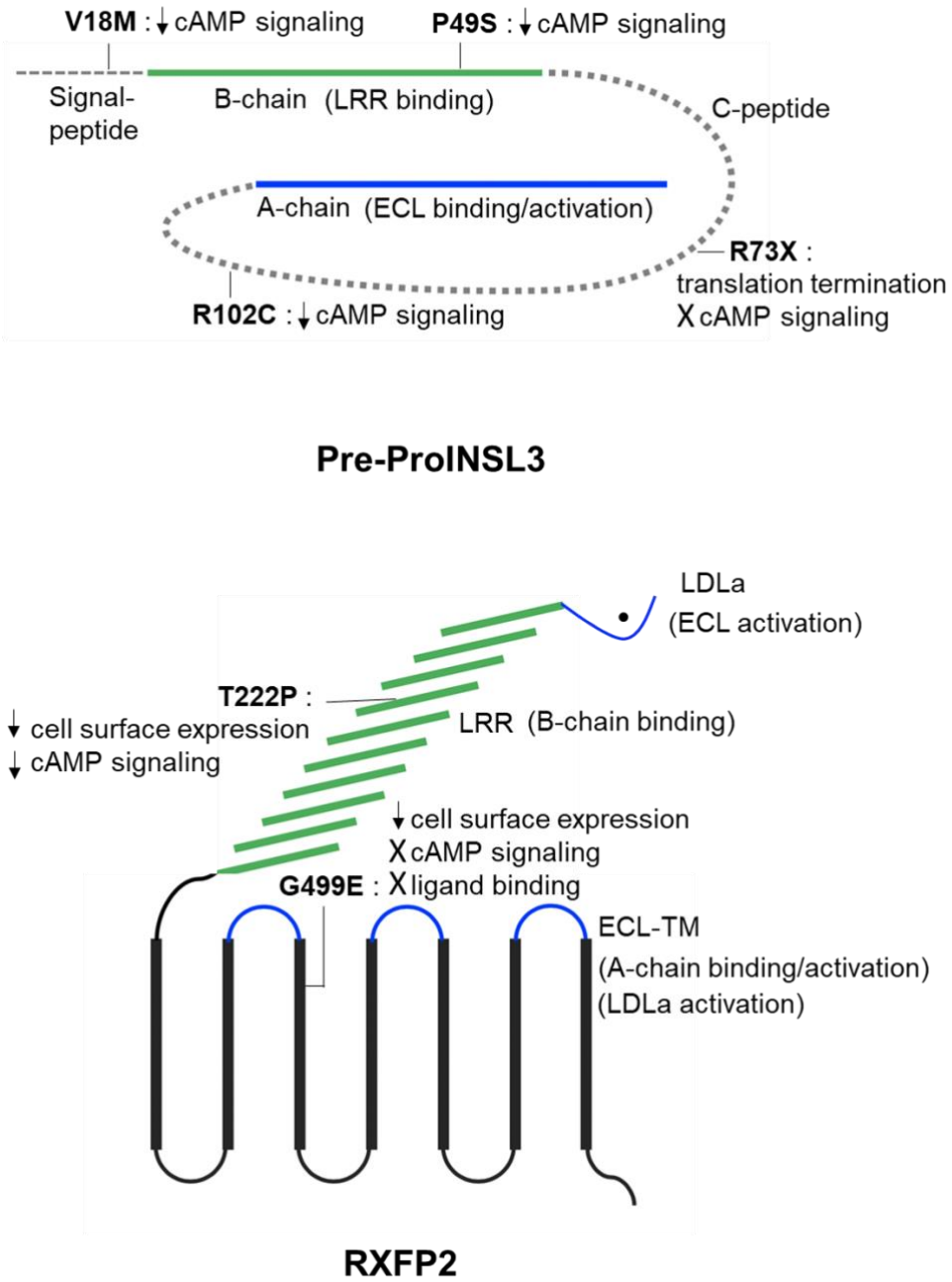

Figure 5. Mutation sites in *INSL3* and *RXFP2* genes found in cryptorchid patients. Several mutations in INSL3 and RXFP2 have been found clinically relevant based on mutagenesis studies. INSL3 mutants V18M, P49S and R102C have decreased cAMP responses compared to WT INSL3. The mutant R73X produces a truncated INSL3 containing only the B-chain region of the peptide, which is insufficient to induce cAMP signaling. RXFP2 mutants T222P and G499E are not well expressed on the cell surface, which could explain the signaling impairment seen during functional analysis. Mutations INSL3-P49S and RXFP2-T222P are of great importance due to their location in the B-chain-LRR binding site. The newly discovered mutant RXFP2-G499E has void cAMP signaling and binding, suggesting its potential importance in the binding and activation site located in the extracellular loops of the transmembrane domain (ECL-TM).

CHAPTER 2: IDENTIFICATION, OPTIMIZATION, AND CHARACTERIZATION OF SPECIFIC RXFP2 SMALL MOLECULE AGONISTS

2.1 Introduction

High-throughput cAMP assays are powerful tools widely used in GPCR drug discovery (131-134). These platforms serve to screen for agonists or antagonists of GPCRs, including $G_{\alpha s}$-coupled receptors like RXFP1 or RXFP2. Several HTS technologies are commercially available to measure direct cAMP accumulation in cell-based assays, for example, the HTRF and the Amplified Luminescent Proximity Homogeneous Assay (ALPHAScreen), two of the most sensitive methods adopted for high-capacity 384- and 1,536-well cell culture plates (135).

The Molecular Libraries-Small Molecule Repository (MLSMR) at NCATS/NIH has a total of 350,478 compounds that were used in an HTRF cAMP HTS against the RXFP1 receptor. From this HTS screening, several compounds were identified as potential RXFP1 agonists. The specificity and selectivity of these compounds was proven by performing cAMP counter-screen assays in related relaxin receptor RXFP2, and non-related GPCRs like the vasopressin receptor 1b (V1b). An extensive SAR study was performed to increase the activity and efficacy, to improve microsomal stability, solubility, and permeability, and decrease cytotoxicity of the identified RXFP1 agonists. These screening and characterization efforts culminated on the successful discovery of the first-in-class RXFP1 small molecule agonists, with the lead compound ML290 (136-138).

Subsequent studies have demonstrated the therapeutic potential of this compound as an antifibrotic agent in liver and kidney fibrosis mouse models (130, 139).

The aim of the experiments described in this chapter is to identify the first-in-class RXFP2 small molecule agonists using the same approach employed for the discovery and optimization of ML290. Several low molecular weight compounds were identified as agonists of the RXFP2 receptor using the HTRF cAMP HTS of the same MLSMR small molecule library at NCATS/NIH. An extensive SAR campaign led by the NCATS/NIH chemistry team resulted in highly potent and efficient full RXFP2 agonists. Two independent confirmatory cAMP screenings were performed at FIU to validate the activity of the most relevant RXFP2 agonists identified in the primary HTS screening. The specificity and selectivity of these compounds for the RXFP2 receptor was also tested in orthogonal cAMP assays and in counter-screening against the related relaxin receptor RXFP1. A full GPCRome screen using the β-arrestin PRESTO-Tango assay was also performed to further demonstrate the specificity of the compounds against non-related GPCRs. The biological activity of the compounds was then tested by evaluating an induction of mineralization in osteoblasts, which is the most reliable method for assessing bone formation *in vitro*. Finally, cytotoxicity experiments were completed in primary human cells to make sure the compounds are not toxic at biologically relevant concentrations. The experiments described in this chapter led to identification of the final lead compound; a potent, effective, specific, and

biologically active RXFP2 small molecule agonist that was used for testing its osteoanabolic effects *in vivo*.

2.2 Materials and methods

2.2.1 Cell lines maintenance and subculturing

The HEK293T parental cells, HEK293-transfected cell lines were obtained from ATCC (Manassas, VA), produced in our laboratory, or received as a gift from our collaborators. The authenticity of the cell lines was confirmed using STR markers in ATCC. All HEK293T cell lines were revived in 5 mL of HEK growth media containing DMEM (Corning, Corning, NY), 10% FBS (GemCell-GeminiBio, West Sacramento, CA) and 1x Pen/Strep (Corning) and centrifuged at 200 x g for 1 minute to remove DMSO (mpBIO, Solon, OH). Cell pellet was resuspended in 5 mL of HEK growth media, transferred to a T25 tissue culture flask (Falcon-Corning) and cultured at 37°C, 5% CO_2 in a HERAcell vios 160i incubator (Thermo Fisher Scientific, Waltham, MA). Cell lines were passaged one time before seeding for experiment when reaching 90% confluency. Media was removed and cells washed with 1 mL PBS (HyClone-Cytiva, Logan, UT), detached using 0.5 mL of 0.25% trypsin, 0.1% EDTA (Corning) for 1 minute at room temperature and resuspended in 3 mL of complete HEK growth media. Cells were counted using a 1:1 dilution with trypan blue stain 0.4% (Invitrogen, Waltham, MA) in a Countess automated cell counter (Invitrogen). Cells were seeded in complete HEK growth media at the desired concentration in a 10 cm tissue culture dish (Falcon-Corning) for experiment or in a T25 tissue culture flask for maintenance. At this point, selection

reagents were added to the T25 tissue culture flask with the stable cell lines to maintain expression of the inserted genes. 50 µg/mL of hygromycin (Invitrogen) was added for HEK-CRE-Luciferase cell lines, 50 µg/mL of zeocin (Invitrogen) was added for HEK-RXFP2 or -RXFP1 cell lines, and a combination of 50 µg/mL hygromycin and 50 µg/mL zeocin was added for HEK-CRE-Luc-RXFP2 or RXFP1 cell lines.

Primary human calvarial osteoblasts (HCO cells) were purchased from ScienCell (Carlsbad, CA, catalog # 4600), revived following manufacturer instructions, expanded, and cryopreserved at passage 2. Cells were revived in 15 mL of growth medium containing DMEM-F12 (HyClone), 10% FBS and 1x Pen/Strep, transferred to a T75 tissue culture flask (Falcon-Corning) and cultured at 37°C, 5% CO_2. Growth medium was refreshed the next day to remove residual DMSO and unattached cell. When cells reached confluency, media was removed and cells washed with 4 mL PBS, detached using 1 mL of 0.025% Trypsin/EDTA (Lonza, Basel, Switzerland) for 3 minutes at room temperature and resuspended in 5 mL of complete growth medium. Cells were split into 2 T75 flasks to use for experiment after reaching confluency. All experiments with HCO cells were consistently performed at passage 4 to avoid potential variability in primary cell responses after multiple passages.

The reagents and equipment described on this section were also used in the following protocols, unless otherwise stated.

2.2.2 HTRF cAMP assay in HEK293T cells stability expressing RXFP2

HEK293T cells stably transfected with RXFP2 (HEK-RXFP2) were used to identify RXFP2 agonists using the HTRF $G_{\alpha s}$ dynamic cAMP assay kit (catalog # 62AM4PEC, Cisbio-PerkinElmer, Bedford, MA). It is a competitive immunoassay where a TR-FRET signal is produced when exogenous d2-labeled cAMP (acceptor) binds to europium cryptate-conjugated anti-cAMP antibody (donor); no signal is produced when endogenous cAMP binds to the antibody. Thus, the TR-FRET signal is inversely proportional to the concentration of cAMP produced by the cells (140). For this assay, HEK-RXFP2 cells were seeded in 96-well flat-bottom opaque plates (CELLSTAR, Greiner-Bio-One, Kremsmünster, Austria) at 7,500 cells/well in 60 µL/well of serum-free DMEM medium and allowed to attach overnight at 37°C, 5% CO_2. The next morning, cells were treated with 1 µL/well of compound (0.25 nM - 25 µM), 5 µM forskolin (catalog # BP25205, Fisher Scientific, Hampton, NH), or DMSO vehicle. Cells were also treated with 4 µL of INSL3 (0.01 - 100 nM) (catalog # 035-27, Phoenix Pharmaceuticals, Burlingame, CA) as a positive control or vehicle (serum-free DMEM). Cells were incubated for 1 hour at 37°C, 5% CO_2, and after that, 16 µL/well of kit cAMP-d2 and 16 µL/well of anti-cAMP antibody were added as per manufacturer protocol. Plates were incubated for 1 hour at room temperature, and then the signal was read on a CLARIOstar plate reader (BMG Labtech, Ortenberg, Germany) at 665 and 620 nm emission wavelengths. cAMP response induced by the compounds was normalized to cAMP response induced by 100 nM INSL3 as 100% activity and cAMP response induced by DMSO vehicle as 0% activity. Data analysis was performed using GraphPad

Prism 8 (GraphPad Software, San Diego, CA). Compound efficacy and activity expressed as E_{max} and EC_{50} were calculated from efficacy curves generated using four parameters nonlinear fit dose-response stimulation curves, presented as mean ± SEM of 3 independent experiments, each performed in triplicates.

2.2.3 CRE-Luciferase assay in HEK-RXFP2 cells

A confirmatory cAMP assay was done using a HEK293T-CRE-Luc cell line stably transfected with RXFP2 (HEK-CRE-Luc-RXFP2). This cell line contains the firefly luciferase gene under the control of multimerized cAMP response element (CRE) located upstream of a minimal promoter. Activation of the RXFP2 receptor increases intracellular cAMP levels leading to the activation of the cAMP-response element binding protein (CREB) localized in the nucleus and acting as a transcription factor. CREB binds to the CRE inducing luciferase transcription in the nucleus. Thus, luciferase activity in these cells is proportional to cAMP accumulation. For this assay, cells were seeded in 96-well flat-bottom opaque plates at 7,500 cells/well in 60 µL/well of serum-free DMEM medium and allowed to attach overnight at 37°C, 5% CO_2. The next morning, cells were treated with 1 µL/well of compound (0.25 nM - 25 µM), 5 µM forskolin, or DMSO vehicle. Cells were also treated with 4 µL of INSL3 (0.01-100 nM) or vehicle serum-free DMEM. Cells were incubated for 3 hours at 37°C, 5% CO_2, then rested 30 minutes at room temperature for equilibration. After that, 65 µL/well of substrate Amplite™ Luciferase Reporter Gene Assay Kit (catalog # 12519, AAT Bioquest, Sunnyvale, CA) was added. Plates were incubated for 40 minutes at room temperature

protected from light, and then the luminescence signal was read on a CLARIOstar plate reader. Data was normalized as described in above section 2.2.2 and analyzed using GraphPad Prism 8. Efficacy curves were generated using four parameters nonlinear fit dose-response stimulation curves, presented as mean ± SEM of 3 independent experiments, each performed in triplicates.

2.2.4 HTRF cAMP assay in HEK-RXFP1 cells

HEK293T cells stably transfected with RXFP1 (HEK-RXFP1) were used to test compound specificity towards the RXFP2 receptor using the HTRF $G_{\alpha s}$ dynamic cAMP assay kit. For this assay, the HTRF cAMP assay was carried out in the presence of isobutylmethylxanthine phosphodiesterase inhibitor IBMX (catalog # I5879, Sigma-Aldrich, St. Louis, MO) at 200 μM to amplify cAMP signal. For this assay, cells were seeded in 96-well flat-bottom opaque plates at 7,500 cells/well in 60 μL/well of serum-free DMEM medium and allowed to attach overnight at 37°C, 5% CO_2. The next morning, cells were treated with 1 μL/well of compound (25 nM - 25 μM), 2 μM forskolin, or DMSO vehicle. Cells were also treated with 4 μL of 10 nM Relaxin2 (0.01- 100 nM) (catalog # 130-15, Peprotech, Cranbury, NJ) as a positive control or vehicle (serum-free DMEM + IBMX). At this point, the protocol follows as described in the previous section 2.2.2. cAMP dose-response curve induced by relaxin is shown as positive control in comparison to the cAMP response induced by the compounds, all normalized to DMSO vehicle as 0% activity. Data analysis was performed as described in above section 2.2.3 and

presented as mean ± SEM of 3 independent experiments, each performed in triplicates.

2.2.5 PRESTO-Tango assay in HTLA cells transfect with related GPCRs

The PRESTO-Tango GPCRome assay was used to perform a HTS of related GPCRs to study specificity and selectivity of the RXFP2 agonists. A total of 320 GPCR Tango constructs were tested in the National Institute of Mental Health's Psychoactive Drug Screening Program at the University of North Carolina (https://pdsp.unc.edu/pdspweb/content/PDSP%20Protocols%20II%202013-03-28.pdf). Each of the GPCR constructs used in the assay contains a FLAG tag, the GPCR gene of interest, a Vasopressin 2 C-terminal tail, the TEV protease cleavage site, and the Tta transcription factor. The assay was performed using transiently transfected HTLA cells that stably express the β-arrestin2-TEV protease fusion protein and a luciferase reporter gene under the control of the Tta transcription factor. Ligand activation of the transfected GPCR construct induces β-arrestin translocation to the GPCR, where the TEV protease cleaves the Tta transcription factor, causing activation of luciferase transcription in the nucleus. Thus, luciferase activity in these cells is proportional to β-arrestin translocation activity. For this assay, HTLA cells were seeded in Poly-L-Lys (PLL)-coated 384-well white clear-bottom plates at 10,000 cell/well in 40 µl/well DMEM supplemented with 10% FBS. Cells were incubated overnight at 37°C, 5% CO_2 to allow them to attach. The next morning, cells were treated with 10 µL/well of 50% FBS DMEM 1 hour before transfection. Cells were transfected with 20 ng of plasmid diluted in an

equal volume of 0.25 M $CaCl_2$ and HBS (50 mM HEPES, 280 mM NaCl, 10 mM KCl, 1.5 mM Na_2HPO_4, pH 7.00) in a total volume of 6 µl/well using a Hamilton Microlab Star with a 384-well pipetting head. After transfection, cells were incubated overnight at 37°C, 5% CO_2. The next morning, medium was removed and replaced with 40 µl/well of fresh 1% FBS DMEM 2 hours before addition of treatments. Cells were treated with 10 µL/well of 10 µM compound diluted in 1% FBS DMEM and incubated overnight at 37°C, 5% CO_2. The following day, medium was removed and 20 µl/well of BrightGlo reagent (Promega, Madison, WI) diluted 1:20 with Tango assay buffer were added. Plates were incubated for 20 minutes at room temperature protected from light and the luminescence signal was read on a MicroBeta counter (PerkinElmer). Results were calculated as a fold RLU normalized to unstimulated cells as basal for each target. All GPCRs with a minimum of 3.0-fold RLU of basal were considered to have potential agonist activity and were presented as the mean ± SEM of 4 technical replicates in summary excel tables. GPCRs with more than 3.0-fold RLU were re-tested in confirmatory assay using various compound concentrations. Data analysis was performed using GraphPad Prism 8. Efficacy curves were generated using four parameters nonlinear fit dose-response stimulation curves, presented as mean ± SEM of 4 technical replicates.

2.2.6 GloSensor cAMP assay in HEK cells transfected with related GPCRs

The GloSensor cAMP assay was used as a functional assay to measure compound-induced $G_{\alpha i}$- or $G_{\alpha s}$- signaling of the GPCRs identified in the PRESTO-

Tango HTS. The GloSensor luciferase experiences a conformational change with the binding of cAMP, which turns it into an active form able to catalyze a reaction that produces light. Thus, luciferase activity in these cells is proportional to cAMP accumulation. This assay was performed by the National Institute of Mental Health's Psychoactive Drug Screening Program at the University of North Carolina, (https://pdsp.unc.edu/pdspweb/content/PDSP%20Protocols%20II%202013-03-28.pdf). 3 million HEK293T cells were seeded in 10-cm dishes in DMEM supplemented with 10% FBS and incubated overnight at 37°C, 5% CO_2 to allow them to attach. Next morning cells were co-transfected with 10 µg of target receptor (ADORA1) and GloSensor cAMP DNA construct (Promega) diluted in an equal volume of 2 M $CaCl_2$ and HBS in a total volume of 1000 µl. After transfection, cells were incubated overnight at 37°C, 5% CO_2. Cells were then seeded in PLL-coated 384-well white clear-bottom plates at 15,000 – 20,000 cell/well in 40 µl/well of DMEM supplemented with 1% FBS. Cells were incubated overnight at 37°C, 5% CO_2 to allow them to attach. The next morning, medium was replaced with 30 µl of various compound concentrations diluted in assay buffer and cells were incubated for 15 min at room temperature. To measure agonist activity of ADORA1 ($G_{\alpha i}$), Luciferin (4 mM) and Isoproternol (200 nM) were added in a final volume of 10 µl, and the luminescence signal was read after 15 minutes on a MicroBeta counter. Data analysis was performed as described in section 2.2.5 and presented as mean ± SEM of 4 technical replicates.

2.2.7 Cytotoxicity assay

Cytotoxicity induced by the compounds was tested in HCO cells and human aortic vascular smooth muscle cells (HAVSMC) (ATCC) using the CellTiter-Glo Luminescent Cell Viability Assay (catalog # G7571, Promega). This is a luminescence-based assay that determines viable cells by measuring cellular ATP production. The luciferase enzyme requires ATP to catalyze the conversion of beetle luciferin to oxyluciferin and light. Thus, luciferase activity is proportional to ATP accumulation in the cells. For this assay, 96-well flat-bottom opaque plates were seeded with HCO cells at 3,000 cells/well in 100 µL/well of growth medium (DMEM, 10% FBS, 1x Pen/Strep) or HAVSMC at 7,000 cells/well in 100 µL/well of growth medium (F-12K, 0.05 mg/mL ascorbic acid, 0.01 mg/mL insulin, 0.01 mg/mL transferrin, 10 ng/mL sodium selenite; 0.03 mg/mL ECGS, 10% FBS, 10 mM HEPES, 10 mM TES). After incubating overnight at 37°C, 5% CO_2 to allow attachment, cells were treated with 1 µL/well of compound (0.1 - 25 µM) or DMSO vehicle and incubated additional 24 hours. Cells were equilibrated for 30 minutes at room temperature and 100 µL/well of CellTiter-Glo Reagent was added. Plates were placed on an orbital shaker for 2 minutes and incubated at room temperature for 10 minutes to stabilize the luminescent signal, which was read immediately after on a CLARIOstar plate reader. ATP inhibition induced by the compounds was normalized to DMSO vehicle control as 0% inhibition. Data analysis was performed using GraphPad Prism 8. Compounds induced toxicity was calculated from four parameters nonlinear fit dose-response inhibition curves presented as mean ± SEM of 3 independent experiments, each performed in triplicates.

2.2.8 Mineralization assay

The biological activity of the RXFP2 agonists was tested in primary HCO cells by measuring their ability to induce osteoblast mineralization using the fluorescent-based OsteoImage Mineralization Assay (catalog # PA-1503, Lonza) that measures hydroxyapatite, which is the main mineral component of bone. For this assay, HCO cells were seeded in 0.1% gelatin-coated 96 well black-walled flat-bottom clear plates (Greiner) at 7,000 cells/well in 100 µL/well of growth medium (DMEM-F12, 10% FBS, 1X Pen/Strep) and allowed to attach overnight at 37°C, 5% CO_2. The next day, growth medium was changed to 100 µL/well of mineralization medium (growth medium + 10 mM β-glycerophosphate, 50 µg/ml ascorbic acid, 10 nM dexamethasone), along with the respective treatments. Cells were treated with 1 µL/well of compound (1, 3, or 5 µM) or vehicle (serum-free DMEM, 0.05% DMSO). Medium and treatments were replaced every 2-3 days and cells were incubated at 37°C, 5% CO_2 for 14 days. Mineralization medium stock was prepared fresh every week with sterile filtered β-glycerophosphate (catalog # G9422, Sigma-Aldrich), ascorbic acid (catalog # a8960, Sigma-Aldrich), and dexamethasone (catalog # 190040, mpBIO). Hydroxyapatite deposits were evaluated using the OsteoImage Mineralization Assay (Lonza). At treatment day 14, cells were rested 30 minutes at room temperature for equilibration, medium was removed, cells washed with 200 µL/well PBS and fixed in 100 µL/well 4% formaldehyde for 15 minutes. Cells were washed once with 200 µL/well assay wash buffer and 100 µL/well of assay staining reagent was added as per manufacturer's protocol. Cells were incubated at room temperature for 30 minutes,

protected from light. After staining, cells were washed 3 times with 200 µL/well wash buffer and wells were filled with a final 200 µL/well wash buffer. Mineralization was then quantified using a CLARIOstar plate reader with 492 nm excitation and 520 nm emission wavelengths. Representative images of the hydroxyapatite bone-like nodules were also captured using a fluorescence Nikon Eclipse TS100 microscope attached to an OLIMPUS DP70 camera (Nikon Corporation, Tokyo, Japan). Mineralization activity induced by compounds was normalized to mineralization activity induced by DMSO vehicle as 100% mineralization. Data analysis was performed using GraphPad Prism 8. The results represent the means ± SEM of 3 independent experiments in bar graph format, each performed in triplicates. Statistical significance was calculated using ordinary 1-way ANOVA with Dunnett's multiple comparison post-test vs. DMSO vehicle and was defined by $p<0.05$ (indicated by *) and $p<0.001$ (indicated by ***).

2.2.9 RNA extraction

Parallel experiments were performed to study the changes in gene expression induced by compound 6641. HCO cells were seeded in 0.1% gelatin-coated 12 well flat-bottom clear plates (Falcon-Corning) at 100,000 cells/well in 1 mL/well of growth medium (DMEM-F12, 10% FBS, 1X Pen/Strep) and allowed to attach overnight at 37°C, 5% CO_2. The next day, growth medium was changed to 1 mL/well of mineralization medium (growth medium + 10 mM β-glycerophosphate, 50 µg/ml ascorbic acid, 10 nM dexamethasone), along with compound (5 µM) or vehicle (0.0005% DMSO) treatments pre-diluted in the total volume of

mineralization medium. Medium and treatments were replaced every 2-3 days and cells were incubated at 37°C, 5% CO_2 for 7 and 14 days. At these points, culture medium was removed, 1 mL of TRIzol reagent (Ambion-Life technologies, Austin, TX) per well was added and the cells were homogenized by pipetting. The homogenates were transferred to DNase/RNase free 1.5 mL Eppendorf tubes to store at -80°C until further processing. RNA isolation was performed using the GeneJET RNA purification kit (catalog # K0731, Thermo Fisher Scientific). Samples were thawed, vortexed for 1 minute and incubated for 15 minutes at room temperature. 200 µL of chloroform per tube were added, shaken by hand for 15 seconds, and incubated for 3 minutes at room temperature for the phase separation to take place. The upper aqueous phase containing the RNA was carefully collected and transferred to a clean DNase/RNase free 1.5 mL Eppendorf tubes. An equal volume of 70% EtOH was added to each tube and mixed thoroughly by pipetting. The total volume was transferred to GeneJET columns, spined at 12,000 rpm for 1 minute, and the flow-through was discarded. Afterwards, 3 consecutive washing steps were performed as instructed by the manufacturer protocol. 700 µL of wash buffer 1 were added to each column, spined at 12,000 rpm for 1 minute, and the flow-through was discarded. Then, 600 µL of wash buffer 2 were added, spined at 12,000 rpm for 1 minute, and the flow-through was discarded. The last wash with 250 µL of wash buffer 2 was performed at 12,000 rpm for 2 minutes to ensure the complete removal of ethanol from the column. The GeneJET columns were then transferred to clean DNase/RNase free 1.5 mL Eppendorf tubes and RNA was eluted in 40 uL RNase-free water at 12,000

rpm for 1 minute. RNA samples were kept in ice while concentration (0.1 – 1 µg) and purity (260/280 nm OD ratio ≥ 2) were measured using a NanoVue spectrophotometer (GE Healthcare, Chicago, IL) before transferring them to -80°C for storage.

2.2.10 RNA-seq analysis

RNA samples from HCO cells treated with 6641 compound or DMSO vehicle for 14 days (4 technical replicates per condition) were sent to the company Novogene (Beijing, China) for RNA sequencing (RNA-seq) analysis. A full report including RNA quality control, mapping, quantification, differential expression analysis, and enrichment analysis was provided by the Novogene bioinformatics team. Briefly, the raw reads were filtered to remove low quality reads and obtain the clean reads used on the following analysis. STAR software was used to map the clean reads to the reference genome (homo sapiens GRCh38) and the transcripts abundance was determined by FPKM method. Significance thresholds were set at fold change > 1.5 and $p_{adj} < 0.05$.

2.2.11 cDNA generation

cDNA was generated using the Verso cDNA synthesis kit (catalog # AB-1453/B, Thermo Fisher Scientific) following manufacturer instructions. 4 µL of 5x cDNA synthesis buffer, 2 µL of dNTP mix, 1 µL of RNA primers, 1 µL of Verso Enzyme mix, 1 µL RT enhancer, 1 µg of RNA and nuclease-free water were added for each sample to obtain a 20 µL final reaction volume. cDNA synthesis was performed

using 1 cycle at 42°C for 30 minutes followed by 1 cycle inactivation step at 95°C for 2 minutes in a DNA Engine Thermal Cycler (Bio-Rad, Hercules, CA). cDNA was stored at -20°C until used.

2.2.12 Quantitative RT-PCR procedure

Quantitative RT-PCR was performed to validate the findings from the RNA-seq analysis using the GoTaq qPCR master mix (catalog # A6002, Promega) following manufacturer instructions. The reaction mix per sample was prepared by combining 10 uL of GoTaq qPCR Master Mix, 0.5 µL of each qPCR primer (forward and reverse) and 8 uL of nuclease-free water. 19 µL of the reaction mix were added to each PCR tube (TempAssure white PCR 8-tube strips with optical caps, USA Scientific, Ocala, Florida) followed by the addition of 1 µL template cDNA or nuclease-free water as control (NTC). Quantitative RT-PCR protocol was established for SYBR Green assays with GoTaq qPCR Master Mix using the qPCR Real Time PCR Thermo Cycler RealPlex 2 ep gradient (Eppendorf, Hamburg, Germany), consisting of 1 cycle for GoTaq Hot Start Polymerase activation at 95°C for 2 minutes and 40 cycles of denaturalization at 95°C for 15 seconds followed by annealing/extension at 60°C for 1 minute. Relative expression values of the specific genes of interest were calculated by the $2^{-\Delta\Delta Ct}$ method using the gene *RPLP0* as normalizer. The sequences of the primers are summarized in Table 1. Data analysis was performed using GraphPad Prism 8. The results represent the means ± SEM of 3 independent experiments in bar graph format, each performed in triplicates. Statistical significance was calculated using unpaired two-tailed

Student's t-test and was defined by $p<0.01$ (indicated by **), $p<0.001$ (indicated by ***) and $p<0.0001$ (indicated by ****).

2.2.13 Statistical analysis

Data were analyzed using GraphPad Prism 8. One-way ANOVA was used to compare three or more groups followed by a Dunnett's multiple comparison test. Unpaired two-tailed Student's t-test was used to determine the statistical difference between two groups. Values are presented as mean ± SEM of independent experiments unless stated otherwise. A value of $p < 0.05$ was considered statistically significant.

2.3 Results

2.3.1 Identification of potent and effective RXFP2 small molecule agonists

A quantitative HTS of more than 80,000 compounds of the NIH/NCATS diversity collection was performed at four concentrations in HEK293T cells stably expressing RXFP2 to identify candidate agonists. An HTRF assay was used to directly detect compound-induced cAMP accumulation, with forskolin or human recombinant INSL3 serving as positive controls. Approximately 150 active compounds (EC_{50} < 10 µM, efficacy > 40% of 10 nM INSL3, robust dose-dependent agonism, and no HTRF reagent artifacts) were re-synthesized and re-tested in the same assay. Selected compounds with reasonable activity in dose response were also tested in a secondary orthogonal cAMP screening using HEK-CRE-Luc-RXFP2 cells, and in counter-screen with HEK293T cells transfected with

RXFP1. Finally, we performed an extensive SAR campaign to increase both the agonist efficacy and potency of the lead series. Optimized molecules displayed high potency and efficacy in cAMP assay. The cAMP responses for several lead compounds from the HTS are shown in Figure 6b. All compounds tested are very potent, with EC_{50} below 1 µM. The compounds activity based on the E_{max} ranked from highest to lowest as follows: 6641 (106.99 ± 8.77), 4337 (78.53 ± 18.81), 4340 (53.14 ± 4.88) and 1715 (41.32 ± 3.58). A confirmatory CRE-luciferase cAMP screen was used to eliminate any potential false positives due to assay detection artifacts (Figure 6c). These results showed that all compounds 6641, 4337, 4340 and 1715 are indeed potent and effective agonists of RXFP2.

2.3.2 Small molecules are specific and selective RXFP2 agonists

The RXFP1 receptor has the highest sequence similarity with RXFP2 (49, 141). To demonstrate the specificity and selectivity of the identified small molecule RXFP2 agonists, a HEK293T cell line stably transfected with human RXFP1 was used. The results from the HTRF cAMP assay showed that the compounds 4337, 4340 and 6641 do not activate the RXFP1 receptor, since cAMP accumulation was not detected after stimulation of the receptor with compounds (Figure 7).

β-arrestin is an important GPCR adaptor protein that mediates several receptor processes including signaling, desensitization and trafficking (142). The PRESTO-Tango GPCRome assay was further used to test specificity and selectivity of lead RXFP2 agonists 6641 and 4337. GPCR-mediated β-arrestin recruitment for a

panel of 320 GPCRs was studied in transiently transfected HTLA cells treated with 10 µM compound. The results for all 320 GPCRs tested are summarized in Table 2. Compound 6641 was found to induce β-arrestin recruitment above the basal level of detection (3-fold RLU) for 3 GPCRs (mean ± SEM): ADORA1 (3.92 ± 0.15), CCKAR (3.42 ± 0.15) and FPR1 (3.11 ± 0.29). Compound 4337 activated β -arrestin recruitment in 7 GPCRs: ADORA1 (5.24 ± 0.31), FPR1 (4.89 ± 0.12), GPR20 (4.22 ± 0.91), CCKAR (3.57 ± 0.17), CXCR7 (3.44 ± 0.48), P2RY1 (3.07 ± 0.14) and MRGPRF (3.01 ± 0.19). A follow-up test of ADORA1, FPR1, GPR20 and CCKAR using multiple compound concentrations revealed that only the adenosine A1 receptor (ADORA1) responded to compound 6641 and 4337 at concentrations above 1 µM, but with much lower efficacy than the ADORA1 agonist 5′-(N-Ethylcarboxamido)adenosine (NECA) (Figure 8). ADORA1 activation by an agonist results in $G_{\alpha i}$ protein binding, an inhibition of adenylate cyclase and, therefore, a decrease in the cAMP concentration. Analysis of cAMP inhibition after treatment of ADORA1-HEK293T transfected cells with both compounds failed to detect any significant changes (Figure 9). Thus, while compounds appear to bind to ADORA1, they do not trigger receptor mediated G protein signaling. Of note, RXFP2-mediated β-arrestin recruitment induced by compounds 6641 and 4437 was not detected by the PRESTO-Tango assay. This finding agrees with previous data showing a lack of RXFP2-mediated β-arrestin recruitment after treatment with INSL3 (81). All together, these results identified compound 6641 as one of the most effective and selective RXFP2 agonist of our series.

2.3.3 RXFP2 small molecule agonists induce osteoblasts mineralization *in vitro*

The identification of potent, effective, and specific RXFP2 agonist during the cAMP screening in HEK-RXFP2 cells was followed by studying the ability of these compounds to induce osteoblasts mineralization *in vitro*. Primary human osteoblasts are relevant for pre-clinical studies and preferable to immortalized osteoblasts cell lines since they better reproduce the phenotypic changes during mineralization of the bone matrix (143). Commercially HCO cells are patient derived osteoblasts isolated form the human calvariae that mineralize *in vitro* and endogenously express RXFP2, being the desired cell model used for this study. A preliminary study was performed with HCO cells to determine the timeline of osteoblasts mineralization, which was established at 14 days in culture. HCO cells were treated for 14 days and extracellular mineral deposition was quantified by measuring hydroxyapatite, the main mineral component of the bone-like nodules deposited by osteoblasts (144). The results showed that osteoblast mineralization is significantly increased by compound 6641 at the concentration of 5 µM (340% ± 64.68) and 3 µM (240.15% ± 30.93), but no significant changes were observed at 1 µM in comparison to control DMSO treatment (Figure 10a). A significant increase in osteoblast mineralization was also found after treatment with 5 µM of compound 4337 (320.31% ± 53.09) and 4340 (261.08% ± 46.77) in comparison to control DMSO treatment, but no significant changes were found after 3 µM or 1 µM treatment with either of these two compounds (Figure 10a). No significant effects on osteoblast mineralization were found after treatment with compound 1715 (5, 3

or 1 µM) in comparison to control DMSO treatment (Figure 10a). Representative images of the amount of green-fluorescent hydroxyapatite nodules further validated the results obtained with the plate reader quantification (Figure 10b).

2.3.4 RXFP2 small molecule agonists are no cytotoxic *in vitro*

Cell viability studies were undertaken to identify potential cytotoxicity effects of RXFP2 agonists that could rule them out as desirable drug candidates. HCO and HAVSMC cells were treated for 24 hours, and the toxicity was quantified by measuring changes in ATP production. The results in HCO cells indicated that there is some modest toxicity at the highest concentration of 25 µM with compounds 6641 (12.87% ± 2.64), 4337 (12.29% ± 1.88), and 4340 (21.99% ± 7.58), but no toxicity was found at 8.3 µM and lower concentrations of the three compounds (Figure 11a). In HAVSMC cells, there was toxicity at the highest concentration of 25 µM with compounds 6641 (34.20% ± 3.98), 4337 (19.87% ± 7.24), and 4340 (40.64% ± 3.10), but at 8.3 µM and lower concentrations all toxicities were below 20%, 6641 (18.32% ± 2.90), 4337 (10.89% ± 6.62), and 4340 (15.44% ± 0.80) (Figure 11b).

2.3.5 Compound 6641 induces changes in osteoblasts gene expression profiles

In other to investigate the signaling pathways that compound 6641 is activating to induce mineralization in primary human osteoblasts, an RNA-seq analysis was performed after treatment with 5 µM 6641 for 14 days. A total of 677 genes were

found differentially expressed: 319 up-regulated and 358 down-regulated (Figure 12). A gene ontology analysis of the up-regulated genes revealed that the most significantly enriched biological processes were all related to type I interferon (α, β), interferon γ, immune and inflammatory responses to virus (Figure 13a). The most significantly enriched biological processes for the down-regulated genes were associated to the cell cycle and cell division, as well as kidney and skeletal system development, chondrocyte differentiation and sensory organ morphogenesis (Figure 13b). A list of the most differentially expressed genes is shown in Table 3. The most up-regulated genes are interferon-regulated resistance GTP-Binding proteins (*MX2*, *MX1*), interferon inducible proteins (*IFI27*, *IFI44L*, *IFI6*, *IFITM1*, *IFIT1*, *IFIT3*, *IFIT2*), members of the 2-5A synthetase family (*OAS2*, *OASL*, *OAS3*) and interferon regulatory factors (*IRF7*, *IRF9*), all of which are related to interferon signaling. The most down-regulated genes are involved in cell cycle and division (*MYBL2*, *DTL*, *ASPM*, *BIRC5*, *CEP55*, *KIF20A*, *NCAPG*, *KIFC1*, *BUB1*, *ANLN*), skeletal system development (*ACAN*, GPC3, *BMP4*, *ADAMTS7*, *LEP*, *IGFBP5*). To validate the RNA-seq results we performed quantitative RT-PCR of 4 upregulated (*OAS2*, *IFI44L*, *IFITM1*, *ISG15*) and 4 downregulated genes (*ACAN*, *RGS5*, *GPC3*, *IGFBP5*) (Figure 14). The reproducibility of the changes in *IFITM1*, *ISG15*, *GPC3* and *IGFBP5* gene expression was demonstrated in 3 independent experiments after 14- and 7-days treatment with compound 6641 at 5 µM (Figure 15 and 16 respectively). In agreement with the RNA-seq results, not significant changes were observed for the most common markers of osteoblast mineralization *ALP*, *OSTEOCALCIN*,

OSTEONECTIN and *COL1A1* after 14-days treatment (Figure 15), but a significant increase in *OSTEONECTIN* expression was observed after 7-days treatment (Figure 16).

2.4 Figures and tables

Table 1. Sequences of human primers used for quantitative RT-PCR. F (forward), R (reverse)

PRIMERS	SEQUENCES
***OAS2* F**	5'-TACCCTCGCTGTCTCCGTAT-3'
***OAS2* R**	5'-TCTTTTCTGCACCCCTGTTC-3'
***IFI44L* F**	5'-TTGTGTGACACTATGGGGCTA-3'
***IFI44L* R**	5'-AATTGGTTTACGGGAATTAAA -3'
***ISG15* F**	5'-CTCTGAGCATCCTGGTGAGGAA-3'
***ISG15* R**	5'-AAGGTCAGCCAGAACAGGTCGT-3'
***IFITM1* F**	5'-AGCACCATCCTTCCAAGGTCC-3'
***IFITM1* R**	5'-TAACAGGATGAATCCAATGGTC-3'
***GPC3* F**	5'-GATGAAGATGAGTGCATTGGAG-3'
***GPC3* R**	5'-CATCCAGATCATAGGCCAGTT-3'
***IGFBP5* F**	5'-GTGCTGTGTACCTGCCCAAT-3'
***IGFBP5* R**	5'-CGTCAACGTACTCCATGCCT-3'
***ACAN* F**	5'-TGCCATCGACTCTTTCACAT-3'
***ACAN* R**	5'-TTCCAGCCCTCCTCACATAC-3'
***RGS5* F**	5'-CAGCTTTGCCCCACTCAT-3'
***RGS5* R**	5'-TTTCTCTGGCTTCTCATTGTACGG-3'
***ALP* F**	5'-CCATCCTGTATGGCAATGG-3'
***ALP* R**	5'-GCGCCTGGTAGTTGTTGTG-3'
***OSTEOCALCIN* F**	5'-AGGAGGGCAGCGAGGTAGTGAA-3'
***OSTEOCALCIN* R**	5'-CCTCCTGAAAGCCGATGTGGT-3'
***OSTEONECTIN* F**	5'-ACAAGCTCCACCTGGACTACATC-3'
***OSTEONECTIN* R**	5'-GGGAATTCGGTCAGCTCAGA-3'
***COL1A1* F**	5'-AGACAGTGATTGAATACAAAACCA-3'
***COL1A1* R**	5'-GGAGTTTACAGGAAGCAGACA-3'
***RPLP0* F**	5'-CCTTCTCCTTTGGGCTGGTCATCCA-3'
***RPLP0* R**	5'-CAGACACTGGCAACATTGCGGACAC-3'

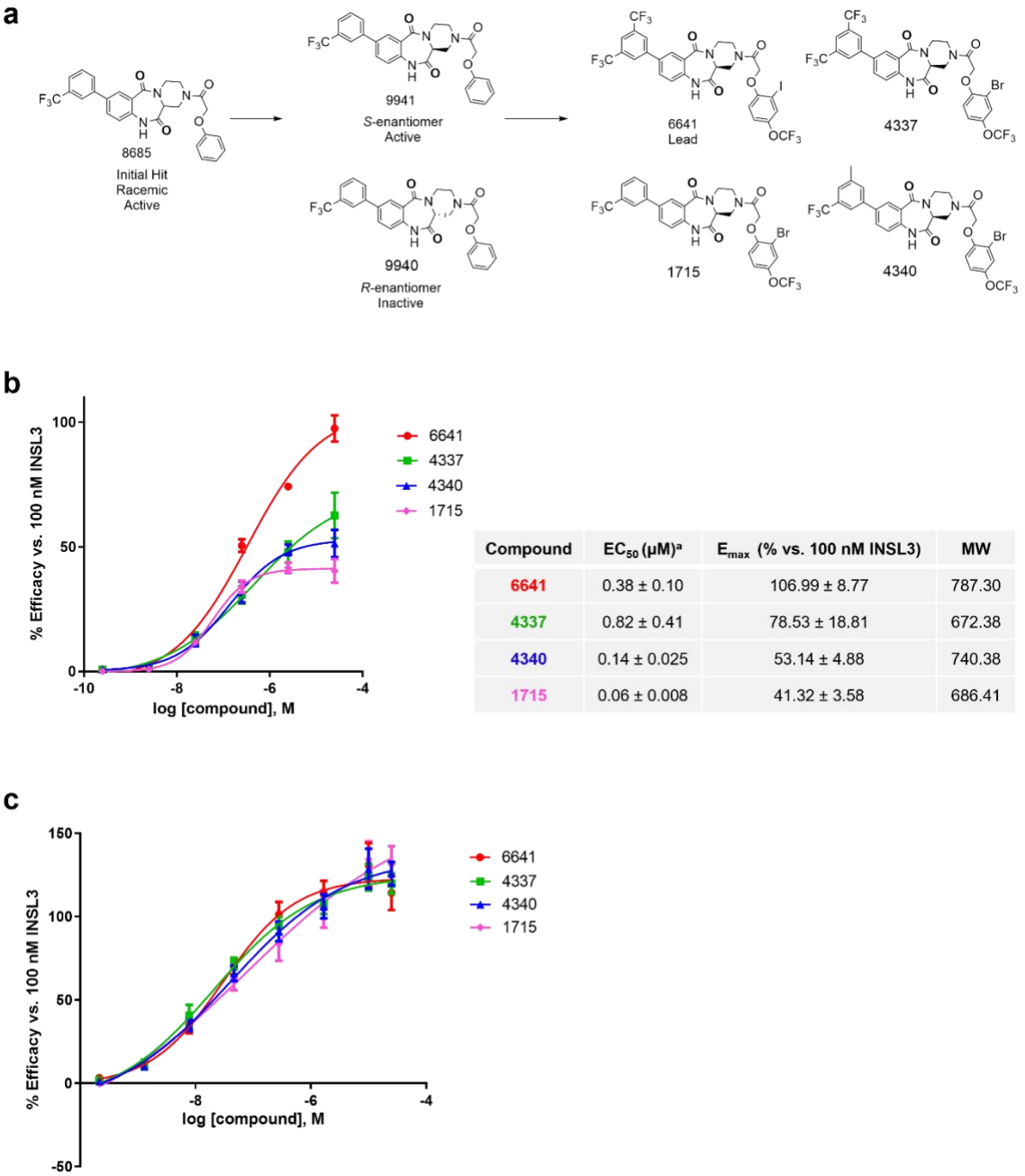

Compound	EC_{50} (μM)[a]	E_{max} (% vs. 100 nM INSL3)	MW
6641	0.38 ± 0.10	106.99 ± 8.77	787.30
4337	0.82 ± 0.41	78.53 ± 18.81	672.38
4340	0.14 ± 0.025	53.14 ± 4.88	740.38
1715	0.06 ± 0.008	41.32 ± 3.58	686.41

Figure 6. RXFP2 agonist screening and SAR study. a) Schematic representation of SAR study showing the initial hit and active enantiomer configuration that led to the final 4 compound, including the lead compound 6641. **b)** Ranking of the RXFP2 agonists activity by HTRF cAMP assay in HEK-RXFP2 cells. **c)** Confirmatory CRE-Luciferase screening of RXFP2 agonists in HEK-CRE-Luc-RXFP2 cells. Compounds efficacy was normalized to 100 nM INSL3 as 100% efficacy. E_{max} and EC_{50} were calculated using four parameter nonlinear fit dose-response curves. Results are expressed as mean ± SEM of 3 independent experiments. [a] The EC_{50} is expressed in micromolar and is the concentration necessary to reach 50% of maximum cAMP signal. Molecular weight (MW).

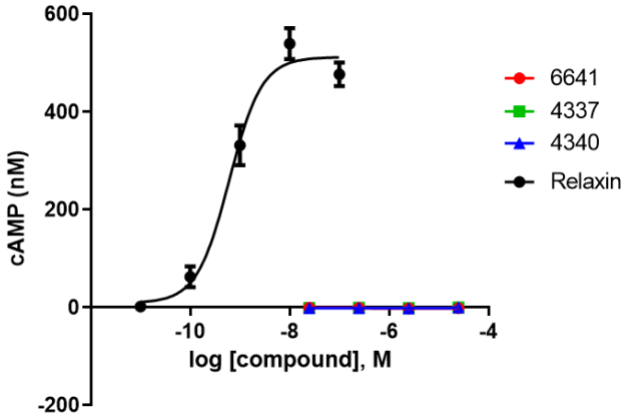

Figure 7. RXFP2 agonists do not activate RXFP1 receptor. HTRF cAMP counter-screen of RXFP2 agonists in HEK293T cells expressing human RXFP1. Relaxin was used as positive control for RXFP1 receptor activation. Results are expressed as mean ± SEM of 3 independent experiments.

Table 2. PRESTO-Tango GPCRome in transiently transfected HTLA cells.

GPCR	6641 fold RLU
ADORA1	3.92 ± 0.15
CCKAR	3.42 ± 0.15
FPR1	3.11 ± 0.29
MRGPRF	2.98 ± 0.17
CXCR7	2.83 ± 0.29
GPR20	2.74 ± 0.42
CCKBR	2.50 ± 0.28
GPR120	2.36 ± 0.89
P2RY1	2.18 ± 0.15
GAL1	2.13 ± 0.28
MRGPRE	2.12 ± 0.20
S1PR4	2.06 ± 0.18
CHRM3	2.04 ± 0.07
PTAFR	2.02 ± 0.15
ADRA2B	2.01 ± 0.80
NPBW2	2.01 ± 0.31
GPR34	2.00 ± 0.19
CHRM2	1.80 ± 0.27
GPR116	1.79 ± 0.16
UTS2R	1.78 ± 0.28
ADRB3	1.70 ± 0.99
GPR126	1.62 ± 0.17
CD97	1.61 ± 0.39
FFA1	1.57 ± 0.18
MRGPRX3	1.55 ± 0.74
MLNR	1.53 ± 0.44
LPAR1	1.51 ± 0.04
GPR17	1.48 ± 0.11
P2RY14	1.48 ± 0.03
GPR183	1.46 ± 0.35
GPR101	1.45 ± 0.05

GPCR	4337 fold RLU
ADORA1	5.24 ± 0.31
FPR1	4.89 ± 0.12
GPR20	4.22 ± 0.91
CCKAR	3.57 ± 0.17
CXCR7	3.44 ± 0.48
P2RY1	3.07 ± 0.14
MRGPRF	3.01 ± 0.19
MRGPRE	2.99 ± 0.16
GPR34	2.85 ± 0.37
GAL1	2.82 ± 0.71
CHRM3	2.65 ± 0.07
GPR120	2.63 ± 0.55
GPR116	2.46 ± 0.30
CHRM2	2.40 ± 0.15
ADCYAP1R1	2.37 ± 0.16
DRD4	2.23 ± 0.34
P2RY13	2.13 ± 0.18
NPFF1	2.11 ± 0.28
GPR149	2.02 ± 0.84
UTS2R	1.95 ± 0.25
LPAR1	1.90 ± 0.12
GPR126	1.90 ± 0.22
GPR22	1.88 ± 0.14
HTR1B	1.88 ± 0.06
PTAFR	1.85 ± 0.14
P2RY14	1.84 ± 0.12
PTGER1	1.84 ± 0.11
MLNR	1.83 ± 0.19
GMR2	1.83 ± 0.17
NMBR	1.83 ± 0.22
TACR2	1.80 ± 0.19

HTR2CVGV	1.41 ± 0.23
GAL2	1.39 ± 0.05
SSTR1	1.38 ± 0.10
ADCYAP1R1	1.37 ± 0.10
GPR156	1.32 ± 0.27
HTR4	1.32 ± 0.20
CCRL2	1.30 ± 0.22
GPR78	1.30 ± 0.12
GPR141	1.30 ± 0.06
CX3CR1	1.28 ± 0.37
GPR176	1.27 ± 0.07
FPR3	1.26 ± 0.03
PTGER1	1.25 ± 0.04
GPR111	1.23 ± 0.37
GPBA	1.23 ± 0.06
TACR2	1.23 ± 0.05
HTR1B	1.19 ± 0.08
TACR3	1.19 ± 0.12
P2RY13	1.18 ± 0.08
SSTR2	1.16 ± 0.30
GPR87	1.15 ± 0.13
ADRA2A	1.14 ± 0.07
CXCR2	1.14 ± 0.04
MRGPRX2	1.13 ± 0.13
NPFF1	1.11 ± 0.11
P2RY6	1.11 ± 0.03
CXCR5	1.10 ± 0.07
LPAR6	1.10 ± 0.41
GPR149	1.09 ± 0.16
NTSR1	1.07 ± 0.09
GPR22	1.07 ± 0.08
GPR75	1.07 ± 0.04
GPR182	1.06 ± 0.14
GPR31	1.05 ± 0.04
Empty	1.04 ± 0.20
HTR5	1.04 ± 0.01
ADRB1	1.04 ± 0.06
TACR1	1.02 ± 0.04
CHRM1	1.02 ± 0.25
PTGER3	1.01 ± 0.06
GPR45	1.00 ± 0.25
GPR12	1.00 ± 0.06
GPR173	0.99 ± 0.24
MRGPRX1	0.99 ± 0.02
Empty	0.99 ± 0.26
CXCR6	0.98 ± 0.19
OXTR	0.97 ± 0.18
VIPR1	0.97 ± 0.08
PTGDR	0.96 ± 0.05
HRH1	0.96 ± 0.05
ELTD1	0.95 ± 0.03
NMBR	0.95 ± 0.17

FPR3	1.75 ± 0.13
GPR17	1.75 ± 0.09
ADRA2B	1.75 ± 0.71
P2RY6	1.73 ± 0.04
CXCR2	1.73 ± 0.10
SSTR1	1.66 ± 0.17
CXCR5	1.66 ± 0.14
CCKBR	1.64 ± 0.16
PTGER3	1.64 ± 0.11
ADRA2A	1.63 ± 0.12
NPBW2	1.62 ± 0.14
MC2R	1.62 ± 0.14
GPR101	1.60 ± 0.07
HRH4	1.58 ± 0.16
MRGPRX2	1.57 ± 0.11
GPR156	1.57 ± 0.84
GAL2	1.55 ± 0.10
HTR2CVGV	1.55 ± 0.35
CCR10	1.54 ± 0.26
TAAR2	1.53 ± 0.77
CCRL2	1.53 ± 0.17
GPR141	1.53 ± 0.06
GPR78	1.53 ± 0.46
S1PR4	1.52 ± 0.11
GPBA	1.51 ± 0.11
GPR55	1.50 ± 0.20
TACR1	1.49 ± 0.06
OPRM1	1.49 ± 0.39
GPR87	1.49 ± 0.10
TACR3	1.48 ± 0.06
OXTR	1.48 ± 0.10
GPR12	1.46 ± 0.08
GPR176	1.43 ± 0.09
GPR18	1.42 ± 0.53
GPR52	1.41 ± 0.05
FFA1	1.38 ± 0.25
P2RY2	1.38 ± 0.07
GPRC5A	1.38 ± 0.27
ADRB1	1.37 ± 0.17
GPR84	1.35 ± 0.09
HTR4	1.35 ± 0.13
EDNRB	1.35 ± 0.44
CX3CR1	1.33 ± 0.21
CD97	1.32 ± 0.18
VIPR1	1.31 ± 0.20
NMUR1	1.31 ± 0.34
AVPR2	1.31 ± 0.13
HCA1	1.30 ± 0.13
GPR35	1.30 ± 0.11
NPY1R	1.29 ± 0.30
DRD2	1.28 ± 0.37
GRM6	1.26 ± 0.21

GHRHR	0.95 ± 0.19
AVPR2	0.94 ± 0.05
HRH3	0.93 ± 0.52
HTR2C VNV	0.93 ± 0.33
RXFP2	0.92 ± 0.08
GPR114	0.92 ± 0.35
GPR55	0.91 ± 0.09
GPR37	0.91 ± 0.07
VIPR2	0.91 ± 0.08
HRH4	0.90 ± 0.25
GRM1	0.89 ± 0.29
GPR44	0.89 ± 0.17
GPR1	0.89 ± 0.04
CCR10	0.88 ± 0.07
AGTR1	0.88 ± 0.12
BB3	0.87 ± 0.08
CXCR4	0.87 ± 0.03
SSTR5	0.86 ± 0.10
HTR2C INI	0.86 ± 0.05
P2RY2	0.85 ± 0.07
GPR35	0.84 ± 0.03
APJ	0.83 ± 0.13
MC4R	0.83 ± 0.13
CRHR1	0.82 ± 0.06
GPR135	0.81 ± 0.05
TAAR2	0.81 ± 0.10
GRM6	0.81 ± 0.26
NMUR1	0.80 ± 0.11
GPR52	0.80 ± 0.02
CYSLTR2	0.79 ± 0.06
S1PR3	0.79 ± 0.13
AGTR2	0.79 ± 0.03
GPRC5D	0.79 ± 0.21
CALCRb	0.79 ± 0.10
HTR1E	0.79 ± 0.07
GMR2	0.78 ± 0.09
HTR1F	0.78 ± 0.22
DRD2	0.77 ± 0.11
GPR27	0.77 ± 0.31
GPR157	0.77 ± 0.28
AVPR1B	0.77 ± 0.09
DRD3	0.76 ± 0.28
KISSPEPTIN	0.76 ± 0.13
MC5R	0.76 ± 0.05
HTR2B	0.76 ± 0.03
GPR110	0.74 ± 0.21
HTR1D	0.74 ± 0.04
MTNR1B	0.74 ± 0.03
GPR97	0.74 ± 0.08
S1PR1	0.73 ± 0.12
PTGER2	0.73 ± 0.05
OPN5	0.73 ± 0.05

GPR75	1.26 ± 0.05
MRGPRX1	1.25 ± 0.19
VIPR2	1.25 ± 0.22
HRH1	1.25 ± 0.12
S1PR2	1.23 ± 0.15
ELTD1	1.23 ± 0.05
P2RY4	1.22 ± 0.07
HTR1E	1.21 ± 0.14
SSTR2	1.21 ± 0.34
GPR114	1.21 ± 0.22
NTSR1	1.20 ± 0.14
HCTR2	1.18 ± 0.35
GPR1	1.18 ± 0.04
GPR31	1.17 ± 0.01
GPR97	1.16 ± 0.12
AGTR2	1.16 ± 0.07
GPR171	1.15 ± 0.05
OXGR1	1.15 ± 0.24
Empty	1.15 ± 0.29
AGTR1	1.14 ± 0.12
GPR63	1.14 ± 0.04
SSTR4	1.14 ± 0.17
GPR37	1.12 ± 0.08
PTGDR	1.11 ± 0.04
HTR1D	1.08 ± 0.06
CALCRb	1.07 ± 0.07
P2RY10	1.07 ± 0.10
GPR173	1.07 ± 0.20
SCTR	1.06 ± 0.21
GPR182	1.05 ± 0.08
CXCR4	1.05 ± 0.04
OPN5	1.05 ± 0.06
MRGPRD	1.04 ± 0.45
GPR44	1.03 ± 0.13
GPR135	1.03 ± 0.08
OPRK1	1.02 ± 0.12
HTR5	1.02 ± 0.05
GRM8	1.01 ± 0.46
HTR1A	1.01 ± 0.09
BB3	1.01 ± 0.31
GPRC5D	0.99 ± 0.13
RXFP3	0.98 ± 0.06
HRH2	0.98 ± 0.05
GPR88	0.98 ± 0.09
HTR6	0.97 ± 0.14
LPAR5	0.96 ± 0.10
NPY4R	0.96 ± 0.14
AVPR1A	0.96 ± 0.06
PTGER2	0.96 ± 0.07
ADRA1A	0.96 ± 0.19
NPS	0.96 ± 0.04
GPR85	0.95 ± 0.10

GPR63	0.73 ± 0.07
MC2R	0.72 ± 0.02
S1PR5	0.72 ± 0.14
DRD4	0.72 ± 0.07
PTGIR	0.72 ± 0.37
ADRA2C	0.71 ± 0.13
GPRC5A	0.71 ± 0.12
GPR77	0.71 ± 0.04
EDNRB	0.71 ± 0.19
NPY5R	0.71 ± 0.09
HTR6	0.70 ± 0.15
OXGR1	0.69 ± 0.16
GPR62	0.69 ± 0.13
MRGPRX4	0.69 ± 0.03
NPY4R	0.68 ± 0.07
FPR2	0.68 ± 0.13
RXFP4	0.68 ± 0.12
P2RY4	0.68 ± 0.04
GPR88	0.67 ± 0.06
GPR148	0.67 ± 0.23
LHCGR	0.66 ± 0.04
CCR6	0.66 ± 0.04
OPRK1	0.66 ± 0.15
SSTR4	0.66 ± 0.05
SCTR	0.66 ± 0.12
S1PR2	0.66 ± 0.10
LTB4R	0.65 ± 0.06
GRM5	0.65 ± 0.06
GPR125	0.65 ± 0.10
HCA1	0.64 ± 0.07
CHRM4	0.64 ± 0.09
MTNR1A	0.64 ± 0.07
ADRA1D	0.63 ± 0.14
GPR84	0.63 ± 0.04
HTR1A	0.62 ± 0.11
P2RY10	0.62 ± 0.10
GPR64	0.61 ± 0.02
GPR85	0.61 ± 0.08
GPR21	0.60 ± 0.07
CALCRL	0.59 ± 0.05
ADRA1A	0.58 ± 0.17
GAL3	0.57 ± 0.10
PK2	0.57 ± 0.09
GPR113	0.57 ± 0.06
GCGR	0.57 ± 0.12
CRHR2	0.57 ± 0.07
GPRC5B	0.57 ± 0.07
HCA2	0.56 ± 0.04
CCR7	0.56 ± 0.07
GPR25	0.56 ± 0.07
ADORA2A	0.56 ± 0.02
GPR3	0.56 ± 0.23

CRHR1	0.95 ± 0.06
NPY5R	0.94 ± 0.12
MTNR1B	0.94 ± 0.13
GPR144	0.94 ± 0.14
CYSLTR2	0.93 ± 0.07
GPR77	0.93 ± 0.13
HCA2	0.93 ± 0.07
S1PR5	0.91 ± 0.20
CHRM4	0.91 ± 0.13
GPR183	0.90 ± 0.12
GPR25	0.90 ± 0.04
CRHR2	0.89 ± 0.17
AVPR1B	0.88 ± 0.08
GPR15	0.88 ± 0.11
PTGIR	0.88 ± 0.10
LTB4R	0.87 ± 0.13
KISSPEPTIN	0.87 ± 0.08
BDKBR1	0.87 ± 0.10
S1PR3	0.87 ± 0.09
GPR113	0.87 ± 0.23
GPR21	0.86 ± 0.04
SSTR5	0.86 ± 0.11
MC5R	0.86 ± 0.03
PK2	0.86 ± 0.14
MC1R	0.85 ± 0.09
APJ	0.85 ± 0.03
GPR162	0.85 ± 0.07
GPR110	0.84 ± 0.16
LPAR6	0.84 ± 0.06
RXFP2	0.84 ± 0.08
MCHR1R	0.84 ± 0.06
GPRC5B	0.84 ± 0.06
OPRL1	0.83 ± 0.26
CCR6	0.82 ± 0.05
HTR2C INI	0.82 ± 0.02
ADORA2A	0.81 ± 0.06
GPR111	0.81 ± 0.26
MC4R	0.79 ± 0.05
GAL3	0.78 ± 0.20
MC3Rb	0.78 ± 0.10
GPR64	0.77 ± 0.01
CCR7	0.77 ± 0.10
GPR150	0.77 ± 0.18
GPR45	0.77 ± 0.05
GPR56	0.76 ± 0.08
GPR148	0.76 ± 0.25
CCR2	0.75 ± 0.05
GPR3	0.74 ± 0.03
CCR3	0.74 ± 0.06
RXFP4	0.74 ± 0.18
S1PR1	0.73 ± 0.13
GPR26	0.73 ± 0.04

MCHR1R	0.55 ± 0.02
LPAR5	0.55 ± 0.05
GRM4	0.54 ± 0.01
MRGPRD	0.54 ± 0.14
GHSR	0.54 ± 0.05
GPR174	0.54 ± 0.11
GPR143	0.54 ± 0.03
GRM8	0.53 ± 0.16
GPR18	0.53 ± 0.11
CMKLR1	0.52 ± 0.07
HRH2	0.52 ± 0.11
GPR26	0.52 ± 0.03
CXCR3	0.52 ± 0.03
OPRL1	0.52 ± 0.08
AVPR1A	0.52 ± 0.08
OPRM1	0.52 ± 0.15
GPR171	0.52 ± 0.05
GPR56	0.51 ± 0.09
GPR158	0.51 ± 0.24
HCTR2	0.50 ± 0.08
PK1	0.50 ± 0.06
GPR146	0.50 ± 0.09
MC1R	0.49 ± 0.03
CCR8	0.49 ± 0.20
C5A	0.49 ± 0.08
GPR150	0.48 ± 0.08
TA1	0.47 ± 0.02
CHRM5	0.47 ± 0.03
MAS1	0.47 ± 0.02
GPR142	0.46 ± 0.10
BDKBR2	0.46 ± 0.09
CCR2	0.45 ± 0.04
GPER	0.45 ± 0.03
NPFF2	0.44 ± v0.04
GPR6	0.44 ± 0.01
DRD5	0.43 ± 0.06
P2RY11	0.43 ± 0.02
GABBR1	0.43 ± 0.06
CCR3	0.43 ± 0.03
GPR65	0.42 ± 0.02
GPR153	0.42 ± 0.04
F2R-L1	0.42 ± 0.05
GPR144	0.42 ± 0.06
NPBW1	0.42 ± 0.02
GPR162	0.41 ± 0.07
GPR151	0.41 ± 0.02
GPRC5C	0.41 ± 0.14
HTR2C VSV	0.41 ± 0.12
RXFP3	0.41 ± 0.06
GPR15	0.41 ± 0.05
C3AR1	0.40 ± 0.08
QRFP	0.40 ± 0.06

FPR2	0.72 ± 0.10
GPER	0.72 ± 0.05
BDKBR2	0.72 ± 0.12
CHRM1	0.72 ± 0.10
P2RY11	0.72 ± 0.04
ADRB3	0.71 ± 0.21
GRM5	0.71 ± 0.08
TA1	0.71 ± 0.04
GPR6	0.70 ± 0.06
MRGPRX4	0.70 ± 0.07
NPBW1	0.69 ± 0.07
MTNR1A	0.69 ± 0.05
LHCGR	0.68 ± 0.05
C5A	0.68 ± 0.12
GHRHR	0.67 ± 0.16
TBXA2R	0.67 ± 0.12
HRH3	0.65 ± 0.34
GPR146	0.64 ± 0.16
QRFP	0.64 ± 0.02
CHRM5	0.64 ± 0.04
GPR125	0.64 ± 0.07
ADRA1D	0.63 ± 0.05
PK1	0.62 ± 0.09
GPR123	0.61 ± 0.09
F2R-L1	0.61 ± 0.02
CXCR1	0.60 ± 0.04
GCGR	0.60 ± 0.16
GNRHR	0.60 ± 0.14
P2RY12	0.59 ± 0.05
FFA2	0.59 ± 0.06
GHSR	0.59 ± 0.04
GPR65	0.59 ± 0.02
PRRP	0.58 ± 0.02
GIPR	0.58 ± 0.17
CMKLR1	0.57 ± 0.11
CXCR6	0.57 ± 0.05
GPR174	0.55 ± 0.12
GPR157	0.55 ± 0.11
PTGER4	0.55 ± 0.11
GPRC6A	0.54 ± 0.05
NTSR2	0.53 ± 0.02
NMUR2	0.53 ± 0.05
FSHR	0.53 ± 0.08
CALCRL	0.53 ± 0.11
HTR2C VNV	0.53 ± 0.07
CYSLTR1	0.52 ± 0.11
GRM4	0.52 ± 0.03
DRD1	0.52 ± 0.09
HTR2B	0.52 ± 0.02
F2RL2	0.52 ± 0.03
HTR2A	0.52 ± 0.08
HTR1F	0.51 ± 0.16

OPN3	0.40 ± 0.06
CYSLTR1	0.40 ± 0.04
ADORA2B	0.40 ± 0.02
SUCNR1	0.40 ± 0.10
PTGER4	0.39 ± 0.10
NTSR2	0.39 ± 0.01
GNRHR	0.39 ± 0.19
TAAR6	0.39 ± 0.02
NPS	0.39 ± 0.07
TBXA2R	0.39 ± 0.07
F2RL2	0.38 ± 0.01
GPR32	0.38 ± 0.05
P2RY12	0.37 ± 0.04
FFA2	0.37 ± 0.03
MC3Rb	0.37 ± 0.04
SSTR3	0.36 ± 0.03
HTR2A	0.36 ± 0.04
GPRC6A	0.36 ± 0.02
NPY1R	0.35 ± 0.06
GPR119	0.35 ± 0.10
OXER1	0.35 ± 0.04
DRD1	0.35 ± 0.09
NMUR2	0.34 ± 0.03
F2R	0.34 ± 0.02
PRRP	0.34 ± 0.03
GIPR	0.34 ± 0.09
LPA4	0.33 ± 0.04
ADRB2	0.33 ± 0.07
GPR115	0.33 ± 0.01
F2RL3	0.33 ± 0.03
GPR123	0.32 ± 0.02
OPRD1	0.32 ± 0.04
GPR82	0.31 ± 0.01
CXCR1	0.31 ± 0.02
HCA3	0.31 ± 0.04
GRM7	0.30 ± 0.02
GRPR	0.30 ± 0.05
GLP2R	0.30 ± 0.08
NPY2R	0.30 ± 0.02
MCHR2R	0.29 ± 0.08
PTH2R	0.29 ± 0.04
ADORA3	0.29 ± 0.01
PTH1R	0.29 ± 0.02
GLP1R	0.28 ± 0.01
GPR68	0.28 ± 0.03
HCTR1	0.28 ± 0.00
GPR37L1	0.28 ± 0.08
HTR7	0.28 ± 0.02
GPR132	0.28 ± 0.01
LPAR2	0.28 ± 0.04
GPR161	0.27 ± 0.04
GPR152	0.26 ± 0.01

GPR62	0.51 ± 0.11
MAS1	0.51 ± 0.01
Empty	0.50 ± 0.08
GPR143	0.50 ± 0.02
GPR27	0.50 ± 0.09
GPR153	0.50 ± 0.03
ADRA2C	0.49 ± 0.11
F2RL3	0.49 ± 0.06
NPFF2	0.49 ± 0.04
TAAR6	0.48 ± 0.04
F2R	0.48 ± 0.04
SUCNR1	0.48 ± 0.06
GPR115	0.48 ± 0.02
GRM1	0.47 ± 0.03
GPR119	0.47 ± 0.05
SSTR3	0.47 ± 0.05
GPR50	0.47 ± 0.004
ADORA2B	0.47 ± 0.07
HCTR1	0.46 ± 0.03
RXFP1	0.45 ± 0.05
GPR152	0.45 ± 0.01
GPR151	0.44 ± 0.05
CCR8	0.44 ± 0.07
HTR7	0.44 ± 0.02
OPRD1	0.43 ± 0.05
CNR2	0.42 ± 0.05
DRD5	0.42 ± 0.05
GPR32	0.42 ± 0.04
GPR82	0.42 ± 0.03
C3AR1	0.42 ± 0.06
HTR2C VSV	0.42 ± 0.11
MRGPRX3	0.40 ± 0.05
OPN3	0.40 ± 0.03
CNR1	0.39 ± 0.04
NPY2R	0.39 ± 0.02
GPR161	0.39 ± 0.05
GPRC5C	0.39 ± 0.08
GABBR1	0.39 ± 0.14
GPR160	0.39 ± 0.03
TSHR	0.38 ± 0.01
MCHR2R	0.38 ± 0.02
GPR142	0.38 ± 0.04
GRPR	0.38 ± 0.07
CCR4	0.37 ± 0.02
OXER1	0.37 ± 0.04
ADORA3	0.36 ± 0.04
CXCR3	0.36 ± 0.02
PTH2R	0.36 ± 0.06
GPR37L1	0.36 ± 0.04
DRD3	0.35 ± 0.08
FFA3	0.35 ± 0.01
GPR158	0.35 ± 0.04

TAAR8	0.26 ± 0.02
GPR50	0.25 ± 0.03
GPR160	0.25 ± 0.03
ADRA1B	0.25 ± 0.02
CCR4	0.25 ± 0.01
BDKBR1	0.25 ± 0.04
P2RY8	0.25 ± 0.05
CNR1	0.25 ± 0.03
CCR5	0.24 ± 0.01
FSHR	0.23 ± 0.04
MRGPRG	0.23 ± 0.03
GPR124	0.23 ± 0.03
TSHR	0.23 ± 0.02
GPR19	0.22 ± 0.005
PTGFR	0.22 ± 0.02
GPR39	0.22 ± 0.02
RXFP1	0.22 ± 0.02
LTB4R2B	0.21 ± 0.02
EDNRA	0.21 ± 0.02
CNR2	0.21 ± 0.03
GPR133	0.20 ± 0.02
MAS1L	0.20 ± 0.03
FFA3	0.20 ± 0.02
TAAR9	0.17 ± 0.01
TAAR5	0.17 ± 0.01
CASR	0.17 ± 0.03
GPR4	0.16 ± 0.03
GPR61	0.14 ± 0.01
GPR83	0.13 ± 0.02

PTH1R	0.34 ± 0.03
GPR39	0.34 ± 0.07
PTGFR	0.34 ± 0.08
GRM7	0.34 ± 0.04
LPAR2	0.34 ± 0.03
GPR19	0.34 ± 0.03
LPA4	0.33 ± 0.04
GPR133	0.33 ± 0.03
ADRB2	0.33 ± 0.05
CCR5	0.33 ± 0.05
GPR132	0.32 ± 0.02
LTB4R2B	0.32 ± 0.02
ADRA1B	0.31 ± 0.04
MAS1L	0.31 ± 0.005
HCA3	0.31 ± 0.05
P2RY8	0.31 ± 0.06
GLP1R	0.30 ± 0.09
GPR124	0.30 ± 0.03
TAAR8	0.29 ± 0.04
EDNRA	0.29 ± 0.05
GPR68	0.27 ± 0.03
GLP2R	0.27 ± 0.03
GPR61	0.25 ± 0.01
MRGPRG	0.25 ± 0.07
CASR	0.25 ± 0.09
TAAR9	0.24 ± 0.02
GPR83	0.23 ± 0.03
GPR4	0.22 ± 0.03
TAAR5	0.20 ± 0.02

Compound 6641 and 4337 high-throughput counter-screen against 320 GPCRs. Compounds response was calculated as fold RLU of unstimulated cells. GPCRs with more than 3.0-fold RLU were considered a potential target (showed in red). Results represent the mean ± SEM of 4 technical replicates.

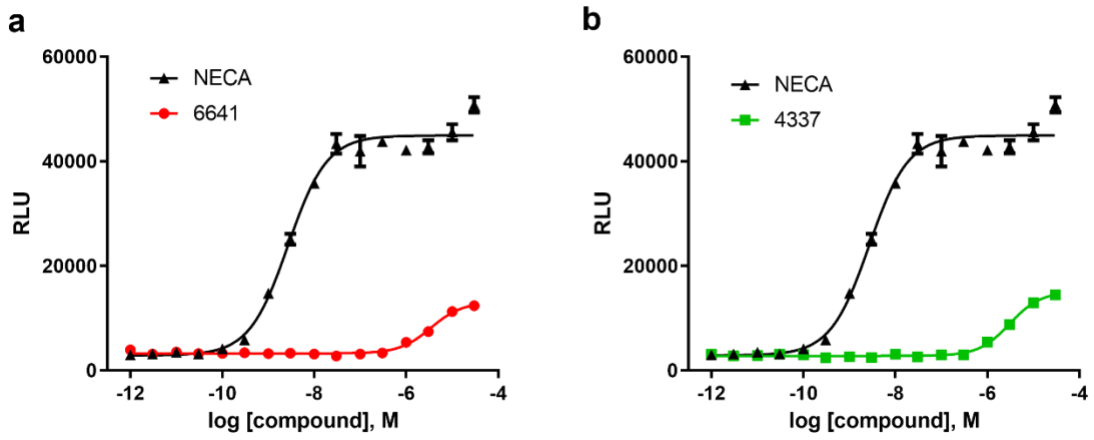

Figure 8. Compounds 6641 and 4337 induce β-arrestin binding to ADORA1. β-arrestin translocation activity induced by **a)** 6641 and **b)** 4337 in ADORA1 transiently transfected HTLA cells. NECA was used as positive control for ADORA1 receptor activation. Results are reported as raw RLU values and represent the mean ± SEM of 4 technical replicates.

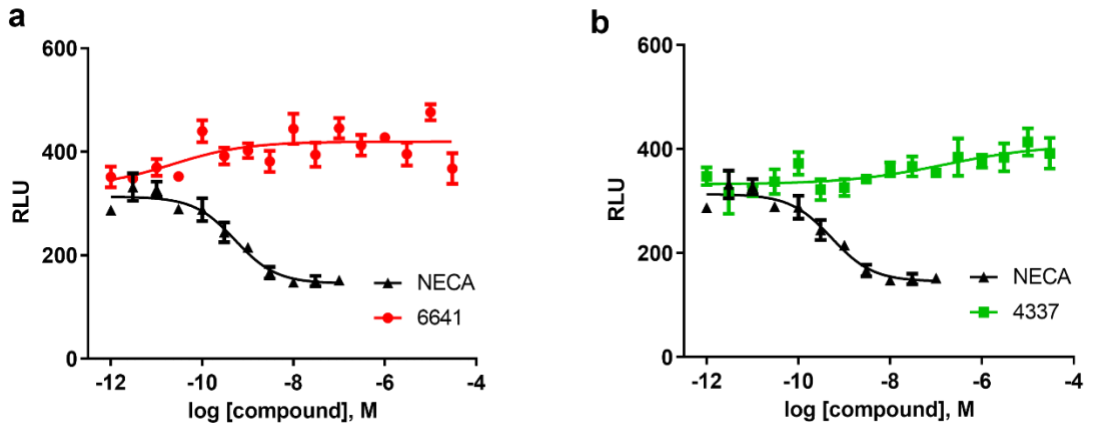

Figure 9. Compounds 6641 and 4337 do not activate ADORA1 cAMP signaling. cAMP inhibition by positive control NECA and compounds **a)** 6641 and **b)** 4337 in HEK293T cells transiently transfect with ADORA1. Results are reported as raw RLU values and represent the mean ± SEM of 4 technical replicates.

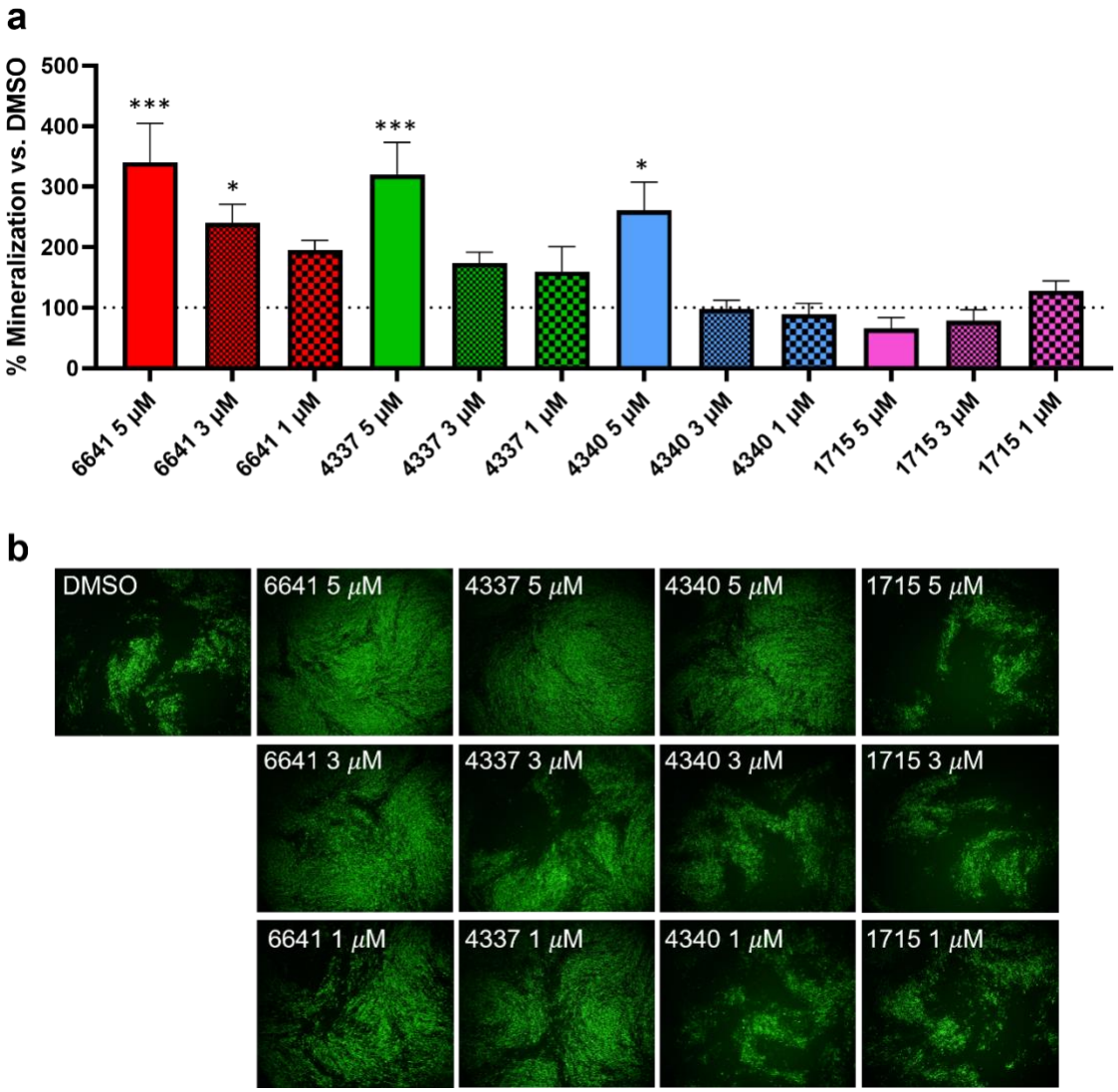

Figure 10. RXFP2 agonists induce mineralization of primary human osteoblasts. a) Mineral hydroxyapatite fluorescent quantification after 14-day treatment in HCO cells. Results were normalized to control DMSO as 100% mineralization. **b)** Representative images of the hydroxyapatite bone-like nodules. Results are expressed as mean ± SEM of 3 independent experiments. *$p<0.05$, *** $p<0.001$ vs. DMSO using 1-way ANOVA.

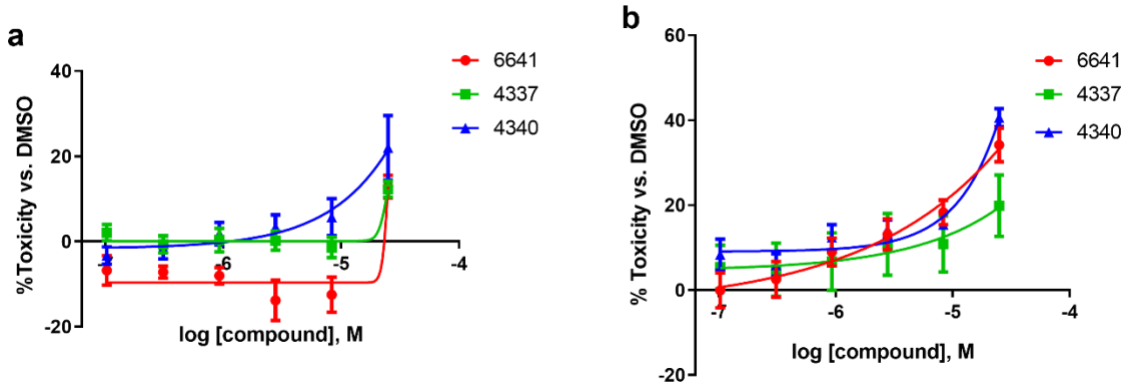

Figure 11. RXFP2 agonists are non-cytotoxic *in vitro*. a) HCO and **b)** HAVSMC toxicity after 24-hour treatment with RXFP2 agonists, normalized to DMSO treatment as 0% toxicity. Results are expressed as mean ± SEM of 3 independent experiments.

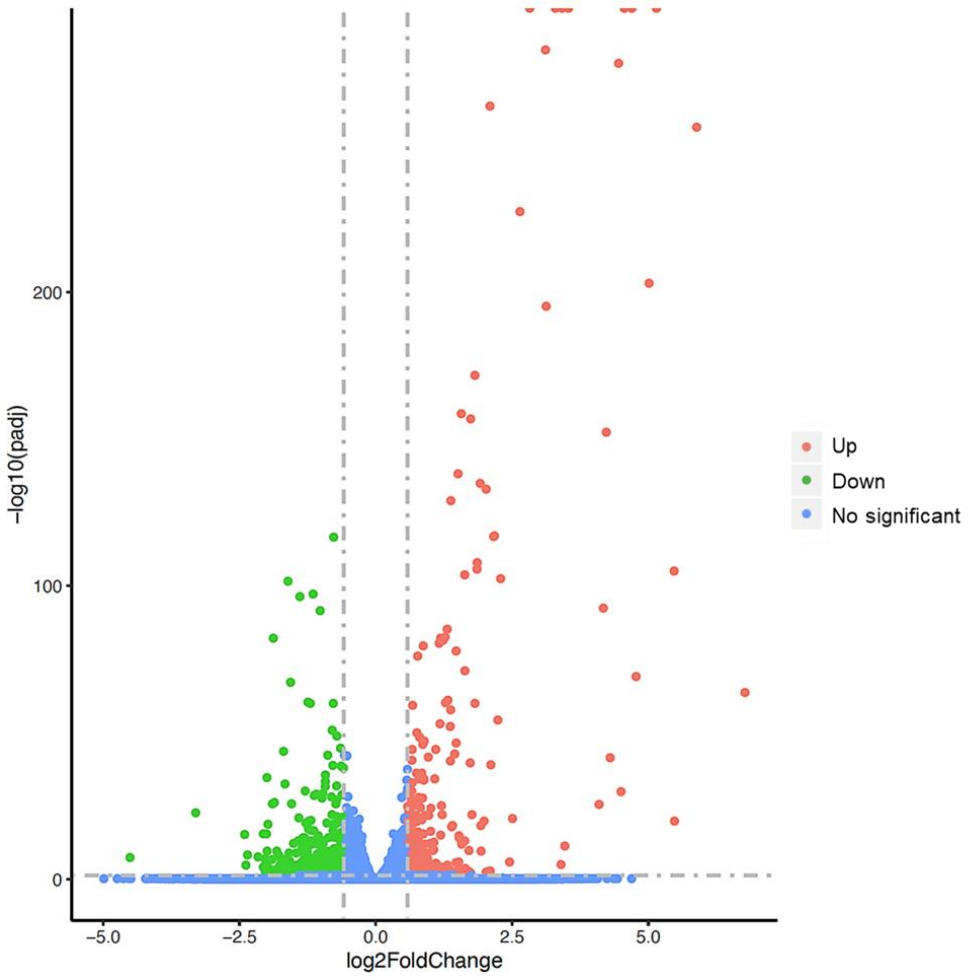

Figure 12. Transcriptional analysis of HCO cells treated with compound 6641. The volcano plot shows differentially expressed genes after a 14-day treatment with 5 μM 6641 in comparison to DMSO vehicle (control) treatment. A total of 319 genes were up-regulated (red dots) and 358 genes were down-regulated (green dots). Results are expressed as the mean of 4 technical replicates. Log_2 fold change>0.585 and padj<0.05 vs. DMSO.

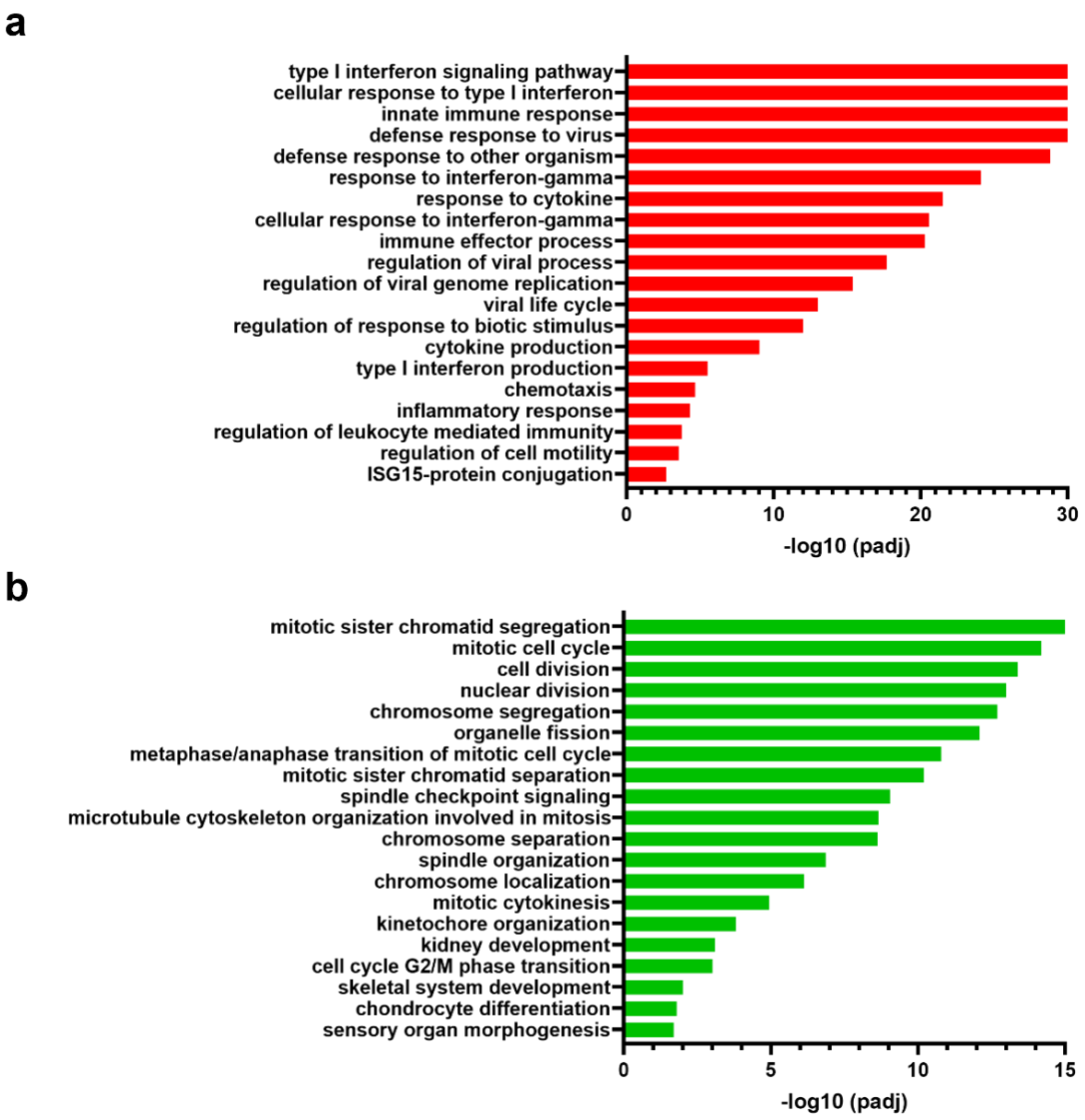

Figure 13. Gene ontology analysis of differentially expressed genes in HCO cells treated with compound 6641. Gene enrichment pathway analysis for **a**) up-regulated or **b)** down-regulated biological processes after a 14-day treatment with 5 μM 6641 in comparison to DMSO vehicle (control) treatment. padj<0.05 vs. DMSO.

Table 3. Summary of differentially expressed genes in HCO cells treated with compound 6641.

Gene Name	Log_2 Fold Change	-Log10 (padj)
RSAD2	6.77	63.48
MX2	5.89	256.04
BST2	5.48	19.61
MX1	5.47	104.93
OAS2	5.15	ND
IFI27	5.01	203.02
IFI44L	4.69	ND
IFI6	4.56	ND
OASL	4.30	41.18
ISG15	4.23	152.09
OAS1	4.17	92.30
IFITM1	3.42	ND
IFIT1	3.29	ND
OAS3	3.11	282.42
IFIT3	2.82	ND
IRF7	2.16	116.65
STAT1	2.09	263.40
IFIT2	2.02	132.83
STAT2	1.60	59.10
IRF9	1.39	17.66

Gene Name	Log_2 Fold Change	-Log10 (padj)
ACAN	-3.30	22.54
MYBL2	-2.16	7.57
LEP	-2.06	4
DTL	-2.04	6.84
RGS5	-2.00	34.58
NTN1	-1.90	25.64
GPC3	-1.88	82.03
IGFBP5	-1.61	101.32
BMP4	-1.51	3.07
ASPM	-1.46	8.74
ADAMTS7	-1.39	96.19
BIRC5	-1.30	4.20
CEP55	-1.25	3.86
KIF20A	-1.23	4.07
NCAPG	-1.18	5.53
KIFC1	-1.17	3.15
MFAP5	-1.15	97.06
TNXB	-1.13	28.35
BUB1	-1.08	3.37
ANLN	-1.07	11.88

List of the most significant differentially expressed genes after a 14-day treatment with 5 μM 6641 in comparison to DMSO vehicle (control) treatment. Results are expressed as the mean of 4 technical replicates. Log_2 fold change>1 and padj<0.05 vs. DMSO. If padj was not calculated due to very high significance, it was expressed as ND (not determined).

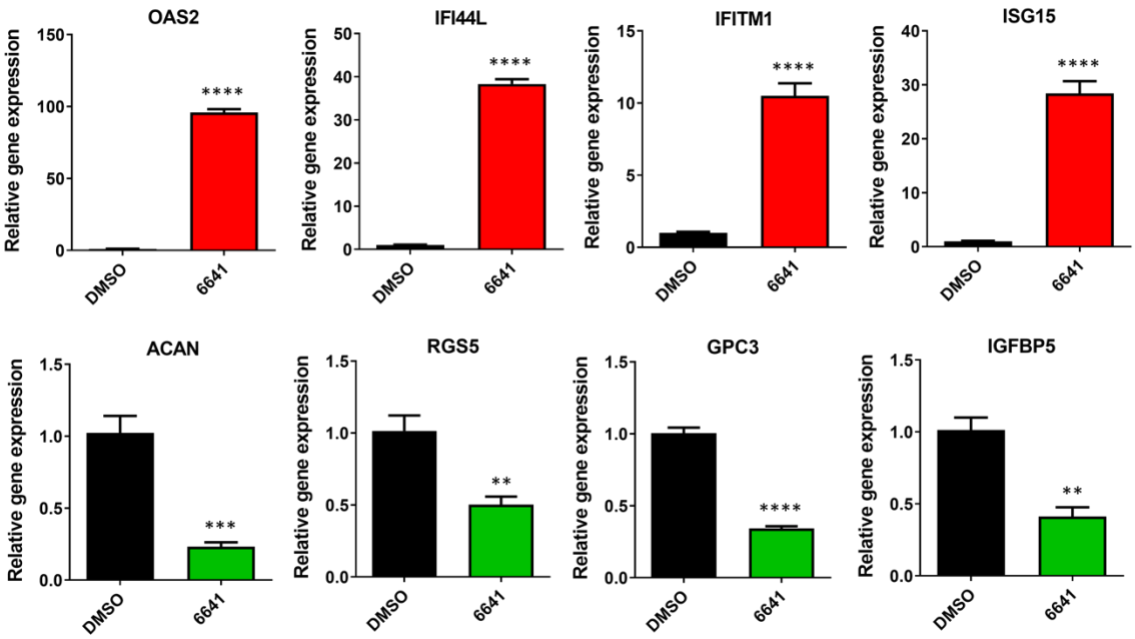

Figure 14. Validation of the RNA-seq results by quantitative RT-PCR. Representative up-regulated (red columns) and down-regulated (green columns) genes after a 14-day treatment with 5 µM 6641 in comparison to DMSO vehicle (control) treatment were normalized to *RPLP0* gene expression as an internal control. Results are expressed as the mean ± SEM of 4 technical replicates. **p<0.01, *** p<0.001, **** p<0.0001 vs. DMSO using Student's t-test.

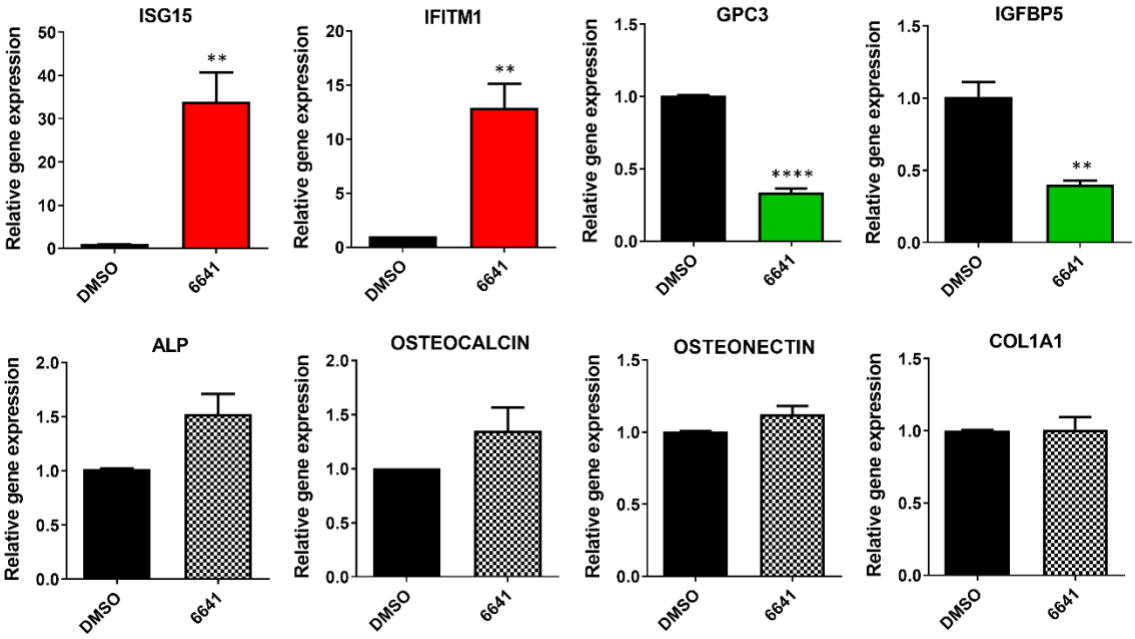

Figure 15. Quantitative RT-PCR analysis in HCO cells after a 14-day treatment with 6641. Expression levels of genes identified in the RNA-seq study (*ISG15*, *IFITM1*, *GPC3* and *IGFBP5*) and genes involved in osteoblast maturation (*ALP*, *OSTEOCALCIN*, *OSTEONECTIN* and *COL1A1*) after a 14-day treatment with 5 µM 6641 in comparison to DMSO vehicle (control)

treatment were normalized to *RPLP0* gene expression as an internal control. Results are expressed as mean ± SEM of 3 independent experiments. **p<0.01, **** p<0.0001 vs. DMSO using Student's t-test.

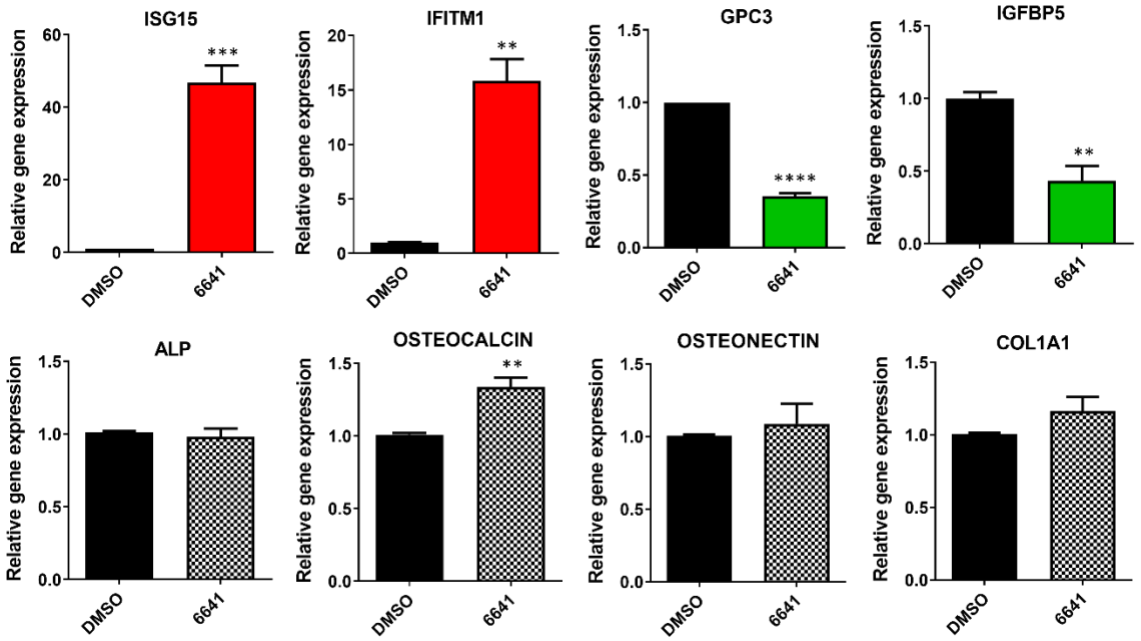

Figure 16. Quantitative RT-PCR analysis in HCO cells after a 7-day treatment with 6641. Expression levels of genes identified in the RNA-seq study (*ISG15*, *IFITM1*, *GPC3* and *IGFBP5*) and genes involved in osteoblast maturation (*ALP*, *OSTEOCALCIN*, *OSTEONECTIN* and *COL1A1*) after a 7-day treatment with 5 μM 6641 in comparison to DMSO vehicle (control) treatment were normalized to *RPLP0* gene expression as an internal control. Results are expressed as mean ± SEM of 3 independent experiments. **p<0.01, *** p<0.001, **** p<0.0001 vs. DMSO using Student's t-test.

2.5 Discussion

This chapter presents the discovery of the first-in-class RXFP2 agonists, starting with a HTRF cAMP HTS campaign of a small molecule library at NCATS/NIH against the RXFP2 receptor, and resulting in the identification of a suitable active chemotype that underwent optimization to create agonists with favorable properties for *in vivo* testing. Here we describe 4 of the lead molecules from the SAR study: compounds 6641, 4337, 4340, and 1715. The direct HTRF cAMP

assay in HEK-RXFP2 cells showed that the efficacy and activity of compound 6641 (EC50 = 0.38 μM, Emax = 107%) is significantly better than the other 3 compounds, with the maximum efficacy of response equivalent to the natural ligand INSL3 (Figure 6b). A validation screen using HEK-CRE-Luc-RXFP2 cells utilizing a luciferase reporter driven by a CRE-regulated promoter confirmed that all 4 compounds activate RXFP2 receptor signaling. However, due to the accumulation of luciferase, this assay lacks the sensitivity to detect differences in efficacy (Figure 6c). Several counter-screens were implemented to demonstrate the specificity of the small molecule RXFP2 agonists. Compounds 6641, 4337 and 4340 were not able to induce a cAMP response through the activation of the highly homologous RXFP1 receptor (Figure 7). Moreover, a PRESTO-Tango assay of 320 non-related GPCRs showed that 6641 and 4337 only induced β-arrestin recruitment through activation of one receptor, ADORA1, at concentrations above 1 μM (Figure 8). Importantly, binding of small molecule agonists did not result in activation of ADORA1 mediated G protein signaling (Figure 9). Interestingly, the PRESTO-Tango assay also showed that β-arrestin recruitment was not activated by 6641 or 4337 through the RXFP2 receptor. This supports results from our lab that after treatment with natural ligand INSL3 or compound 6641, β-arrestin is not recruited to RXFP2 (data not shown). These results indicate that the RXFP2 receptor could remain activated for long periods of time without undergoing receptor desensitization (81), which might be beneficial, as it potentially reduces the amount of drug needed to induce a biological response for this target.

To evaluate the effects of RXFP2 small molecule agonists on bone cells, we first looked at their ability to induce mineralization of primary human osteoblasts expressing RXFP2. We demonstrated that the mineralization activity induced by the compounds 6641, 4337, 4340 and 1715 correlated with their respective cAMP responses observed in HEK-RXFP2 cells (Figure 10). This indicates that RXFP2 activation of cAMP signaling is a key cellular pathway that promotes mineralization in osteoblast cells. The importance of cAMP signaling during bone formation has been previously described for the GPCR parathyroid hormone 1 receptor (PTHR1) after activation with the ligand PTH. The PTH/PTHR1 ligand-receptor pair signals primarily by coupling to $G_{\alpha S}$ and inducing an increase in cAMP intracellularly that activates the protein kinase A (PKA) pathway to regulate bone formation and calcium homeostasis (145). PTH activation of the cAMP-PKA signaling pathway has also been associated with downstream activation of the WNT/β-catenin signaling pathway that increases bone formation by promoting osteoblast maturation (146). Interestingly, previous studies from our lab discovered that deletion of *Rxfp2* in male mice gubernaculum drastically decreases expression of β-catenin, indicating that it could be also an important target of RXFP2 signaling in bones (99). Additionally, the results of the RNAseq analysis in HCO cells after treatment with 6641 identified interferon signaling as the most up regulated signaling pathway (Figure 13a, Table 3). Although interferon signaling is not one of the common pathways in osteoblasts differentiation and maturation, recent studies have investigated the possible roles of interferon responses in bone-forming cells. Upregulation of type-I interferon signaling has been shown to

suppresses osteogenesis (147, 148). On the other hand, a study demonstrated that the osteoporosis treatment alendronate increases bone formation in ovariectomized rats via upregulation of the IFN-β/STAT1 signaling pathway in osteoblasts (149). Activation of IFN-γ signaling in osteoblast and osteoprogenitor cells also increases bone formation and has been proposed as a potential pharmacological target for osteoporosis treatment (150, 151). Interestingly, some of the upregulated interferon genes like *IFITM1* and *ISG15* have been shown to increase bone formation by enhancing osteoblasts differentiation (152, 153). Therefore, it appears that activation of interferon signaling could have a dual function inhibiting and promoting bone formation. More research needs to be done to understand the molecular bases and of this duality. The decrease in the expression of genes involve in cell cycle and division (Figure 13b) correlates with the maturation stage of the osteoblast cells. In contrast to pre-osteoblasts, after extracellular matrix mineralization mature osteoblasts do not divide or proliferate any longer (154). The osteoblasts treated with compound 6641 are significantly more mineralized at 14 days than the DMSO treated control, hence they are in a non-proliferate stage. Some downregulate genes were found to be involved in skeletal system development. *BMP4* expression is important for normal chondrogenesis and osteogenesis (155). Mutations in the *GPC3* gene have been linked to skeletal malformations and overgrowth (156). Moreover, the downregulation of *GPC3* in human calvarial suture mesenchymal cells has been shown to stimulate premature ossification and fusion of the cranial plates (157). Interestingly, the downregulation of the gene *IGFBP5* after compound 6641

treatment could have a protective effect in bone, as overexpression of *IGFBP5* has been shown to decrease osteoblasts differentiation, skeletal development, and bone volume (158-160). Bone marrow stromal mesenchymal cells can differentiate into adipocytes, chondrocytes, or osteoblasts. *LEP* is a very important gene that drives adipogenesis and inhibits osteogenesis (161, 162). Downregulation of *LEP* expression in osteoblast cells after compound treatment could be associated with maintaining their osteoblastic phenotype. Although not differences in gene expression were found for the main markers of osteoblasts mineralization or traditional pathways of bone formation, overall, these RNAseq analysis identified the interferon signaling as a potential RXFP2-downstream pathway activated by small molecule agonist 6641 to induce bone formation. Future experiments will investigate the link between RXFP2 and interferon signaling, and its role in osteoblasts mineralization. Nevertheless, compound 6641 is the compound with the highest mineralization activity (Figure 10) and the lowest toxicity (Figure 11) *in vitro,* and it was selected as the final agonists for further functional testing *in vivo.* In summary, we have identified several specific RXFP2 small molecule agonists with high potency and efficacy. We have also demonstrated that RXFP2 small molecule agonists significantly increase mineralization activity in primary human osteoblasts without notable toxicity and potentially identified interferon signaling as a new RXFP2-downstream pathway. Based on the results presented in this chapter we selected compound 6641 as the lead compound to test *in vivo,* as it is the compound with the highest mineralization activity and minimal toxicity.

CHAPTER 3: IDENTIFICATION OF AGONIST-RECEPTOR INTERACTIONS FOR RXFP2 ACTIVATION

3.1 Introduction

Small molecule agonists of GPCRs often bind to allosteric receptor sites to induce downstream signaling. In many cases, this may result in biased cellular signaling with more specific therapeutic activity and fewer side effects (163, 164). This chapter analyzes the mechanisms of receptor activation by compound 6641 in comparison to the natural ligand INSL3 to assess if it is indeed an allosteric agonist of RXFP2.

The current INSL3/RXFP2 binding model shows that the B-chain of the INSL3 heterodimer binds with high affinity to the LRR domain of RXFP2 (66, 67, 165). Conversely, the INSL3 B-chain homodimer is an RXFP2 antagonist which binds to the LRR domain of RXFP2 without inducing a cAMP response (72, 73, 166). Co-treatment with this RXFP2 antagonist will help elucidate if compound 6641 is also interacting with the LRR domain. Experiments described in Chapter 2 demonstrated that compound 6641 is a specific agonist of the RXFP2 receptor and do not activate RXFP1. Here, complementary RXFP2-1 and RXFP1-2 chimeric receptors were used to further investigate the involvement of the RXFP2 LRR and TM in 6641 activation of the receptor using the HTRF cAMP assay.

Class A constitute the largest family of GPCRs, and several of these receptors have been already crystallized in their active state binding to different small molecule allosteric modulators (163). The Beta2-adrenergic receptor (β_2AR) is one of the most characterized members of the Class A family of GPCRs. The Cmp-15PA is an allosteric antagonist that binds the intracellular region of β_2AR, interacting with residues of the TM1, TM2, TM6, TM7 and ICL1 (167). There are 5 subtypes of muscarinic acetylcholine receptors (M1−M5). Crystal structures have elucidated how the muscarinic allosteric agonist LY2119620 binds the M2 receptor subtype. The allosteric binding sites of LY2119620 are located in the top half portion of the TM2, TM6, TM7 as well as the ECL2, ECL3 (168). The luteinizing hormone–choriogonadotropin receptor (LHCGR) is another receptor that belongs to Class A GPCR family. Org43553 is a recently described drug candidate that acts on LHCGR receptor as an allosteric agonist, revealed by cryo-EM studies. Residues in the top half portion of the TM3, TM5, TM6, TM7 and the ECL2, ECL3 are involved in establishing the binding pocket of the receptor, mainly by forming hydrophobic interactions with Org43553. Mutation studies showed that having large bulky amino acid side chains can prevent effective binding and placement of Org43553 in the binding pocket of the receptor, hence diminishing receptor activation (169). Previous studies of the allosteric small molecule agonist ML290 binding and activation mechanism have found that it interacts with specific residues located in the top half of the TM7 and also the ECL3 of the RXFP1 receptor (170). The final aim of this chapter is to identify the specific residues that

are involved in 6641/RXFP2 interaction by undertaking an extensive site-directed mutagenesis study in combination with computational modeling analysis.

3.2 Materials and methods

3.2.1 Cell lines maintenance and subculturing

HEK293T cell lines were maintained as described in materials and methods section 2.2.1 and all cell culture reagents used for the following protocols are the same as described previously, unless stated otherwise.

3.2.2 HTRF cAMP assay with RXFP2 antagonist

The RXFP2 antagonist (INSL3 B dimer) was kindly donated by Dr. Akhter Hossain at The Florey Institute of Neuroscience and Mental Health in Australia and was used to co-treat HEK-RXFP2 cells with RXFP2 agonist (6641) or INSL3 and measure induction of cAMP using the HTRF assay. The HTRF cAMP assay was carried out in the presence of 200 μM IBMX. For this assay, cells were seeded in 96-well flat-bottom opaque plates at 7,500 cells/well in 60 μL/well of serum-free DMEM medium and allowed to attach overnight at 37°C, 5% CO2. The next morning, cells were treated with 2 μL of INSL3 B dimer antagonist (0.21 nM – 10 μM) and 2 μL of 30 nM INSL3 or 4 μL of vehicle (serum-free DMEM + 200 μM IBMX). Cells were also treated with 1 μL/well of 0.28 μM compound, 2 μM forskolin, or DMSO vehicle. At this point, the protocol follows as described in materials and methods section 2.2.2. The cAMP inhibition induced by the RXFP2 antagonist was normalized to the cAMP response induced by 6641 (0.28 μM) and INSL3 (30 nM)

respectively as 0% inhibition. Data analysis was performed with the GraphPad Prism 8 software, using four parameters nonlinear fit dose-response inhibition curves presented as mean ± SEM of 3 independent experiments, each performed in triplicates.

3.2.3 Plasmid amplification and DNA preparation

E. Coli competent cells (catalog # 636763, Takara, Shiga, Japan) were used to amplify all plasmids used for transfection experiment. Competent cells were transformed with 100 ng of plasmid DNA stock, incubated for 30 minutes in ice, heat shocked at 42°C for 40 seconds, and placed back on ice for 1 minute. Cells were transferred to 15 mL LB broth containing 100 µg/mL of ampicillin (Sigma-Aldrich) and incubated overnight in a 37°C Excella E24 incubator shaker (New Brunswick Scientific, Edison, NJ) at 225 rpm. Next morning cells were centrifuged at 3000 x g for 6 minutes and the pellets were used for DNA miniprep. The GeneJET Plasmid Miniprep kit (catalog # K0503, Thermo Fisher Scientific) was used as instructed by the manufacturer. Each bacterial pellet was resuspended in 250 µL of kit resuspension solution, lysed in 250 µL of kit lysis solution and neutralized in 350 µL of kit neutralization solution. The neutralized bacteria lysate was centrifuged at 12,000 x g for 5 minutes. The supernatant was transferred to a GeneJET spin column, centrifuged a 12,000 x g for 1 minute and flow-through was discarded. Two consecutive washing steps were performed with 500 µL of kit wash solution at 12,000 x g for 1 minute and one more centrifugation step was performed to ensure complete removal of ethanol from the column. The GeneJET columns

were then transferred to clean DNase/RNase free 1.5 mL Eppendorf tubes and plasmid DNA was eluted in 30 µL of nuclease-free water at 12,000 x g for 2 minutes. Plasmid DNA concentrations (0.1 – 1 µg) and purities (260/280 nm OD ratio ≥ 1.8) were measured using a NanoVue spectrophotometer before transferring them to -20°C for storage.

3.2.4 Construction of chimeric receptors:

The chimeric receptors RXFP2-1 and RXFP1-2 used for these experiments were donated by Dr. Ross Bathgate at The Florey Institute of Neuroscience and Mental Health in Australia and were generated as previously described (69). The chimeric receptors RXFP2-1 ECL2, RXFP2-1 TM5 and RXFP2-1 TM7, were generated by ligation of various fragments of full-length human RXFP1 and RXFP2 receptor constructs shown in Figure 17 and 18 respectively, cloned into pcDNA3.1™/Zeo(+) AmpR mammalian expression vector. PCR was performed using Pfu Turbo high-fidelity DNA polymerase (catalog # #600250, Agilent Technologies) as instructed by the manufacturer and overlapping primers were designed as shown in Table 4. T7 and BGH primers for the pcDNA3.1™/Zeo(+) AmpR mammalian expression vector were used as shown in Table 5 for amplification of the desired template fragment. Thermal cycling was carried out in a DNA Engine Thermal Cycler for 1 cycle of polymerase activation at 94°C for 3 minutes, 3 step PCR with 30 cycles of 30 seconds of denaturation at 94°C followed by annealing at 55°C and 2 minutes extension at 72°C. PCR products were digested with 1 µL of DpnI (catalog # R0176S, New England Biolabs, Ipswich, MA) at 37°C overnight, run on a 0.8%

agarose gel and purified using the GeneJET Gel extraction kit (catalog # K0831, Thermo Scientific). Briefly, the 200 mg gel slide containing the DNA fragment was incubated in 200 µL of extraction buffer at 54°C for 10 minutes until dissolved. 200 µL of 100% ethanol were added into the mix, transferred to a DNA Purification Micro Column, and centrifuged for 1 minute at 14,000 x g. Column was washed twice with 700 µL of kit wash buffer for 1 minute at 14,000 x g and a final centrifugation step was performed to remove residual wash buffer from the column before eluting the DNA in 10 µL of nuclease-free water. The purified DNA fragments were then ligated into the BamHI (catalog # R0136S, New England Biolabs) and XhoI (catalog # R0146S, New England Biolabs) pre-digested pcDNA3.1™/Zeo(+) AmpR mammalian expression vector using the In-Fusion HD enzyme premix (catalog # 1509492A, Clontech, Mountain View, CA) at 50°C for 15 minutes. The resulting vectors were used to transform Stellar competent cells as described in above section 3.2.3 and cells were grown at 37°C overnight on agar plates containing 100 µg/mL ampicillin for selection. Individual clones were grown in LB broth containing 100 µg/mL of ampicillin and plasmid DNA was extracted as described in above section 3.2.3. The cDNA inserts were fully sequenced to confirm the presence of the desired chimeric constructs and the absence of additional mutations.

3.2.5 Construction of point mutant receptors

Point mutant receptors were generated by site-directed mutagenesis using full-length human RXFP2 receptor construct shown in Figure 18, cloned into

pcDNA3.1™/Zeo(+) AmpR mammalian expression vector. PCR was performed using Pfu Turbo high-fidelity DNA polymerase as instructed by the manufacturer and specific primers were designed as shown in Table 6. Thermal cycling was carried out in a DNA Engine Thermal Cycler for 1 cycle of polymerase activation at 94°C for 3 minutes, 3 step PCR with 25 cycles of 30 seconds of denaturation at 94°C followed by annealing at 55°C and 7 minutes extension at 68°C. PCR products were digested with 1 µL of DpnI at 37°C overnight and used to transform Stellar competent cells, amplify individual clones and extract plasmid DNA as described in the previous section 3.2.3. The *RXFP2* cDNA inserts were fully sequenced to confirm the presence of the desired mutation and the absence of additional mutations.

3.2.6 HTRF cAMP assay in transiently transfected HEK293T cells

The point mutant and chimeric receptors were used to transiently transfect HEK293T cells and measure differences in cAMP induction by INSL3 and 6641 using the HTRF assay. The assay was carried out in the presence of 200 µM IBMX. For this assay, HEK293T cells were seeded in 6-well flat-bottom clear plates (Falcon-Corning) at 0.5 million cells/well in 2mL/well of growth medium (DMEM, 10% FBS, 1x Pen/Strep) and allowed to attach overnight at 37°C, 5% CO2. The next morning, cells were transfected with 2 µg of plasmid (point mutants, chimeric receptors, WT RXFP2, or WT RXFP1) and 6 µl of Lipofectamine2000 (Invitrogen) in a total volume of 200 µl/well Opti-MEM I reduced serum medium (gibco) and allowed to incubate an additional 24 hours. The next day, transfected cells were

seeded in 96-well flat-bottom opaque plates at 30,000 cells/well in 60 µL/well of serum-free DMEM medium and allowed to attach overnight at 37°C, 5% CO2. The next morning, cells were treated with 1 µL/well of compound (0.25 nM – 25 µM), 2 µM forskolin, or DMSO vehicle. Cells were also treated with 4 µL of INSL3 (0.01 – 100 nM), Relaxin2 (10 – 100 nM), or vehicle (serum-free DMEM + 200 µM IBMX). At this point, the protocol follows as described in materials and methods section 2.2.2. cAMP response induced by 6641 and INSL3 for each receptor was normalized to its own 2 µM forskolin cAMP response as 100% activity and DMSO vehicle as 0% activity. Data analysis was performed using GraphPad Prism 8. 6641 and INSL3 efficacies (expressed as E_{max} and EC_{50}) were calculated from efficacy curves generated using four parameters nonlinear fit dose-response stimulation curves. Results are presented as mean ± SEM of 3 independent experiments, each performed in triplicates, or as mean of 1 experiment performed in triplicates.

3.2.7 Cell surface expression assay of FLAG tagged receptors

All receptor constructs contain a FLAG tag that allows measurement of receptor expression on the cell surface via flow cytometry. For this assay, HEK293T cells were seeded in 6-well flat-bottom clear plates at 0.6 million cells/well in 2mL/well of growth medium (DMEM, 10% FBS, 1x Pen/Strep) and allowed to attach overnight at 37°C, 5% CO2. The next morning, cells were transfected with 2 µg of plasmid (empty vector pcDNA3.1, point mutants, chimeric receptors, WT RXFP2 or WT RXFP1) and Lipofectamine2000 as previously described in above section

3.2.6. 24 hours after transfection, cells were harvested in 1.5 mL/well of PBS + 5 mM EDTA (Sigma-Aldrich). 750 µL of the cell suspension was used for surface staining and 750 µL permeabilized for total staining. Cells were centrifuged at 2,000 x rpm for 3 minutes, resuspended in 400 µl PBS and fixed for 10 minutes in 3.7% formaldehyde/PBS. Cells were centrifuged, washed twice with 0.5 mL of stain buffer for surface detection (2% FBS, TBS, 1 mM CaCl2) or with permeabilization buffer for total staining (stain buffer + 0.2% Tween-20) and incubated with 0.5 µg anti-FLAG M1 Ab (catalog # F3040, Sigma-Aldrich) for 1 hour at 4°C in 100 µL of the respective buffer. Cells were washed again with 1 mL of stain or permeabilization buffer and incubated with 1 µg Alexa Fluor 488 goat anti-mouse IgG (catalog # A11001, Invitrogene) for 20 minutes at 4°C protected from light in 100 µL of the respective buffer. Cells were washed a final time with 1 mL of the respective buffer and resuspended in 300 µl stain buffer for analysis on an Accuri C6 flow cytometer (BD Biosciences, Franklin Lakes, NJ). Cells transfected with the empty vector were used to set background staining. Data analysis was performed using GraphPad Prism 8. The surface and total expression of the point mutants and chimeric receptors was normalized to the expression of the respective WT receptor as 100% expression and resented as mean ± SEM of 3 independent experiments, each performed in triplicates, or as mean of 1 experiment performed in triplicates.

3.2.8 3D Docking modeling

The homology model of the active state of human RXFP2 was obtained using the SWISS-MODEL server (171) by Dr. Abhijeet Kapoor at NCATS/NIH. The active state structure of LHCGR (PDB ID:7FIH), corresponding to the best Global Model Quality Estimate (GMQE) score was used as the template structure for modeling. Both the ectodomain and the transmembrane region of the RXFP2 was modeled with the final model consisting of residues T140-H709. The homology model was then used to dock compound 6641 using the default settings of the Glide induced fit docking protocol except for using extra precision (XP) methodology in the second docking stage (172-174). The homology model was prepared for docking using default settings of rotein Prep Wizard in the Schrodinger suite 2020-4 (Schrödinger Inc, New York, NY), which involved adding missing hydrogen atoms, protonation state assignment, and energy minimization using the OPLS3e force field. 6641 was prepared for docking using the default procedure in the Schrodinger's Ligprep utility. A docking grid was positioned at the receptor's orthosteric site in the TM (identified using Schrodinger's SiteMap tool and overlapping with the agonist binding site in LHCGR (169)), and the outer box dimension large enough to cover the entire extracellular region of the receptor. Top five resulting complexes were visually inspected, and a final model was selected that showed favorable interactions. The selected 6641-RXFP2 complex from induced fit docking was further refined using 50 ns molecular dynamics (MD) simulation carried out using Desmond (175). System Builder in Schrodinger Suite 2020-4 was used to embed the receptor model in a 1-palmitoyl-2-oleoylphosphatidylcholine (POPC) bilayer, further solvated in an orthorhombic box

with a 10 Å buffer in each dimension consisting of SPC water molecules and 0.15 M NaCl and neutralized with chloride ions. Before running 50 ns production simulation, the system was equilibrated for 35 ns following the standard membrane relaxation protocol in Desmond and gradually decreasing positional restraints on the heavy atoms of lipids, protein sidechain, protein backbone, and 6641 atoms. The simulation was run using default parameters using NPgT ensemble and system temperature and pressure maintained at 300K and 1 bar, respectively, using the Nose-Hoover thermostat and a semi-isotropic MTK barostat. RESPA integrator (176) was used with a timestep of 2 fs for bonded and short-range non-bonded interactions and 6 fs for long-range nonbonded interactions.

3.2.9 Ligand-Receptor Structural Interaction Fingerprint

The interaction between 6641 ligand and each residue of the RXFP2 receptor during MD simulation was calculated using an in-house python script at NCATS/NIH. For each receptor residue, interaction with 6641 was calculated as a nine-bit representation based on the following nine types of interactions: apolar interactions (carbon-carbon atoms in contact), face-to-face (Aro_F2F) and edge-to-face (Aro_E2F) aromatic interactions, hydrogen-bond interactions with the protein as the hydrogen-bond donor (Hbond_proD) or hydrogen-bond acceptor (Hbond_proA), electrostatic interactions between a charged atom on the ligand with positively (Elec_ProP) or negatively charged (Elec_ProN) residues, and one-water-mediated H-bond (Hbond_1wat), and two-water-mediated H-bond (Hbond_2wat). A distance cutoff of 4.5 Å was used to define apolar interactions,

while a cutoff of 4 Å was used to describe aromatic and electrostatic interactions. Hydrogen bond was defined with a distance cutoff of 3.5 Å between the donor (D)-acceptor (A) atoms and a D-H-A angle in the range of 90-180 degrees. Interactions were calculated for sidechain atoms only.

3.3 Results

3.3.1 Compound 6641 is an allosteric agonist of RXFP2

The INSL3 B dimer antagonist was used to co-treated HEK-RXFP2 cells with INSL3 or 6641 respectively, and measured induction of cAMP by using the HTRF cAMP assay. The results of the HTRF assay showed that the INSL3 B dimer antagonist inhibited the cAMP response induced by INSL3 (30 nM) in a dose-dependent manner. On the contrary, the antagonist had no effect on the cAMP response induced by compound 6641 (0.28 μM) (Figure 19). These results suggest that 6641 activates RXFP2 in a different manner than INSL3 and the extracellular LRR domain of RXFP2 is most likely not involved in agonist-receptor interactions.

Complementary RXFP2-1 and RXFP1-2 chimeric receptors were used to further investigate the involvement of the RXFP2 EC and TM in 6641 agonist activation of the receptor using the HTRF assay. The chimera RXFP2-1 contains the EC of RXFP2 and the TM of RXFP1, while the complementary chimera RXFP1-2 contains the EC of RXFP1 and the TM of RXFP2. The results showed that the chimera RXFP2-1 had no response to 6641 (inactive) but responded to INSL3 at levels comparable to WT RXFP2. On the contrary, the RXFP1-2 chimera did not

respond to INSL3 (inactive) but responded to 6641 at levels comparable to WT RXFP2, and to Relaxin at levels comparable to WT RXFP1 (Figure 20). These results again suggest that the EC of RXFP2 is not involved in 6641 activation of the receptor, and points to the TM as the primary region for agonist interaction.

RXFP2-1 chimeras in the TM were used to try to identify the specific TM that is involved in 6641 activation of RXFP2. The chimera RXFP2-1 ECL2 is RXFP2 form N-terminal until the amino acid K560, where it switches to be RXFP1 all the way to the C-terminal. The same way, the chimera RXFP2-1 TM5 switches from RXFP2 to RXFP1 in the amino acid V606, and the chimera RXFP2-1 TM7 switches from RXFP2 to RXFP1 in the amino acid T672. When these chimeras were tested in the HTRF cAMP assay, the chimera ECL2 showed no response to 6641 (inactive), the chimera TM5 responded to 6641 with lower potency and efficacy that the WT RXFP2, and the chimera TM7 responded to 6641 at levels comparable to WT RXFP2. All these chimeras responded to INSL3 at levels comparable to WT RXFP2, which is used as a positive control to test activation of the chimeric receptors (Figure 21a). These results suggest that the ECL2 and the TM5 are crucial for 6641 receptor activation and that the TM6 and ECL3 are necessary to achieve full 6641 efficacy (Figure 21b). Expression levels of the chimeric receptors were measured by flow cytometry. The cell surface expression levels of chimeras RXFP1-2, RXFP2-1, and RXFP2-1 TM5 are similar to the WT receptor expression, which demonstrates that the observed changes in cAMP activity are not a result of the chimeric receptor not being expressed on the cell surface. The chimera

RXFP2-1 ECL2 is expressed in the cell surface at 62% of WT RXFP2 levels, but this level of expression seems to be sufficient to achieve the maximum INSL3 response. Similarly, the chimera RXFP2-1 TM7 is expressed in the cell surface at 73% of WT RXFP2 levels, but this level of expression is sufficient to achieve maximum INSL3 and 6641 responses. (Figure 22).

3.3.2 Compound 6641 binding model: Identification of RXFP2 TM residues involved in 6641 interactions

The “vertical” binding model is commonly seen with many agonists/antagonists binding to the TM of GPCRs (169, 177). Due to the high structure similarity with RXFP2, the recently resolved cryo-electron microscopy structure of the class A LHCGR was used as a template to develop our active RXFP2 homology model (169). Figure 23 shows the MD refined predicted binding mode of 6641 obtained from induced fit docking to RXFP2 homology model. During the simulation, 6641 stayed stable as indicated by the time evolution of root mean squared deviation (RMSD) of the 6641 heavy atoms with respect to its position in the docking predicted complex (Figure 23a). In the predicted pose (Figure 23b), 6641 established both polar and nonpolar interactions to stabilize the RXFP2 active state (Figure 24). Two of the carbonyl moieties on 6641 engaged in direct or water-mediated hydrogen bond network (indicated as black dashed lines in Figure 23b) with sidechain atoms of residues T506, E507, N598, and K658 (Figure 23b and Figure 24). Additionally, the trifluoromethoxy group on 6641 also engaged in a network of water-mediated hydrogen bonds with residues D461, S509, N683,

S684, and N687. Residue W651 formed aromatic interactions with 6641, while several residues on TM3 (V510 and L513), TM5 (L591 and L595), TM6 (V654, F655, and L662), and L680 on TM7 participated in stable hydrophobic interactions with 6641.

An extensive site-directed mutagenesis study was conducted to verify the 6641-RXFP2 binding model proposed previously. A total of 30 RXFP2 residues were mutated and tested for 6641 and INSL3 activation using the HTRF cAMP assay, in comparison to the WT RXFP2 receptor activity (Table 7). The D475A mutation in the TM2 caused a significant decrease in potency for 6641 and completely inactivated the response for INSL3 compared to the WT RXFP2 responses. Six residues (M498, A502, M503, T506, E507 and V510) were mutated in the TM3. The M498D mutation render the receptor completely inactive. Mutant A502F was significantly less active with both 6641 and INSL3, while mutants M503I and V510F did not influence 6641 or INSL3 responses compared to WT. The T506A mutation drastically impaired 6641 activation and had a minor effect on INSL3 efficacy. The E507A mutation completely abolished the INSL3 response without significantly affecting 6641 efficacy but generating a 10-fold decrease in 6641 potency. Four residues (L591, F594, L595 and N598) were mutated in the TM5. Mutant L591Y showed a small decrease in 6641 and INSL3 activities, which was further accentuated when mutating this residue to aspartic acid. Mutants F594A, L595D and N598I completely abolished the INSL3 response without affecting 6641 activity. Six residues were studied in the TM6 (W651, V654, F655, K658, S661,

and L662). Mutants V654F, K658A and S661A had no impact on 6641 or INSL3 receptor activation. However, when residue V654 was mutated to aspartic acid, the 6641 response was significantly reduced and INSL3 activity completely abolished. The W651A mutation drastically impaired 6641 activity without affecting INSL3 response and mutant F655A was found to have a minor effect on 6641 and INSL3 efficacies. However, when residue F655 was mutated to glutamic acid, the 6641 potency decreased by 10-fold and the INSL3 activity was completely abolished. The L662D mutation drastically impaired INSL3 activity without affecting the 6641 response. Four residues (W674, I677, L680 and N683) were mutated in the TM7. The mutant N683A had no significant effect on 6641 or INSL3 activities. The mutant W674A was significantly less active for INSL3, while mutant I677F completely abolished the activity of INSL3, all without impairing the 6641 response. The L680A mutation render the receptor completely inactive. Six mutants were tested in the ECL2 (G564K, L576A, Y577A, Y578A, D579A and Q580A). None of these mutants affected the activation induced by 6641, and only mutant L576A was found to significantly decrease the response for INSL3. Interestingly, out of these six residues, L576 was the only conserved residue in RXFP1. Previous chapters demonstrated that 6641 is selective towards human and mouse RXFP2 and does not activate human or mouse RXFP1. Moreover, the results of the transmembrane RXFP2-1 chimeric receptors (Figure 21) further point to the ECL2 as a crucial region for 6641 activation of RXFP2. The motif Y577/Y578/D579/Q580 was believed to be crucial for human RXFP2 structural selectivity, as it is strikingly different in human RXFP1 (H577/S578/E579/D580).

The four-point mutant Y577H/Y578S/D579E/Q580D was tested to study the importance of this motif for 6641 activation, but no changes were observed for 6641 or INSL3 responses, suggesting that this motif may not be involved in receptor selectivity after all. Finally, three mutants were also tested in the ECL3 (D669G/M671I and T670A). Although they are not part of the 6641-RXFP2 predicted binding model, they were found to be key residues for ML290 and Relaxin binding to RXFP1 (170) and based on the results from the transmembrane RXFP2-1 chimeric receptors (Figure 21), they may also play a role in 6641 activation of RXFP2. However, these mutants had no effect on 6641 or INSL3 activities (Table 7).

The surface expression of the mutant and WT receptors was also measured to better interpret the cAMP activity results. Although some of the mutant receptors were expressed in the cell surface at significantly lower levels than the WT receptor (D475A, M503I, E507A, Y577H/Y578S/D579E/Q580D, N598I and F655A), all were expressed above 40% of WT, which was shown to be sufficient to achieve a maximum response in these mutants by INSL3 or 6641. However, other mutants with significantly reduced surface receptor expression as well as impaired INSL3 and 6641 activities (M498D, L591D, V654D and L680A), that make it difficult to draw definitive conclusions about the role of these amino acids in ligand binding and receptor activation (Table 7).

3.4 Figures and tables

Human RXFP1 (PRL-FLAG-hRXFP1) in pcDNA3.1 zeo(+)

```
ATGGACAGCAAAGGTTCGTCGCAGAAAGGGTCCCGCCTGCTCCTGCTGCTGGTGGTGTCAAATCTACTCT
TGTGCCAGGGTGTGGTCTCCGATTACAAAGATGATGATGATGTCGACCAGGATGTCAAGTGCTCCCTTGG
CTATTTCCCCTGTGGGAACATCACAAAGTGCTTGCCTCAGCTCCTGCACTGTAACGGTGTGGACGACTGC
GGGAATCAGGCCGATGAGGACAACTGTGGAGACAACAATGGATGGTCTCTGCAATTTGACAAATATTTTG
CCAGTTACTACAAAATGACTTCCCAATATCCTTTTGAGGCAGAAACACCTGAATGTTTGGTCGGTTCTGT
GCCAGTGCAATGTCTTTGCCAAGGTCTGGAGCTTGACTGTGATGAAACCAATTTACGAGCTGTTCCATCG
GTTTCTTCAAATGTGACTGCAATGTCACTTCAGTGGAACTTAATAAGAAAGCTTCCTCCTGATTGCTTCA
AGAATTATCATGATCTTCAGAAGCTGTACCTGCAAAACAATAAGATTACATCCATCTCCATCTATGCTTT
CAGAGGACTGAATAGCCTTACTAAACTGTATCTCAGTCATAACAGAATAACCTTCCTGAAGCCGGGTGTT
TTTGAAGATCTTCACAGACTAGAATGGCTGATAATTGAAGATAATCACCTCAGTCGAATTTCCCCACCAA
CATTTTATGGACTAAATTCTCTTATTCTCTTAGTCCTGATGAATAACGTCCTCACCCGTTTACCTGATAA
ACCTCTCTGTCAACACATGCCAAGACTACATTGGCTGGACCTTGAAGGCAACCATATCCATAATTTAAGA
AATTTGACTTTTATTTCCTGCAGTAATTTAACTGTTTTAGTGATGAGGAAAAACAAAATTAATCACTTAA
ATGAAAATACTTTTGCACCTCTCCAGAAACTGGATGAATTGGATTTAGGAAGTAATAAGATTGAAAATCT
TCCACCGCTTATATTCAAGGACCTGAAGGAGCTGTCACAATTGAATCTTTCCTATAATCCAATCCAGAAA
ATTCAAGCAAACCAATTTGATTATCTTGTCAAACTCAAGTCTCTCAGCCTAGAAGGGATTGAAATTTCAA
ATATCCAACAAAGGATGTTTAGACCTCTTATGAATCTCTCTCACATATATTTTAAGAAATTCCAGTACTG
TGGGTATGCACCACATGTTCGCAGCTGTAAACCAAACACTGATGGAATTTCATCTCTAGAGAATCTCTTG
GCAAGCATTATTCAGAGAGTATTTGTCTGGGTTGTATCTGCAGTTACCTGCTTTGGAAACATTTTTGTCA
TTTGCATGCGACCTTATATCAGGTCTGAGAACAAGCTGTATGCCATGTCAATCATTTCTCTCTGCTGTGC
CGACTGCTTAATGGGAATATATTTATTCGTGATCGGAGGCTTTGACCTAAAGTTTCGTGGAGAATACAAT
AAGCATGCGCAGCTGTGGATGGAGAGTACTCATTGTCAGCTTGTAGGATCTTTGGCCATTCTGTCCACAG
AAGTATCAGTTTTACTGTTAACATTTCTGACATTGGAAAAATACATCTGCATTGTCTATCCTTTTAGATG
TGTGAGACCTGGAAAATGCAGAACAATTACAGTTCTGATTCTCATTTGGATTACTGGTTTTATAGTGGCT
TTCATTCCATTGAGCAATAAGGAATTTTTCAAAAACTACTATGGCACCAATGGAGTATGCTTCCCTCTTC
ATTCAGAAGATACAGAAAGTATTGGAGCCCAGATTTATTCAGTGGCAATTTTTCTTGGTATTAATTTGGC
CGCATTTATCATCATAGTTTTTTCCTATGGAAGCATGTTTTATAGTGTTCATCAAAGTGCCATAACAGCA
ACTGAAATACGGAATCAAGTTAAAAAAGAGATGATCCTTGCCAAACGTTTTTTCTTTATAGTATTTACTG
ATGCATTATGCTGGATACCCATTTTTGTAGTGAAATTTCTTTCACTGCTTCAGGTAGAAATACCAGGTAC
CATAACCTCTTGGGTAGTGATTTTTATTCTGCCCATTAACAGTGCTTTGAACCCAATTCTCTATACTCTG
ACCACAAGACCATTTAAAGAAATGATTCATCGGTTTTGGTATAACTACAGACAAAGAAAATCTATGGACA
GCAAAGGTCAGAAAACATATGCTCCATCATTCATCTGGGTGGAAATGTGGCCACTGCAGGAGATGCCACC
TGAGTTAATGAAGCCGGACCTTTTCACATACCCCTGTGAAATGTCACTGATTTCTCAATCAACGAGACTC
AATTCCTATTCATGA

MDSKGSSQKGSRLLLLLVVSNLLLCQGVVSDYKDDDDVDQDVKCSLGYFPCGNITKCLPQ
LLHCNGVDDCGNQADEDNCGDNNGWSLQFDKYFASYYKMTSQYPFEAETPECLVGSVPVQ
CLCQGLELDCDETNLRAVPSVSSNVTAMSLQWNLIRKLPPDCFKNYHDLQKLYLQNNKIT
SISIYAFRGLNSLTKLYLSHNRITFLKPGVFEDLHRLEWLIIEDNHLSRISPPTFYGLNS
LILLVLMNNVLTRLPDKPLCQHMPRLHWLDLEGNHIHNLRNLTFISCSNLTVLVMRKNKI
NHLNENTFAPLQKLDELDLGSNKIENLPPLIFKDLKELSQLNLSYNPIQKIQANQFDYLV
KLKSLSLEGIEISNIQQRMFRPLMNLSHIYFKKFQYCGYAPHVRSCKPNTDGISSLENLL
ASIIQRVFVWVVSAVTCFGNIFVICMRPYIRSENKLYAMSIISLCCADCLMGIYLFVIGG
FDLKFRGEYNKHAQLWMESTHCQLVGSLAILSTEVSVLLLTFLTLEKYICIVYPFRCVRP
GKCRTITVLILIWITGFIVAFIPLSNKEFFKNYYGTNGVCFPLHSEDTESIGAQIYSVAI
FLGINLAAFIIIVFSYGSMFYSVHQSAITATEIRNQVKKEMILAKRFFFIVFTDALCWIP
IFVVKFLSLLQVEIPGTITSWVVIFILPINSALNPILYTLTTRPFKEMIHRFWYNYRQRK
SMDSKGQKTYAPSFIWVEMWPLQEMPPELMKPDLFTYPCEMSLISQSTRLNSYS
```

Figure 17. Human RXFP1 nucleotide and amino acid sequences. The highlighted yellow sequence corresponds to the prolactin signal peptide, while the highlighted green sequence corresponds to the FLAG-Tag.

Human RXFP2 (PRL-FLAG-hRXFP2) in pcDNA3.1 zeo(+)

```
ATGGACAGCAAAGGTTCGTCGCAGAAAGGGTCCCGCCTGCTCCTGCTGCTGGTGGTGTCAAATCTACTCT
TGTGCCAGGGTGTGGTCTCCGATTACAAAGATGATGATGATGTCGACCAAGGTAGCATGATCACTCCTTC
ATGCCAAAAAGGATATTTTCCCTGTGGGAATCTTACCAAGTGCTTACCCCGAGCTTTTCACTGTGATGGC
AAGGATGACTGTGGGAACGGGGCGGACGAAGAGAACTGTGGTGACACTAGTGGATGGGCGACCATATTTG
GCACAGTGCATGGAAATGCTAACAGCGTGGCCTTAACACAGGAGTGCTTTCTAAAACAGTATCCACAATG
CTGTGACTGCAAAGAAACTGAATTGGAATGTGTAAATGGTGACTTAAAGTCTGTGCCGATGATTTCTAAC
AATGTGACATTACTGTCTCTTAAGAAAAACAAAATCCACAGTCTTCCAGATAAAGTTTTCATCAAATACA
CAAAACTTAAAAAGATATTTCTTCAGCATAATTGCATTAGACACATATCCAGGAAAGCATTTTTTGGATT
ATGTAATCTGCAAATATTATATCTCAACCACAACTGCATCACAACCCTCAGACCTGGAATATTCAAAGAC
TTACATCAGCTAACTTGGCTAATTCTAGATGACAATcCAAtAACCAGAATTTCACAGCGCTTGTTTACGG
GATTAAATTCCTTGTTTTTCCTGTCTATGGTTAATAACTACTTAGAAGCTCTTCCCAAGCAGATGTGTGC
CCAAATGCCTCAACTCAACTGGGTGGATTTGGAAGGCAATAGAATAAAGTATCTCACAAATTCTACGTTT
CTGTCGTGCGATTCGCTCACAGTGCTGTTTCTGCCTAGAAATCAAATTGGTTTTGTTCCAGAGAAGACAT
TTTCTTCATTAAAAAATTTAGGAGAACTGGATCTGTCTAGCAATACGATAACGGAGCTATCACCTCACCT
TTTTAAAGACTTGAAGCTTCTACAAAAGCTGAACCTGTCATCCAATCCTCTTATGTATCTTCACAAGAAC
CAGTTTGAAAGTCTTAAACAACTTCAGTCTCTAGACCTGGAAAGGATAGAGATTCCAAATATAAACACAC
GAATGTTTCAACCCATGAAGAATCTTTCTCACATTTATTTCAAAAACTTTCGATACTGCTCCTATGCTCC
CCATGTCCGAATATGTATGCCCTTGACGGACGGCATTTCTTCATTTGAGGACCTCTTGGCTAACAATATC
CTCAGAATATTTGTCTGGGTTATAGCTTTCATTACCTGCTTTGGAAATCTTTTTGTCATTGGCATGAGAT
CTTTCATTAAAGCTGAAAATACAACTCACGCTATGTCCATCAAAATCCTTTGTTGTGCTGATTGCCTGAT
GGGTGTTTACTTGTTCTTTGTTGGCATTTTCGATATAAAATACCGAGGGCAGTATCAGAAGTATGCCTTG
CTGTGGATGGAGAGCGTGCAGTGCCGCCTCATGGGGTTCCTGGCCATGCTGTCCACCGAAGTCTCTGTTC
TGCTACTGACCTACTTGACTTTGGAGAAGTTCCTGGTCATTGTCTTCCCCTTCAGTAACATTCGACCTGG
AAAACGGCAGACCTCAGTCATCCTCATTTGCATCTGGATGGCGGGATTTTTAATAGCTGTAATTCCATTT
TGGAATAAGGATTATTTTGGAAACTTTTATGGGAAAAATGGAGTATGTTTCCCACTTTATTATGACCAAA
CAGAAGATATTGGAAGCAAAGGGTATTCTCTTGGAATTTTCCTAGGTGTGAACTTGCTGGCTTTTCTCAT
CATTGTGTTTTCCTATATTACTATGTTCTGTTCCATTCAAAAAACCGCCTTGCAGACCACAGAAGTAAGG
AATTGTTTTGGAAGAGAGGTGGCTGTTGCAAATCGTTTCTTTTTTATAGTGTTCTCTGATGCCATCTGCT
GGATTCCTGTATTTGTAGTTAAaATCCTTTCccTCTTCCGGGTggaAATACCAGACACAATGACTTCCTG
GATAGTGATTTTTTTCCTTCCAGTTAACAGTGCTTTGAATCCAATCCTCTATACTCTCACAACCAACTTT
TTTAAGGACAAGTTGAAACAGCTGCTGCACAAACATCAGAGGAAATCAATTTTCAAAATTAAAAAAAAAA
GTTTATCTACATCCATTGTGTGGATAGAGGACTCCTCTTCCCTGAAACTTGGGGTTTTGAACAAAATAAC
ACTTGGAGACAGTATAATGAAACCAGTTTCCTAG

MDSKGSSQKGSRLLLLLVVSNLLLCQGVVSDYKDDDDVDQGSMITPSCQKGYFPCGNLTK
CLPRAFHCDGKDDCGNGADEENCGDTSGWATIFGTVHGNANSVALTQECFLKQYPQCCDC
KETELECVNGDLKSVPMISNNVTLLSLKKNKIHSLPDKVFIKYTKLKKIFLQHNCIRHIS
RKAFFGLCNLQILYLNHNCITTLRPGIFKDLHQLTWLILDDNPITRISQRLFTGLNSLFF
LSMVNNYLEALPKQMCAQMPQLNWVDLEGNRIKYLTNSTFLSCDSLTVLFLPRNQIGFVP
EKTFSSLKNLGELDLSSNTITELSPHLFKDLKLLQKLNLSSNPLMYLHKNQFESLKQLQS
LDLERIEIPNINTRMFQPMKNLSHIYFKNFRYCSYAPHVRICMPLTDGISSFEDLLANNI
LRIFVWVIAFITCFGNLFVIGMRSFIKAENTTHAMSIKILCCADCLMGVYLFFVGIFDIK
YRGQYQKYALLWMESVQCRLMGFLAMLSTEVSVLLLTYLTLEKFLVIVFPFSNIRPGKRQ
TSVILICIWMAGFLIAVIPFWNKDYFGNFYGKNGVCFPLYYDQTEDIGSKGYSLGIFLGV
NLLAFLIIVFSYITMFCSIQKTALQTTEVRNCFGREVAVANRFFFIVFSDAICWIPVFVV
KILSLFRVEIPDTMTSWIVIFFLPVNSALNPILYTLTTNFFKDKLKQLLHKHQRKSIFKI
KKKSLSTSIVWIEDSSSLKLGVLNKITLGDSIMKPVS
```

Figure 18. Human RXFP2 nucleotide and amino acid sequences. The highlighted yellow sequence corresponds to the prolactin signal peptide, while the highlighted green sequence corresponds to the FLAG-Tag.

Table 4. Primers used for chimeric constructs.

PRIMERS	SEQUENCES
RXFP2-1 ECL2 F	5'-CTGTAATTCCATTTTGGAATAAGGAATTTTTCAAAAACTACTATGGC-3'
RXFP2-1 ECL2 R	5'-GCCATAGTAGTTTTTGAAAAATTCCTTATTCCAAAATGGAATTACAG-3'
RXFP2-1 TM5 F	5'-GAACTTGCTGGCTTTTCTCATCATAGTTTTTTCCTATGGAAGCA-3'
RXFP2-1 TM5 R	5'-TGCTTCCATAGGAAAAAACTATGATGAGAAAAGCCAGCAAGTTC-3'
RXFP2-1 TM7 F	5'-GGGTGGAAATACCAGACACAATGACCTCTTGGGTAGTGATTTTTATT-3'
RXFP2-1 TM7 R	5'-AATAAAAATCACTACCCAAGAGGTCATTGTGTCTGGTATTTCCACCC-3'
T7 F	5'-TAGAAGGCACAGTCGAGG-3'
BGH R	5'-TAATACGACTCACTATAGGG-3'

The primer DNA sequence highlighted in yellow corresponds to RXFP2, while the highlighted in green corresponds to RXFP1. The blue highlighted sequence corresponds to the overlap between both RXFP2 and RXFP1, used to create the chimera.

Table 5. Primer pairs and DNA template used to generate the fragments for ligation and production of the desired chimeric construct.

F PRIMER	R PRIMER	TEMPLATE	FRAGMENT
RXFP2-1 ECL2 F	BGH R	PRL-FLAG-hRXFP1	650 bp
T7 F	**RXFP2-1 ECL2 R**	PRL-FLAG-hRXFP2	1.7 kb
RXFP2-1 TM5 F	BGH R	PRL-FLAG-hRXFP1	500 bp
T7 F	**RXFP2-1 TM5 R**	PRL-FLAG-hRXFP2	1.8 kb
RXFP2-1 TM7 F	BGH R	PRL-FLAG-hRXFP1	300 bp
T7 F	**RXFP2-1 TM7 R**	PRL-FLAG-hRXFP2	2 kb

Table 6. Primers used for site-directed mutagenesis.

PRIMERS	SEQUENCES
D475A F	5'-TTGTTCTTTGTTGGCATTTTCGCTATAAAATACCGAGGGCAGTATCA-3'
D475A R	5'-TGATACTGCCCTCGGTATTTTATAGCGAAAATGCCAACAAAGAACAA-3'
M498D F	5'-AGAGCGTGCAGTGCCGCCTCGATGGGTTCCTGGCCATGCTGT-3'
M498D R	5'-ACAGCATGGCCAGGAACCCATCGAGGCGGCACTGCACGCTCT-3'
A502F F	5'-TCATGGGGTTCCTGTTCATGCTGTCCACCGAAGTCTCTGTTCT-3'
A502F R	5'-AGAACAGAGACTTCGGTGGACAGCATGAACAGGAACCCCATGA-3'
M503I F	5'-TCATGGGGTTCCTGGCCATACTGTCCACCGAAGTCTCTGT-3'
M503I R	5'-ACAGAGACTTCGGTGGACAGTATGGCCAGGAACCCCATGA-3'
T506A F	5'-GTTCCTGGCCATGCTGTCCGCCGAAGTCTCTGTTCTGCTA-3'
T506A R	5'-TAGCAGAACAGAGACTTCGGCGGACAGCATGGCCAGGAAC-3'
E507A F	5'-TTCCTGGCCATGCTGTCCACCGCAGTCTCTGTTCTGCTACTGA-3'
E507A R	5'-TCAGTAGCAGAACAGAGACTGCGGTGGACAGCATGGCCAGGAA-3'
V510F F	5'-ATGCTGTCCACCGAAGTCTCTTTTCTGCTACTGACCTACTTGACT-3'
V510F R	5'-AGTCAAGTAGGTCAGTAGCAGAAAAGAGACTTCGGTGGACAGCAT-3'
G564K F	5'-TTGGAATAAGGATTATTTTAAAAAACTTTTATGGGAAAAATGGAG-3'
G564K R	5'-CTCCATTTTTCCCATAAAAGTTTTTAAAATAATCCTTATTCCAA-3'
L576A F	5'-AAAATGGAGTATGTTTCCCAGCTTATTATGACCAAACAGAAGATATT-3'
L576A R	5'-AATATCTTCTGTTTGGTCATAATAAGCTGGGAAACATACTCCATTTT-3'
Y577A F	5'-ATGGAGTATGTTTCCCACTTGCTTATGACCAAACAGAAGATATTGG-3'
Y577A R	5'-CCAATATCTTCTGTTTGGTCATAAGCAAGTGGGAAACATACTCCAT-3'
Y578A F	5'-AGTATGTTTCCCACTTTATGCTGACCAAACAGAAGATATTGGAA-3'
Y578A R	5'-TTCCAATATCTTCTGTTTGGTCAGCATAAAGTGGGAAACATACT-3'
D579A F	5'-TATGTTTCCCACTTTATTATGCCCAAACAGAAGATATTGGAAGCAA-3'
D579A R	5'-TTGCTTCCAATATCTTCTGTTTGGGCATAATAAAGTGGGAAACATA-3'
Q580A F	5'-TATGTTTCCCACTTTATTATGACGCAACAGAAGATATTGGAAGCAA-3'
Q580A R	5'-TTGCTTCCAATATCTTCTGTTGCGTCATAATAAAGTGGGAAACATA-3'

Y577H/Y578S/ D579E/Q580D F	5'-ATGTTTCCCACTTCATTCTGAAGATACAGAAGATATTGGAAGCAAAG-3'
Y577H/Y578S/ D579E/Q580D R	5'-CTTTGCTTCCAATATCTTCTGTATCTTCAGAATGAAGTGGGAAACAT-3'
L591Y F	5'-ATTGGAAGCAAAGGGTATTCTTATGGAATTTTCCTAGGTGTGAAC-3'
L591Y R	5'-GTTCACACCTAGGAAAATTCCATAAGAATACCCTTTGCTTCCAAT-3'
L591D F	5'-ATTGGAAGCAAAGGGTATTCTGATGGAATTTTCCTAGGTGTG-3'
L591D R	5'-CACACCTAGGAAAATTCCATCAGAATACCCTTTGCTTCCAAT-3'
F594A F	5'-AAAGGGTATTCTCTTGGAATTGCCCTAGGTGTGAACTTGCTGGCTTTT-3'
F594A R	5'-AAAAGCCAGCAAGTTCACACCTAGGGCAATTCCAAGAGAATACCCTTT-3'
L595D F	5'-TATTCTCTTGGAATTTTCGACGGTGTGAACTTGCTGGCTTTT-3'
L595D R	5'-AAAAGCCAGCAAGTTCACACCGTCGAAAATTCCAAGAGAATA-3'
N598I F	5'-CTTGGAATTTTCCTAGGTGTGATCTTGCTGGCTTTTCTCATCATT-3'
N598I R	5'-AATGATGAGAAAAGCCAGCAAGATCACACCTAGGAAAATTCCAAG-3'
W651A F	5'-GTGTTCTCTGATGCCATCTGCGCGATTCCTGTATTTGTAGTTAAA-3'
W651A R	5'-TTTAACTACAAATACAGGAATCGCGCAGATGGCATCAGAGAACAC-3'
V654F F	5'-ATGCCATCTGCTGGATTCCTTTTTTTGTAGTTAAAATCCTTTCCCTC-3'
V654F R	5'-GAGGGAAAGGATTTTAACTACAAAAAAAGGAATCCAGCAGATGGCAT-3'
V654D F	5'-ATGCCATCTGCTGGATTCCTGACTTTGTAGTTAAAATCCTTT-3'
V654D R	5'-AAAGGATTTTAACTACAAAGTCAGGAATCCAGCAGATGGCAT-3'
F655A F	5'-GCCATCTGCTGGATTCCTGTAGCTGTAGTTAAAATCCTTTCCCTC-3'
F655A R	5'-GAGGGAAAGGATTTTAACTACAGCTACAGGAATCCAGCAGATGGC-3'
F655E F	5'-GCCATCTGCTGGATTCCTGTAGAAGTAGTTAAAATCCTTTCCCTC-3'
F655E R	5'-GAGGGAAAGGATTTTAACTACTTCTACAGGAATCCAGCAGATGGC-3'
K658A F	5'-GCTGGATTCCTGTATTTGTAGTTGCAATCCTTTCCCTCTTCCGGG-3'
K658A R	5'-CCCGGAAGAGGGAAAGGATTGCAACTACAAATACAGGAATCCAGC-3'
D669G/M671I F	5'-CTCTTCCGGGTGGAAATACCAGGGCACAATCACTTCCTGGATAGTGATTTTT-3'
D669G/M671I R	5'-AAAAATCACTATCCAGGAAGTGATTGTGCCTGGTATTTCCACCCGGAAGAG-3'
T670A F	5'-CGGGTGGAAATACCAGACGCAATGACTTCCTGGATAGTGAT-3'
T670A R	5'-ATCACTATCCAGGAAGTCATTGCGTCTGGTATTTCCACCCG-3'

S661A F	5'-GTATTTGTAGTTAAAATCCTTGCCCTCTTCCGGGTGGAAATA-3'
S661A R	5'-TATTTCCACCCGGAAGAGGGCAAGGATTTTAACTACAAATAC-3'
L662D F	5'-TTTGTAGTTAAAATCCTTTCCGACTTCCGGGTGGAAATACCA-3'
L662D R	5'-TGGTATTTCCACCCGGAAGTCGGAAAGGATTTTAACTACAAA-3'
W674A F	5'-TACCAGACACAATGACTTCCGCGATAGTGATTTTTTTCCTTCCAGTTAACAG-3'
W674A R	5'-CTGTTAACTGGAAGGAAAAAAATCACTATCGCGGAAGTCATTGTGTCTGGTA-3'
I677F F	5'-ACAATGACTTCCTGGATAGTGTTTTTTTTCCTTCCAGTTAACAGTG-3'
I677F R	5'-CACTGTTAACTGGAAGGAAAAAAAACACTATCCAGGAAGTCATTGT-3'
L680A F	5'-GACTTCCTGGATAGTGATTTTTTTCGCTCCAGTTAACAGTGCTTTGAATC-3'
L680A R	5'-GATTCAAAGCACTGTTAACTGGAGCGAAAAAAATCACTATCCAGGAAGTC-3'
N683A F	5'-GTGATTTTTTTCCTTCCAGTTGCCAGTGCTTTGAATCCAATC-3'
N683A R	5'-GATTGGATTCAAAGCACTGGCAACTGGAAGGAAAAAAATCAC-3'

The mutated amino acid codon is underlined, and mutated nucleotides are highlighted in red.

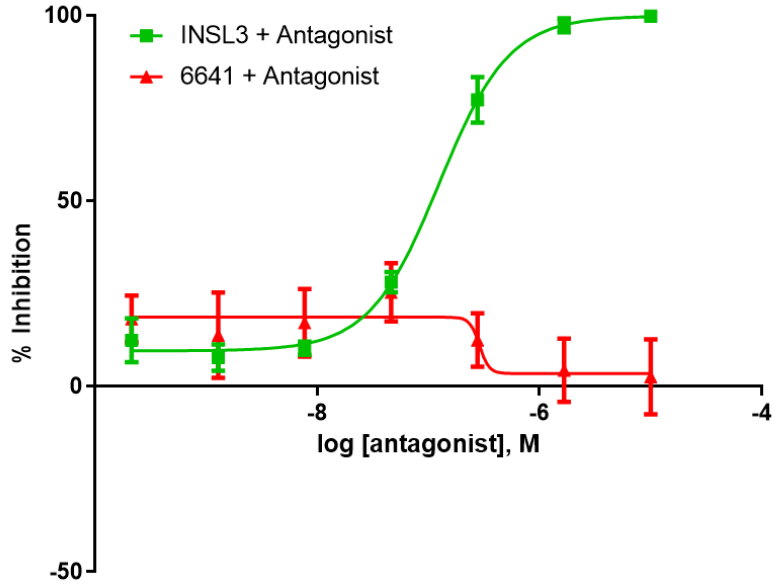

Figure 19. Compound 6641 is an allosteric agonist of RXFP2. HEK-RXFP2 cells co-treated with serial dilutions of RXFP2 antagonist and 30 nM INSL3 or 0.28 µM 6641. HTRF cAMP dose-response inhibition curves were normalized to activity without antagonist co-treatment as 0% inhibition. Results are expressed as mean ± SEM of 3 independent experiments.

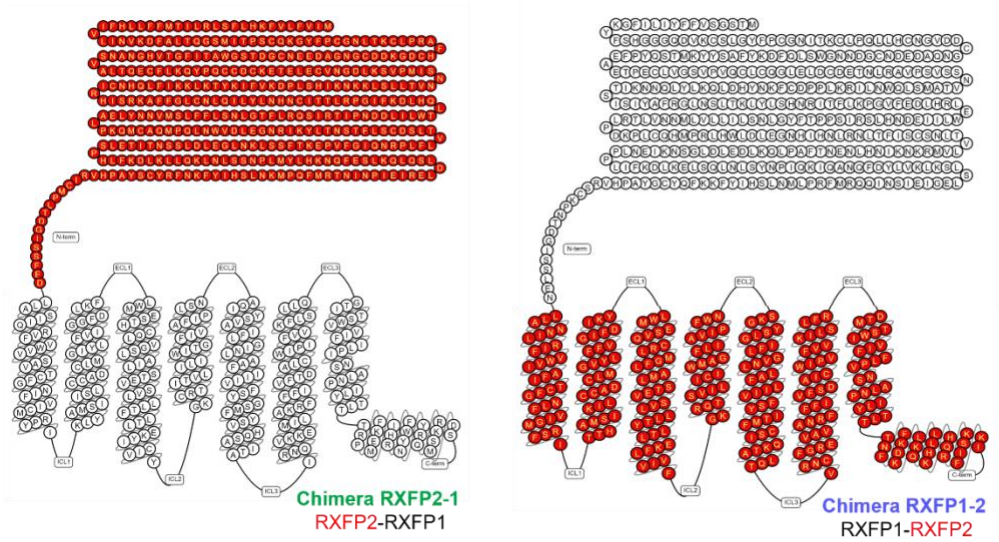

6641	EC_{50} (μM)	E_{max}
WT RXFP2	0.012 ± 0.008	86.31 ± 3.38
RXFP2-1	Inactive	Inactive
WT RXFP1	Inactive	Inactive
RXFP1-2	0.016 ± 0.002	96.47 ± 0.43

INSL3	EC_{50} (nM)	E_{max}
WT RXFP2	0.50 ± 0.35	78.38 ± 11.24
RXFP2-1	0.74 ± 0.61	92.30 ± 21.82
WT RXFP1	Inactive	Inactive
RXFP1-2	Inactive	Inactive

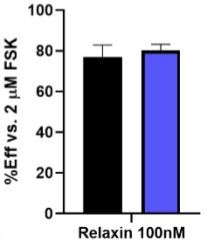

Figure 20. Compound 6641 interacts with the RXFP2 TM. HTRF cAMP assay in HEK293T cells transiently transfected with WT or chimeric receptors. The RXFP2 amino acid sequence for the chimeras is depicted in red, while the RXFP1 amino acid sequence is shown in white. For each receptor, 6641 and INSL3 responses were normalized to FSK (2 μM) as 100% efficacy. E_{max} and EC_{50} were calculated using four parameter nonlinear fit dose-response curves. Relaxin was used as a positive control for WT RXFP1 and RXFP1-2 receptors. Results are expressed as mean ± SEM of 3 independent experiments. Diagrams of the chimeric receptors were produced using GPCRdb.org (178, 179).

a

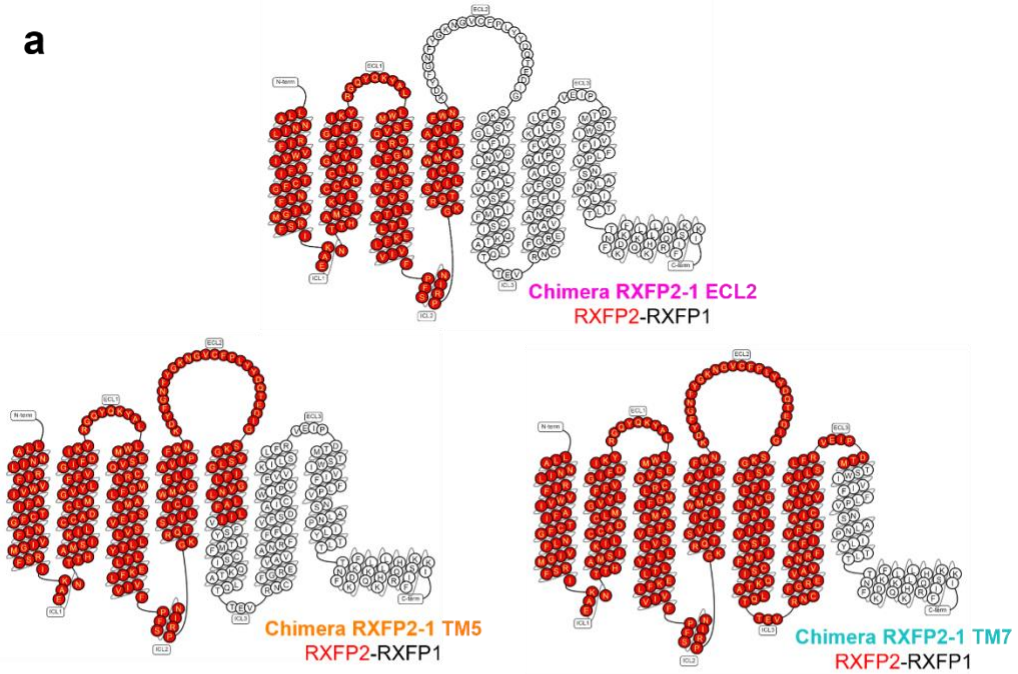

6641	EC_{50} (μM)	E_{max}
WT RXFP2	0.012 ± 0.008	86.31 ± 3.38
RXFP2-1 ECL2	Inactive	Inactive
RXFP2-1 TM5	1.11 ± 0.39	53.05 ± 8.05
RXFP2-1 TM7	0.32 ± 0.23	82.48 ± 1.33

INSL3	EC_{50} (nM)	E_{max}
WT RXFP2	0.50 ± 0.35	78.38 ± 11.24
RXFP2-1 ECL2	0.76 ± 0.45	69.91 ± 4.86
RXFP2-1 TM5	1.08 ± 0.34	62.28 ± 9.33
RXFP2-1 TM7	0.44 ± 0.23	76.70 ± 4.24

b

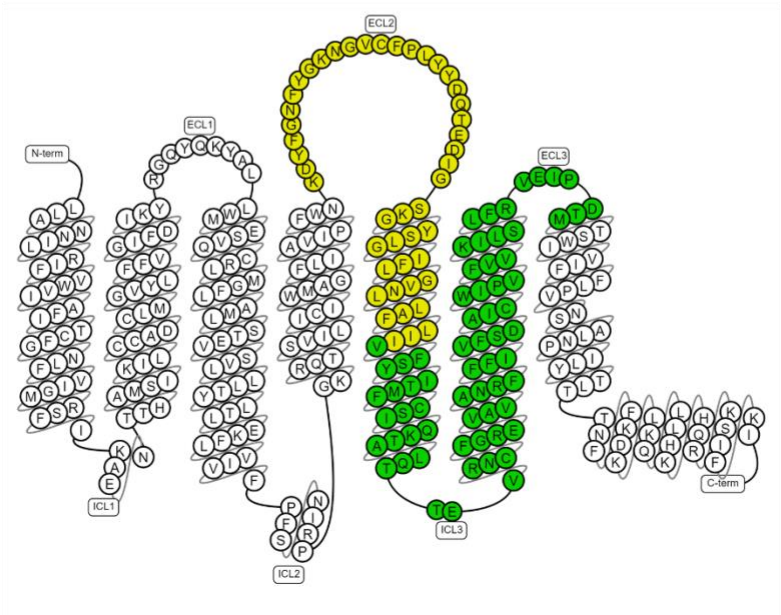

Figure 21. Compound 6641 interacts with the ECL2, ECL3, TM5 and TM6 of RXFP2. a) HTRF cAMP assay in HEK293T cells transiently transfected with WT or chimeric receptors. The RXFP2 amino acid sequence for the chimeras is depicted in red, while the RXFP1 amino acid sequence is shown in white. For each receptor, 6641 and INSL3 responses were normalized to FSK (2 µM) as 100% efficacy. E_{max} and EC_{50} were calculated using four parameter nonlinear fit dose-response curves. **b)** The RXFP2 amino acid sequence involved in 6641 receptor activation is depicted in yellow and the amino acid sequence necessary for archiving full 6641 efficacy is shown in green. Results are expressed as mean ± SEM of 3 independent experiments. Diagrams of the chimeric receptors were produced using GPCRdb.org (178, 179).

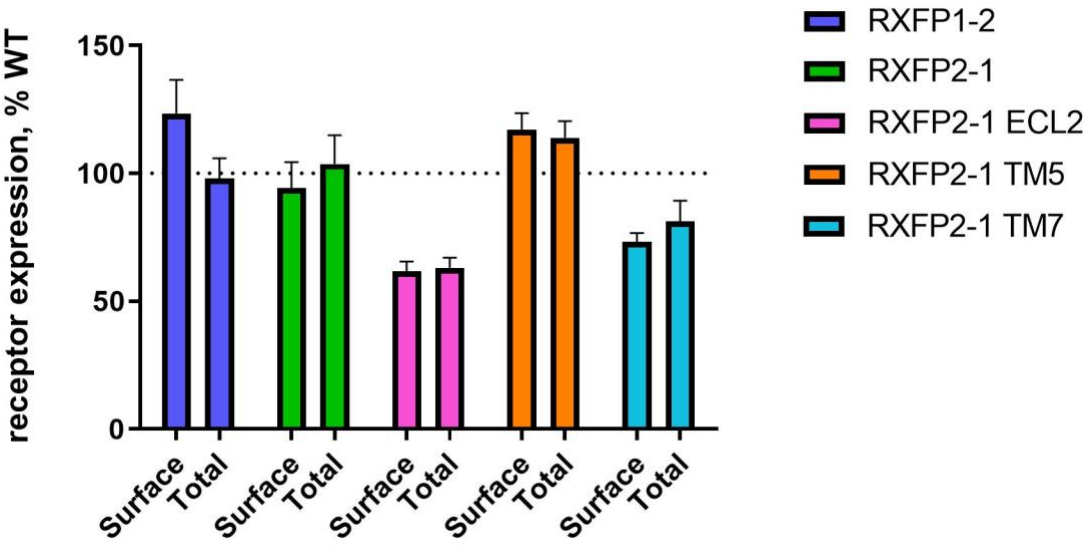

Figure 22. Chimeric receptor expression on the cell surface of transfected HEK293T cells. Flow cytometry of FLAG-tagged receptors was analyzed for surface and total expression of the chimeric receptors and normalized to the respective WT RXFP2 or RXFP1 receptor as 100% expression. Empty pcDNA3.1/Zeo(+) AmpR mammalian expression vector was used to establish background staining. Results are expressed as mean ± SEM of 3 independent experiments.

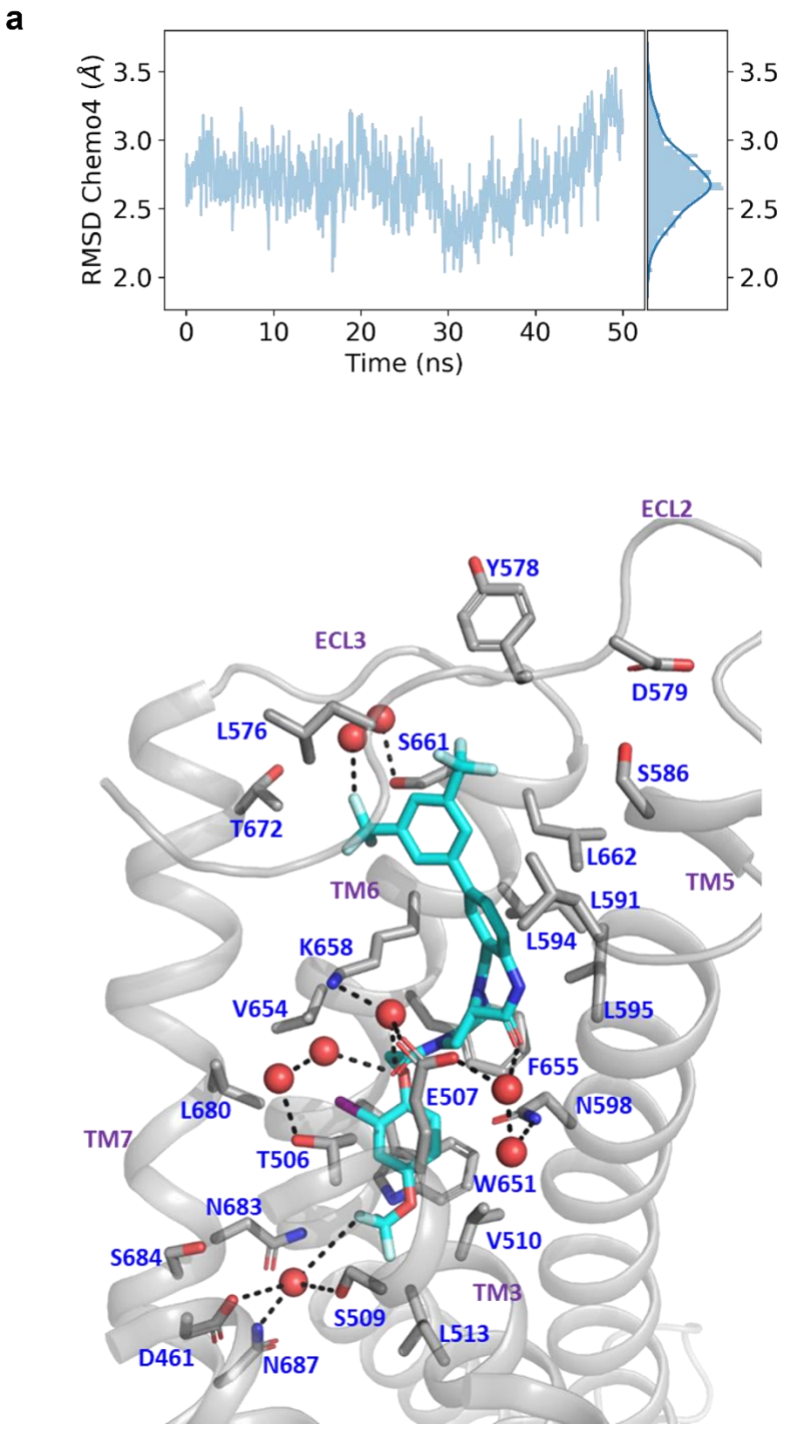

Figure 23. Predicted binding mode of 6641 in the TM of the active RXFP2. a) Time evolution of the RMSD of 6641 from its initial docking conformation. **b)** Representative conformation of the 6641 (cyan sticks) in the active RXFP2 binding pocket from 50 ns MD simulation. Residue sidechains are shown as gray sticks. Red spheres indicate water molecules. The black dashed line depicts hydrogen bonds.

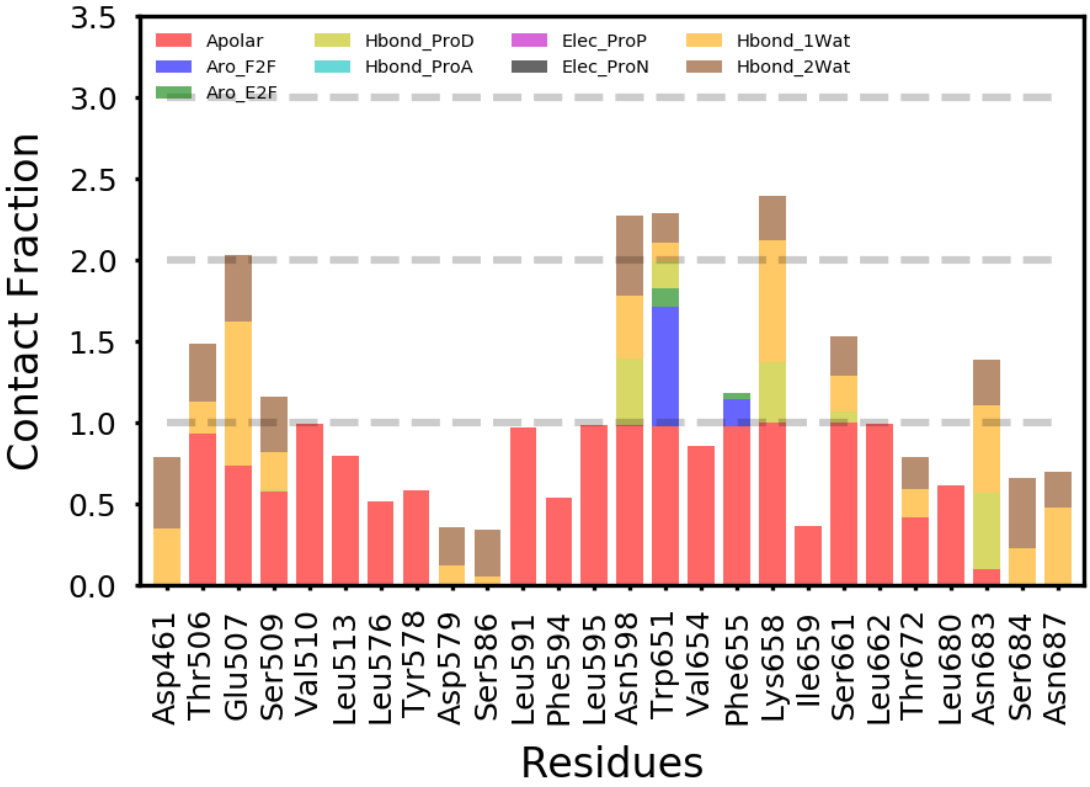

Figure 24. 6641-RXFP2 interactions formed during MD simulation. Different colors depict the following interaction types formed by each residue with 6641: carbon-carbon contact (Apolar, red), face-to-face aromatic (Aro_F2F, blue), edge-to-face aromatic (Aro_E2F, green), a hydrogen bond with the protein as the hydrogen-bond donor (Hbond_ProD, yellow), a hydrogen bond with the protein as the hydrogen-bond acceptor (Hbond_ProA, cyan), and one-water-mediated (Hbond_1Wat, orange) and two-water-mediated (Hbond_2Wat, brown) hydrogen-bond interactions. The contact fraction on the y axis represents the fraction of trajectory frames in which a given interaction is formed. For each interaction type, the contact fraction varies from 0 to 1.

Table 7. Summary of the site-directed mutagenesis study.

Mutant (Domain)	6641 EC_{50} (µM)	6641 E_{max} (% 2 µM FSK)	INSL3 EC_{50} (nM)	INSL3 E_{max} (% 2 µM FSK)	Surface Expression (% WT)
WT RXFP2	0.014 ± 0.002	99.35 ± 3.33	0.23 ± 0.039	91.55 ± 3.79	100
D475A (TM2)	0.75 ± 0.084	82.33 ± 2.26	Inactive	Inactive	38.22 ± 5.11
M498D (TM3)	Inactive	Inactive	Inactive	Inactive	47.81
A502F (TM3)	2.52 ± 0.18	60.75 ± 7.77	2.40 ± 1.45	48.28 ± 5.62	83.71 ± 0.60
M503I (TM3)	0.010 ± 0.006	95.69 ± 0.41	0.27 ± 0.032	82.45 ± 3.85	74.16 ± 0.35
T506A (TM3)	Inactive	22.73 ± 7.43	0.11 ± 0.042	74.11 ± 6.28	86.35 ± 5.98
E507A (TM3)	0.15 ± 0.027	102.63 ± 2.09	Inactive	Inactive	45.60 ± 5.22
V510F (TM3)	0.005	105.4	0.62	88.65	114.93
G564K (ECL2)	0.035 ± 0.010	96.11 ± 6.96	0.60 ± 0.23	79.49 ± 3.22	93.48 ± 2.25
L576A (ECL2)	0.002 ± 0	110.57 ± 2.71	1.35 ± 0.68	67.07 ± 0.80	88.86 ± 0.80
Y577A (ECL2)	0.033 ± 0.003	91.29 ± 3.24	0.38 ± 0.048	82.14 ± 6.40	83.14 ± 3.60
Y578A (ECL2)	0.046 ± 0.018	102.66 ± 5.41	0.63 ± 0.15	86.81 ± 4.93	84.78 ± 5.21
D579A (ECL2)	0.054 ± 0.016	111.77 ± 9.58	0.19 ± 0.032	98.65 ± 5.40	79.75 ± 8.15
Q580A (ECL2)	0.024 ± 0.013	110.64 ± 10.18	0.38 ± 0.057	83.88 ± 3.75	87.09 ± 5.41
Y577H/Y578S/ D579E/Q580D (ECL2)	0.016 ± 0.004	95.10 ± 2.12	0.13 ± 0.055	92.71 ± 0.96	57.96 ± 3.44
L591Y (TM5)	0.008	78.10	0.26	74.05	78.28
L591D (TM5)	0.081	56.51	0.48	62.15	46.74
F594A (TM5)	0.004	89.21	Inactive	Inactive	91.09
L595D (TM5)	0.011	106.1	Inactive	11.50	Not tested
N598I (TM5)	0.024 ± 0.007	105.12 ± 6.57	Inactive	Inactive	Not tested
W651A (TM6)	Inactive	32.35 ± 5.42	0.093 ± 0.020	82.22 ± 2.72	85.08 ± 8.98
V654F (TM6)	0.063 ± 0.010	97.29 ± 1.41	0.22 ± 0.033	92.43 ± 1.15	99.76 ± 5.96
V654D (TM6)	2.80	54.11	Inactive	Inactive	47.35
F655A (TM6)	0.038 ± 0.006	76.29 ± 4.34	0.34 ± 0.13	77.45 ± 5.51	74.75 ± 3.40
F655E (TM6)	0.19	82.78	Inactive	Inactive	64
K658A (TM6)	0.051 ± 0.024	84.24 ± 6.76	0.20 ± 0.057	78.14 ± 4.10	86.78 ± 5.62
S661A (TM6)	0.004	99.16	0.29	96.95	Not tested
L662D (TM6)	0.018	101.8	Inactive	34.25	Not tested
D669G/M671I (ECL3)	0.018 ± 0.002	93.55 ± 2.47	0.22 ± 0.042	75.28 ± 2.98	88.29 ± 4.99
T670A (ECL3)	0.010 ± 0.003	105.37 ± 3.11	0.32 ± 0.094	96.22 ± 3.09	87.68 ± 2.10
W674A (TM7)	0.032 ± 0.003	107.30 ± 1.38	2.19 ± 0.79	65.87 ± 4.17	96.25 ± 4.60
I677F (TM7)	0.018 ± 0.002	115.97 ± 2.12	Inactive	Inactive	106.41 ± 3.27
L680A (TM7)	Inactive	Inactive	Inactive	Inactive	12.67
N683A (TM7)	0.012	94.53	0.43	72.12	Not tested

HTRF cAMP assay in HEK293T cells transiently transfected with WT RXFP2 or point mutant receptors. For each receptor, 6641 and INSL3 responses were normalized to FSK (2 µM) as 100%

efficacy. E_{max} and EC_{50} were calculated using four parameter nonlinear fit dose-response curves. Flow cytometry of FLAG-tagged mutant receptors was analyzed for cell surface expression and normalized to WT RXFP2 as 100% surface expression. Empty pcDNA3.1/Zeo(+) AmpR mammalian expression vector was used to establish background staining. Results are expressed as mean ± SEM of 3 independent experiments or mean of 1 experiment performed in triplicates.

3.5 Discussion

The results described in this chapter demonstrate that the small molecule 6641 is an allosteric agonist of RXFP2 (Figure 19). The crucial region for 6641 activity is located in the RXFP2 TM, specifically the ECL2, ECL3, TM5 and TM6, which differs from the main INSL3 binding sites located in the LRRs of EC (Figure 20, 21). Moreover, using site-directed mutagenesis in combination with structural modeling, we were able to identify residues T506 and W651 in the RXFP2 TM that are mediating the interaction with compound 6641 (Table 7). The presumed receptor activation toggle switch residue W651 in the TM6 is conserved in other GPCRs, including RXFP1 (180), but mutations of this residue in RXFP1 did not change the receptor activation by ML290 or Relaxin (170). In contrast, a significant decrease in activity was observed with 6641 after mutation of the homologous residue in RXFP2. This result suggests that although W651 is conserved between both receptors, there must be a difference on the conformational change required for receptor activation which could be responsible for the receptor specificity observed for both ML290 and 6641.

Based on the modeling data, residues E507 in the TM3 and N598 in the TM5 are part of the 6641 binding site, however, the mutagenesis study demonstrated that

there is not a direct effect of these residues for 6641 activation of RXFP2. However, both of these amino acids are crucial for receptor activation by INSL3. These two residues are located deep inside the binding pocket to be involved in direct binding with INSL3 but may be important for the conformational change to maintain the specific receptor active state after INSL3 binding.

Mutation analysis have also identified several residues crucial for achieving the active state of the RXFP2 receptor after stimulation with both 6441 and INSL3. The aspartic acid D475 in the TM2 does not appear to be a part of the 6641 binding site, but it is located near the hinge region connecting the EC with the TM and it may be important for maintaining the receptor active state. The alanine A502 in the TM3 is also not part of the 6641 binding site, but mutation to phenylalanine results in an important clash with surrounding residues, which could explain the significant decrease in activity observed with both 6641 and INSL3. Based on the proposed model the phenylalanine F655 in the TM6 forms hydrophobic interactions with 6641 and it was found to significantly decrease 6641 potency and abolish INSL3 activity when mutated, which suggests this is an important activation toggle switch residue for RXFP2.

The mutagenesis study also revealed some similarities between the RXFP1 and RXFP2 active states. The residue L576 in the ECL2 is conserved in RXFP1 and a recent publication of the cryo-electron microscopy structure of the RXFP1 active state showed that this residue is important for Relaxin activation of RXFP1 (181),

correlating with our data showing the role of this residue for INSL3 activation of RXFP2. The residues W674 and I677 in the TM7 are also conserved in RXFP1 and have been shown to significantly decrease Relaxin binding and activation (170). The same result was found for INSL3 when mutating these residues in RXFP2, suggesting that this region in both receptors is involved in forming interactions with their respective natural ligands Relaxin and INSL3. Furthermore, the fact that none of these residues were found to be important for 6641 activation of RXFP2 further proves the allosteric nature of these small molecule agonist.

However, using site-directed mutagenesis, we did not find any residues in the ECL2 or TM5 that seem important for 6641 binding and activation, while in the contrary, found several residues that are necessary for INSL3 activation of RXFP2. (Table 7). This challenges the results obtained with the transmembrane RXFP2-1 chimeric receptors, where we found that the ECL2 and TM5 domains are crucial for 6641 activation of RXFP2, but do not seem to be involve in INSL3 activation (Figure 21). This suggests that there may be important conformational changes happening after INSL3 and 6641 binding to RXFP2, that are being disrupted by artificially creating the new chimeric receptor. Because there is no available cryo-EM structure for the RXFP2 receptor, our study is limited to the use of homology models. Hence, there is also a possibility that the key residues in the ECL2 and TM5 have not been yet identified, since we focused on mutating non-conserved residues and residues predicted by the 3D Docking model.

In summary, Chapter 3 has identified the RXFP2 TM as the allosteric region for 6641 receptor binding and discovered two important allosteric residues mediating this interaction (T506 and W651). Based on the modeling data, the residue T506 in the TM3 is mediating hydrogen bond interactions with 6641, while the residue W651 in the TM6 is mediating aromatic interactions with 6641. Understanding the binding and activation of the small molecule 6641 with RXFP2, and how it compares to the binding and activation of the natural ligand INSL3, is of great importance to be able to successfully perform improvements of the compound. Future SAR campaigns will rely on the 6641-RXFP2 interactions described in this chapter to focus on enhancing the physical properties of the compound for potential therapeutic use, specifically the permeability, solubility, metabolic stability.

CHAPTER 4: DETERMINATION OF THE BIOLOGICAL ACTIVITY OF LEAD RXFP2 AGONISTS *IN VIVO*

4.1 Introduction

The previously identified RXFP1 small molecule agonist, compound ML290, does not activate the mouse RXFP1 receptor (136) , which required the development of an expensive and complicated humanized mouse model to study its efficacy as a therapeutic agent *in vivo* (182). Data presented in Chapter 2 showed that we have identified potent, effective, and specific small molecule agonists of the human RXFP2 receptor with significant mineralization activity in osteoblasts. Chapter 4 aims are to prove that these compounds can also activate the mouse RXFP2 receptor both *in vitro* and *in vivo*.

The most well characterized biological function of the RXFP2 receptor and its ligand INSL3 is the induction of male gubernaculum development during embryogenesis required for testicular descent (55, 57, 88). INSL3 is not produced in female embryos (183), therefore the gubernaculum does not develop but remains present as a vestigial structure, providing a natural model to test activity and specificity of the RXFP2 small molecule agonists *in vivo*.

Previous studies from our lab have demonstrated that the genetic ablation of *Rxfp2* significantly decreases bone density in mice (63). The second aim of this Chapter 4 attempts to demonstrate that the RXFP2 receptor can be pharmacologically

targeted to promote bone formation *in vivo*. For this aim, a transgenic mouse model overexpressing INSL3 was used and an efficacy study of the lead RXFP2 small molecule agonist, compound 6641, was also performed in WT mice. Age-related changes in bone architecture begin in the trabecular bone and they are more pronounce in females than males (184). In fact, WT C57BL/6J female mice start losing bone mass naturally after they are 2 months old, which provides a model to study the anabolic effects of compound 6641 without the need to use genetic or induced models of osteoporosis such as ovariectomy model. Changes in trabecular bone parameters were studied by micro-CT scan, a powerful X-ray imaging system to create high-resolution bone 3D models, and bone strength was measured using biomechanical testing.

4.2 Materials and methods

4.2.1 Cell lines maintenance and subculturing

HEK293T cell lines were maintained as described in materials and methods section 2.2.1. All cell culture reagents used for the following protocols are the same as described previously, unless stated otherwise.

4.2.2 Plasmid amplification and DNA preparation

Plasmid amplification and DNA preparation were performed as described in materials and methods section 3.2.3.

4.2.3 CRE-Luciferase assay in HEK293T cells transiently transfected with mouse RXFP2

HEK-CRE-Luc cells were transiently transfected with mouse RXFP2 in pcDNA3.1™/Zeo(+) mammalian expression vector, which was kindly donated by Dr. Ross Bathgate at The Florey Institute of Neuroscience and Mental Health in Australia. The oligonucleotide and amino acid sequence of the plasmid construct is shown Figure 25. For this assay, cells were seeded in 6-well flat-bottom clear plates at 0.4 million cells/well in 2mL/well of growth medium (DMEM, 10% FBS, 1x Pen/Strep) and allowed to attach overnight at 37°C, 5% CO_2. The next morning, cells were transfected as previously described in section 3.2.6. After 24 hours, the transfected cells were then harvested and seeded in 96-well flat-bottom opaque plates at 30,000 cells/well and the assay was performed and analyzed as previously described in material and methods 2.2.3. Results are presented as mean ± SEM of 3 independent experiments, each performed in triplicates.

4.2.4 HTRF cAMP assay in HEK293T cells stably expressing mouse RXFP1

HEK293T cells stably transfected with mouse RXFP1 were used to test compound specificity towards the mouse RXFP2 receptor using the HTRF $G_{\alpha s}$ dynamic cAMP assay kit. For this assay, cells were seeded in 96-well flat-bottom opaque plates at 30,000 cells/well and the assay was performed and analyzed as previously described in material and methods section 2.2.4. Results are presented as mean ± SEM of 3 independent experiments, each performed in triplicates.

4.2.5 Pharmacokinetic studies

Pharmacokinetic studies were performed by the company Pharmaron (Beijing, China) to determine the compound 6641 therapeutic range for pre-clinical studies in mice. 2-month-old WT C57BL/6J female mice were used to study the pharmacokinetic profile of the compound 6641 in plasma, liver, and long bones using liquid chromatography tandem mass spectrometry (LC-MS/MS). The compound 6641 was formulated in 75% PEG300 + 25% of 40% aq. HPBCD for intravenous (IV) injection and oral (PO) administration and in 60% Phosal + 40% PEG300 for intraperitoneal (IP) injection. Samples were collected at 0.083, 0.25, 0.5, 1, 3, 7, 24, and 48 hours after a single IV administration (3 mg/kg), a single PO administration (10 mg/kg), and a last PO administration for 3 consecutive days (10 mg/kg/day). Samples were collected at 0.083, 0.25, 0.5, 1, 2, 4, 8, and 12 hours after a single IP administration (30 mg/kg). All tissue samples were homogenized in water at a tissue weight to water volume ratio 1:3. Data was presented using GraphPad Prism 8 in concentration-time curves as the mean ± SEM of 3 mice per time point and the following parameters were calculated: maximum concentration (C_{max}, ng/g), time to C_{max} (t_{max}, h), area under the concentration-time curve (AUC_{last}, hr*ng/g), terminal half-life ($t_{1/2}$, h) and bioavailability (F, %).

4.2.6 Animal studies

All animal studies were conducted in accordance with the NIH Guide for the Care and Use of Laboratory Animals and approved under protocols 19-009 and 20-027 by the FIU Institutional Animal Care and Use Committee. All mice were maintained

in the FIU animal facilities in a controlled temperature and humidity environment with 12-hours light/12-hours dark cycles and free access to food and water.

For the RXFP2 specificity study *in vivo*, WT C57BL/6J pregnant female mice were used. At embryonic day 14.5, INSL3 starts driving gubernacular development for the transabdominal stage of testicular descent in male mice, which is finalized by embryonic day 17.5 (185). In order to study the ability of the compounds to induce gubernacular development in female embryos, WT C57BL/6J female and mice were mated and pregnancy was determined by the presence of a vaginal plug, timed as embryonic day 0.5. Pregnant females were given 6 daily intraperitoneal injections with 30 mg/kg of compound 6641, 4337 and 4340 or vehicle (60% Phosal – 40% PEG300) from embryonic day 12.5 to 17.5. At embryonic day 18.5, the pregnant females were euthanized by isoflurane inhalation overdose and the embryos were extracted for the histological analysis. Figure 26 shows a schematic representation of the experimental protocol.

For the INSL3 overexpression study, the INSL3 transgenic mouse model was used. These mice were originally generated on an FVB/N background by Ibrahim M. Adham et al. (98), and were available in our laboratory. Briefly, the mouse *Insl3* cDNA was fused to a rat insulin II promoter to specifically induce INSL3 overexpression in pancreatic β-cells. Hence, INSL3 overexpression levels in these mice are increased after feeding due to activation of insulin promoter. INSL3 transgenic female mice were maintained as heterozygotes and mated with WT

FVB/N males to obtain heterozygotes and WT offspring. Mice were genotyped and ear tagged at weaning (21 days) for identification. WT and INSL3 heterozygotes 22-week-old females, as well as WT male littermates were fasted overnight and euthanized by isoflurane inhalation overdose. Whole blood was collected by retro-orbital bleeding from all mice and allowed to clot in ice before centrifugation at 4°C for 5 minutes at 2,000 x g. Serum supernatant was collected, aliquoted to avoid repeated freeze-thaw cycles and stored at -80°C until used. Femurs and L1 to L5 lumbar spine were collected from female mice only, fixed in Harleco 10% neutral buffered formalin (Sigma-Aldrich) for 24 hours and kept in 100% EtOH at 4°C until used. Tibias were collected from female mice only, cleaned from muscle tissue and bone marrow was flushed with cold PBS. Clean tibias were then frozen at -80°C until used.

For the small molecule study, WT C57BL/6J female mice were used. Male and female mice were purchased from The Jackson Laboratory (catalog # 000664) and mated in FIU animal facilities to ensure experiments were performed on the inbred littermates. Female offspring was ear tagged at weaning age for identification and separated from males. At 8- and 20-week-old, female mice were randomly allocated into 2 treatment groups (vehicle or compound). Mice were treated with RXFP2 small molecule agonist (compound 6641) or vehicle formulation (75% PEG 300 + 25% of 40% aq. HPBCD) for 8 weeks by oral gavage at a concentration of 10 mg/kg using 18G, 1.5-inch, 2 mm ball flexible PTFE sterile plastic feeding needles. Mice were anesthetized with 2% isoflurane for less than 3 minutes before

administrating the treatments to prevent disserts and esophageal lesions. The 8-week-old group (16-week-old at the time of sacrifice) received the treatment every other day (Monday, Wednesday, and Friday), while the 20-week-old group (28-week-old at the time of sacrifice) received it every day (Monday through Friday). All mice were closely monitored, and body weight recorded throughout the study to detect any symptoms of distress. Mice were euthanized by isoflurane inhalation overdose, and the blood was collected by retro-orbital bleeding, as well as liver, kidneys, femurs, tibias, and L1 to L5 lumbar spine. Whole blood samples were processed as previously described and serum samples stored at -80°C until used. Kidneys and liver were visually inspected and weighted at necropsy to assess any potential signs of toxicity. Left femur and L1 to L3 lumbar spine were cleaned from muscle tissue, wrapped in a PBS-soaked gauze and frozen at −20°C until use. Right femur and L4 to L5 lumbar spine were fixed in 5% sucrose Surgipath 10% Millonig's formalin fixative at pH 7.4 (Leica, Wetzlar, Germany) for 24 hours and kept in 100% EtOH at 4C for potential histomorphometry study. Tibias were cleaned from muscle tissue and bone marrow was flushed with cold PBS, after which clean tibias were frozen at -80°C until used.

For the RXFP2 gene expression study, 8- and 28-week-old WT C57BL/6J female and male mice were used. Mice were euthanized by isoflurane inhalation overdose, and femurs and L1 to L5 lumbar spine were collected. Bones were cleaned from muscle tissue and bone marrow and medulla was flushed with cold

PBS from the femurs and spine respectively. Clean bones were frozen at -80°C until used.

4.2.7 Genotyping

All embryos were genotyped for sex determination by PCR. DNA was extracted from the tail of the mouse embryo by boiling the tissue for 1 hour at 100°C in 100 µL of 50 mM NaOH. Reaction was stopped by adding 15 µL of 50 mM Tris (pH 8), samples were centrifuged at 13,000 rpm for 5 minutes, and stored at -20°C until used. The primers mouse Sry forward 5'-GGTGTGGTCCCGTGGTG-3' and mouse Sry reverse 5'-TTTGGGTATTTCTCTCTGTGTAGG-3' were designed to amplify a 174 bp region of the Y chromosomal Sry gene. Male embryos were identified by the presence of a band at 174 bp and the female embryos by the absence of band. Mice were genotyped for the *Insl3* transgene by PCR. DNA was extracted from a small piece of the mouse ear following the genotyping protocol as previously described. The primers rat Insl2 forward 5'-CTCTGAGCTCTGAAG CAAGCA-3' and rat Insl2 reverse 5'-CCCAGGAGGCTGCAGTTGTT-3' were designed to amplify a 300 bp region of the rat insulin II promoter. Transgenic mice were identified by the presence of a band at 300 bp and the WT mice by the absence of band. Briefly, the 20 µL PCR reaction mix per sample contained 10 µL of amfiEco 2X Reaction Buffer, 0.6 µL of the amfiEco Taq DNA Polymerase (catalog # P0701 GenDEPOT, Katy, TX), 0.4 µL of each forward and reverse primers, 7.6 µL of nuclease-free water and 1 µL of sample DNA or for negative control. Thermal cycling was carried out in a DNA Engine Thermal Cycler using

denaturation step at 95°C for 3 minutes and 30 cycles of 30 seconds of denaturation at 95°C followed by annealing at 55°C and extension step at 72°C. The PCR products were directly loaded on a 1.5 % agarose gel since the amfiEco Taq DNA Polymerase already contains red and yellow loading dyes to visualize the DNA products. The 1 Kb Plus DNA Ladder (Invitrogen) was used for visualization of the DNA band sizes. Gel DNA bands were visualized under UV light transilluminator on a Gel Logic 2200 imaging system (Kodak, Rochester, NY).

4.2.8 Serum INSL3 determination

There is no commercially available ELISA kit to detect serum mouse INSL3 with high specificity and sensitivity. To determine the circulating levels of INSL3 in the transgenic mice, the HEK-RXFP2 cell were treated with mouse sera collected from transgenic and WT mice and induction of cAMP was measured using the HTRF $G_{\alpha s}$ dynamic cAMP assay kit. For this assay, HEK-RXFP2 cells were seeded in 96-well flat-bottom opaque plates at 30,000 cells/well in 60 µL/well of serum-free DMEM medium and allowed to attach overnight at 37°C, 5% CO_2. The next morning, cells were treated with 3 µL/well of serum or 1 µM forskolin. Cells were also treated with 4 µL of 200 µM IBMX diluted in serum-free DMEM. At this point, the protocol follows as described in materials and methods section 2.2.2. Data analysis was performed using GraphPad Prism 8. The cAMP response induced by the INSL3 present in the mouse serum is shown as the mean ± SEM of 7 female mice per group in bar graph format, each tested in triplicates. Sera from WT male mice (n=7) was also used as a positive control. Statistical significance was

calculated using unpaired two-tailed Student's t-test and was defined by $p<0.01$ (indicated by **).

4.2.9 Histological preparation and sectioning

For this assay, whole embryos were fixed in 10% formaldehyde for 24 hours at 4°C on a gentle saker. Afterwards, embryos were washed twice with PBS for 1 hour, followed by 3 consecutive washes with increasing concentrations of ethanol (30%, 50% and 70%) for 30 minutes. Fixed embryos were prepared for histology in TRUFLOW tissue cassettes (Fisher Scientific), processed using a TP 1020 automatic tissue processor (Leica) and embedded in paraffin wax using a Shandon Histocentre 3 paraffin embedding station (Thermo Electron, Waltham, MA). 5 - 7 µm sagittal serial sections were cut using a RM2255 automated rotary microtome (Leica) and sections were placed on a tissue flotation bath (Boekel, Feasterville-Trevose, PA) with water at 40°C to expand. Sections were transferred to Superfrost Plus microscope slides (Fisher Scientific) and dried overnight in a slide drying bench (Fisher Scientific) with low heat.

4.2.10 H&E staining

H&E histological analysis was used to determine changes in the gubernaculum morphology of female embryos treated with RXFP2 agonists compared to controls. Paraffin sections were de-waxed using Histo-clear II (National Diagnostics, Charlotte, NC), hydrated through several washes in decreasing concentrations of ethanol (100%, 70% and 50%), and rinsed with water. The sections were stained

with Harleco Harris Hematoxylin (Sigma-Aldrich), rinsed with water, and treated with Shandon Blueing and Define Clarifier reagents (Fisher Scientific). Sections were rinsed again with water, counterstained with Eosin-Y (Fisher Scientific) and dehydrated though several washes with 100% ethanol. Finally, sections were cleaned in Histo-clear II and mounted with coverslips using Permount mounting medium (Fisher Scientific). Representative gubernaculum images were taken using an AXIO Scope.A1 microscope connected to an Axiocam MRc5 camera (Zeiss, Jena, Germany). At least 4 female embryos were analyzed per treatment group. Male untreated embryos were also used as controls.

4.2.11 Ki67 staining

Ki67 histological analysis was used to determine changes in gubernacular cell proliferation of female embryos treated with the compound 6641 compared to controls. Paraffin sections were de-waxed using Histo-clear II, hydrated through several washes in decreasing concentrations of ethanol (100%, 70% and 50%), and rinsed with water. Sections were then boiled in 0.1 M citrate buffer at pH 6.0 for 20 minutes, followed by cooling at room temperature for 40 minutes. Sections were then incubated for 20 minutes in 3% H_2O_2 (Fisher Scientific) to inactivate endogenous horseradish peroxidase (HRP) activity and blocked with 5% BSA (Fisher Scientific) for 1 hour at room temperature. Sections were stained with 1:1200 primary rabbit polyclonal antibody Ki67 Ab-4 (catalog # RB-1510-P1, Fisher Scientific) in 1% BSA, at 4°C overnight in a humidity chamber to prevent drying. Next morning sections were washed twice in PBS-0.1% Triton X-100 (PBS-T) for

10 minutes each with gentle shaking followed by a single 5-minute wash in PBS. The Peroxidase VECTASTAIN Elite ABC kit was used following the manufacturer protocol (catalog # 6101, Vector Laboratories, Burlingame, CA). Sections were stained with anti-rabbit biotinylated secondary antibody for 1 hour at room temperature followed by two washes in PBS-T and once in PBS as previously described. Sections were incubated with the HRP substrate for 30 minutes and washed again as previously described. The Peroxidase ImmPACT DAB Substrate kit was used following the manufacturer protocol (catalog # SK-4105, Vector Laboratories). The sections were incubated in the DAB solution for 2 minutes to develop the peroxidase colorimetric signal and washed with water. Sections were then counterstained with Hematoxylin, treated with Blueing and Clarifier reagents, dehydrated, cleaned, and mounted as previously described. Representative images were taken using an AXIO Scope.A1 microscope connected to an Axiocam MRc5 camera and the number of Ki67 positive gubernacular cells over the total number of cells was quantified and expressed as the % of Ki67 positive cells. Data analysis was performed using GraphPad Prism 8. The results represent the mean ± SEM of at least 4 female embryos per treatment group in bar graph format.

4.2.12 RNA extraction

Frozen bones (femurs, tibias, and spine) were homogenized in 1 mL of TRIzol reagent using a POLYTRON PT 10-35 GT tissue homogenizer (Kinematica, Bohemia, NY) for 1 minute at 15,000 rpm. RNA extraction was performed using the Direct-zol RNA Miniprep Plus kit (catalog # R2072, ZYMO RESEARCH, Irvine,

CA) as instructed by the manufacturer. Samples were first centrifuged at 12,000 x g for 30 seconds to remove particulate debris and equal amounts of 100% EtOH were added to the supernatant, mixed thoroughly, and transferred into a Zymo-Spin column. Columns were centrifuged at 12,000 x g for 30 seconds and flow-through was discarded. A DNase I treatment of the columns was performed at room temperature for 15 minutes. After the DNase treatment, two washing steps were performed to the columns with 400 µL of RNA Pre-Wash. A final washing step was performed using 700 µL of RNA Wash Buffer for 2 minutes to ensure complete removal of the buffer from the columns. RNA was eluted from the columns using 60 µL of RNase-free water at 12,000 x g for 30 seconds and concentrations (< 1 µg) and purities (260/280 nm OD ratio ≥ 2) were measured using a NanoVue spectrophotometer before transferring them to -80°C for storage.

4.2.13 cDNA generation and quantitative RT-PCR procedure

cDNA generation and quantitative RT-PCR procedure were performed as previously described in materials and methods sections 2.2.11 and 2.2.12 respectively. Relative expression values of the specific genes of interest were calculated by the $2^{-\Delta\Delta Ct}$ method using expression of *Rpl13a* gene as normalizer. The sequences of the primers are summarized in Table 8. Data analysis was performed using GraphPad Prism 8. The results represent the mean ± SEM of 7-15 mice per group in scatter dot plot format. Statistical significance was calculated using unpaired two-tailed Student's t-test and was defined by $p<0.05$ (indicated by *), $p<0.01$ (indicated by **) and $p<0.001$ (indicated by ***).

4.2.14 Micro-CT analysis

Fixed L1 to L5 lumbar spine from WT and INSL3 transgenic mice, as well as non-fixed frozen femur and L1 to L3 lumbar spine from 6641 and vehicle treated mice were shipped to UAMS for analysis. Frozen bones were allowed to thaw for at least 2 hours at room temperature before scanning. All micro-CT scan analysis and 3D reconstructions were performed on a Scanco 40 instrument (Scanco Medical, Bassersdorf, Switzerland) using a slice resolution of 12 µm isotropic voxel size. The complete distal femurs from the midshaft portion down and L3-L4 vertebras were scanned with an effective energy of 55 kVp, X-ray tube current of 114 mA, and 200 ms integration time. For the quantification of trabecular bone of the distal femur metaphysis, the region of interest comprised of 151 contoured transverse slices extending 1.8 mm above the distal growth plate. For the trabecular bone quantification of the lumbar vertebrae, the region of interest comprised the entire vertebral body, including the maximum number of slices between both growth plates. All trabecular quantifications were performed applying a grayscale threshold (lower threshold 220, upper threshold 1000) and Gaussian noise filter (sigma 0.8, support 1). Standard nomenclature guidelines were followed to report all micro-CT measurements (186) and the following parameters were calculated: bone volume per tissue volume (BV/TV, %), trabecular thickness (Tb.Th, mm), trabecular number (Tb.N, mm-1), trabecular separation (Tb.Sp, mm), connectivity density (Conn.D (1/mm^3) and material density (Mat.D, VOI-mg HA/ccm). Data analysis was performed using GraphPad Prism 8. The results represent the mean ± SEM of 10-15 mice per group in scatter dot plot format. Statistical significance

was calculated using unpaired two-tailed Student's t-test and was defined by $p<0.05$ (indicated by *) and $p<0.01$ (indicated by **).

4.2.15 Biomechanical analysis

After micro-CT scanning, these same femurs and lumbar vertebras were utilized for biomechanical testing. The femurs were tested in a 3-point bending test and the L3 vertebrae in a compression test using an ElectroForce 5500 Test Instrument (TA Instruments, New Castle, DE) with a ramp rate of 0.05 mm/sec and support span of 8.1 mm and running WinTest software version 8.2. Time, force, and displacement were collected for use in the analysis of mechanical and material properties. The Moment of Inertia (MoI) was calculated based on the micro-CT measurements. Custom MATLAB codes (MathWorks, Natick, MA) were used in the analysis. Force (N) was plotted against displacement (mm). Four points were selected: Point 1 and 2 are along the linear portion of the plot, point 3 was selected at the yield point, and point 4 was selected at the maximum load (Figure 27). The slope between point 1 and 2 was defined as the stiffness (N/mm). The force at point 3 was considered the yield force (N) and the force at point 4 was considered the ultimate force (N). Due to the high variability of animal models and potential downstream effects of genetic alterations, standard mechanical properties (stiffness, yield force, and ultimate force) may not be sufficient in the comparison groups. To remove the effect of bone size, the material properties elastic modulus (MPa), yield stress (MPa), and ultimate stress (MPa) were also calculated. For the three-point bending standard cylinder bending mechanics were used. Data

analysis was performed using GraphPad Prism 8. The results represent the mean ± SEM of 10-15 mice per group in scatter dot plot format.

4.2.16 Statistical analysis

Statistical analysis was performed as described in materials and methods section 2.2.13.

4.3 Results

4.3.1 RXFP2 small molecule agonists specifically activate the mouse RXFP2 receptor *in vitro*

To show that the RXFP2 small molecule agonists activate mouse RXFP2 receptor, HEK-CRE-Luc cells were transiently transfected with mouse *Rxfp2* expression vector and treated with the compounds or with INSL3 as a positive control. The results showed that compounds 6641, 4340 and 4337 are inducing a cAMP response at levels comparable to the INSL3 activation (Figure 28). The specificity of the compounds was then tested against mouse RXFP1 receptor in stable expressing HEK293T cells by HTRF cAMP assay. No cAMP accumulation was found after treatment with the RXFP2 small molecule agonists in comparison to positive control Relaxin (Figure 29). These results certainly demonstrate that like human receptors, the identified compounds are specific agonists of the mouse RXFP2 receptor and do not activate mouse RXFP1.

4.3.2 RXFP2 small molecule agonists specifically activate the mouse Rxfp2 receptor *in vivo*

It was previously shown that transgenic overexpression of INSL3 in female embryos resulted in partial gubernacular development, descent of the ovaries into a low intraabdominal position and development of an inguinal hernia (98). Therefore, we hypothesized that the small molecule agonists of RXFP2 would show similar effects in female mice. Compound activity was tested by injecting pregnant females with the RXFP2 agonists starting from day E12.5 to E17.5 of embryonic development followed by histological evaluation of the gubernaculum in developing female embryos.

To define the pharmacokinetic properties of our lead compound 6641, an initial study was performed to evaluate the level of exposure in different tissues upon single dose intraperitoneal injection in female mice at 30 mg/kg. At this dose, compound 6641 provides stable levels in the range of single/double digit µM in plasma, liver, and bone for at least 12 hours (Figure 30). At E18.5 the *processus vaginalis* or outpouching of the peritoneum occurs in males at the site of gubernacular caudal connection (187). The female embryos treated with compounds 6641, 4337 and 4340 exhibited a male-like invagination of the gubernaculum into the peritoneum (Figure 31). This phenotype was not observed in control untreated and vehicle-treated female embryos at this age, suggesting that the small molecule compounds passed through the placental barrier and induced INSL3-like effects in female gubernaculum *in vivo.* No differences were

detected in the position of the ovaries in compound-treated female embryos and controls (data not shown).

INSL3 has been shown to induce proliferation of gubernacular cells (188, 189) and osteoblast cells (63) *in vitro*. Here, the proliferative effect of compound 6641 was tested *in vivo*, but no significant differences were observed in gubernacular cell proliferation of female embryos treated with compound 6641 in comparison to untreated and vehicle controls (Figure 32).

4.3.3 INSL3 overexpression in female mice increases bone mass in vertebrae and *Alp* expression in tibia

To demonstrate that the INSL3/RXFP2 axis can be a pharmacological target to preserve/increase bone mass, as a proof of concept we first used an INSL3 transgenic mouse model overexpressing mouse INSL3. No significant changes in body weight were observed between INSL3 transgenic and WT female mice (Figure 33a). To evaluate the biological activity of circulating INSL3 in transgenic mice overexpressing the peptide, we applied sera isolated from WT and INSL3 transgenic females onto the HEK-RXFP2 cell assay. As expected, peripheral blood collected from transgenic females exhibited significantly higher cAMP activation of the RXFP2 expressing cells (Figure 33b). A micro-CT analysis of the trabecular bone in the L4 vertebral body of 22-week-old females revealed a significant increase in BV/TV of INSL3 transgenic females compared to WT mice (Figure 34a). INSL3 transgenic mice also showed a small increase in Tb.N and Tb.Th, as well as a small decrease in Tb.Sp, although these differences were not statistically

significant. Interestingly, Conn.D and Mat.D values were significantly higher in INSL3 transgenic mice, which suggest an increase in trabecular connections and mineralization respectively, both indicative of stronger bones (Figure 34a).

Quantitative RT-PCR analysis of the tibia showed significantly increased mRNA levels of the osteoblast activity marker *Alp* in INSL3 transgenic mice compared to WT mice, but no differences were found in bone formation markers *Col1a1* and *Osteocalcin* or osteoblast differentiation marker *Runx2* (Figure 34b).

4.3.4 Compound 6641 has an optimal and safe pharmacological profile

To better understand the pharmacokinetic properties of compound 6641 and fine tuning the adequate dose in our efficacy studies, several pharmacokinetic studies of compound 6641 in female mice were carried out upon single IV dose at 3 mg/kg, single PO dose at 10 mg/kg and multiple 10 mg/kg PO daily dose administration for 3 consecutive days. On average, the compound exhibited a half-life of between 4 – 6.5 hours depending on the route of administration, with no accumulation at 10 mg/kg. Despite its oral bioavailability around 25 - 31% (Figure 35a), the molecule displayed good levels of exposure above its cAMP assay EC_{50} in different tissues for extensive period of time: in bone tissue at a maximum concentration of 1072 ng/g for IV administration and between 170 - 300 ng/g for PO administration (Figure 35c). Based on this data we selected 10 mg/kg PO administration to carry out our initial efficacy study *in vivo*, since the dose and route of administration seems more suitable and clinically relevant for future long-term treatments.

A 6641 long-term study was performed in female mice as described in the methods section, using the 10 mg/kg PO administration. The body weight of all mice was recorded during treatment, as well as the weight of the liver and kidneys at sacrifice. No changes were observed in body weight (Figure 36a, b) or organs weight (Figure 36c, d) between the treatment groups. A histological analysis of the livers and kidneys did not show any changes in cell morphology of compound-treated mice (Figure 36e). No mortality was observed during the study. The results therefore suggest that there were no major toxicity issues with the PO administration of compound 6641.

4.3.5 Compound 6641 increases vertebral trabecular thickness and number in young female mice but has no effect on vertebral strength

The bone anabolic properties of compound 6641 were studied by micro-CT and compression test in the L3 vertebral body of young (8-week-old) and adult (20-week-old) female mice. 8-week-old WT C57BL/6J female mice were treated 3 times per week for 8 weeks. A significant increase in Tb.N and Tb.Th was found in compound-treated mice compared to vehicle-treated mice, while there was a trend toward increased BV/TV and decreased Tb.Sp after compound treatment, respectively (Figure 37). No changes were found in Conn.D and Mat.D of the vertebral body between vehicle- and compound-treated mice (Figure 37). No significant differences in any of the trabecular bone parameters measured were found after micro-CT assessment in the L3 vertebral body of the 20-week-old WT C57BL/6J female mice treated 5 times per week for 8 weeks (Figure 38).

Biomechanical testing of the L3 vertebral body was performed to study changes in bone strength, but no significant differences were found between vehicle and compound treated mice at any of the ages tested (Figure 39).

4.3.6 Compound 6641 has no effect on femur microstructure or strength but increases *Osteocalcin* gene expression in tibia from young female mice

The bone anabolic effects of compound 6641 were also studied by micro-CT analysis and 3-point bending test in the femur of young and adult female mice. At the time of sacrifice (16- and 28-week-old respectively), no significant differences were found between vehicle and compound treated mice after micro-CT assessment of the trabecular bone parameters in the distal femur (Figure 40). Consistently, no significant changes were observed in any of the biomechanical bone strength properties between vehicle and compound treated mice (Figure 41). However, a quantitative RT-PCR analysis of the tibias from the 16-week-old female mice showed a significant increase in gene expression levels of the osteoblast mineralization marker *Osteocalcin* and a decrease of the early osteoblast differentiation marker *Runx2* in compound-treated mice compared to vehicle-treated mice, suggesting a cell population shift from immature osteoblasts to the mature osteoblasts required for bone formation and ossification (Figure 42). No significant differences were found in *Alp* and *Col1a1* mRNA levels between groups (Figure 42).

4.3.7 Bone *Rxfp2* gene expression patterns in female mice change with age and bone tissue, but do not present gender dimorphism

To assess if the *Rxfp2* gene expression levels fluctuate with age and gender, a study to measure the *Rxfp2* mRNA level of expression in femur and lumbar spine was carried out in young (8-week-old) and adult (28-week-old) females, as well as young (8-week-old) males. Quantitative RT-PCR analysis of bones from 8- and 28-week-old female mice showed significantly increased *Rxfp2* mRNA levels in spine vs femur (Figure 43a). The *Rxfp2* mRNA levels in spine and femur were also found elevated in 8- vs 28-week-old females, while the difference was only significant in spine (Figure 43b). No changes in the *Rxfp2* gene expression levels of femur and spine were found between 8-week-old females and males (Figure 43c).

4.4 Figures and tables

Mouse RXFP2 (PRL-FLAG-mRXFP2) in pcDNA3.1 zeo(+)

```
ATGGACAGCAAAGGTTCGTCGCAGAAAGGGTCCCGCCTGCTCCTGCTGCTGGTGGTGTCAAATCTACTCT
TGTGCCAGGGTGTGGTCTCCGATTACAAAGATGATGATGATAAAGAATTCGACAGCAGTATGGTGGCTCC
TCTGTGCCCCAAAGGGTATTTTCCCTGTGGGAATCTCACCAAATGCTTGCCCCGAGCCTTTCACTGCGAT
GGTGTGGATGATTGCGGGAATGGTGCCGACGAGGACAACTGTGGTGACACTAGTGGATGGACAACCATAT
TTGGCACAGTCCATGGGAATGTCAATAAAGTGACATTGACACAGGAGTGCTTTCTCAGCCAGTATCCACA
GCACTGTTACTGCAGAGAAAATGAACTGGAATGTGTAAAGGCTGACTTAAAAGCTGTGCCAAAGGTTTCC
AGCAACGTAACATTACTATCTCTTAAGAAAAACAAAATCCACAGACTTCCAGTCAAGGTCTTCAGCAGAT
ACACAGAACTCAGAAAGATATACCTTCAGCACAACTGCATCACACACATCTCCAGGAGAGCATTCCTTGG
ATTACATAATCTACAAATACTGTATCTCAGCCATAACTGCATTACCTCTCTCAGGCCTGGGATATTCAAA
GACTTGCATCAGCTTGCTTGGCTAATTTTAGATGACAACCCGATCACCAGAATCTCACAGAAGTCCTTTA
TGGGGTTAAACTCCTTGTTTTTCTTGTCCATGGTGGGTAACCGGCTCGAGGCCCTTCCTGAAACATTGTG
TGCTCAGATGCCTCAACTCAACTGGGTGGATCTGGCAAACAATGGAATAAAGTACATAACGAACTCCACC
TTCCTAACGTGCGACTCGCTCACGGTTCTGTTTCTGCCTAGAAATCAAATTGGTTTTGTTCCAGAGAAGA
CATTTTCTTCATTAAAAAATTTAGGAGAACTGGACCTGTCTAGCAATATGATAACAAAACTCCCAGTCCA
CCTTTTCAGCGACCTTCATCTTCTCCAGAAGCTGAACCTGTCATCCAACCCTCTTCTGTATGTCCACAAG
AACCAGTTTGGAAGTCTCAAACAACTTCAGTCTCTAGACCTGGAAAGGATAGAGATTCCAAACATAAGCA
CAGGAATGTTCCAGCCAATGAAGAACCTTTCTCACATTTATTTGAAAACCTTTCGATACTGCTCCTATGT
CCCCCATGTCCGAATCTGTATGCCGTCGACTGATGGTATTTCTTCGTCTGAGGACCTCTTGGCTAACGGT
ATCCTCAGAGTGTCTGTCTGGGTTATAGCTTTCATTACCTGCGTTGGGAATTTCCTTGTCATAGCCGTGA
GATCTCTCATTAAGGCTGAGAATACAACTCACGCTATGTCCATCAAAATCCTTTGTTGTGCCGATTGCCT
GATGGGGGTGTACCTGTTCTCCGTGGGCGTCTTTGACATCAAGTACCGAGGGCAGTATCAGAAGTATGCG
CTGCTGTGGATGGAGAGTGTGCCCTGCCGCCTGCTGGGCTTCCTGGCCACGCTGTCCACAGAGGTCTCGG
TGCTGCTGCTGACATTCCTGACGCTGGAGAAGTTCCTTGTCATAGTATTCCCTTTCAGCAACCTGCGCCT
GGGCAAGCGCCAGACTGCTGTGGCCCTCGCCAGCATCTGGGTGGTGGGATTTCTCATAGCGGCCGTTCCG
TTCACCAGAGAGGATTATTTCGGCAACTTTTATGGGAAAAATGGAGTCTGCTTCCCACTTCATTATGACC
AAGCAGAAGATTTTGGAAGTAGAGGGTACTCCCTTGGGATTTTCCTAGGTGTGAACTTGCTGGCTTTCCT
CGTCATCGTGATTTCCTATGTCACCATGTTCTGCTCCATTCATAAAACAGCCCTTCAGACTGCAGAAGTG
AGGAGCCACATCGGGAAGGAGGTGGCTGTTGCAAACCGGTTCTTTTTTATCGTGTTCTCTGATGCCATCT
GCTGGATCCCTGTGTTTGTCGTTAAGATCCTGTCTCTCCTTCAAGTGGAGATACCAGGCACAATCACTTC
CTGGATCGTGGTTTTTTTCCTTCCGGTGAACAGCGCCTTAAACCCCATCCTCTACACTCTGACGACCTCC
TTTTTTAAGGACAAGTTGAAACAGTTGCTGCACAAACATCGGAGGAAACCCATCTTCAAAGTTAAGAAGA
AAAGTTTATCCGCTTCCATTGTGTGGACAGACGAGTCTTCACTTAAACTTGGAGTGTTGAGCAAAATAGC
CCTTGGGGACAGTATAATGAAGCCGGTCTCCCCGTAG

MDSKGSSQKGSRLLLLLVVSNLLLCQGVVSDYKDDDDKEFDSSMVAPLCPKGYFPCGNLT
KCLPRAFHCDGVDDCGNGADEDNCGDTSGWTTIFGTVHGNVNKVTLTQECFLSQYPQHCY
CRENELECVKADLKAVPKVSSNVTLLSLKKNKIHRLPVKVFSRYTELRKIYLQHNCITHI
SRRAFLGLHNLQILYLSHNCITSLRPGIFKDLHQLAWLILDDNPITRISQKSFMGLNSLF
FLSMVGNRLEALPETLCAQMPQLNWVDLANNGIKYITNSTFLTCDSLTVLFLPRNQIGFV
PEKTFSSLKNLGELDLSSNMITKLPVHLFSDLHLLQKLNLSSNPLLYVHKNQFGSLKQLQ
SLDLERIEIPNISTGMFQPMKNLSHIYLKTFRYCSYVPHVRICMPSTDGISSSEDLLANG
ILRVSVWVIAFITCVGNFLVIAVRSLIKAENTTHAMSIKILCCADCLMGVYLFSVGVFDI
KYRGQYQKYALLWMESVPCRLLGFLATLSTEVSVLLLTFLTLEKFLVIVFPFSNLRLGKR
QTAVALASIWVVGFLIAAVPFTREDYFGNFYGKNGVCFPLHYDQAEDFGSRGYSLGIFLG
VNLLAFLVIVISYVTMFCSIHKTALQTAEVRSHIGKEVAVANRFFFIVFSDAICWIPVFV
VKILSLLQVEIPGTITSWIVVFFLPVNSALNPILYTLTTSFFKDKLKQLLHKHRRKPIFK
VKKKSLSASIVWTDESSLKLGVLSKIALGDSIMKPVSP
```

Figure 25. Mouse RXFP2 nucleotide and amino acid sequences. The highlighted yellow sequence corresponds to the prolactin signal peptide, while the highlighted green sequence corresponds to the FLAG-Tag.

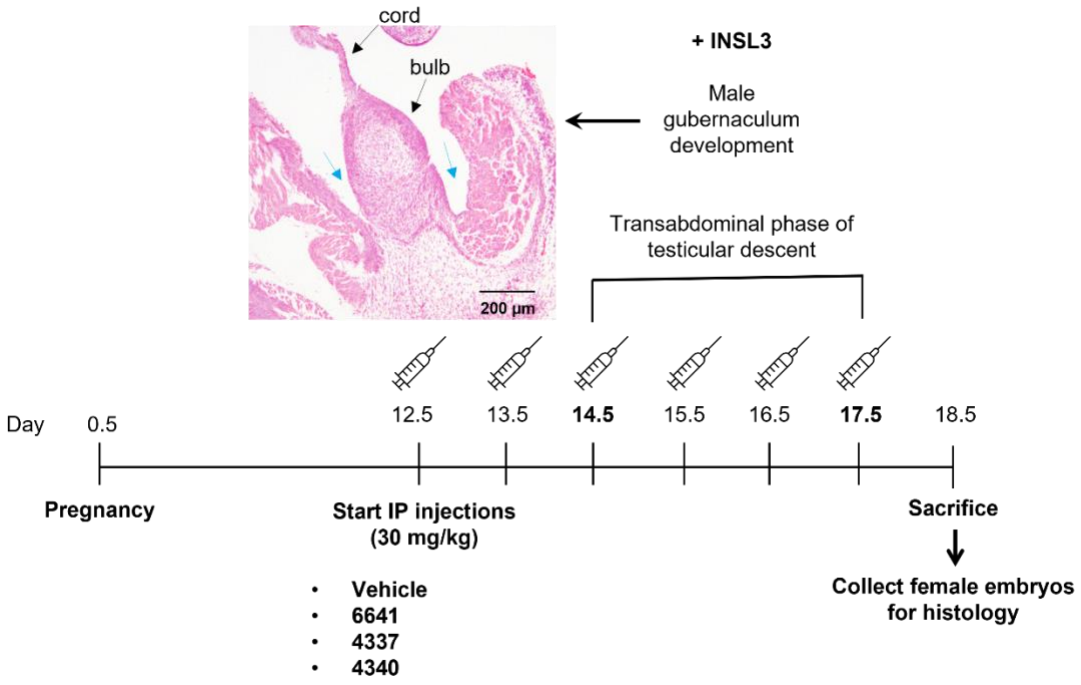

Figure 26. Diagram of the treatment protocol for assessing gubernaculum development in female embryos. Representative histological section of the developed male gubernaculum at embryonic day 18.5 (upper left). Invagination of the male gubernaculum is denotated by the blue arrows.

Table 8. Sequences of mouse primers used for quantitative RT-PCR. F (forward), R (reverse)

PRIMERS	SEQUENCES
***Runx2* F**	5'-TCAGCAAAGCTTCTTTTGGGAT-3'
***Runx2* R**	5'-GGGCTCACGTCGCTCAT-3'
***Osteocalcin* F**	5'-ACCCTGGCTGCGCTCTGTCTCT-3'
***Osteocalcin* R**	5'-GATGCGTTTGTAGGCGGTCTTCA-3'
***Alp* F**	5'-TCCACCAGCAAGAAGAAGCC-3'
***Alp* R**	5'-AAACCCAGA CACAAGCATTCCC-3'
***Col1a1* F**	5'-CCTCAGGGTATTGCTGGACAAC-3'
***Col1a1* R**	5'-ACCACTTGATCCAGAAGGACCTT-3'
***Rxfp2* F**	5'-TGTGCTCAGATGCCTCAAC-3'
***Rxfp2* R**	5'-AGGAAGGTGGAGTTCGTTATG-3'
***Rpl13a* F**	5'-CCCT GCTGCTCTCAAGGTT-3'
***Rpl13a* R**	5'-GGTACTTCCACC CGACCTC-3'

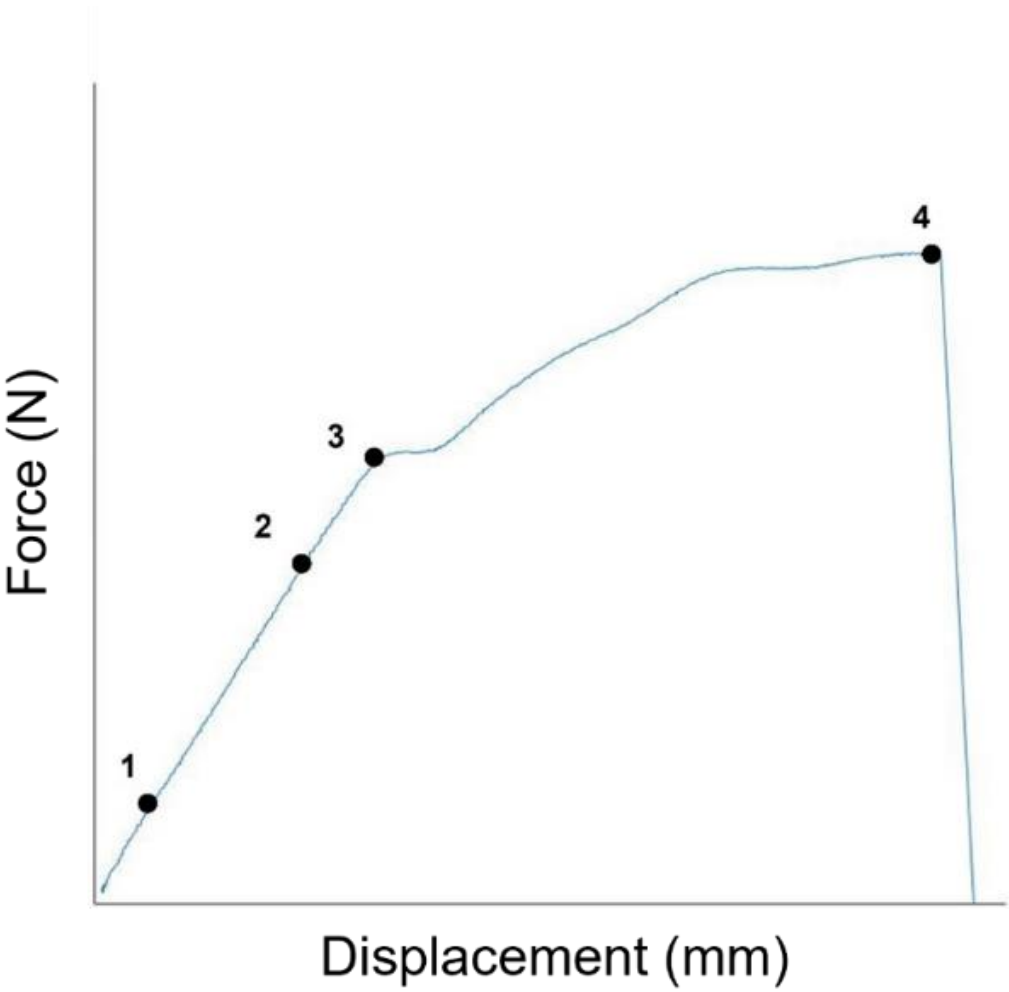

Figure 27. Representative biomechanical Force/Displacement curve. The slope between point 1 and 2 corresponds to the stiffness, point 3 corresponds to the yield point, and point 4 corresponds to the maximum load.

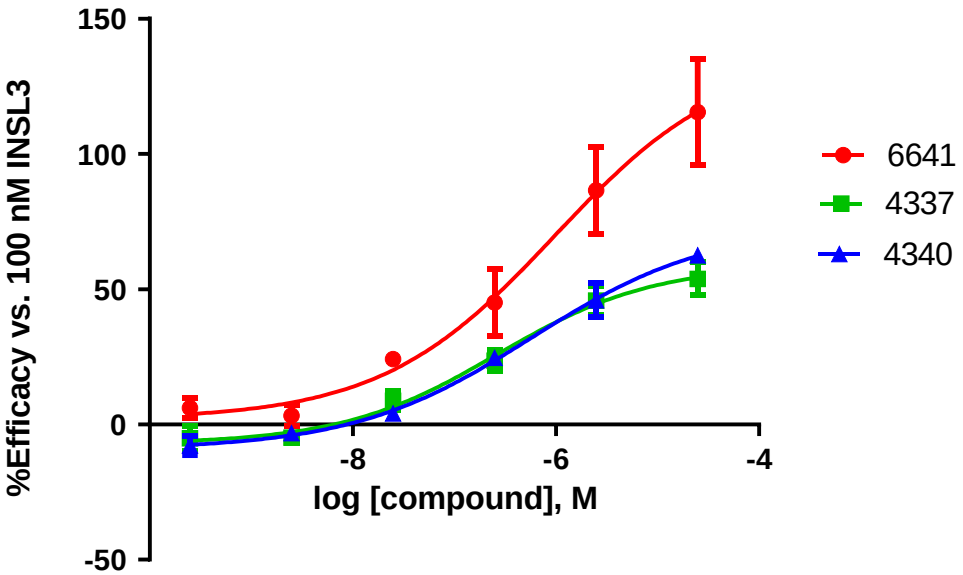

Figure 28. RXFP2 agonists activate the mouse RXFP2 receptor. Activation of mouse RXFP2 receptor by the compounds in transiently transfected HEK293T-CRE-Luc cells. Compound response was normalized to 100 nM INSL3 as 100% efficacy and DMSO vehicle as 0% efficacy. Results are expressed as mean ± SEM of 3 independent experiments.

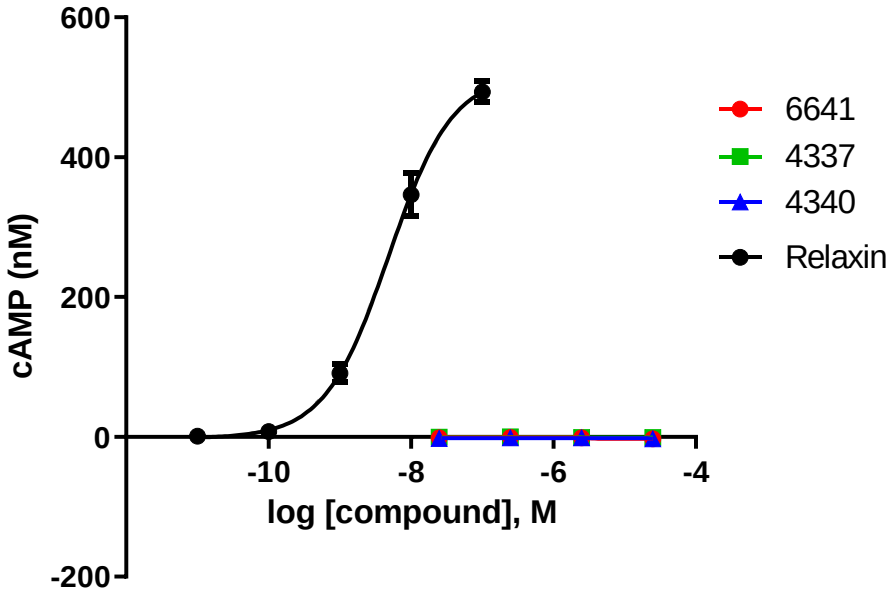

Figure 29. RXFP2 agonists do not activate the mouse RXFP1 receptor. HTRF cAMP counter-screen of RXFP2 agonists in HEK293T cells stability expressing the mouse RXFP1 receptor. Relaxin was used as positive control for RXFP1 receptor activation. Results are expressed as mean ± SEM of 3 independent experiments.

a

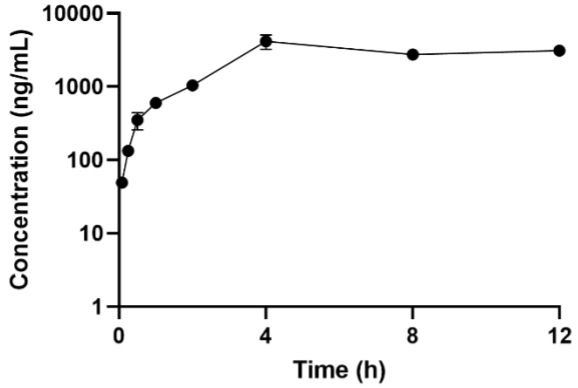

Route	Dosing Level (mg/kg)	Cl_obs (mL/min/kg)	$t_{1/2}$ (h)	t_{max} (h)	C_{max} (ng/mL)	AUC_{last} (h*ng/mL)	AUC_{Inf} (h*ng/mL)	AUC_%Extrap (%)	MRT (h)	AUC_{last}/D (h*mg/mL)	V_{ss}_obs (L/kg)	F (%)
IP	30	NA	19.2	4.00	4140	31791	117888	73.0	NA	1060	NA	NA

b

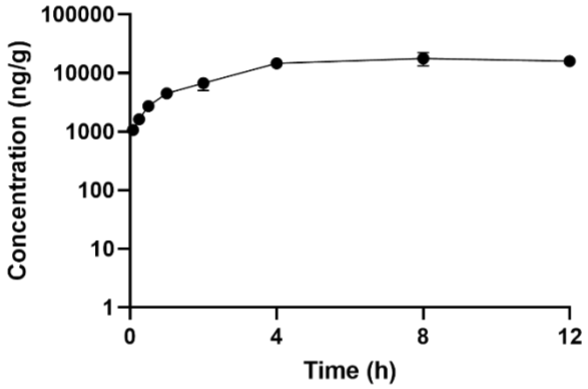

Route	Dosing Level (mg/kg)	t_{max} (h)	C_{max} (ng/g)	AUC_{last} (h*ng/g)	AUC_{Inf} (h*ng/g)	C_{max} Ratio (Liver/ Plasma)	AUC_{Last} Ratio (Liver/ Plasma)
IP	30	8.00	17773	161570	NA	4.29	5.08

c

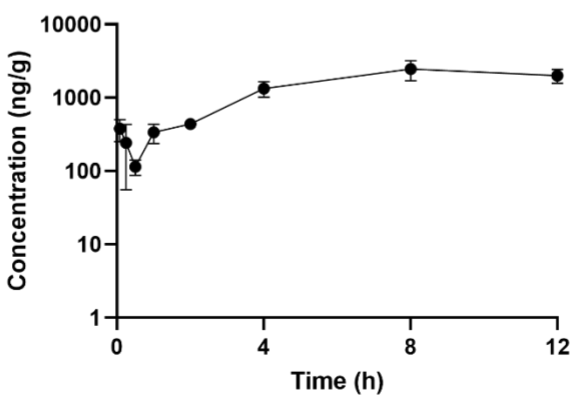

Route	Dosing Level (mg/kg)	t_{max} (h)	C_{max} (ng/g)	AUC_{last} (h*ng/g)	AUC_{Inf} (h*ng/g)	C_{max} Ratio (Bone/ Plasma)	AUC_{Last} Ratio (Bone/ Plasma)
IP	30	8.00	2456	18885	NA	0.593	0.594

Figure 30. Compound 6641 pharmacokinetic study after 30 mg/kg single dose IP administration. a) Plasma, **b)** liver and **c)** bone profiles in female mice. The actual concentration (ng/g) is the detected value (ng/mL) multiplied by 4. Drug vehicle is 60% Phosal – 40% PEG300. 3 mice were used per time point. Results are expressed as the mean ± SEM.

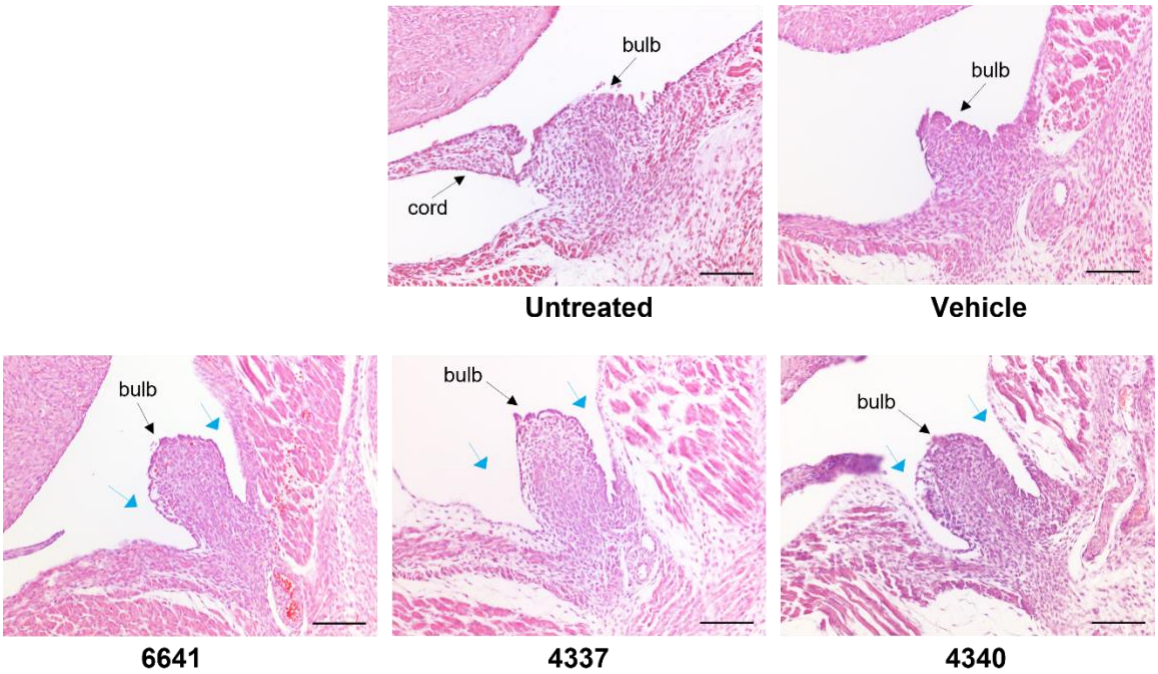

Figure 31. RXFP2 agonists are biologically active and selective *in vivo*. Representative histological sections showing a male-like invagination of the female gubernaculum in all compound-treated embryos (blue arrows) at E18.5. At least 4 female embryos were analyzed per group. Scale bar = 100 µm.

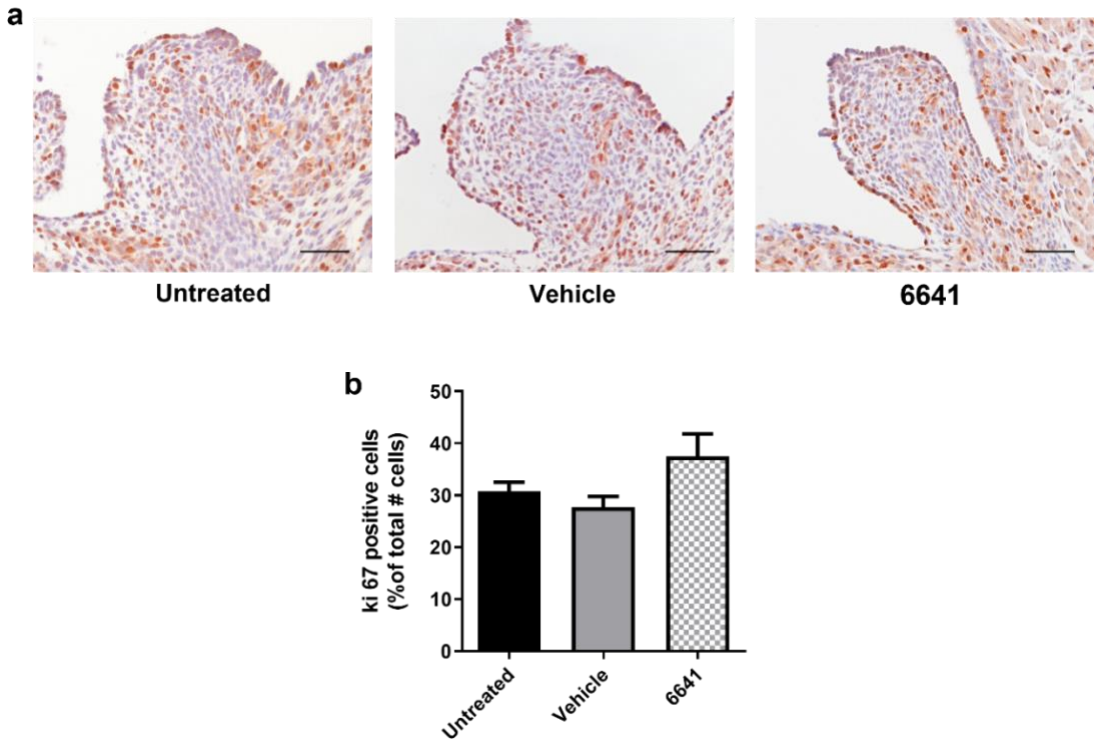

Figure 32. RXFP2 agonists do not affect gubernacular cell proliferation. a) Representative histological sections of the control- and compound-treated female gubernaculum at E18.5 after staining with Ki67 antibody and counterstaining with hematoxylin. Scale bar = 50 µm. **b)** Quantification of the number of Ki67 positive cells as a percentage of the total number of cells. Results represent the mean ± SEM of at least 4 female embryos per group.

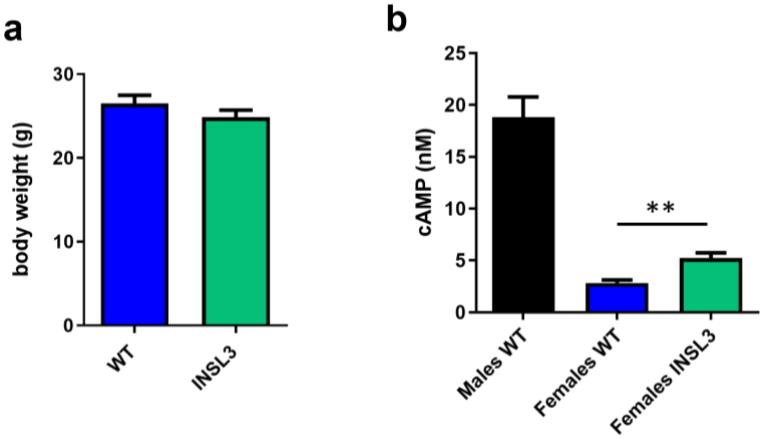

Figure 33. Validation of INSL3 transgenic mouse model. a) *Insl3* overexpression does not affect body weight in female mice. **b)** cAMP activity induced in HEK-RXFP2 cells by INSL3 present in serum from WT and INSL3 female mice. Serum from WT males was used as positive control. Results represent the mean ± SEM of 7 mice per group. **p<0.01 vs. WT females using Student's t-test.

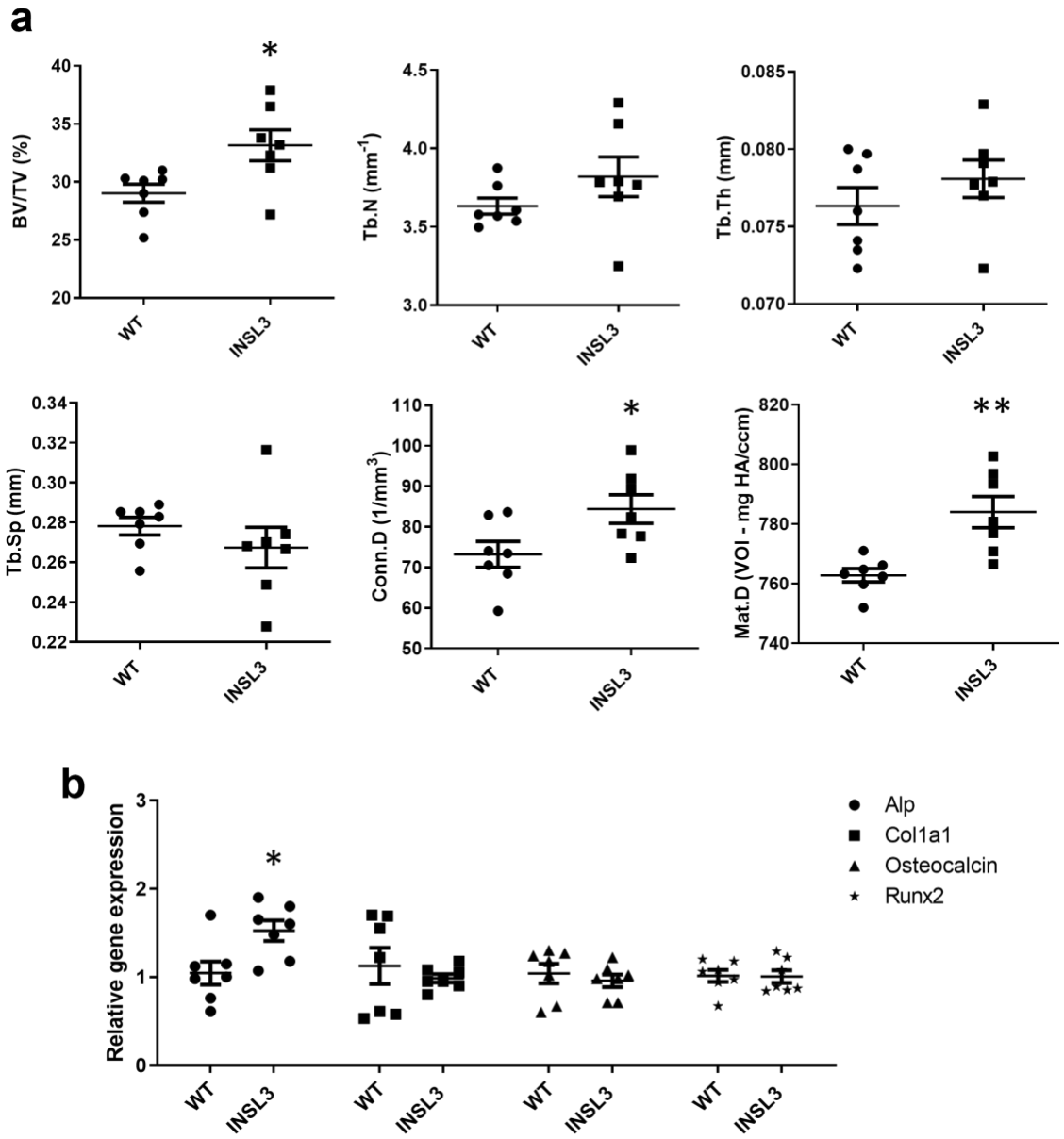

Figure 34. *Insl3* overexpression increases bone formation in female mice. a) Trabecular micro-CT parameters in lumbar vertebrae of WT and INSL3 transgenic female mice. **b)** Gene expression levels of osteoblast markers in tibias from WT and INSL3 female mice measured by quantitative RT-PCR and normalized to *Rpl13a* gene expression as an internal control. Results represent the mean ± SEM of 7 mice per group. *p<0.05, **p<0.01 vs. WT using Student's t-test.

a

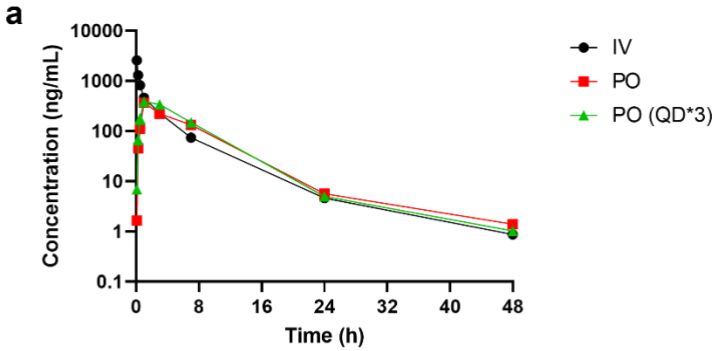

Route	Dosing Level (mg/kg)	Cl_obs (mL/min/kg)	$t_{1/2}$ (h)	t_{max} (h)	C_0 (ng/mL)	AUC_{last} (h*ng/mL)	AUC_{Inf} (h*ng/mL)	AUC_% Extrap (%)	MRT (h)	AUC_{last}/D (h*mg/mL)	V_{ss}_obs (L/kg)	F (%)
IV	3	15.6	6.56	NA	3593	3191	3199	0.258	3.47	1064	3.38	NA
Route	Dosing Level (mg/kg)	Cl_obs (mL/min/kg)	$t_{1/2}$ (h)	t_{max} (h)	C_{max} (ng/mL)	AUC_{last} (h*ng/mL)	AUC_{Inf} (h*ng/mL)	AUC_% Extrap (%)	MRT (h)	AUC_{last}/D (h*mg/mL)	V_{ss}_obs (L/kg)	F (%)
PO	10	NA	3.89	1.00	366	2615	2647	1.20	NA	262	NA	24.8
PO (QD*3)	10	NA	5.88	1.00	389	3261	3269	0.265	NA	326	NA	30.7

b

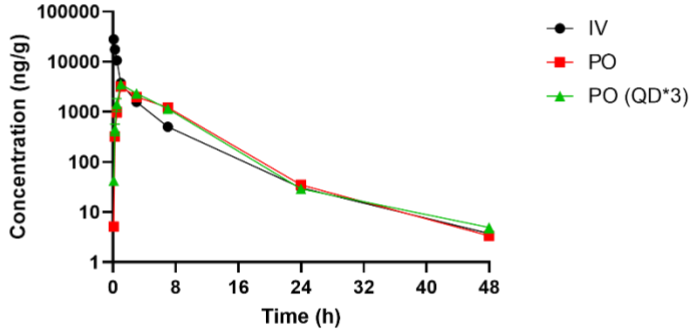

Route	Dosing Level (mg/kg)	t_{max} (h)	C_{max} (ng/g)	AUC_{last} (h*ng/g)	AUC_{Inf} (h*ng/g)	C_{Max} Ratio (Liver/ Plasma)	AUC_{Last} Ratio (Liver/ Plasma)
IV	3	0.083	28040	26492	26524	10.9	8.30
PO	10	1.00	3214	24146	24170	8.78	9.23
PO (QD*3)	10	1.00	3570	24927	24965	9.18	7.64

c

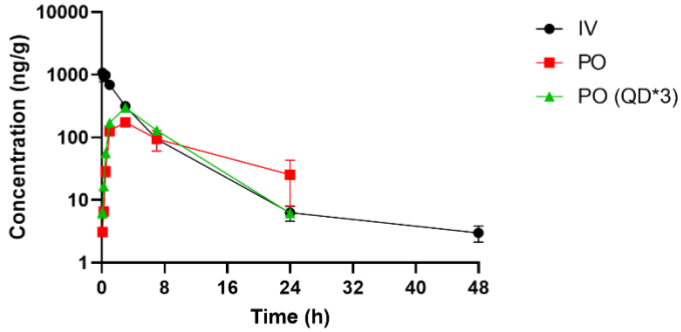

Route	Dosing Level (mg/kg)	t_{max} (h)	C_{max} (ng/g)	AUC_{last} (h*ng/g)	AUC_{Inf} (h*ng/g)	C_{Max} Ratio (Bone/ Plasma)	AUC_{Last} Ratio (Bone/ Plasma)
IV	3	0.083	1072	3650	3687	0.419	1.14
PO	10	3.00	174	1897	2190	0.475	0.725
PO (QD*3)	10	3.000	298	2539	2573	0.766	0.779

Figure 35. Compound 6641 pharmacokinetic study after one 3 mg/kg IV administration, one 10 mg/kg PO administration and three 10 mg/kg PO administrations (QD*3). a) Plasma, **b)** liver and **c)** bone profiles in female mice. The actual concentration (ng/g) is the detected value (ng/mL) multiplied by 4. Drug vehicle is 25% aq. 40% HP-b-CD - 75% PEG300. 3 mice were used per time point. Results are expressed as the mean ± SEM.

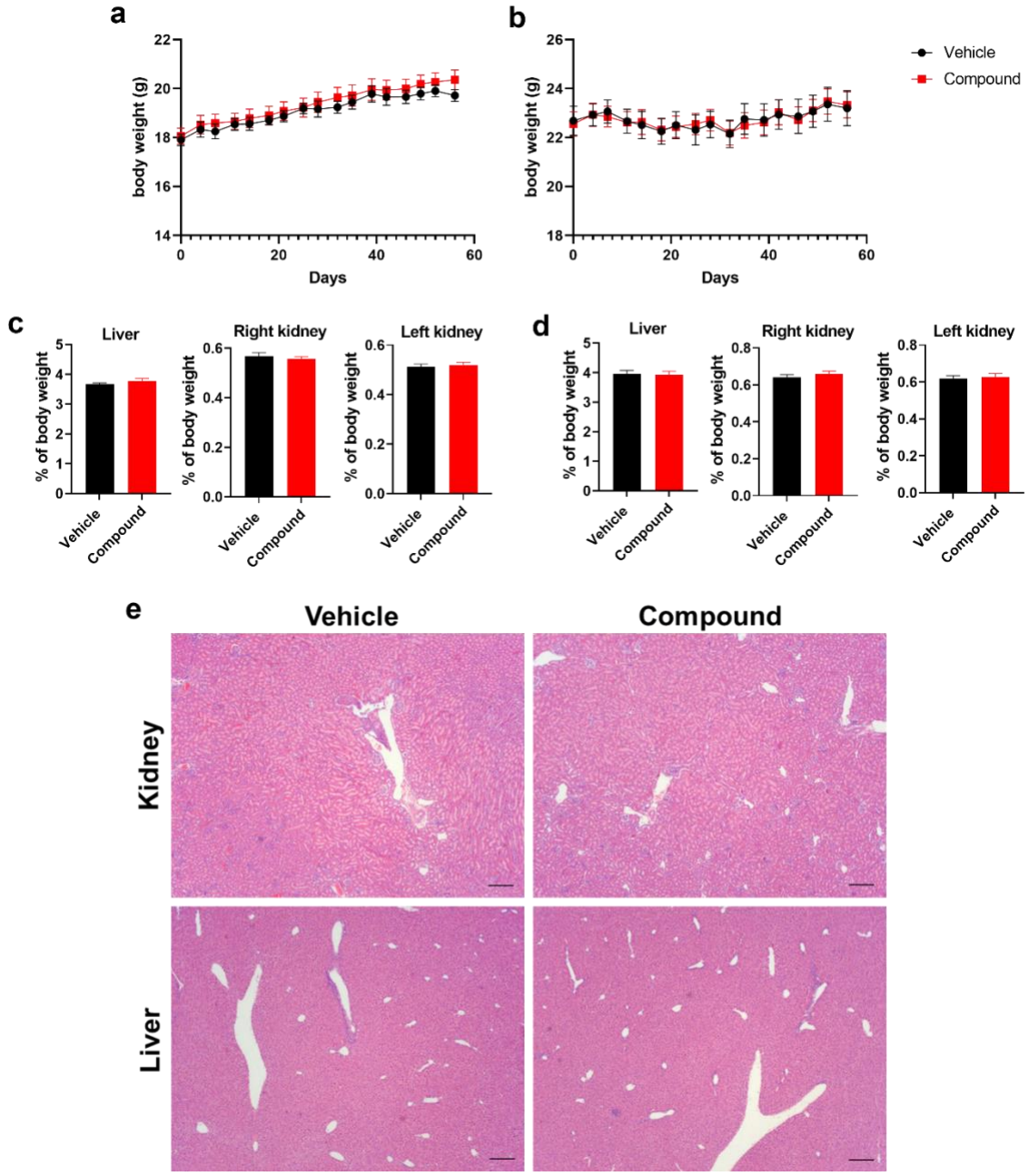

Figure 36. Compound 6641 does not show toxicity *in vivo.* Body weight of all vehicle- and compound-treated **a)** 8- and **b)** 20-week-old female mice recorded during the oral 8-week treatment with 10 mg/kg of compound 6641. Liver and kidney organ weight normalized to body weight at necropsy from all **c)** 16- and **d)** 28-week-old female mice. Results represent the mean ± SEM of

10-15 mice per group. **e)** Representative histological sections of liver and kidney from 16-week-old female mice. Organs from at least 3 animals were analyzed per treatment group. Scale bar = 200 µm.

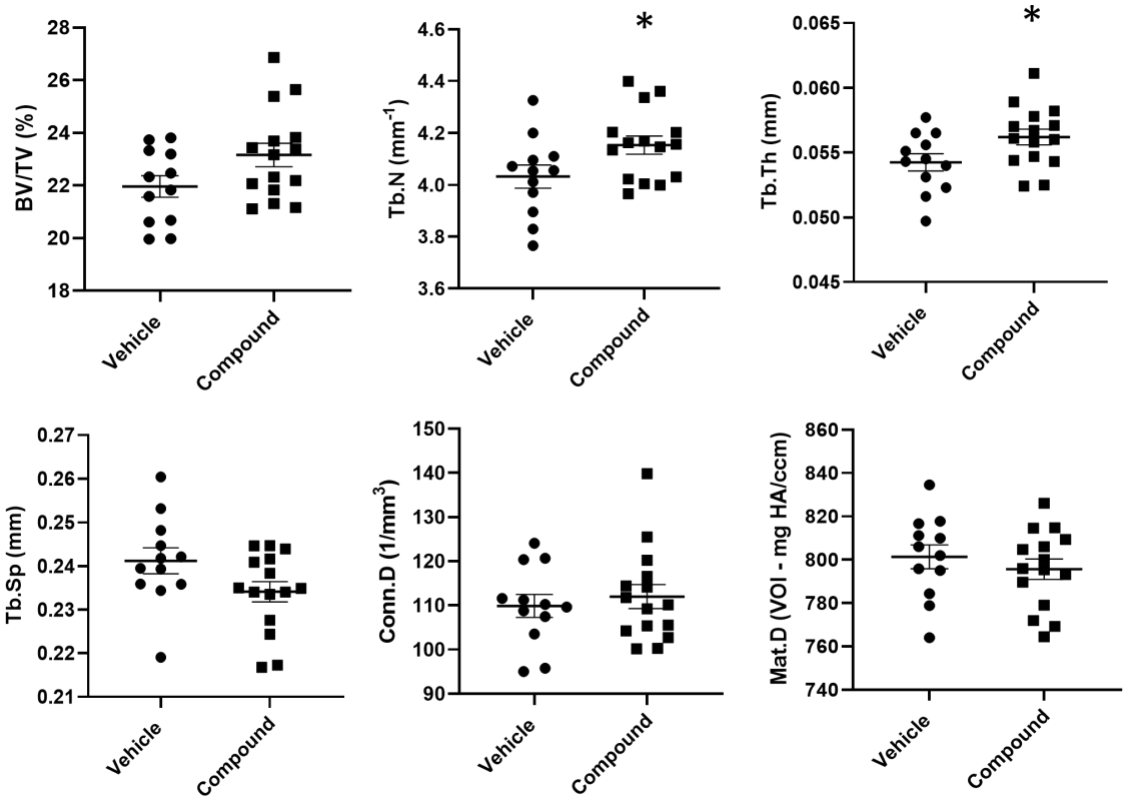

Figure 37. Compound 6641 increases bone formation in vertebrae of young female mice. Trabecular micro-ct parameters in lumbar vertebrae of 8-week-old female mice treated orally with vehicle or 10 mg/kg of compound 6641 for 8 weeks. 12 and 15 mice were used in the vehicle and compound groups respectively. Results are expressed as the mean ± SEM. *p<0.05 vs. vehicle using Student's t-test.

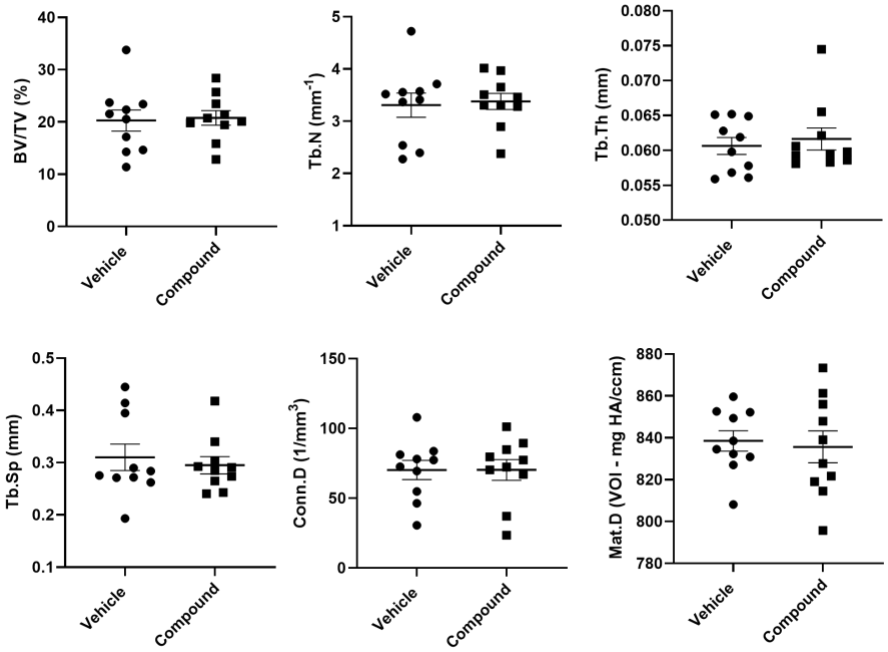

Figure 38. Compound 6641 does not increase bone formation in vertebrae of adult female mice. Trabecular micro-ct parameters in lumbar vertebrae of 20-week-old female mice treated orally with vehicle or 10 mg/kg of compound 6641 for 8 weeks. Results represent the mean ± SEM of 10 mice per group.

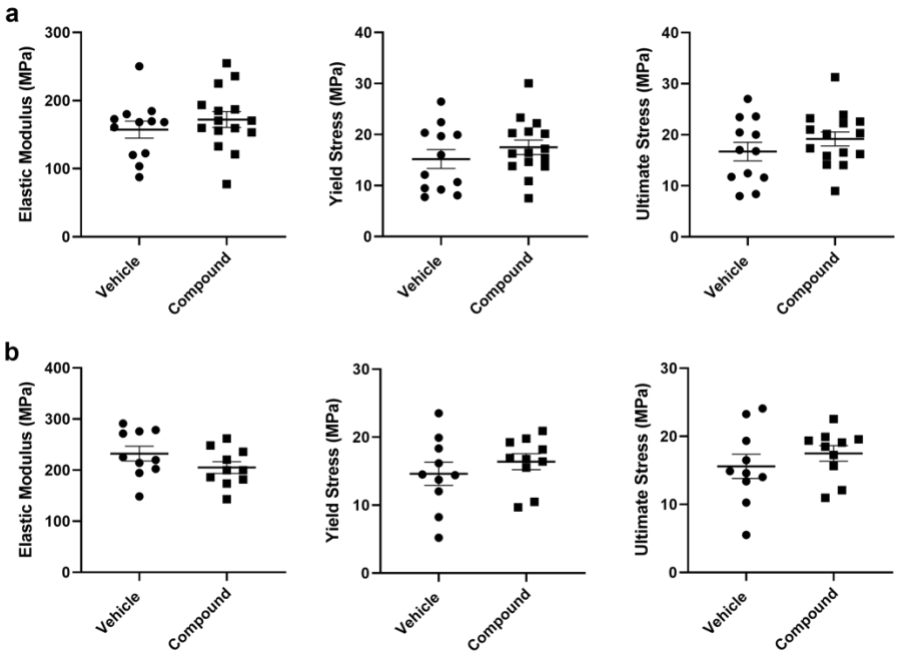

Figure 39. Compound 6641 does not change vertebrae strength in female mice. Biomechanical material properties in lumbar vertebrae of **a)** 8-week-old female mice and **b)** 20-week-old female mice treated orally with vehicle or 10 mg/kg of compound 6641 for 8 weeks. Results represent the mean ± SEM of 10-15 mice per group.

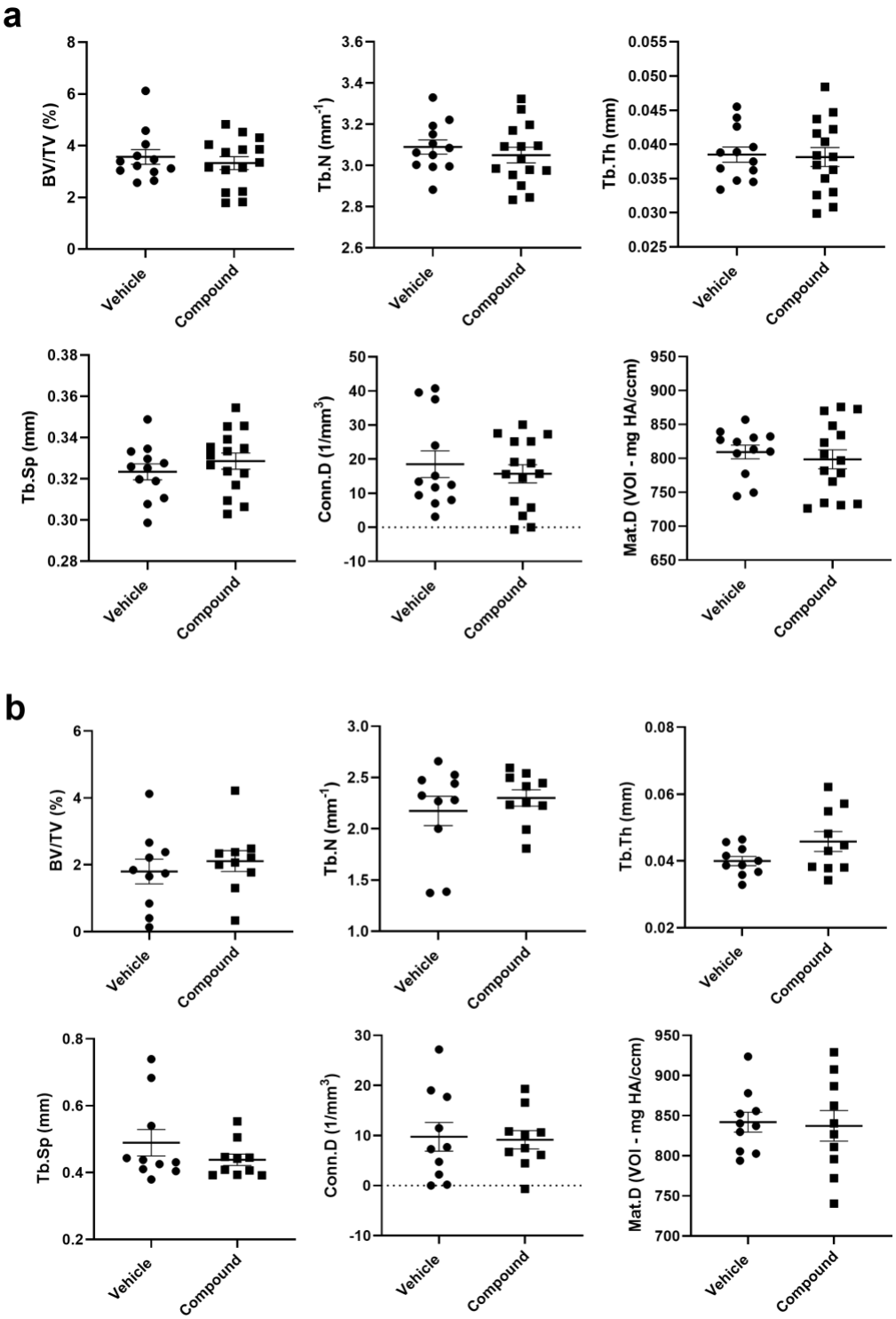

Figure 40. Compound 6641 does not increase bone formation in femur of female mice. Trabecular micro-ct parameters in femur of **a)** 8-week-old female mice and **b)** 20-week-old female mice treated orally with vehicle or 10 mg/kg of compound 6641 for 8 weeks. Results represent the mean ± SEM of 10-15 mice per group.

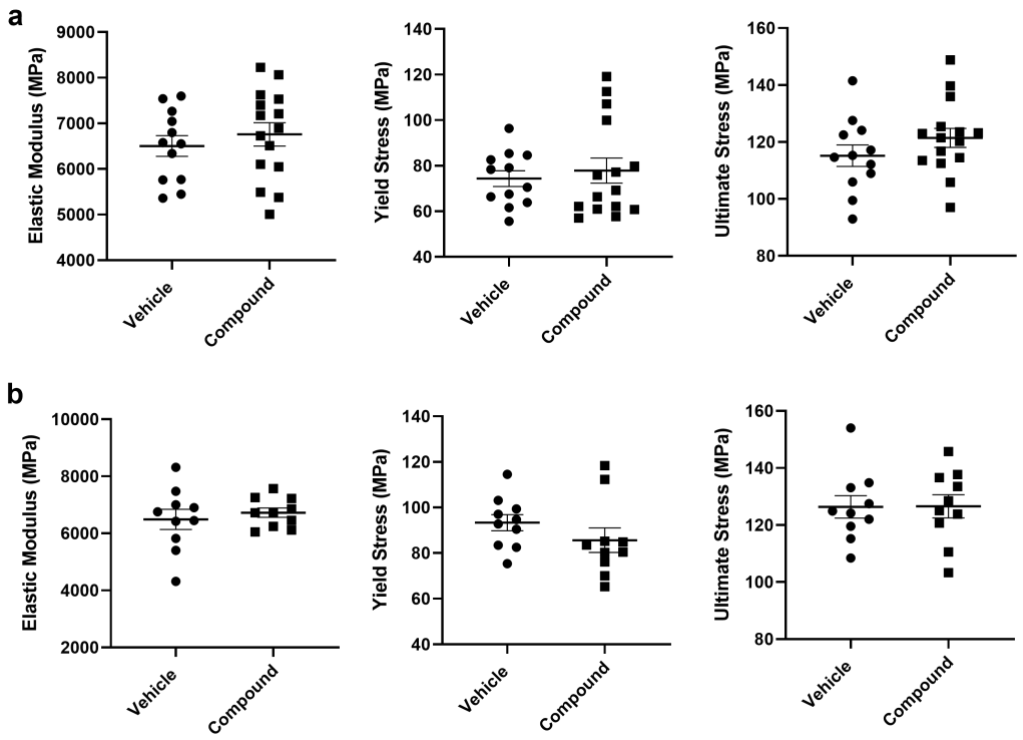

Figure 41. Compound 6641 does not change femur strength in female mice. Biomechanical material properties in femur of **a)** 8-week-old female mice and **b)** 20-week-old female mice treated orally with vehicle or 10 mg/kg of compound 6641 for 8 weeks. Results represent the mean ± SEM of 10-15 mice per group.

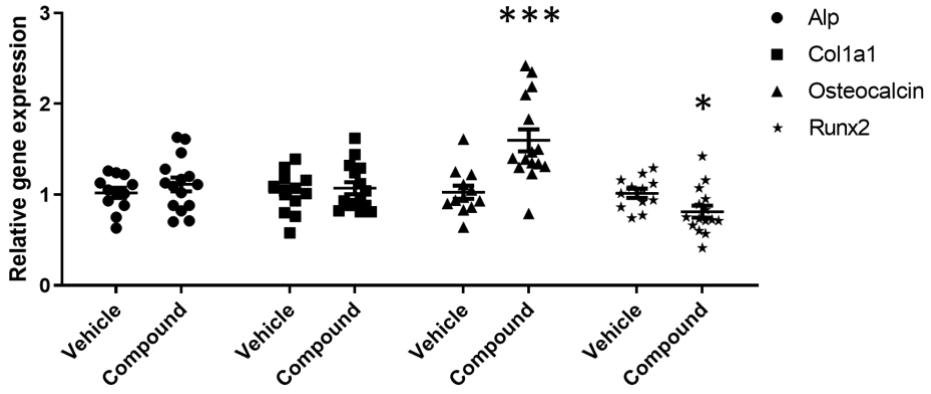

Figure 42. Compound 6641 induces osteoblasts maturation *in vivo*. Gene expression levels of osteoblast markers in tibias from 8-week-old female mice treated orally with vehicle or 10 mg/kg of compound 6641 for 8 weeks measured by quantitative RT-PCR and normalized to *Rpl13a* gene expression as an internal control. 12 and 15 mice were used in the vehicle and compound groups respectively. Results are expressed as the mean ± SEM. *p<0.05, ***p<0.001 vs. vehicle using Student's t-test.

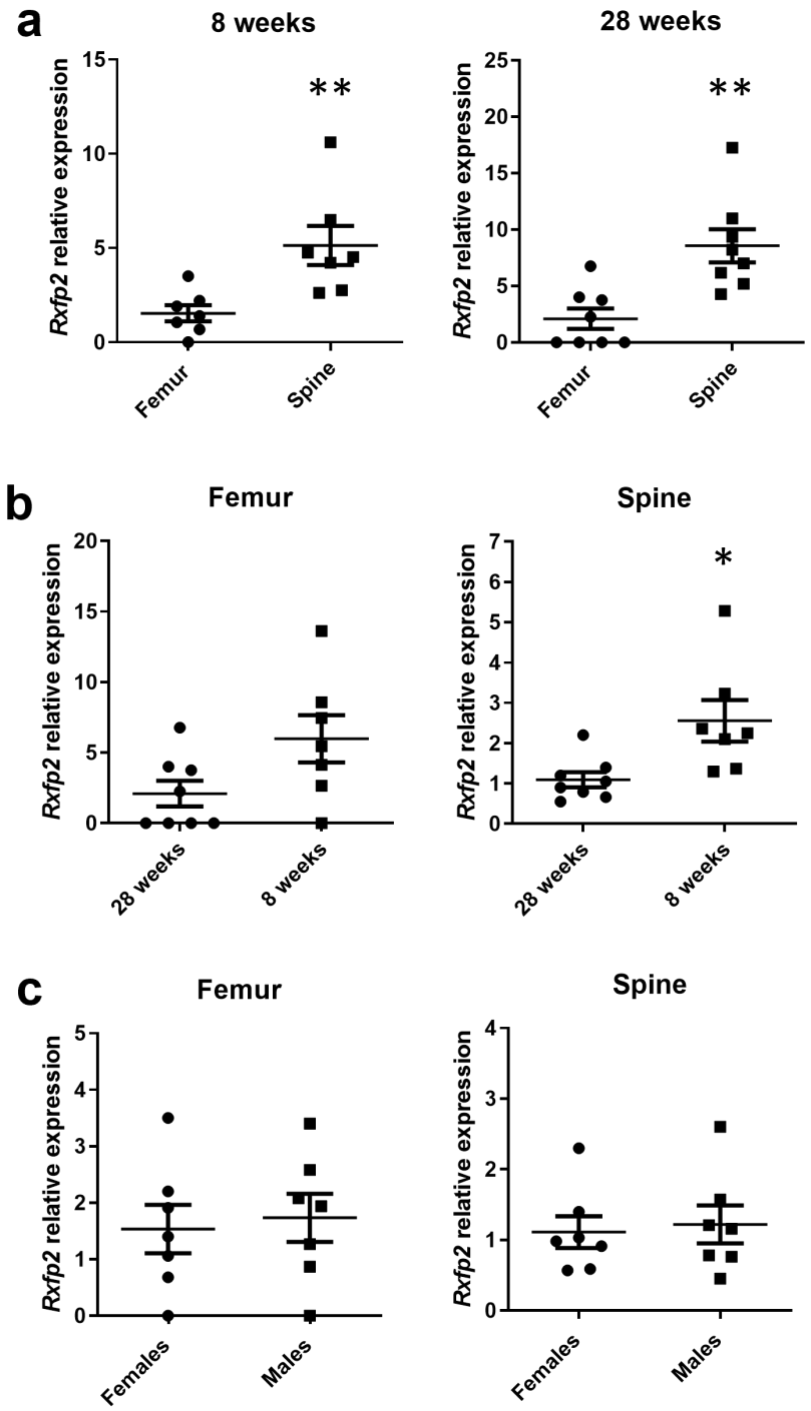

Figure 43. *Rxfp2 gene* expression in bones from young and adult mice. Gene expression levels of *Rxfp2* in femur and lumbar spine from 8- and 28-week-old female mice, as well as 8-week-old male mice, measured by quantitative RT-PCR and normalized to *Rpl13a* gene expression as an internal control. Results are expressed as the mean ± SEM of 7-8 mice per group. *p<0.05 vs. 28 weeks, **p<0.01 vs. femur using Student's t-test.

4.5 Discussion

In contrast to the species selectivity of RFXP1 observed with compound ML290 (136, 170), activation of the mouse RXFP2 receptor by agonist compounds was apparent both *in vitro* (Figure 28) and *in vivo* (Figure 31). Deletion of *Rxfp2* or *Insl3* in male mice causes cryptorchidism due to the failure of the gubernacular bulb to expand and anchor the testis to the low abdominal wall position at E17.5 (55, 57, 88). Deletion of *Ar* in male mice causes failure of the testis to descend from the abdominal wall into the final scrotal position due to post-natal inhibition of the gubernacular eversion process (190, 191). Moreover, overexpression of INSL3 in female mice induces the descent of the ovaries and development of inguinal hernias due to gubernaculum differentiation and eversion, showcasing the effect of RXFP2 signaling during both intrabdominal and inguinoscrotal phases of testis descent (98). Therefore, in normal male embryos, the androgen-independent gubernaculum differentiation leads to the initiation of the *processus vaginalis* or gubernaculum bulb eversion, which is not observed in female embryos due to the absence of INSL3 expression (183). Here we showed that the treatment of pregnant mice with RXFP2 small molecule agonists results in the initiation of the gubernacular eversion in female embryos. As this process is sex- and INSL3/RXFP2-dependent, the result strongly suggests that the compounds pass through the placental barrier to the embryos, resulting in RXFP2 activation and gubernacular bulb differentiation (Figure 31). The absence of changes in the gubernacular cord and ovary position are most likely due to low compound

exposure in comparison to INSL3 in male embryos or in female mice with transgenic overexpression of INSL3 (98).

Based on the high mineralization activity (Figure 10) and low toxicity (Figure 11) *in vitro* demonstrated in Chapter 2, compound 6641 was selected as the lead RXFP2 agonist for *in vivo* testing. Pharmacokinetic (Figure 30, 35) and cytotoxicity studies (Figure 36) *in vivo* suggested the safe use of compound 6641 as a pharmacological agent. Pharmacokinetic studies revealed significant bone exposure and bioavailability after oral gavage (Figure 30, 35). Micro-CT analysis of the lumbar spine of 8-week-old WT C57BL/6J female mice after an 8-week treatment administered orally 3 times a week demonstrated the ability of compound 6641 to improve trabecular bone parameters, especially Tb.N and Tb.Th (Figure 37), but no changes were found in femur trabecular bone (Figure 40a) or the biomechanical properties of either bone (Figure 39a, 41a). Similar results were observed in the trabecular bone of the lumbar spine of INSL3 transgenic female mice, although with a greater increase in BV/TV and striking difference in Conn.D and Mat.D (Figure 34a), which are consistent with the trabecular changes observed in the lumbar spine after treatment of WT C57BL/6J female mice with current PTH analogs prescribed for osteoporosis (192). In the transgenic model, constant INSL3 exposure since birth could account for these differences, which suggest that increasing the frequency of 6641 administration could significantly improve the overall trabecular bone mass. Quantitative RT-PCR analysis of tibias from INSL3 transgenic and 6641-treated mice also revealed that

there may be differences in the molecular mechanisms activated to trigger the increase in bone formation. As previously reported, INSL3 induces an increase in *Alp* in primary human osteoblasts (80) (Figure 34b) and 6641 induces an increase in *Osteocalcin* (Figure 42). A quantitative RT-PCR revealed a significantly higher *Rxfp2* gene expression in lumbar spine compared to femur of matching age WT C57BL/6J female mice (Figure 43a) which could explain the discrepancies observed between micro-CT results in vertebrae and femur. A significantly higher expression of *Rxfp2* was also found in spine of 8-week-old compared to 28-week-old WT C57BL/6J female mice (Figure 43b), which could explain why the RXFP2 agonist 6641 caused an increase in lumbar vertebrae trabecular bone formation parameters in young mice (Figure 37) but not in adult mice (Figure 38). Since *RXFP2* expression has been found in osteoblasts and osteocytes (63, 120), and these two bone cell types are known to decrease in number with age (193), this could explain the decrease in *Rxfp2* expression observed in aging mice. Further studies will need to stablish if this phenomenon were *RXFP2* expression in bone tissue decreases with age occurs in human patients with osteoporosis in order to find appropriate therapeutic dosage and treatment frequency.

In summary, this chapter demonstrated that the RXFP2 small molecule agonists activate the mouse RXFP2 receptor and induce gubernaculum invagination in female embryos. More importantly, this chapter proved that the compound 6641 has potential as an orally bioavailable anabolic drug to increase bone formation in female mice.

CHAPTER 5: FINAL DISCUSSION, CONCLUSIONS AND FUTURE DIRECTIONS

GPCRs are the largest family of membrane receptors and the target for 35% of all FDA-approved drugs (194). The focus of this thesis was to develop a first-in-class small molecule agonist of the RXFP2 receptor, a GPCR that has been recently shown to be important for maintaining an optimal bone density both in human and mouse. We hypothesized that such RXFP2 small molecule agonist could be a potential therapeutic candidate for the treatment of diseases associated with bone loss, primary osteoporosis. Small molecules have several advantages over the current monoclonal antibody and peptide-based osteoporosis medications. They are easy to synthesize and can be administered orally, which will substantially decrease the elevated price of the current osteoporosis treatments. However, to date, no small molecule drugs have been developed for treating osteoporosis.

A HTS of a small molecule library followed by an extensive SAR to improve the efficacies and potencies of the identified hits led to the final RXFP2 small molecule agonists described in this thesis, compounds 6641, 4337 and 4340. These compounds have been thoroughly characterized in terms of potency, efficacy, and specificity *in vitro*. While the EC_{50} for 6641 is 0.38 µM compared to 0.82 µM for 4337 and 0.14 µM for 4340, the E_{max} for 6641 is 106.99% of the maximum INSL3 response, being the highest when compared to 78.53% for 4337 and 53.14% for 4340. The specificity of compounds 6641, 4337 and 4340 for the human and

mouse RXFP2 receptor was proven by the inability to activate cAMP signaling through the human or mouse RXFP1 receptor. Moreover, an extensive GPCRsome study concluded that compounds 6641 and 4337 slightly activate β-arrestin recruitment in ADORA1 at μM concentrations, but they do not induce cAMP receptor activation. However, since ADORA1 is an important receptor regulating critical functions of the autonomic nervous system, we would like to follow up with a functional activity assay to determine if there is any additional stimulation of ADORA1 signaling by 6641 and 4337 through β-arrestin and GPCR kinases.

The extensive point mutagenesis study presented in Chapter 3 identified two allosteric residues (T506 and W651) for compound 6641 activation of the RXFP2 receptor, however these residues are conserved in RXFP1, which does not explain the compound selectivity for RXFP2. Since the compound 6641 is somewhat bulky compared to ML290 and other small molecule agonists, we believe that a better approach to find the exact residues of the binding pocket will be to use co-immunoprecipitation coupled with mass spectroscopy. This method will allow us to understand the big picture of the 6641-RXP2 interactions compared to the point mutagenesis study, and hopefully identify the critical non-conserved allosteric residues for the RXFP2 selectivity of compound 6641 over RXFP1.

Chapter 2 demonstrated the ability of compounds 6641, 4337 and 4340 to significantly enhance mineralization of the extracellular matrix in primary human

osteoblasts without notable toxicity. This was the first indication that the compounds have an anabolic effect in bone and that they are successfully targeting osteoblasts. Out of the three compounds, 6641 showed the highest mineralization activity (340%) compared to 4337 (320.31%) and 4340 (261.08%) at 5 µM. Moreover, at the concentration of 3 µM, significant mineralization was found for 6641 (240.15%), but not for 4337 (173.98%) or 4340 (98.5%). In order to identify the signaling pathways and molecular mechanisms activated by compound 6641 leading to the osteoblast mineralization, we performed a whole genome transcriptome RNAseq analysis in primary human osteoblasts. The highlight of this study was a significant up-regulation of interferon-α, β and γ stimulated genes and the interferon JAK-STAT signaling pathway. Interferon-β and γ have been shown to inhibit two essential mediators of the RANKL signaling pathway (c-Fos and TRAF6 respectively) necessary for osteoclast differentiation (195, 196). During the activation of the Interferon-β signaling pathway, STAT1 and STAT2 proteins in combination with IRF9 form the heterotrimeric complex ISGF3. Once in the nucleus, ISGF3 promotes the expression of interferon-inducible genes that will inhibit the expression of c-Fos, and therefore, its binding to DNA and induction of osteoclast differentiation genes. Activation of Interferon-γ signaling in osteoclasts causes dimerization of the STAT1 protein to form the transcriptional regulator GAF that induces expression of genes involved in activating the ubiquitin-proteasome system to degrade the RANK adapter protein TRAF6 (195). While it appears to be a consensus on the inhibitory effect of interferon signaling in osteoclasts, it has a dual inhibitory and stimulatory function in osteoblasts as discussed in Chapter 2.

We are particularly interested in the interferon-induced gene *ISG15*, which was found significantly upregulated by compound 6641 in primary human osteoblasts. ISG15 encodes for a ubiquitin-like modifier protein that has the ability to conjugate target proteins in a process called ISGylation. A study of Wnt signaling in mouse osteoblast identified the serpentine receptor Frizzled-9 as a novel positive regulator of osteoblast function through the non-canonical Wnt signaling pathway (152). The authors found that *Fzd9* deficient mice (*Fzd9*$^{-/-}$) develop osteoporosis due to an impairment of osteoblast mineralization activity leading to a significantly decreased bone formation rate. A comparative GeneChip hybridization analysis of primary osteoblasts from WT and *Fzd9*$^{-/-}$ mice found no changes in well-established osteoblast differentiation markers such as *Col1a1*, *Alp*, *Runx2* or *Osteocalcin*. However, they noticed a significant decrease in expression of interferon-regulated genes in *Fzd9*$^{-/-}$ osteoblasts, including some that we also identified as being up-regulated by compound 6641 in the RNAseq study presented in Chapter 2 (*Ifit1*, *Ifi44*, *Isg15* and *Stat1*). Moreover, the ISGylation of specific proteins in *Fzd9*$^{-/-}$ osteoblasts was found significantly decreased compared to WT osteoblasts and the increase of *Isg15* expression in *Fzd9*$^{-/-}$ osteoblasts was able to restore their mineralization activity, suggesting that *Isg15* is a downstream target of *Fzd9*. *Isg15* deficient mice (*Isg15*$^{-/-}$) also develop osteoporosis and *Isg15*$^{-/-}$ osteoblasts have reduced mineralization activity as seen in *Fzd9*$^{-/-}$ osteoblasts, further proving *Isg15* role as a positive regulator of bone formation (152). We hypothesize that ISG15 could be a downstream target of RXFP2 driving the bone anabolic activity induced by compound 6641. INSL3

induces ERK1/2 phosphorylation in osteoblasts (80) and *Fzd9*$^{-/-}$ osteoblasts show reduced levels of ERK1/2 phosphorylation (152). Some studies have described that ERK1/2 activation induces phosphorylation of STAT1 (197, 198). We hypothesize that 6641 could activate the ERK1/2 phosphorylation via the AC/cAMP/PKA pathway and further induce the phosphorylation of STAT1 and STAT2 to form the ISGF3 complex for the transcriptional activation of ISG15 (Figure 44). Additional studies will need to validate this hypothesis and stablish the connection between RXFP2 and the interferon signaling pathways in osteoblasts. Since osteoblasts are cells that migrate from the bone marrow mesenchymal niche during differentiation and became incorporated into the bone matrix as they mature to become osteocytes, a better approach to preserve their functionality and cell-cell interactions *in vitro* could be to develop spheroid three-dimensional (3D) cultures using primary human or mouse osteoblasts and perform proteomics analysis after treatment with compound 6641.

The *in vivo* bone anabolic effect of compound 6641 was demonstrated in 8-week-old WT C57BL/6J female mice treated orally 3 times per week for a total of 8 weeks at a concentration of 10 mg/kg. The increase in the BV/TV of the lumbar vertebral body from these mice treated with compound 6641 was 6%, while this same parameter in the 22-week-old INSL3 transgenic female mice was a 14% increase. A recently published study using 16-week-old WT C57BL/6J female mice treated with the PTH analog Teriparatide administer subcutaneously 5 times per week for total of 3 weeks at a concentration of 0.1 mg/kg revealed that the increase in BV/TV

of the lumbar vertebral body from these mice was 18% (192). These comparisons highlight that the INSL3 exposure since birth in the transgenic mice and the PTH analog treatment are similarly effective in boosting bone mass, and that increasing the dosage and frequency of compound 6641 could considerably increase bone mass to the levels observed with the PTH analog treatment. Compound 6641 inability to increase bone formation in 20-week-old WT C57BL/6J female mice, probably due to the decrease of RXFP2 expression observed in bone with age, also suggests that increasing the treatment duration and dosage will be necessary to see and effect in older mice. Future studies will investigate if administering compound 6641 continuously after weaning will improve the gain in bone mass. One approach for such strategy would be to incorporate compound 6641 in the mouse chow to deliver compound at a concentration of 30 mg/kg per day. In experiments described in Chapter 4 the compound was found safe in a preliminary pharmacokinetics study. 21-day-old WT C57BL/6J female and male mice will be treated for a total of 12 weeks to study bone formation and strength by micro-CT and biomechanical analysis respectively. These mice will be also IP injected with two fluorescent vital dyes that bind calcium to perform a histomorphometry study of the dynamic parameters of bone formation. Based on their age, mice will be injected with 30 mg/kg of alizarin-3-methyliminodiacetic acid 7 days before sacrifice and 30 mg/kg of calcein 2 days before sacrifice. This analysis will provide data on the mineral apposition and bone formation rates as well as osteocyte, osteoclast, and osteoblast surfaces which ultimately will help us identify if compound 6641 is also affecting the bone resorption process. Toxicity in these

mice will be meticulously examine by measuring serum markers indicative of liver and kidney toxicity at the end of the treatment as previously published (130). Since ADORA1 receptor is highly expressed in the brain and it was found as a potential off-target, this experiment will be a good opportunity to study if compound 6641 is crossing the blood-brain-barrier and accumulating in the brain. The brain from all mice will be collected at necropsy and analyzed by LC-MS/MS for the presence of compound 6641.

Although WT C57BL/6J mice start losing bone mass naturally after they are 8-week-old, this process is not driven by the decrease in estrogen levels that triggers postmenopausal osteoporosis. To study the anabolic effects of compound 6641 in osteoporosis, additional pre-clinical disease models are needed. There are several induced and genetic mouse models of postmenopausal osteoporosis available, but the most commonly use is the ovariectomy model that eliminates the source of ovarian derived estrogen. 4-week-old WT C57BL/6J female mice will be ovariectomize. Significant bone loss is seen in the lumbar vertebral body between 4- and 8-week post-surgery (199-201). After that period, the 6641 treatment will be administered orally at a concentration of 30 mg/kg every day for a total of 12 to 16 weeks and changes in bone formation and strength assessed by micro-CT and biomechanical analysis respectively. An alternative method to ovariectomy is the pharmaceutical intervention by administration of gonadotropin releasing hormone agonist, estrogen receptor antagonist, aromatase inhibitors or glucocorticoids (202). However, this method is not recommended for testing of new drug

candidates as it sometimes results in an incomplete osteoporosis phenotype and the systemic administration of multiple drugs could add additional variables which may lead to undesired cross-reactivity or toxicity.

We hypothesize that based on the increase in vertebrae trabecular bone observed with 6641 in 8-week-old WT C57BL/6J female mice, this compound could be used also in combination therapy with current first-line antiresorptive medication. The dual effect of both treatments (activation of bone formation and inhibition of bone resorption) could result in more bone gain, and potentially decrease the dosage of antiresorptive medication reducing side effects. During the early stages of osteoporosis, there is a high incidence in vertebral fractures due to a decrease in trabecular bone mass (14, 15). Hence, we believe that compound 6641 will be effective as an early osteoporosis medication, or even as a prophylactic therapy to preserve vertebral bone mass.

Osteogenesis imperfecta, also known as brittle bone disease, is a genetic disorder characterized by soft and occasionally malformed bones that fracture easily. The estimated incidence of osteogenesis imperfecta is about 1 in 20,000 births, and most cases are associated with mutations in the two genes encoding for type I collagen, *COL1A1* and *COL1A2* (203, 204). There are various types of the disease based on the genetic inheritance and degree of severity, however approximately 50% of all affected children present with Type I osteogenesis imperfecta, which is a mild form of the disease showing bone fragility and minimal deformities (205).

There is no existing cure for osteogenesis imperfecta, and the treatments available are primarily osteoporosis medication to increase bone density and prevent fractures (204). Consequently, we believe that our compound 6641 could be a new therapy for osteogenesis imperfecta as well. The *Col1a2*$^{G610C/+}$ knock-in mouse with a glycine substitution in COL1A2 presents a mild to moderate model of osteogenesis imperfecta (Type I and IV) that was discovered in the Old Order Amish of Lancaster County in Pennsylvania. 10-week-old male and female *Col1a2*$^{G610C/+}$ mice exhibit significantly reduced bone mass and defective bone mechanical properties (brittle phenotype), providing a useful model for testing the effect of compound in 6641 osteogenesis imperfecta (206).

In conclusion, the studies provided in this thesis have identified and characterized the first-in-class RXFP2 small molecule agonist, the allosteric compound 6641, demonstrating its potential as an orally bioavailable drug candidate to treat diseases associated with bone loss. This study also provided new insights into the RXFP2 signaling pathway in osteoblasts and the different binding mechanism for INSL3 and 6641 to induce receptor activation, which will be of great interest for future therapeutic applications targeting RXFP2 signaling.

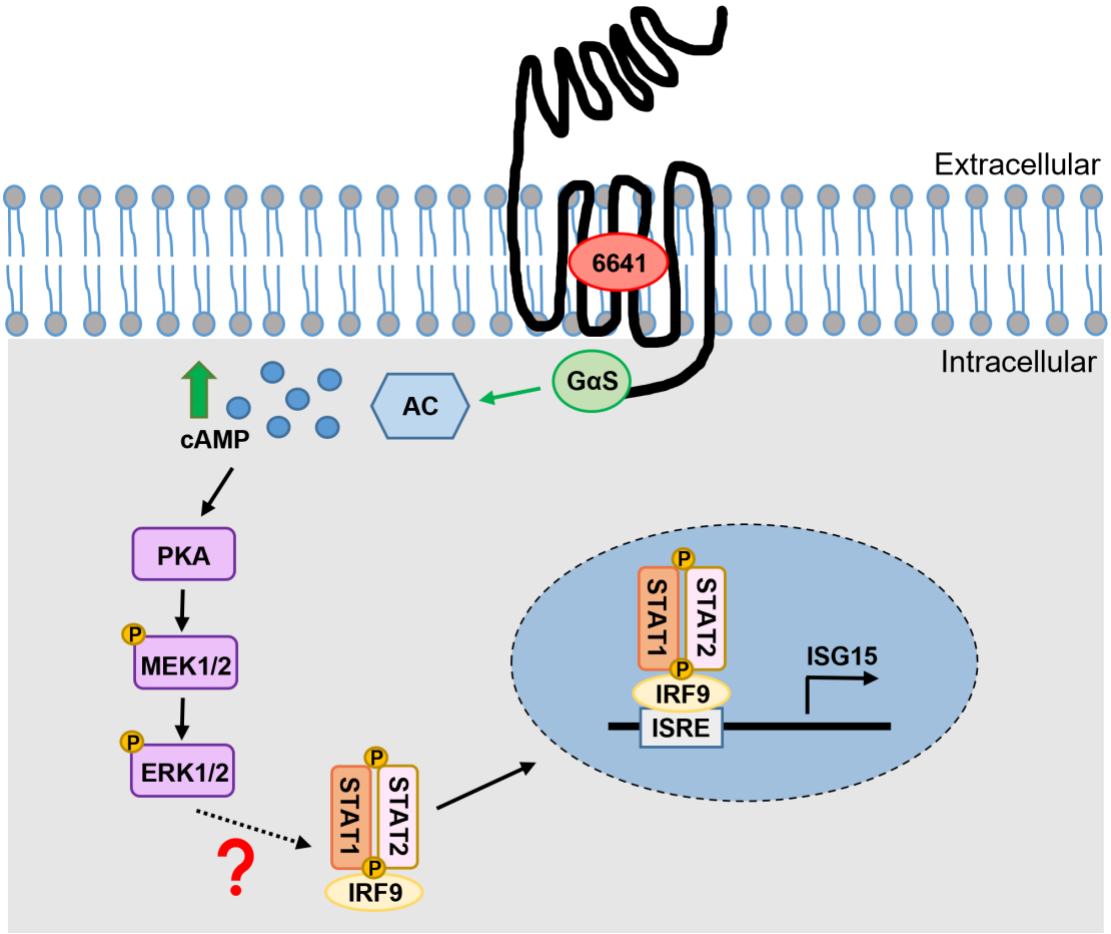

Figure 44. Proposed 6641-RXFP2 signaling pathway in osteoblasts. Compound 6641 activates the RXFP2 receptor causing coupling to the Gαs subunit, which activates adenylyl cyclase and increases cAMP levels, further activating PKA and phosphorylation of MEK1/2 and ERK1/2. Activated ERK1/2 may lead to the phosphorylation of STAT1 and STAT2, which couple to IRF9 to form the ISGF3 complex. Consecutively, the ISGF3 complex binds the ISRE motif in the nucleus and induces the expression of ISG15, as well as STAT1, STAT2 and IRF9 which may result in enhanced signal transduction.

REFERENCES

1. Wright, N. C., Looker, A. C., Saag, K. G., Curtis, J. R., Delzell, E. S., Randall, S., and Dawson-Hughes, B. (2014) The recent prevalence of osteoporosis and low bone mass in the United States based on bone mineral density at the femoral neck or lumbar spine. *Journal of bone and mineral research : the official journal of the American Society for Bone and Mineral Research* **29**, 2520-2526

2. Eastell, R., O'Neill, T. W., Hofbauer, L. C., Langdahl, B., Reid, I. R., Gold, D. T., and Cummings, S. R. (2016) Postmenopausal osteoporosis. *Nature reviews. Disease primers* **2**, 16069

3. Klotzbuecher, C. M., Ross, P. D., Landsman, P. B., Abbott, T. A., 3rd, and Berger, M. (2000) Patients with prior fractures have an increased risk of future fractures: a summary of the literature and statistical synthesis. *J Bone Miner Res* **15**, 721-739

4. Sahota, O. (2000) Osteoporosis and the role of vitamin D and calcium-vitamin D deficiency, vitamin D insufficiency and vitamin D sufficiency. *Age Ageing* **29**, 301-304

5. Castrogiovanni, P., Trovato, F. M., Szychlinska, M. A., Nsir, H., Imbesi, R., and Musumeci, G. (2016) The importance of physical activity in osteoporosis. From the molecular pathways to the clinical evidence. *Histology and histopathology* **31**, 1183-1194

6. Adami, G., and Saag, K. G. (2019) Glucocorticoid-induced osteoporosis: 2019 concise clinical review. *Osteoporosis international : a journal established as result of cooperation between the European Foundation for Osteoporosis and the National Osteoporosis Foundation of the USA*

7. Stehman-Breen, C. (2004) Osteoporosis and chronic kidney disease. *Seminars in nephrology* **24**, 78-81

8. Marquette, M., and Haworth, C. S. (2016) Bone health and disease in cystic fibrosis. *Paediatric respiratory reviews* **20 Suppl**, 2-5

9. DeShields, S. C., and Cunningham, T. D. (2018) Comparison of osteoporosis in US adults with type 1 and type 2 diabetes mellitus. *Journal of endocrinological investigation* **41**, 1051-1060

10. Ganji, R., Moghbeli, M., Sadeghi, R., Bayat, G., and Ganji, A. (2019) Prevalence of osteoporosis and osteopenia in men and premenopausal women with celiac disease: a systematic review. *Nutrition journal* **18**, 9

11. Ott, S. M. (2018) Cortical or Trabecular Bone: What's the Difference? *Am J Nephrol* **47**, 373-375

12. Manolagas, S. C., O'Brien, C. A., and Almeida, M. (2013) The role of estrogen and androgen receptors in bone health and disease. *Nat Rev Endocrinol* **9**, 699-712

13. Clowes, J. A., Riggs, B. L., and Khosla, S. (2005) The role of the immune system in the pathophysiology of osteoporosis. *Immunol Rev* **208**, 207-227

14. Felsenberg, D., Silman, A. J., Lunt, M., Armbrecht, G., Ismail, A. A., Finn, J. D., Cockerill, W. C., Banzer, D., Benevolenskaya, L. I., Bhalla, A., Bruges Armas, J., Cannata, J. B., Cooper, C., Dequeker, J., Eastell, R., Felsch, B., Gowin, W., Havelka, S., Hoszowski, K., Jajic, I., Janott, J., Johnell, O., Kanis, J. A., Kragl, G., Lopes Vaz, A., Lorenc, R., Lyritis, G., Masaryk, P., Matthis, C., Miazgowski, T., Parisi, G., Pols, H. A., Poor, G., Raspe, H. H., Reid, D. M., Reisinger, W., Schedit-Nave, C., Stepan, J. J., Todd, C. J., Weber, K., Woolf, A. D., Yershova, O. B., Reeve, J., and O'Neill, T. W. (2002) Incidence of vertebral fracture in europe: results from the European Prospective Osteoporosis Study (EPOS). *J Bone Miner Res* **17**, 716-724

15. Curtis, E. M., van der Velde, R., Moon, R. J., van den Bergh, J. P., Geusens, P., de Vries, F., van Staa, T. P., Cooper, C., and Harvey, N. C. (2016) Epidemiology of fractures in the United Kingdom 1988-2012: Variation with age, sex, geography, ethnicity and socioeconomic status. *Bone* **87**, 19-26

16. Singer, A., Exuzides, A., Spangler, L., O'Malley, C., Colby, C., Johnston, K., Agodoa, I., Baker, J., and Kagan, R. (2015) Burden of illness for osteoporotic fractures compared with other serious diseases among postmenopausal women in the United States. *Mayo Clin Proc* **90**, 53-62

17. National Osteoporosis Foundation (NOF). Annual Report 2017. https://cdn.nof.org/wp-content/uploads/2017_NOF_Annual_report_v6_final.pdf.

18. Lewiecki, E. M., Ortendahl, J. D., Vanderpuye-Orgle, J., Grauer, A., Arellano, J., Lemay, J., Harmon, A. L., Broder, M. S., and Singer, A. J. (2019) Healthcare Policy Changes in Osteoporosis Can Improve Outcomes and Reduce Costs in the United States. *JBMR Plus* **3**, e10192

19. Ensrud, K. E., Black, D. M., Palermo, L., Bauer, D. C., Barrett-Connor, E., Quandt, S. A., Thompson, D. E., and Karpf, D. B. (1997) Treatment with alendronate prevents fractures in women at highest risk: results from the Fracture Intervention Trial. *Arch Intern Med* **157**, 2617-2624

20. de Vernejoul, M. C. (1989) Bone remodelling in osteoporosis. *Clinical rheumatology* **8 Suppl 2**, 13-15

21. Sözen, T., Özışık, L., and Başaran, N. (2017) An overview and management of osteoporosis. *European journal of rheumatology* **4**, 46-56

22. Amarasekara, D. S., Kim, S., and Rho, J. (2021) Regulation of Osteoblast Differentiation by Cytokine Networks. *International journal of molecular sciences* **22**

23. Renn, J., and Winkler, C. (2009) Osterix-mCherry transgenic medaka for in vivo imaging of bone formation. *Dev Dyn* **238**, 241-248

24. Stein, G. S., and Lian, J. B. (1993) Molecular mechanisms mediating proliferation/differentiation interrelationships during progressive development of the osteoblast phenotype. *Endocr Rev* **14**, 424-442

25. Dallas, S. L., Prideaux, M., and Bonewald, L. F. (2013) The osteocyte: an endocrine cell ... and more. *Endocrine reviews* **34**, 658-690

26. Feng, X., and Teitelbaum, S. L. (2013) Osteoclasts: New Insights. *Bone research* **1**, 11-26

27. Boyce, B. F., and Xing, L. (2008) Functions of RANKL/RANK/OPG in bone modeling and remodeling. *Archives of biochemistry and biophysics* **473**, 139-146

28. Drake, M. T., Clarke, B. L., and Khosla, S. (2008) Bisphosphonates: mechanism of action and role in clinical practice. *Mayo Clin Proc* **83**, 1032-1045

29. Russell, R. G., Watts, N. B., Ebetino, F. H., and Rogers, M. J. (2008) Mechanisms of action of bisphosphonates: similarities and differences and their potential influence on clinical efficacy. *Osteoporosis international : a journal established as result of cooperation between the European Foundation for Osteoporosis and the National Osteoporosis Foundation of the USA* **19**, 733-759

30. Hanley, D. A., Adachi, J. D., Bell, A., and Brown, V. (2012) Denosumab: mechanism of action and clinical outcomes. *International journal of clinical practice* **66**, 1139-1146

31. Heng, C., Badner, V. M., Vakkas, T. G., Johnson, R., and Yeo, Y. (2012) Bisphosphonate-related osteonecrosis of the jaw in patients with osteoporosis. *American family physician* **85**, 1134-1141

32. Ma, S., Goh, E. L., Jin, A., Bhattacharya, R., Boughton, O. R., Patel, B., Karunaratne, A., Vo, N. T., Atwood, R., Cobb, J. P., Hansen, U., and Abel, R. L. (2017) Long-term effects of bisphosphonate therapy: perforations, microcracks and mechanical properties. *Scientific reports* **7**, 43399

33. Papapoulos, S., Lippuner, K., Roux, C., Lin, C. J., Kendler, D. L., Lewiecki, E. M., Brandi, M. L., Czerwiński, E., Franek, E., Lakatos, P., Mautalen, C., Minisola, S., Reginster, J. Y., Jensen, S., Daizadeh, N. S., Wang, A., Gavin, M., Libanati, C., Wagman, R. B., and Bone, H. G. (2015) The effect of 8 or 5 years of denosumab treatment in postmenopausal women with osteoporosis: results from the FREEDOM Extension study. *Osteoporosis international : a journal established as result of cooperation between the European Foundation for Osteoporosis and the National Osteoporosis Foundation of the USA* **26**, 2773-2783

34. Chomsky-Higgins, K. H., Rochefort, H. M., Seib, C. D., Gosnell, J. E., Shen, W. T., Duh, Q.-Y., and Suh, I. (2018) Recombinant Parathyroid Hormone Versus Usual Care: Do the Outcomes Justify the Cost? *World journal of surgery* **42**, 431-436

35. Eastell, R., and Walsh, J. S. (2017) Anabolic treatment for osteoporosis: teriparatide. *Clinical cases in mineral and bone metabolism : the official journal of the Italian Society of Osteoporosis, Mineral Metabolism, and Skeletal Diseases* **14**, 173-178

36. Dobnig, H., and Turner, R. T. (1995) Evidence that intermittent treatment with parathyroid hormone increases bone formation in adult rats by activation of bone lining cells. *Endocrinology* **136**, 3632-3638

37. Jilka, R. L., Weinstein, R. S., Bellido, T., Roberson, P., Parfitt, A. M., and Manolagas, S. C. (1999) Increased bone formation by prevention of osteoblast apoptosis with parathyroid hormone. *J Clin Invest* **104**, 439-446

38. Scott, D. K., Brakenhoff, K. D., Clohisy, J. C., Quinn, C. O., and Partridge, N. C. (1992) Parathyroid hormone induces transcription of collagenase in rat osteoblastic cells by a mechanism using cyclic adenosine 3',5'-monophosphate and requiring protein synthesis. *Mol Endocrinol* **6**, 2153-2159

39. Slusarski, D. C., Corces, V. G., and Moon, R. T. (1997) Interaction of Wnt and a Frizzled homologue triggers G-protein-linked phosphatidylinositol signalling. *Nature* **390**, 410-413

40. Uusitalo, M., Heikkilä, M., and Vainio, S. (1999) Molecular genetic studies of Wnt signaling in the mouse. *Exp Cell Res* **253**, 336-348

41. Baron, R., and Kneissel, M. (2013) WNT signaling in bone homeostasis and disease: from human mutations to treatments. *Nature Medicine* **19**, 179-192

42. Padhi, D., Allison, M., Kivitz, A. J., Gutierrez, M. J., Stouch, B., Wang, C., and Jang, G. (2014) Multiple doses of sclerostin antibody romosozumab in healthy men and postmenopausal women with low bone mass: a

randomized, double-blind, placebo-controlled study. *Journal of clinical pharmacology* **54**, 168-178

43. McClung, M. R., Grauer, A., Boonen, S., Bolognese, M. A., Brown, J. P., Diez-Perez, A., Langdahl, B. L., Reginster, J.-Y., Zanchetta, J. R., Wasserman, S. M., Katz, L., Maddox, J., Yang, Y.-C., Libanati, C., and Bone, H. G. (2014) Romosozumab in Postmenopausal Women with Low Bone Mineral Density. *New England Journal of Medicine* **370**, 412-420

44. Poole, K. E., van Bezooijen, R. L., Loveridge, N., Hamersma, H., Papapoulos, S. E., Löwik, C. W., and Reeve, J. (2005) Sclerostin is a delayed secreted product of osteocytes that inhibits bone formation. *Faseb j* **19**, 1842-1844

45. van Bezooijen, R. L., Svensson, J. P., Eefting, D., Visser, A., van der Horst, G., Karperien, M., Quax, P. H., Vrieling, H., Papapoulos, S. E., ten Dijke, P., and Löwik, C. W. (2007) Wnt but not BMP signaling is involved in the inhibitory action of sclerostin on BMP-stimulated bone formation. *J Bone Miner Res* **22**, 19-28

46. Wijenayaka, A. R., Kogawa, M., Lim, H. P., Bonewald, L. F., Findlay, D. M., and Atkins, G. J. (2011) Sclerostin stimulates osteocyte support of osteoclast activity by a RANKL-dependent pathway. *PLoS One* **6**, e25900

47. Paik, J., and Scott, L. J. (2020) Romosozumab: A Review in Postmenopausal Osteoporosis. *Drugs & Aging* **37**, 845-855

48. Lv, F., Cai, X., Yang, W., Gao, L., Chen, L., Wu, J., and Ji, L. (2020) Denosumab or romosozumab therapy and risk of cardiovascular events in patients with primary osteoporosis: Systematic review and meta- analysis. *Bone* **130**, 115121

49. Halls, M. L., van der Westhuizen, E. T., Bathgate, R. A., and Summers, R. J. (2007) Relaxin family peptide receptors--former orphans reunite with their parent ligands to activate multiple signalling pathways. *Br J Pharmacol* **150**, 677-691

50. Kumagai, J., Hsu, S. Y., Matsumi, H., Roh, J. S., Fu, P., Wade, J. D., Bathgate, R. A., and Hsueh, A. J. (2002) INSL3/Leydig insulin-like peptide activates the LGR8 receptor important in testis descent. *The Journal of biological chemistry* **277**, 31283-31286

51. Rosengren, K. J., Zhang, S., Lin, F., Daly, N. L., Scott, D. J., Hughes, R. A., Bathgate, R. A., Craik, D. J., and Wade, J. D. (2006) Solution structure and characterization of the LGR8 receptor binding surface of insulin-like peptide 3. *The Journal of biological chemistry* **281**, 28287-28295

52. Lin, F., Otvos, L., Jr., Kumagai, J., Tregear, G. W., Bathgate, R. A., and Wade, J. D. (2004) Synthetic human insulin 4 does not activate the G-protein-coupled receptors LGR7 or LGR8. *Journal of peptide science : an official publication of the European Peptide Society* **10**, 257-264

53. Halls, M. L., Bond, C. P., Sudo, S., Kumagai, J., Ferraro, T., Layfield, S., Bathgate, R. A., and Summers, R. J. (2005) Multiple binding sites revealed by interaction of relaxin family peptides with native and chimeric relaxin family peptide receptors 1 and 2 (LGR7 and LGR8). *The Journal of pharmacology and experimental therapeutics* **313**, 677-687

54. Bathgate, R. A., Lin, F., Hanson, N. F., Otvos, L., Jr., Guidolin, A., Giannakis, C., Bastiras, S., Layfield, S. L., Ferraro, T., Ma, S., Zhao, C., Gundlach, A. L., Samuel, C. S., Tregear, G. W., and Wade, J. D. (2006) Relaxin-3: improved synthesis strategy and demonstration of its high-affinity interaction with the relaxin receptor LGR7 both in vitro and in vivo. *Biochemistry* **45**, 1043-1053

55. Nef, S., and Parada, L. F. (1999) Cryptorchidism in mice mutant for Insl3. *Nature genetics* **22**, 295-299

56. Zimmermann, S., Steding, G., Emmen, J. M., Brinkmann, A. O., Nayernia, K., Holstein, A. F., Engel, W., and Adham, I. M. (1999) Targeted disruption of the Insl3 gene causes bilateral cryptorchidism. *Molecular endocrinology (Baltimore, Md.)* **13**, 681-691

57. Overbeek, P. A., Gorlov, I. P., Sutherland, R. W., Houston, J. B., Harrison, W. R., Boettger-Tong, H. L., Bishop, C. E., and Agoulnik, A. I. (2001) A

transgenic insertion causing cryptorchidism in mice. *Genesis (New York, N.Y. : 2000)* **30**, 26-35

58. Kurz, D. (2016) Current Management of Undescended Testes. *Current treatment options in pediatrics* **2**, 43-51

59. Berkowitz, G. S., Lapinski, R. H., Dolgin, S. E., Gazella, J. G., Bodian, C. A., and Holzman, I. R. (1993) Prevalence and natural history of cryptorchidism. *Pediatrics* **92**, 44-49

60. WENZLER, D. L., BLOOM, D. A., and PARK, J. M. (2004) What is the Rate of Spontaneous Testicular Descent in Infants With Cryptorchidism? *Journal of Urology* **171**, 849-851

61. Ferguson, L., and Agoulnik, A. I. (2013) Testicular cancer and cryptorchidism. *Frontiers in endocrinology* **4**, 32

62. Pelusi, C., Fanelli, F., Pariali, M., Zanotti, L., Gambineri, A., and Pasquali, R. (2013) Parallel variations of insulin-like peptide 3 (INSL3) and antimullerian hormone (AMH) in women with the polycystic ovary syndrome according to menstrual cycle pattern. *The Journal of clinical endocrinology and metabolism* **98**, E1575-1582

63. Ferlin, A., Pepe, A., Gianesello, L., Garolla, A., Feng, S., Giannini, S., Zaccolo, M., Facciolli, A., Morello, R., Agoulnik, A. I., and Foresta, C. (2008) Mutations in the insulin-like factor 3 receptor are associated with osteoporosis. *J Bone Miner Res* **23**, 683-693

64. Bogatcheva, N. V., Ferlin, A., Feng, S., Truong, A., Gianesello, L., Foresta, C., and Agoulnik, A. I. (2007) T222P mutation of the insulin-like 3 hormone receptor LGR8 is associated with testicular maldescent and hinders receptor expression on the cell surface membrane. *American journal of physiology. Endocrinology and metabolism* **292**, E138-144

65. Scott, D. J., Layfield, S., Yan, Y., Sudo, S., Hsueh, A. J., Tregear, G. W., and Bathgate, R. A. (2006) Characterization of novel splice variants of LGR7 and LGR8 reveals that receptor signaling is mediated by their unique

low density lipoprotein class A modules. *The Journal of biological chemistry* **281**, 34942-34954

66. Bruell, S., Sethi, A., Smith, N., Scott, D. J., Hossain, M. A., Wu, Q. P., Guo, Z. Y., Petrie, E. J., Gooley, P. R., and Bathgate, R. A. D. (2017) Distinct activation modes of the Relaxin Family Peptide Receptor 2 in response to insulin-like peptide 3 and relaxin. *Scientific reports* **7**, 3294

67. Scott, D. J., Wilkinson, T. N., Zhang, S., Ferraro, T., Wade, J. D., Tregear, G. W., and Bathgate, R. A. (2007) Defining the LGR8 residues involved in binding insulin-like peptide 3. *Molecular endocrinology (Baltimore, Md.)* **21**, 1699-1712

68. Muda, M., He, C., Martini, P. G., Ferraro, T., Layfield, S., Taylor, D., Chevrier, C., Schweickhardt, R., Kelton, C., Ryan, P. L., and Bathgate, R. A. (2005) Splice variants of the relaxin and INSL3 receptors reveal unanticipated molecular complexity. *Molecular human reproduction* **11**, 591-600

69. Sudo, S., Kumagai, J., Nishi, S., Layfield, S., Ferraro, T., Bathgate, R. A., and Hsueh, A. J. (2003) H3 relaxin is a specific ligand for LGR7 and activates the receptor by interacting with both the ectodomain and the exoloop 2. *The Journal of biological chemistry* **278**, 7855-7862

70. Bullesbach, E. E., and Schwabe, C. (1999) Tryptophan B27 in the relaxin-like factor (RLF) is crucial for RLF receptor-binding. *Biochemistry* **38**, 3073-3078

71. Shabanpoor, F., Hughes, R. A., Zhang, S., Bathgate, R. A., Layfield, S., Hossain, M. A., Tregear, G. W., Separovic, F., and Wade, J. D. (2010) Effect of helix-promoting strategies on the biological activity of novel analogues of the B-chain of INSL3. *Amino acids* **38**, 121-131

72. Del Borgo, M. P., Hughes, R. A., Bathgate, R. A., Lin, F., Kawamura, K., and Wade, J. D. (2006) Analogs of insulin-like peptide 3 (INSL3) B-chain are LGR8 antagonists in vitro and in vivo. *The Journal of biological chemistry* **281**, 13068-13074

73. Shabanpoor, F., Bathgate, R. A., Hossain, M. A., Giannakis, E., Wade, J. D., and Hughes, R. A. (2007) Design, synthesis and pharmacological evaluation of cyclic mimetics of the insulin-like peptide 3 (INSL3) B-chain. *Journal of peptide science : an official publication of the European Peptide Society* **13**, 113-120

74. Halls, M. L., Bathgate, R. A., and Summers, R. J. (2007) Comparison of signaling pathways activated by the relaxin family peptide receptors, RXFP1 and RXFP2, using reporter genes. *The Journal of pharmacology and experimental therapeutics* **320**, 281-290

75. Halls, M. L., Bathgate, R. A., and Summers, R. J. (2006) Relaxin family peptide receptors RXFP1 and RXFP2 modulate cAMP signaling by distinct mechanisms. *Molecular pharmacology* **70**, 214-226

76. Halls, M. L., van der Westhuizen, E. T., Wade, J. D., Evans, B. A., Bathgate, R. A., and Summers, R. J. (2009) Relaxin family peptide receptor (RXFP1) coupling to G(alpha)i3 involves the C-terminal Arg752 and localization within membrane Raft Microdomains. *Molecular pharmacology* **75**, 415-428

77. Pathirana, I. N., Kawate, N., Büllesbach, E. E., Takahashi, M., Hatoya, S., Inaba, T., and Tamada, H. (2012) Insulin-like peptide 3 stimulates testosterone secretion in mouse Leydig cells via cAMP pathway. *Regulatory peptides* **178**, 102-106

78. Kawamura, K., Kumagai, J., Sudo, S., Chun, S. Y., Pisarska, M., Morita, H., Toppari, J., Fu, P., Wade, J. D., Bathgate, R. A., and Hsueh, A. J. (2004) Paracrine regulation of mammalian oocyte maturation and male germ cell survival. *Proceedings of the National Academy of Sciences of the United States of America* **101**, 7323-7328

79. Ferlin, A., De Toni, L., Agoulnik, A. I., Lunardon, G., Armani, A., Bortolanza, S., Blaauw, B., Sandri, M., and Foresta, C. (2018) Protective Role of Testicular Hormone INSL3 From Atrophy and Weakness in Skeletal Muscle. *Frontiers in endocrinology* **9**, 562

80. Ferlin, A., Perilli, L., Gianesello, L., Taglialavoro, G., and Foresta, C. (2011) Profiling insulin like factor 3 (INSL3) signaling in human osteoblasts. *PLoS One* **6**, e29733

81. Callander, G. E., Thomas, W. G., and Bathgate, R. A. (2009) Prolonged RXFP1 and RXFP2 signaling can be explained by poor internalization and a lack of beta-arrestin recruitment. *American journal of physiology. Cell physiology* **296**, C1058-1066

82. Johnson, K. J., Robbins, A. K., Wang, Y., McCahan, S. M., Chacko, J. K., and Barthold, J. S. (2010) Insulin-like 3 exposure of the fetal rat gubernaculum modulates expression of genes involved in neural pathways. *Biology of reproduction* **83**, 774-782

83. Balvers, M., Spiess, A. N., Domagalski, R., Hunt, N., Kilic, E., Mukhopadhyay, A. K., Hanks, E., Charlton, H. M., and Ivell, R. (1998) Relaxin-like factor expression as a marker of differentiation in the mouse testis and ovary. *Endocrinology* **139**, 2960-2970

84. Zarreh-Hoshyari-Khah, M. R., Einspanier, A., and Ivell, R. (1999) Differential splicing and expression of the relaxin-like factor gene in reproductive tissues of the marmoset monkey (Callithrix jacchus). *Biology of reproduction* **60**, 445-453

85. Ivell, R., Balvers, M., Domagalski, R., Ungefroren, H., Hunt, N., and Schulze, W. (1997) Relaxin-like factor: a highly specific and constitutive new marker for Leydig cells in the human testis. *Molecular human reproduction* **3**, 459-466

86. Pitia, A. M., Uchiyama, K., Sano, H., Kinukawa, M., Minato, Y., Sasada, H., and Kohsaka, T. (2017) Functional insulin-like factor 3 (INSL3) hormone-receptor system in the testes and spermatozoa of domestic ruminants and its potential as a predictor of sire fertility. *Anim Sci J* **88**, 678-690

87. Feng, S., Bogatcheva, N. V., Truong, A., Korchin, B., Bishop, C. E., Klonisch, T., Agoulnik, I. U., and Agoulnik, A. I. (2007) Developmental expression and gene regulation of insulin-like 3 receptor RXFP2 in mouse male reproductive organs. *Biology of reproduction* **77**, 671-680

88. Huang, Z., Rivas, B., and Agoulnik, A. I. (2012) Insulin-like 3 signaling is important for testicular descent but dispensable for spermatogenesis and germ cell survival in adult mice. *Biology of reproduction* **87**, 143

89. Ivell, R., Wade, J. D., and Anand-Ivell, R. (2013) INSL3 as a biomarker of Leydig cell functionality. *Biology of reproduction* **88**, 147

90. Bay, K., Cohen, A. S., Jorgensen, F. S., Jorgensen, C., Lind, A. M., Skakkebaek, N. E., and Andersson, A. M. (2008) Insulin-like factor 3 levels in second-trimester amniotic fluid. *The Journal of clinical endocrinology and metabolism* **93**, 4048-4051

91. Bay, K., Virtanen, H. E., Hartung, S., Ivell, R., Main, K. M., Skakkebaek, N. E., Andersson, A. M., and Toppari, J. (2007) Insulin-like factor 3 levels in cord blood and serum from children: effects of age, postnatal hypothalamic-pituitary-gonadal axis activation, and cryptorchidism. *The Journal of clinical endocrinology and metabolism* **92**, 4020-4027

92. Bay, K., Hartung, S., Ivell, R., Schumacher, M., Jürgensen, D., Jorgensen, N., Holm, M., Skakkebaek, N. E., and Andersson, A. M. (2005) Insulin-like factor 3 serum levels in 135 normal men and 85 men with testicular disorders: relationship to the luteinizing hormone-testosterone axis. *The Journal of clinical endocrinology and metabolism* **90**, 3410-3418

93. Ferlin, A., Garolla, A., Rigon, F., Rasi Caldogno, L., Lenzi, A., and Foresta, C. (2006) Changes in serum insulin-like factor 3 during normal male puberty. *The Journal of clinical endocrinology and metabolism* **91**, 3426-3431

94. Ferlin, A., and Foresta, C. (2005) Insulin-like factor 3: a novel circulating hormone of testicular origin in humans. *Annals of the New York Academy of Sciences* **1041**, 497-505

95. Bay, K., Matthiesson, K. L., McLachlan, R. I., and Andersson, A. M. (2006) The effects of gonadotropin suppression and selective replacement on insulin-like factor 3 secretion in normal adult men. *The Journal of clinical endocrinology and metabolism* **91**, 1108-1111

96. Sadeghian, H., Anand-Ivell, R., Balvers, M., Relan, V., and Ivell, R. (2005) Constitutive regulation of the Insl3 gene in rat Leydig cells. *Molecular and cellular endocrinology* **241**, 10-20

97. Yuan, F. P., Li, X., Lin, J., Schwabe, C., Bullesbach, E. E., Rao, C. V., and Lei, Z. M. (2010) The role of RXFP2 in mediating androgen-induced inguinoscrotal testis descent in LH receptor knockout mice. *Reproduction (Cambridge, England)* **139**, 759-769

98. Adham, I. M., Steding, G., Thamm, T., Bullesbach, E. E., Schwabe, C., Paprotta, I., and Engel, W. (2002) The overexpression of the insl3 in female mice causes descent of the ovaries. *Molecular endocrinology (Baltimore, Md.)* **16**, 244-252

99. Kaftanovskaya, E. M., Feng, S., Huang, Z., Tan, Y., Barbara, A. M., Kaur, S., Truong, A., Gorlov, I. P., and Agoulnik, A. I. (2011) Suppression of insulin-like3 receptor reveals the role of beta-catenin and Notch signaling in gubernaculum development. *Molecular endocrinology (Baltimore, Md.)* **25**, 170-183

100. Sharma, V., Lehmann, T., Stuckas, H., Funke, L., and Hiller, M. (2018) Loss of RXFP2 and INSL3 genes in Afrotheria shows that testicular descent is the ancestral condition in placental mammals. *PLoS Biol* **16**, e2005293

101. Amory, J. K., Page, S. T., Anawalt, B. D., Coviello, A. D., Matsumoto, A. M., and Bremner, W. J. (2007) Elevated end-of-treatment serum INSL3 is associated with failure to completely suppress spermatogenesis in men receiving male hormonal contraception. *J Androl* **28**, 548-554

102. Minagawa, I., Murata, Y., Terada, K., Shibata, M., Park, E. Y., Sasada, H., and Kohsaka, T. (2018) Evidence for the role of INSL3 on sperm production in boars by passive immunisation. *Andrologia* **50**, e13010

103. El Houate, B., Rouba, H., Sibai, H., Barakat, A., Chafik, A., Chadli el, B., Imken, L., Bogatcheva, N. V., Feng, S., Agoulnik, A. I., and McElreavey, K. (2007) Novel mutations involving the INSL3 gene associated with cryptorchidism. *The Journal of urology* **177**, 1947-1951

104. Bogatcheva, N. V., Truong, A., Feng, S., Engel, W., Adham, I. M., and Agoulnik, A. I. (2003) GREAT/LGR8 is the only receptor for insulin-like 3 peptide. *Molecular endocrinology (Baltimore, Md.)* **17**, 2639-2646

105. Gorlov, I. P., Kamat, A., Bogatcheva, N. V., Jones, E., Lamb, D. J., Truong, A., Bishop, C. E., McElreavey, K., and Agoulnik, A. I. (2002) Mutations of the GREAT gene cause cryptorchidism. *Human molecular genetics* **11**, 2309-2318

106. Ayers, K., Kumar, R., Robevska, G., Bruell, S., Bell, K., Malik, M. A., Bathgate, R. A., and Sinclair, A. (2019) Familial bilateral cryptorchidism is caused by recessive variants in RXFP2. *Journal of medical genetics*

107. Capra, A. P., Ferro, E., La Rosa, M. A., Briuglia, S., Russo, T., Arena, S., Salpietro Damiano, C., Romeo, C., and Impellizzeri, P. (2018) Genetic analysis of the human insulin-like 3 gene in pediatric patients with testicular torsion. *Pediatric surgery international* **34**, 807-812

108. Lim, H. N., Raipert-de Meyts, E., Skakkebaek, N. E., Hawkins, J. R., and Hughes, I. A. (2001) Genetic analysis of the INSL3 gene in patients with maldescent of the testis. *European journal of endocrinology* **144**, 129-137

109. Ars, E., Lo Giacco, D., Bassas, L., Nuti, F., Rajmil, O., Ruiz, P., Garat, J. M., Ruiz-Castane, E., and Krausz, C. (2011) Further insights into the role of T222P variant of RXFP2 in non-syndromic cryptorchidism in two Mediterranean populations. *Int J Androl* **34**, 333-338

110. Bamberger, A. M., Ivell, R., Balvers, M., Kelp, B., Bamberger, C. M., Riethdorf, L., and Loning, T. (1999) Relaxin-like factor (RLF): a new specific marker for Leydig cells in the ovary. *Int J Gynecol Pathol* **18**, 163-168

111. Dai, Y., Ivell, R., Liu, X., Janowski, D., and Anand-Ivell, R. (2017) Relaxin-Family Peptide Receptors 1 and 2 Are Fully Functional in the Bovine. *Frontiers in physiology* **8**, 359

112. Li, Z., Feng, S., Lopez, V., Elhammady, G., Anderson, M. L., Kaftanovskaya, E. M., and Agoulnik, A. I. (2011) Uterine cysts in female

mice deficient for caveolin-1 and insulin-like 3 receptor RXFP2. *Endocrinology* **152**, 2474-2482

113. Hagen, C. P., Mieritz, M. G., Nielsen, J. E., Anand-Ivell, R., Ivell, R., and Juul, A. (2015) Longitudinal assessment of circulating insulin-like peptide 3 levels in healthy peripubertal girls. *Fertility and sterility* **103**, 780-786.e781

114. Anand-Ivell, R., Tremellen, K., Dai, Y., Heng, K., Yoshida, M., Knight, P. G., Hale, G. E., and Ivell, R. (2013) Circulating insulin-like factor 3 (INSL3) in healthy and infertile women. *Human reproduction (Oxford, England)* **28**, 3093-3102

115. Anand-Ivell, R., Wohlgemuth, J., Haren, M. T., Hope, P. J., Hatzinikolas, G., Wittert, G., and Ivell, R. (2006) Peripheral INSL3 concentrations decline with age in a large population of Australian men. *Int J Androl* **29**, 618-626

116. Dai, Y., Ivell, R., and Anand-Ivell, R. (2017) Theca Cell INSL3 and Steroids Together Orchestrate the Growing Bovine Antral Follicle. *Frontiers in physiology* **8**, 1033

117. Glister, C., Satchell, L., Bathgate, R. A., Wade, J. D., Dai, Y., Ivell, R., Anand-Ivell, R., Rodgers, R. J., and Knight, P. G. (2013) Functional link between bone morphogenetic proteins and insulin-like peptide 3 signaling in modulating ovarian androgen production. *Proceedings of the National Academy of Sciences of the United States of America* **110**, E1426-1435

118. Seyam, E., and Hefzy, E. (2018) Evaluation of the correlation between insulin like factor 3, polycystic ovary syndrome, and ovarian maldescent. *Gynecological endocrinology : the official journal of the International Society of Gynecological Endocrinology* **34**, 481-488

119. Shaikh, N., Dadachanji, R., Meherji, P., Shah, N., and Mukherjee, S. (2016) Polymorphisms and haplotypes of insulin-like factor 3 gene are associated with risk of polycystic ovary syndrome in Indian women. *Gene* **577**, 180-186

120. Di Nisio, A., De Toni, L., Rocca, M. S., Ghezzi, M., Selice, R., Taglialavoro, G., Ferlin, A., and Foresta, C. (2018) Negative Association Between

Sclerostin and INSL3 in Isolated Human Osteocytes and in Klinefelter Syndrome: New Hints for Testis-Bone Crosstalk. *The Journal of clinical endocrinology and metabolism* **103**, 2033-2041

121. Sedaghat, K., Shen, P. J., Finkelstein, D. I., Henderson, J. M., and Gundlach, A. L. (2008) Leucine-rich repeat-containing G-protein-coupled receptor 8 in the rat brain: Enrichment in thalamic neurons and their efferent projections. *Neuroscience* **156**, 319-333

122. Hampel, U., Klonisch, T., Sel, S., Schulze, U., Garreis, F., Seitmann, H., Zouboulis, C. C., and Paulsen, F. P. (2013) Insulin-like factor 3 promotes wound healing at the ocular surface. *Endocrinology* **154**, 2034-2045

123. Fu, P., Shen, P. J., Zhao, C. X., Scott, D. J., Samuel, C. S., Wade, J. D., Tregear, G. W., Bathgate, R. A., and Gundlach, A. L. (2006) Leucine-rich repeat-containing G-protein-coupled receptor 8 in mature glomeruli of developing and adult rat kidney and inhibition by insulin-like peptide-3 of glomerular cell proliferation. *The Journal of endocrinology* **189**, 397-408

124. Klonisch, T., Muller-Huesmann, H., Riedel, M., Kehlen, A., Bialek, J., Radestock, Y., Holzhausen, H. J., Steger, K., Ludwig, M., Weidner, W., Hoang-Vu, C., and Hombach-Klonisch, S. (2005) INSL3 in the benign hyperplastic and neoplastic human prostate gland. *International journal of oncology* **27**, 307-315

125. Hombach-Klonisch, S., Bialek, J., Radestock, Y., Truong, A., Agoulnik, A. I., Fiebig, B., Willing, C., Weber, E., Hoang-Vu, C., and Klonisch, T. (2010) INSL3 has tumor-promoting activity in thyroid cancer. *International journal of cancer* **127**, 521-531

126. Anand-Ivell, R., Heng, K., Hafen, B., Setchell, B., and Ivell, R. (2009) Dynamics of INSL3 peptide expression in the rodent testis. *Biology of reproduction* **81**, 480-487

127. Nagorniewicz, B., Mardhian, D. F., Booijink, R., Storm, G., Prakash, J., and Bansal, R. (2019) Engineered Relaxin as theranostic nanomedicine to diagnose and ameliorate liver cirrhosis. *Nanomedicine* **17**, 106-118

128. Muppidi, A., Lee, S. J., Hsu, C. H., Zou, H., Lee, C., Pflimlin, E., Mahankali, M., Yang, P., Chao, E., Ahmad, I., Crameri, A., Wang, D., Woods, A., and Shen, W. (2019) Design and Synthesis of Potent, Long-Acting Lipidated Relaxin-2 Analogs. *Bioconjug Chem* **30**, 83-89

129. Sun, J., Hao, W., Fillmore, N., Ma, H., Springer, D., Yu, Z. X., Sadowska, A., Garcia, A., Chen, R., Muniz-Medina, V., Rosenthal, K., Lin, J., Kuruvilla, D., Osbourn, J., Karathanasis, S. K., Walker, J., and Murphy, E. (2019) Human Relaxin-2 Fusion Protein Treatment Prevents and Reverses Isoproterenol-Induced Hypertrophy and Fibrosis in Mouse Heart. *J Am Heart Assoc* **8**, e013465

130. Kaftanovskaya, E. M., Ng, H. H., Soula, M., Rivas, B., Myhr, C., Ho, B. A., Cervantes, B. A., Shupe, T. D., Devarasetty, M., Hu, X., Xu, X., Patnaik, S., Wilson, K. J., Barnaeva, E., Ferrer, M., Southall, N. T., Marugan, J. J., Bishop, C. E., Agoulnik, I. U., and Agoulnik, A. I. (2019) Therapeutic effects of a small molecule agonist of the relaxin receptor ML290 in liver fibrosis. *FASEB J*, fj201901046R

131. Vedel, L., Bräuner-Osborne, H., and Mathiesen, J. M. (2015) A cAMP Biosensor-Based High-Throughput Screening Assay for Identification of Gs-Coupled GPCR Ligands and Phosphodiesterase Inhibitors. *Journal of biomolecular screening* **20**, 849-857

132. Williams, C. (2004) cAMP detection methods in HTS: selecting the best from the rest. *Nature Reviews Drug Discovery* **3**, 125-135

133. Titus, S., Neumann, S., Zheng, W., Southall, N., Michael, S., Klumpp, C., Yasgar, A., Shinn, P., Thomas, C. J., Inglese, J., Gershengorn, M. C., and Austin, C. P. (2008) Quantitative high-throughput screening using a live-cell cAMP assay identifies small-molecule agonists of the TSH receptor. *Journal of biomolecular screening* **13**, 120-127

134. Pantel, J., Williams, S. Y., Mi, D., Sebag, J., Corbin, J. D., Weaver, C. D., and Cone, R. D. (2011) Development of a high throughput screen for allosteric modulators of melanocortin-4 receptor signaling using a real time cAMP assay. *European journal of pharmacology* **660**, 139-147

135. Gabriel, D., Vernier, M., Pfeifer, M. J., Dasen, B., Tenaillon, L., and Bouhelal, R. (2003) High throughput screening technologies for direct cyclic AMP measurement. *Assay and drug development technologies* **1**, 291-303

136. Xiao, J., Huang, Z., Chen, C. Z., Agoulnik, I. U., Southall, N., Hu, X., Jones, R. E., Ferrer, M., Zheng, W., Agoulnik, A. I., and Marugan, J. J. (2013) Identification and optimization of small-molecule agonists of the human relaxin hormone receptor RXFP1. *Nature communications* **4**, 1953

137. Xiao, J., Chen, C. Z., Huang, Z., Agoulnik, I. U., Ferrer, M., Southall, N., Hu, X., Zheng, W., Agoulnik, A. I., and Marugan, J. J. (2010) Discovery, optimization, and biological activity of the first potent and selective small-molecule agonist series of human relaxin receptor 1 (RXFP1). In *Probe Reports from the NIH Molecular Libraries Program*, National Center for Biotechnology Information (US), Bethesda (MD)

138. Kocan, M., Sarwar, M., Ang, S. Y., Xiao, J., Marugan, J. J., Hossain, M. A., Wang, C., Hutchinson, D. S., Samuel, C. S., Agoulnik, A. I., Bathgate, R. A. D., and Summers, R. J. (2017) ML290 is a biased allosteric agonist at the relaxin receptor RXFP1. *Scientific reports* **7**, 2968

139. Ng, H. H., Soula, M., Rivas, B., Wilson, K. J., Marugan, J. J., and Agoulnik, A. I. (2021) Anti-apoptotic and Matrix Remodeling Actions of a Small Molecule Agonist of the Human Relaxin Receptor, ML290 in Mice With Unilateral Ureteral Obstruction. *Frontiers in physiology* **12**, 650769

140. Tardieu, J.-L. (2008) Selecting a cyclic AMP kit for assaying GPCR target activation. *Nature Methods* **5**, iii-iv

141. Hsu, S. Y., Nakabayashi, K., Nishi, S., Kumagai, J., Kudo, M., Sherwood, O. D., and Hsueh, A. J. (2002) Activation of orphan receptors by the hormone relaxin. *Science (New York, N.Y.)* **295**, 671-674

142. Jean-Charles, P. Y., Kaur, S., and Shenoy, S. K. (2017) G Protein-Coupled Receptor Signaling Through β-Arrestin-Dependent Mechanisms. *Journal of cardiovascular pharmacology* **70**, 142-158

143. Czekanska, E. M., Stoddart, M. J., Richards, R. G., and Hayes, J. S. (2012) In search of an osteoblast cell model for in vitro research. *European cells & materials* **24**, 1-17

144. Lin, X., Patil, S., Gao, Y.-G., and Qian, A. (2020) The Bone Extracellular Matrix in Bone Formation and Regeneration. *Frontiers in pharmacology* **11**

145. Cheloha, R. W., Gellman, S. H., Vilardaga, J. P., and Gardella, T. J. (2015) PTH receptor-1 signalling-mechanistic insights and therapeutic prospects. *Nature reviews. Endocrinology* **11**, 712-724

146. Kulkarni, N. H., Halladay, D. L., Miles, R. R., Gilbert, L. M., Frolik, C. A., Galvin, R. J., Martin, T. J., Gillespie, M. T., and Onyia, J. E. (2005) Effects of parathyroid hormone on Wnt signaling pathway in bone. *Journal of cellular biochemistry* **95**, 1178-1190

147. Deng, Z., Ng, C., Inoue, K., Chen, Z., Xia, Y., Hu, X., Greenblatt, M., Pernis, A., and Zhao, B. (2020) Def6 regulates endogenous type-I interferon responses in osteoblasts and suppresses osteogenesis. *eLife* **9**

148. Kota, S. K., Roening, C., Patel, N., Kota, S. B., and Baron, R. (2018) PRMT5 inhibition promotes osteogenic differentiation of mesenchymal stromal cells and represses basal interferon stimulated gene expression. *Bone* **117**, 37-46

149. Ma, X., Xu, Z., Ding, S., Yi, G., and Wang, Q. (2018) Alendronate promotes osteoblast differentiation and bone formation in ovariectomy-induced osteoporosis through interferon-β/signal transducer and activator of transcription 1 pathway. *Experimental and therapeutic medicine* **15**, 182-190

150. Duque, G., Huang, D. C., Dion, N., Macoritto, M., Rivas, D., Li, W., Yang, X. F., Li, J., Lian, J., Marino, F. T., Barralet, J., Lascau, V., Deschênes, C., Ste-Marie, L. G., and Kremer, R. (2011) Interferon-γ plays a role in bone formation in vivo and rescues osteoporosis in ovariectomized mice. *J Bone Miner Res* **26**, 1472-1483

151. Duque, G., Huang, D. C., Macoritto, M., Rivas, D., Yang, X. F., Ste-Marie, L. G., and Kremer, R. (2009) Autocrine regulation of interferon gamma in mesenchymal stem cells plays a role in early osteoblastogenesis. *Stem cells (Dayton, Ohio)* **27**, 550-558

152. Albers, J., Schulze, J., Beil, F. T., Gebauer, M., Baranowsky, A., Keller, J., Marshall, R. P., Wintges, K., Friedrich, F. W., Priemel, M., Schilling, A. F., Rueger, J. M., Cornils, K., Fehse, B., Streichert, T., Sauter, G., Jakob, F., Insogna, K. L., Pober, B., Knobeloch, K. P., Francke, U., Amling, M., and Schinke, T. (2011) Control of bone formation by the serpentine receptor Frizzled-9. *The Journal of cell biology* **192**, 1057-1072

153. Kim, B. S., Kim, H. J., Kim, J. S., You, Y. O., Zadeh, H., Shin, H. I., Lee, S. J., Park, Y. J., Takata, T., Pi, S. H., Lee, J., and You, H. K. (2012) IFITM1 increases osteogenesis through Runx2 in human alveolar-derived bone marrow stromal cells. *Bone* **51**, 506-514

154. Infante, A., and Rodríguez, C. I. (2018) Osteogenesis and aging: lessons from mesenchymal stem cells. *Stem Cell Research & Therapy* **9**, 244

155. Bandyopadhyay, A., Tsuji, K., Cox, K., Harfe, B. D., Rosen, V., and Tabin, C. J. (2006) Genetic analysis of the roles of BMP2, BMP4, and BMP7 in limb patterning and skeletogenesis. *PLoS genetics* **2**, e216

156. Paine-Saunders, S., Viviano, B. L., Zupicich, J., Skarnes, W. C., and Saunders, S. (2000) glypican-3 controls cellular responses to Bmp4 in limb patterning and skeletal development. *Developmental biology* **225**, 179-187

157. Dwivedi, P. P., Grose, R. H., Filmus, J., Hii, C. S., Xian, C. J., Anderson, P. J., and Powell, B. C. (2013) Regulation of bone morphogenetic protein signalling and cranial osteogenesis by Gpc1 and Gpc3. *Bone* **55**, 367-376

158. Devlin, R. D., Du, Z., Buccilli, V., Jorgetti, V., and Canalis, E. (2002) Transgenic mice overexpressing insulin-like growth factor binding protein-5 display transiently decreased osteoblastic function and osteopenia. *Endocrinology* **143**, 3955-3962

159. Mukherjee, A., and Rotwein, P. (2008) Insulin-like growth factor-binding protein-5 inhibits osteoblast differentiation and skeletal growth by blocking insulin-like growth factor actions. *Molecular endocrinology (Baltimore, Md.)* **22**, 1238-1250

160. Durant, D., Pereira, R. M., and Canalis, E. (2004) Overexpression of insulin-like growth factor binding protein-5 decreases osteoblastic function in vitro. *Bone* **35**, 1256-1262

161. Robert, A. W., Marcon, B. H., Dallagiovanna, B., and Shigunov, P. (2020) Adipogenesis, Osteogenesis, and Chondrogenesis of Human Mesenchymal Stem/Stromal Cells: A Comparative Transcriptome Approach. *Frontiers in Cell and Developmental Biology* **8**

162. Yue, R., Zhou, B. O., Shimada, I. S., Zhao, Z., and Morrison, S. J. (2016) Leptin Receptor Promotes Adipogenesis and Reduces Osteogenesis by Regulating Mesenchymal Stromal Cells in Adult Bone Marrow. *Cell stem cell* **18**, 782-796

163. Lu, S., and Zhang, J. (2019) Small Molecule Allosteric Modulators of G-Protein-Coupled Receptors: Drug-Target Interactions. *Journal of medicinal chemistry* **62**, 24-45

164. Smith, J. S., Lefkowitz, R. J., and Rajagopal, S. (2018) Biased signalling: from simple switches to allosteric microprocessors. *Nature Reviews Drug Discovery* **17**, 243-260

165. Scott, D. J., Rosengren, K. J., and Bathgate, R. A. (2012) The different ligand-binding modes of relaxin family peptide receptors RXFP1 and RXFP2. *Molecular endocrinology (Baltimore, Md.)* **26**, 1896-1906

166. Shabanpoor, F., Zhang, S., Hughes, R. A., Hossain, M. A., Layfield, S., Ferraro, T., Bathgate, R. A., Separovic, F., and Wade, J. D. (2011) Design and development of analogues of dimers of insulin-like peptide 3 B-chain as high-affinity antagonists of the RXFP2 receptor. *Biopolymers* **96**, 81-87

167. Liu, X., Ahn, S., Kahsai, A. W., Meng, K. C., Latorraca, N. R., Pani, B., Venkatakrishnan, A. J., Masoudi, A., Weis, W. I., Dror, R. O., Chen, X., Lefkowitz, R. J., and Kobilka, B. K. (2017) Mechanism of intracellular allosteric β(2)AR antagonist revealed by X-ray crystal structure. *Nature* **548**, 480-484

168. Kruse, A. C., Ring, A. M., Manglik, A., Hu, J., Hu, K., Eitel, K., Hübner, H., Pardon, E., Valant, C., Sexton, P. M., Christopoulos, A., Felder, C. C., Gmeiner, P., Steyaert, J., Weis, W. I., Garcia, K. C., Wess, J., and Kobilka, B. K. (2013) Activation and allosteric modulation of a muscarinic acetylcholine receptor. *Nature* **504**, 101-106

169. Duan, J., Xu, P., Cheng, X., Mao, C., Croll, T., He, X., Shi, J., Luan, X., Yin, W., You, E., Liu, Q., Zhang, S., Jiang, H., Zhang, Y., Jiang, Y., and Xu, H. E. (2021) Structures of full-length glycoprotein hormone receptor signalling complexes. *Nature* **598**, 688-692

170. Hu, X., Myhr, C., Huang, Z., Xiao, J., Barnaeva, E., Ho, B. A., Agoulnik, I. U., Ferrer, M., Marugan, J. J., Southall, N., and Agoulnik, A. I. (2016) Structural Insights into the Activation of Human Relaxin Family Peptide Receptor 1 by Small-Molecule Agonists. *Biochemistry* **55**, 1772-1783

171. Waterhouse, A., Bertoni, M., Bienert, S., Studer, G., Tauriello, G., Gumienny, R., Heer, F. T., de Beer, T. A P., Rempfer, C., Bordoli, L., Lepore, R., and Schwede, T. (2018) SWISS-MODEL: homology modelling of protein structures and complexes. *Nucleic Acids Research* **46**, W296-W303

172. Friesner, R. A., Banks, J. L., Murphy, R. B., Halgren, T. A., Klicic, J. J., Mainz, D. T., Repasky, M. P., Knoll, E. H., Shelley, M., Perry, J. K., Shaw, D. E., Francis, P., and Shenkin, P. S. (2004) Glide: a new approach for rapid, accurate docking and scoring. 1. Method and assessment of docking accuracy. *Journal of medicinal chemistry* **47**, 1739-1749

173. Halgren, T. A., Murphy, R. B., Friesner, R. A., Beard, H. S., Frye, L. L., Pollard, W. T., and Banks, J. L. (2004) Glide: a new approach for rapid, accurate docking and scoring. 2. Enrichment factors in database screening. *Journal of medicinal chemistry* **47**, 1750-1759

174. Friesner, R. A., Murphy, R. B., Repasky, M. P., Frye, L. L., Greenwood, J. R., Halgren, T. A., Sanschagrin, P. C., and Mainz, D. T. (2006) Extra precision glide: docking and scoring incorporating a model of hydrophobic enclosure for protein-ligand complexes. *Journal of medicinal chemistry* **49**, 6177-6196

175. Bowers, K. J., Chow, E., Xu, H., Dror, R. O., Eastwood, M. P., Gregersen, B. A., Klepeis, J. L., Kolossvary, I., Moraes, M. A., Sacerdoti, F. D., Salmon, J. K., Shan, Y., and Shaw, D. E. (2006) Scalable algorithms for molecular dynamics simulations on commodity clusters. In *Proceedings of the 2006 ACM/IEEE conference on Supercomputing* pp. 84–es, Association for Computing Machinery, Tampa, Florida

176. Tuckerman, M., Berne, B. J., and Martyna, G. J. (1992) Reversible multiple time scale molecular dynamics. *The Journal of Chemical Physics* **97**, 1990-2001

177. Yang, D., Zhou, Q., Labroska, V., Qin, S., Darbalaei, S., Wu, Y., Yuliantie, E., Xie, L., Tao, H., Cheng, J., Liu, Q., Zhao, S., Shui, W., Jiang, Y., and Wang, M.-W. (2021) G protein-coupled receptors: structure- and function-based drug discovery. *Signal Transduction and Targeted Therapy* **6**, 7

178. Kooistra, A. J., Mordalski, S., Pándy-Szekeres, G., Esguerra, M., Mamyrbekov, A., Munk, C., Keserű, G. M., and Gloriam, David E. (2020) GPCRdb in 2021: integrating GPCR sequence, structure and function. *Nucleic Acids Research* **49**, D335-D343

179. Pándy-Szekeres, G., Esguerra, M., Hauser, A. S., Caroli, J., Munk, C., Pilger, S., Keserű, György M., Kooistra, Albert J., and Gloriam, David E. (2021) The G protein database, GproteinDb. *Nucleic Acids Research*

180. Speck, D., Kleinau, G., Meininghaus, M., Erbe, A., Einfeldt, A., Szczepek, M., Scheerer, P., and Pütter, V. (2021) Expression and Characterization of Relaxin Family Peptide Receptor 1 Variants. *Frontiers in pharmacology* **12**, 826112

181. Erlandson, S. C., Rawson, S., Brock, K. P., Liu, X., Paulo, J. A., Mintseris, J., Gygi, S. P., Marks, D. S., Cong, X., and Kruse, A. C. (2022) The relaxin

receptor RXFP1 signals through a mechanism of autoinhibition. *bioRxiv*, 2022.2001.2022.477343

182. Kaftanovskaya, E. M., Soula, M., Myhr, C., Ho, B. A., Moore, S. N., Yoo, C., Cervantes, B., How, J., Marugan, J., Agoulnik, I. U., and Agoulnik, A. I. (2017) Human Relaxin Receptor Is Fully Functional in Humanized Mice and Is Activated by Small Molecule Agonist ML290. *Journal of the Endocrine Society* **1**, 712-725

183. Bay, K., and Andersson, A. M. (2011) Human testicular insulin-like factor 3: in relation to development, reproductive hormones and andrological disorders. *Int J Androl* **34**, 97-109

184. Glatt, V., Canalis, E., Stadmeyer, L., and Bouxsein, M. L. (2007) Age-related changes in trabecular architecture differ in female and male C57BL/6J mice. *J Bone Miner Res* **22**, 1197-1207

185. Nef, S., and Parada, L. F. (2000) Hormones in male sexual development. *Genes & development* **14**, 3075-3086

186. Bouxsein, M. L., Boyd, S. K., Christiansen, B. A., Guldberg, R. E., Jepsen, K. J., and Müller, R. (2010) Guidelines for assessment of bone microstructure in rodents using micro-computed tomography. *J Bone Miner Res* **25**, 1468-1486

187. Buraundi, S., Balic, A., Farmer, P. J., Southwell, B. R., and Hutson, J. M. (2011) Gubernacular development in the mouse is similar to the rat and suggests that the processus vaginalis is derived from the urogenital ridge and is different from the parietal peritoneum. *Journal of pediatric surgery* **46**, 1804-1812

188. Beamer, W. G., Donahue, L. R., Rosen, C. J., and Baylink, D. J. (1996) Genetic variability in adult bone density among inbred strains of mice. *Bone* **18**, 397-403

189. Hsu, S. Y., Nakabayashi, K., Nishi, S., Kumagai, J., Kudo, M., Bathgate, R. A., Sherwood, O. D., and Hsueh, A. J. (2003) Relaxin signaling in reproductive tissues. *Molecular and cellular endocrinology* **202**, 165-170

190. Perera, N., Szarek, M., Vannitamby, A., Vikraman, J., Huan, G., Durston, A., Hutson, J., and Li, R. (2018) An immunohistochemical analysis of the effects of androgen receptor knock out on gubernacular differentiation in the mouse. *Journal of pediatric surgery* **53**, 1776-1780

191. Kaftanovskaya, E. M., Huang, Z., Barbara, A. M., De Gendt, K., Verhoeven, G., Gorlov, I. P., and Agoulnik, A. I. (2012) Cryptorchidism in mice with an androgen receptor ablation in gubernaculum testis. *Molecular endocrinology (Baltimore, Md.)* **26**, 598-607

192. Brent, M. B., Stoltenborg, F. E., Brüel, A., and Thomsen, J. S. (2021) Teriparatide and Abaloparatide Have a Similar Effect on Bone in Mice. *Frontiers in endocrinology* **12**

193. Corrado, A., Cici, D., Rotondo, C., Maruotti, N., and Cantatore, F. P. (2020) Molecular Basis of Bone Aging. *International journal of molecular sciences* **21**

194. Sriram, K., and Insel, P. A. (2018) G Protein-Coupled Receptors as Targets for Approved Drugs: How Many Targets and How Many Drugs? *Molecular pharmacology* **93**, 251-258

195. Takayanagi, H., Kim, S., and Taniguchi, T. (2002) Signaling crosstalk between RANKL and interferons in osteoclast differentiation. *Arthritis Research & Therapy* **4**, S227

196. Alliston, T., and Derynck, R. (2002) Interfering with bone remodelling. *Nature* **416**, 686-687

197. Sun, Q., Liu, L., Mandal, J., Molino, A., Stolz, D., Tamm, M., Lu, S., and Roth, M. (2016) PDGF-BB induces PRMT1 expression through ERK1/2 dependent STAT1 activation and regulates remodeling in primary human lung fibroblasts. *Cellular signalling* **28**, 307-315

198. Song, Z., Xiong, B., Zheng, H., Manyande, A., Guan, X., Cao, F., Ren, L., Zhou, Y., Ye, D., and Tian, Y. (2017) STAT1 as a downstream mediator of ERK signaling contributes to bone cancer pain by regulating MHC II expression in spinal microglia. *Brain, behavior, and immunity* **60**, 161-173

199. Weske, S., Vaidya, M., von Wnuck Lipinski, K., Keul, P., Manthe, K., Burkhart, C., Haberhauer, G., Heusch, G., and Levkau, B. (2019) Agonist-induced activation of the S1P receptor 2 constitutes a novel osteoanabolic therapy for the treatment of osteoporosis in mice. *Bone* **125**, 1-7

200. Jilka, R. L., Hangoc, G., Girasole, G., Passeri, G., Williams, D. C., Abrams, J. S., Boyce, B., Broxmeyer, H., and Manolagas, S. C. (1992) Increased osteoclast development after estrogen loss: mediation by interleukin-6. *Science (New York, N.Y.)* **257**, 88-91

201. Fujita, H., Hinoi, E., Watanabe, T., Iezaki, T., Takamori, M., Ogawa, S., and Yoneda, Y. (2013) Prevention of bone loss after ovariectomy in mice with preferential overexpression of the transcription factor paired box-5 in osteoblasts. *Biological & pharmaceutical bulletin* **36**, 481-484

202. Lelovas, P. P., Xanthos, T. T., Thoma, S. E., Lyritis, G. P., and Dontas, I. A. (2008) The laboratory rat as an animal model for osteoporosis research. *Comparative medicine* **58**, 424-430

203. Marini, J. C., Forlino, A., Bächinger, H. P., Bishop, N. J., Byers, P. H., Paepe, A. D., Fassier, F., Fratzl-Zelman, N., Kozloff, K. M., Krakow, D., Montpetit, K., and Semler, O. (2017) Osteogenesis imperfecta. *Nature Reviews Disease Primers* **3**, 17052

204. Marom, R., Rabenhorst, B. M., and Morello, R. (2020) Osteogenesis imperfecta: an update on clinical features and therapies. *European journal of endocrinology* **183**, R95-r106

205. Lindahl, K., Åström, E., Rubin, C.-J., Grigelioniene, G., Malmgren, B., Ljunggren, Ö., and Kindmark, A. (2015) Genetic epidemiology, prevalence, and genotype–phenotype correlations in the Swedish population with osteogenesis imperfecta. *European Journal of Human Genetics* **23**, 1042-1050

206. Kohler, R., Tastad, C. A., Creecy, A., and Wallace, J. M. (2021) Morphological and mechanical characterization of bone phenotypes in the Amish G610C murine model of osteogenesis imperfecta. *PLoS One* **16**, e0255315

VITA

MARIA ESTEBAN LOPEZ

EDUCATION AND AWARDS

2008 – 2013	Bachelor of Science in Biotechnology Universidad Francisco de Vitoria Madrid, Spain
2015 – 2016	Master of Science in Neurosciences Universitat Autònoma de Barcelona Barcelona, Spain
2017 – 2022	Doctoral Candidate Florida International University Miami, Florida

FIU Doctoral Evidence Acquisition (DEA) Fellowship. Summer 2021

FIU Dissertation Year Fellowship (DYF). Fall 2021 & Spring 2022

ASPET Travel Award. Experimental Biology. April 1-5, 2022

First Place Graduate Student Poster Abstract Award. FIU CTS First South Florida Translational Research Symposium. April 13 & 14, 2022

PUBLICATIONS AND PRESENTATIONS

Esteban-Lopez M, Wilson KJ, Myhr C, Kaftanovskaya EM, Henderson MJ, Southall NT, Xu X, Wang A, Hu X, Barnaeva E, Ye W, George ER, Sherrill JT, Ferrer M, Morello R, Agoulnik IU, Marugan J, Agoulnik AI. Discovery of small molecule agonists of the Relaxin Family Peptide Receptor 2. Communications Biology. 2022 (Under review)

Esteban-Lopez M, Perry MD, Garbinski LD, Manevsk M, Andre M, Ceyhan Y, Caobi A, Paul P, Lau LS, Ramelow J, Owens F, Souchak J, Ales E, El-Hage N. Health effects and known pathologies associated with the use of E-cigarettes. Toxicol Rep. 2022 Jun 16;9:1357-1368. doi: 10.1016/j.toxrep.2022.06.006.

Marugan JJ, Southall NT, Ferrer M, Henderson MJ, Wilson KJ, Agoulnik AI, Myhr CB**,** Esteban-Lopez M, Barnaeva E, Hu X, Ye W, Agoulnik IU. Small Molecule Agonists of the Insulin-like (INSL3) Peptide Receptor RXFP2 and Methods of Use Thereof. 2022. Patent application number 63/308,768.

Esteban-Lopez M, Agoulnik AI. Diverse functions of insulin-like 3 peptide. J Endocrinol. 2020 Oct 1;247(1):R1-R12. doi: 10.1530/JOE-20-0168.

Caobi A, Dutta RK, Garbinski LD, Esteban-Lopez M, Ceyhan Y, Andre M, Manevski M, Ojha CR, Lapierre J, Tiwari S, Parira T, El-Hage N. The Impact of CRISPR-Cas9 on Age-related Disorders: From Pathology to Therapy. Aging Dis. 2020 Jul 23;11(4):895-915. doi: 10.14336/AD.2019.0927.

Ng HH, Esteban-Lopez M, Agoulnik AI. Targeting the relaxin/insulin-like family peptide receptor 1 and 2 with small molecule compounds. Mol Cell Endocrinol. 2019 May 1;487:40-44. doi: 10.1016/j.mce.2018.12.013.

Tiwari S, Lapierre J, Ojha CR, Martins K, Parira T, Dutta RK, Caobi A, Garbinski L, Ceyhan Y, Esteban-Lopez M, El-Hage N. Signaling pathways and therapeutic perspectives related to environmental factors associated with multiple sclerosis. J Neurosci Res. 2018 Dec;96(12):1831-1846. doi: 10.1002/jnr.24322.

“RXFP2 Small Molecule Agonists: Potential Therapeutics for Osteoporosis.” Oral presentation via Zoom at the International Relaxin Seminar Series. May 25, 2022.

“RXFP2 Small Molecule Agonists: Potential Therapeutics for Osteoporosis.” Oral presentation at the FIU-HWCOM 8th Annual Research Symposium. April 22, 2022. Miami, FL

“RXFP2 Small Molecule Agonists: Potential Therapeutics for Osteoporosis.” Poster presentation at the FIU-CTS 1st South Florida Translation Research Symposium. April 13 & 14, 2022. Port Saint Lucie, FL

“RXFP2 Small Molecule Agonists: Potential Therapeutics for Osteoporosis.” Oral and poster presentation at Experimental Biology - ASPET Drug Discovery and Development Division. April 1-5, 2022. Philadelphia, PA

“RXFP2 Small Molecule Agonists: Potential Therapeutics for Osteoporosis.” Oral presentation via Zoom at the Eastern-Atlantic Student Research Forum. February 12 & 13, 2022.